Structural insights into the conformational plasticity and antibody recognition of HIV-1 Env

Thesis by

Kim-Marie Anh Dam

In Partial Fulfillment of the Requirements for

the degree of

Doctor of Philosophy

CALIFORNIA INSTITUTE OF TECHNOLOGY

Pasadena, California

2023

(Defended October 25, 2022)

Kim-Marie Anh Dam
ORCID: 0000-0002-1416-4757

ACKNOWLEDGEMENTS

As I have been preparing my thesis over the past few weeks, I have been reflecting on the people in my life that have provided love, care, support, and the occasional reality check during this journey. I keep circling back to the old proverb; *it takes a village to raise a child.* Although I am no longer a child, this sentiment could not better describe how I feel about my development as a scientist. Through every experience, crossroad, and challenge, I have been fortunate to have a support system to help me through the hard times, celebrate the successes, and everything in between. I am so thankful for each and every one of you and I can only begin to express my gratitude for all you have done.

I want to start by thanking my family, and foremost, my parents. You brought me into this world as a young couple, dreaming of raising children who would have opportunities that for you were out of grasp. Twenty-nine years and five kids later, I can say on behalf of all my brother and sisters, you gave us that and so much more. Not only did you show us the importance of education for success, but you also taught us to move through this world meaningfully—to find a career we could love and master it so we can make an impact. Above all, you taught us to be humble and never forget the importance of family because they will have your back no matter what. *Blood is thicker than water,* as Baba always says. And so, to my siblings—Zach, Miranda, Alec, and Mallory—thank you for being my partners in crime, my harshest critics, and go-to crew when we need a late-night Kopp's run. To my little sister, Miranda, you are my first call when there is need for celebration, when I need a conscious to navigate boy problems, and when I can't decide if I should go wear the classic black boots or slightly uncomfortable, but totally cute, pumps. To Jill, my sister-in-law, my nephew and godson, Liam, grandma and grandpa, aunts and uncles, and cousins, thank you, thank you, thank you. I love you all so much.

Thank you to all of friends, especially my ride-or-dies, Cristian and Atousa. I am so lucky to have such fierce, loving, and brilliant people to enjoy a night out, a vacation get-away, couch time, heartbreak, and all the rest of life's adventures. I am so grateful to have you. I know you are not technically my blood, but you are my family. To my fur babies, Luna and Kiwi,

thank you for making sure I have companions to snug before bed, to lick me awake in the morning, and keep me covered in fur all day.

To everyone in the Bjorkman lab, thank you for your help and support during my time as a graduate student. You have made my time in the lab such a positive and enjoyable experience. To my former work wife, Morgan, I miss our lunchtime conversations and shared struggles in our experiments. To my bay watch crew and dearest friends, Magnus and Zhi, thank you for your friendship and mentorship. You guys are like my big brothers in lab, always looking out for me and pushing me forward when I am stuck. To my bay mate, Chengcheng Fan, thank you for indulging and sharing my daydreams of owning designer purses. To my former bay mate, Nicholas Koranda, thank you for your friendship and our shared love of cats. And, thank you to Marta. You are the heart of the lab. Your nurture and kindness have made me feel so at home, even when I am miles always from my family.

I would like to express my sincere gratitude to all of my professional mentors who have supported and guided me throughout my academic career. I am particularly grateful to my committee members, Sarkis Mazmanian, David Chan, and Rebecca Voorhees, for their invaluable advice and guidance during my graduate studies. I am also grateful to the mentors in the Bjorkman lab who have helped me develop my research skills. Collin Kieffer, who mentored me during my time as an Amgen scholar in the lab, and Beth Stadtmueller, who mentored me during my rotation, providing me with invaluable training and guidance. Andrey Malyutin, Songye Chen, Christopher Barnes, Zhi Yang, and Chengcheng Fan have also played a critical role in my development as a scientist, training me in single-particle cryo-EM and continuing to collaborate and provide guidance on my projects. I would also like to thank Jennifer Keeffe and Magnus Hoffmann, who taught me how to clone and continue to share their expertise to help me through my experiments. Additionally, I am grateful to my former advisor at DePaul University, Catherine Southern, for teaching me the ropes of being a female scientist when I was only a naïve undergraduate with hardly any lab experience. Finally, I would like to express my gratitude to Phillip Funk, who taught me the foundations of biology and immunology during my time at DePaul University, and to my high school science teacher, Ms. Van der Zel, who first sparked my interest in biology.

And, finally, thank you to my advisor, Pamela. As a graduate student in your lab, you have not only provided state-of-the-art professional training, but also served as a role model to me as a successful, hardworking, female scientist. You started your career during a time when women were faced with immense discrimination in academia, and you have made it a point in your career to ensure that women in STEM fields don't face those challenges. I am grateful to have such a champion of female scientist in my corner.

ABSTRACT

Acquired immunodeficiency syndrome (AIDS) and its causal agent, the human immunodeficiency virus 1 (HIV-1), remain a global public health concern since they were first identified in the early 1980s. Diligent research and gradual scientific advances have led to innovative strategies in HIV-1/AIDS prevention and treatment, transforming an obscure and deadly disease into a manageable condition with a normal life expectancy. Despite this progress, researchers have yet to develop a safe and effective vaccine against HIV-1. The work presented here describes a structural perspective related to the HIV-1 Envelope (Env) glycoprotein, the sole viral target of vaccines that seek to elicit neutralizing antibodies.

Env is the only viral protein on the surface of HIV-1 virions and is composed of a homotrimer of gp120/gp41 heterodimers. Env mediates entry into target cells by engaging the host receptor, CD4. CD4 triggers conformational changes in gp120, thereby enabling coreceptor recognition. Interactions with the host coreceptor trigger structural rearrangements in gp41 that facilitate fusion of host and viral membranes leading to infection. Our work builds upon our understanding of Env structural plasticity. First, we evaluated the conformational plasticity of soluble Env constructs using double electron-electron resonance (DEER) spectroscopy. This method measured distances between probes in Env subunits, allowing us to interpret the distribution in distances as Env flexibility. Our findings captured previously unseen nuances in static Env structures including gp41 elasticity and conformational heterogeneity associated with CD4-receptor binding. Although our work gave a new perspective on Env flexibility, it largely corroborated observations from static Env structures. Importantly, this suggested that soluble versions of Env, which serve as templates for immunogen design, retain favorable structural properties.

Informed with these insights in Env structure, we then sought to address a prevailing question related to receptor engagement: how many CD4 receptors are needed to induce gp120 conformation changes that lead to coreceptor binding followed by fusion? Prior work only characterized CD4-induced Env structural changes in Envs complexed with

three soluble CD4 proteins. In our work, we designed and structurally characterized Envs bound to only one or two CD4 receptors. We found that Env engagement of one CD4 resulted in minor changes to the prefusion, closed Env conformation while Env bound to two CD4 molecules led to CD4-induced opening in the CD4-bound gp120s and a partially open conformation in the unliganded gp120.

Structural biology has also been leveraged to characterize the mechanism by which broadly neutralizing antibodies (bNAbs) recognize HIV-1 Env. We include an extensive review of how structural observations from antibodies bound to viral proteins contribute to our understanding of antibody-mediated viral neutralization. We also present a technical evaluation of bNAb binding assays that revealed how Env conformations can be unintentionally altered resulting in misleading antibody binding results and identified ideal methods to ensure reliable data.

Additionally, we report on projects related to bNAbs that target the CD4 binding site (CD4bs) epitope of Env. In the first, we characterized the inferred germline (iGL) precursor of BG24, a VRC01-class bNAb with features that make it a promising target for vaccine design. We solved four cryo-EM structures of BG24iGL constructs complexed with different Envs and provided insight on the mode of iGL accommodation. The second project centers around the IOMA-class of CD4bs bNAbs. We characterized features of IOMA-class bNAbs and measured how different features contribute to neutralization breadth and potency. Taken together, the conclusions from our work provide guidance for the next generation of structure-based, CD4bs-targeting immunogen design.

PUBLISHED CONTENT AND CONTRIBUTIONS

Dam, K. A.*, Fan, C.*, Yang, Z., & Bjorkman, P. J. (2023). Structural characterization of HIV-1 Env heterotrimers bound to one or two CD4 receptors reveals intermediate Env conformations. *In Review & bioRxiv*. 2023.01.27.525985. https://doi.org/10.1101/2023.01.27.525985

Dam, K.A., Barnes, C. O., Gristick, H. B., Schoofs, T., Gnanapragasam, P. N. P., Nussenzweig, M. C., & Bjorkman, P. J. (2022). HIV-1 CD4-binding site germline antibody–Env structures inform vaccine design. *Nature Communications*, 13, 6123. https://doi.org/10.1101/2022.03.25.485873

Dam, K. A., Mutia, P. S., & Bjorkman, P. J. (2022). Comparing methods for immobilizing HIV-1 SOSIPs in ELISAs that evaluate antibody binding. Scientific Reports, 12(1), 11172. https://doi.org/10.1038/s41598-022-15506-x

Abernathy*, M. E., **Dam*, K. A.,** Esswein*, S. R., Jette*, C. A. & Bjorkman, P. J. How Antibodies Recognize Pathogenic Viruses: Structural Correlates of Antibody Neutralization of HIV-1, SARS-CoV-2, and Zika. Viruses 13, 2106 (2021). https://doi.org/10.3390/v13102106

Stadtmueller, B.M., Bridges, M.D., **Dam, K.A.**, Lerch, M.T., Huey-Tubman, K.E., Hubbell, W.L., & Bjorkman, P.J. DEER Spectroscopy Measurements Reveal Multiple Conformations of HIV-1 SOSIP Envelopes that Show Similarities with Envelopes on Native Virions. *Immunity*, *49*(2), 235-246 (2018). https://doi.org/10.1016/j.immuni.2018.06.017

**These authors contributed equally*

TABLE OF CONTENTS

Chapter I

INTRODUCTION

I. HIV-1 is the causative agent of AIDS

In the summer of 1981, clinicians in Los Angeles and New York City began to recognize an unusual pattern of symptoms that caused severe disease, primarily among the homosexual male population[1]. These symptoms included Kaposi sarcoma, opportunistic bacterial infections causing pneumonia, and persistent lymphadenopathy[1]. Within several months, there were approximately 300 cases reported with this unusual pattern of symptoms. Approximately 130 of the individuals in the reported cases had died by the end of the year. Several months later, the Center for Disease Control (CDC) formally defined this disease as acquired immune deficiency syndrome (AIDS). The CDC defined AIDS as "a defect in cell-mediated immunity, occurring in a person with no known cause for diminished resistance to that disease"[2]. Research at the time indicated that AIDS-related immune deficiency was associated with a large decline in the number of $CD4^+$ T cells that play an important role in immune signaling[3].

In the following years, the CDC narrowed down the groups at high risk for developing AIDS to homosexual men, injection drug users, Haitians, and people with hemophilia[4]. Apart from the Haitian risk group, the CDC deduced that the agent responsible for AIDS was spread through sexual transmission and blood transmission, either through individuals sharing needles or blood transfusions. Investigators reasoned that the agent causing AIDS was an infectious microorganism[5]. The discovery of the reverse transcriptase enzyme in the 1970s[6] and results from growing work that sought to identify retroviruses as a causal agent of certain cancers[7,8] eventually led to the theory a novel retrovirus was causing AIDS. By 1985, two independent groups isolated and provided unequivocal laboratory evidence that a new retrovirus, human immunodeficiency virus 1 (HIV-1), causes AIDS[9,10]. AIDS is now considered a late-stage progression of HIV-1 infection.

Forty years later, our understanding of HIV-1/AIDS has grown immensely and led to breakthroughs in treatment such that an HIV-1 diagnosis is no longer an imminent death sentence for many infected individuals. However, the HIV-1/AIDS pandemic remains a critical public health issue with almost 38 million people currently living with HIV-1 and over a million new global infections a year (unaids.org). Sub-Saharan Africa is home to two-thirds of people living with HIV-1, and AIDS is still among the leading causes of death[11]. The lack of resources in these communities, including access to treatment and educational programs, continues to enable the spread of HIV-1. Until there is an effective global infrastructure capable of reducing and preventing HIV-1 transmission, especially in areas with high infection rates, HIV-1/AIDS will continue to be a major public health issue.

i. HIV-1 Pathogenesis

HIV-1 infection is established by a single virus

Sexual transmission is the most common route of HIV-1 infection, with injection drug use and mother-to-fetus transmission being less frequent. During sexual transmission from a chronically infected individual, the virus transfers through the individual's bodily fluids to the recipient's anal or genital tract. The viral lineages of the donor genital tract are distinct from those established in the blood and can either be homogeneous clonally expanded populations or highly diverse[12]. The viral lineages established in the genital tract transfer through bodily fluids and, for donors with homogeneous and diverse genital tract lineages, the initial viral infection is established by a single virus variant in 80% of sexual transmission events[12,13]. Researchers hypothesized that the single virus variant, termed the transmitter founder (T/F) virus, contains characteristics sculpted through selective pressures in the genital tract and the transmission process[12–17].

Genetic and phenotypic characteristics associated with T/F viruses reflect the configuration of the HIV-1 envelope (Env) protein. Env is the sole viral protein on the surface of an HIV-1 virion and is responsible for mediating host cell fusion and subsequent infection. The HIV-1 Env protein is a heavily glycosylated protein, with glycans consisting of approximately

50% of its mass. This structure creates a "glycan shield" that conceals conserved protein epitopes from the host immune system. T/F Envs are associated with less glycosylation, as highly glycosylated T/F Envs are more easily trapped in the transmission fluids associated with sexual activity[18,19]. Other characteristics of T/F Envs include co-receptor tropism and Env density on the virus. To bind host cells, Env interacts with the host CD4 receptor and a co-receptor, CCR5 and/or CXCR4. T/F Envs are almost solely CCR5-tropic, though the selective advantage for this characteristic is unclear[13,20,21].

The HIV-1 viral membrane contains a low Env spike density compared to other viruses[22]. On average, HIV-1 virions contain ~14 Envs that are mostly spaced far apart from each other[22]. For comparison, the influenza viruses contain ~450 spikes per virion[22]. Researchers hypothesized that the relatively lower Env spike density aids the ability of HIV-1 viruses to evade bivalent binding of immunoglobulins that utilize avidity effects to potently neutralize antigens[22]. T/F viruses are associated with approximately twice as many Env proteins than Envs found in chronically derived viruses, potentially increasing the ability of viruses to attach to host cell receptors and initiate infection[14].

HIV-1 infects CD4$^+$ T cells

An HIV-1 virion is approximately 100-150 nanometers (nm)[23] in diameter with an outer architecture that contains the host-derived lipid bilayer membrane and the sole viral receptor, Env. The HIV-1 Env ectodomain is a homotrimer of gp120 and gp41 heterodimers (Figure 1)[24]. These subunits are translated as a single gp160 protein before being cleaved by furin within the cell and non-covalently associated[23]. Env is expressed on the surface of the virion and tethered by a transmembrane domain and cytoplasmic tail[24]. The gp120 unit of a trimer is responsible for binding to the host CD4 receptors and CCR5 or CXCR4 co-receptors[24,25]. The binding events lead to fusion in which gp41 undergoes conformational changes to merge viral and host membranes and release viral components for replication and assembly of new virions[26].

The inner architecture of a mature HIV-1 virion consists of a p17 matrix protein that lines the inside of the lipid membrane and a cone-shaped capsid made from p24 protein subunits[27]. The capsid houses genetic material in the form of two copies of positive sense, single-stranded (ss) RNA that is associated with the nucleocapsid protein, p7[27–29]. The capsid also holds reverse transcriptase, integrase, and protease enzymes along with regulatory proteins like Tat and Rev[27–29].

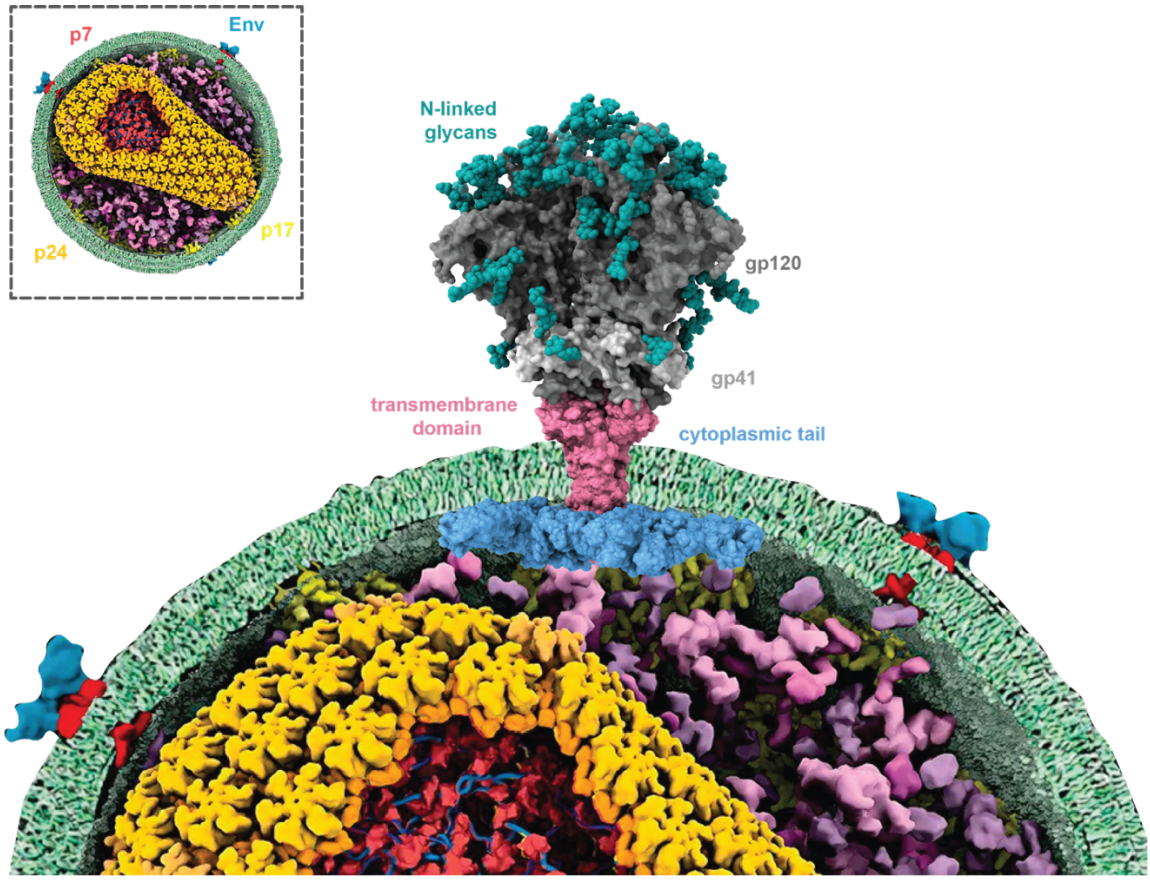

Figure 1: Architecture of an HIV-1 virion A model of a mature virion is shown in the inset with Env, p7, p24, and p17 proteins labeled. A zoomed-in image of the viral membrane is shown with an HIV-1 Env (not to scale) incorporated. The Env (PDB 5T3Z) includes labeled N-linked glycans, gp120, and gp41. The transmembrane domain and cytoplasmic tail

structure (PDB 7LOI) are also shown. The virion model was adopted from work by Janet Iwasa and https://scienceofhiv.org/.

To initiate infection of a host cell, an HIV-1 Env protein binds to the CD4 receptor on a $CD4^+$ T helper cell. Conformational changes in gp120 take place and lead to exposure of the co-receptor binding site and subsequent co-receptor binding[30,31]. This binding causes conformational changes in gp41 that lead to viral and host membrane fusion[24,26,32]. These conformational changes will be discussed in detail in Section II: HIV-1 Env undergoes conformational changes to infect host cells. The HIV-1 capsid then releases into the host cell and viral ssRNA dissociates from the p7 nucleocapsid protein[28,29]. Reverse transcriptase then begins converting ssRNA to complementary (c) DNA[33]. Nucleoporins transfer the capsid into the cell nucleus and the capsid disintegrates to release the viral cDNA genome and proteins[28,29]. Host DNA-dependent DNA polymerase creates complementary DNA from the cDNA template yielding double-stranded viral DNA[33]. The viral integrase enzyme subsequently inserts the viral DNA into the host genome[34]. Viral RNA is transcribed from the newly integrated viral DNA and exported outside the nucleus[35]. The viral RNA either translates to viral proteins necessary for virion packaging and budding or serves as the progeny viral RNA genome. The Env mRNA is processed in the endoplasmic reticulum and transported through the Golgi apparatus for further processing before delivery to the surface of the infected cell[35]. At the inner plasma membrane, the newly transcribed viral Gag (p55) and Gag-Pol (p160) precursors and viral genomic RNA assemble with Env to begin the budding process[36]. Shortly after, the virion matures to become infectious when a viral-encoded protease cleaves p55 and p160 precursors, creating the viral capsid[36]. A summary of this mechanism is depicted in Figure 2. The replication process results in an astounding estimated 1.4×10^{-3} mutations per base per virion, contributing to the high levels of viral diversity unique to HIV-1[37].

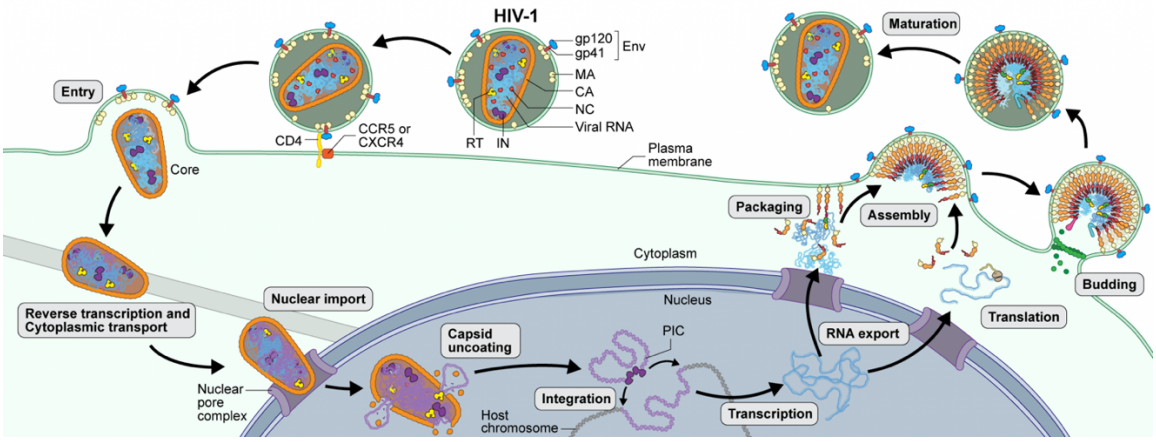

Figure 2: The HIV-1 replication cycle HIV-1 hijacks host cell machinery to replicate. This process begins with HIV-1 entry into the cell and release of the nucleocapsid. Reverse transcription of viral genetic material occurs within the nucleocapsid as it is transported through the cytoplasm and into the nucleus. Once in the nucleus, the nucleocapsid uncoats and the viral genetic material integrates into the host genome. Transcription of viral proteins occurs, and mRNA is transported out of the nucleus for translation. Viral proteins assemble at the cell membrane where viral genetic material is packaged and assembled into budding virions. After budding, the HIV-1 nucleocapsid undergoes maturation and is capable of infecting new host cells. This schematic was adopted from https://scienceofhiv.org/.

Progression of chronic HIV-1 infection: a molecular arms race

Two to four weeks following the viral transmission event, aggressive replication results in acute HIV-1 syndrome characterized by flu-like symptoms in the infected individual[38]. During this acute phase, $CD4^+$ T cells undergo dramatic depletion in the peripheral blood and gut associated lymphoid tissue (GALT)[38,39]. The virus also disseminates to other lymphoid tissues and establishes persistent viral reservoirs[39]. In the absence of antiretroviral therapy (ART), plasma viremia peaks before declining to a steady state, the viral set point, which dictates the rate of disease progression in the absence of ART treatment[39].

The immune system mediates the chronic stage of HIV-1 infection characterized by consistent replication in viral reservoirs. About twelve weeks following transmission, detectable levels of neutralizing antibodies in the plasma appear[40,41]. Antibodies typically circulating the blood during infection are in the form of immunoglobin G (IgG). IgGs are "Y"-shaped proteins composed of two binding arms, antigen-binding fragments (Fabs), and a stalk region, fragment crystallizable (Fc) (Figure 3A). Each Fab arm is composed of heavy and light chains with constant (C_H) and variable domains (V_L) (Figure 3B). The region of the Fab that interacts with antigens is located at the tips of the variable domains where there are three complementary determining loops (CDRs) for each heavy and light chain. DNA recombination is the mechanism that selects and combines different gene segments to encode variable regions[42–44]. Another process, somatic hypermutation (SHM), also occurs and mutates random nucleotides, mostly located with regions encoding CDRs[42]. The combination of somatic recombination and SHM creates unique antigen-binding receptors. These processes result in upwards of 10^{11} possible antigen-binding receptors and contribute to the diversity necessary for the immune system to recognize nefarious foreign antigens[45,46].

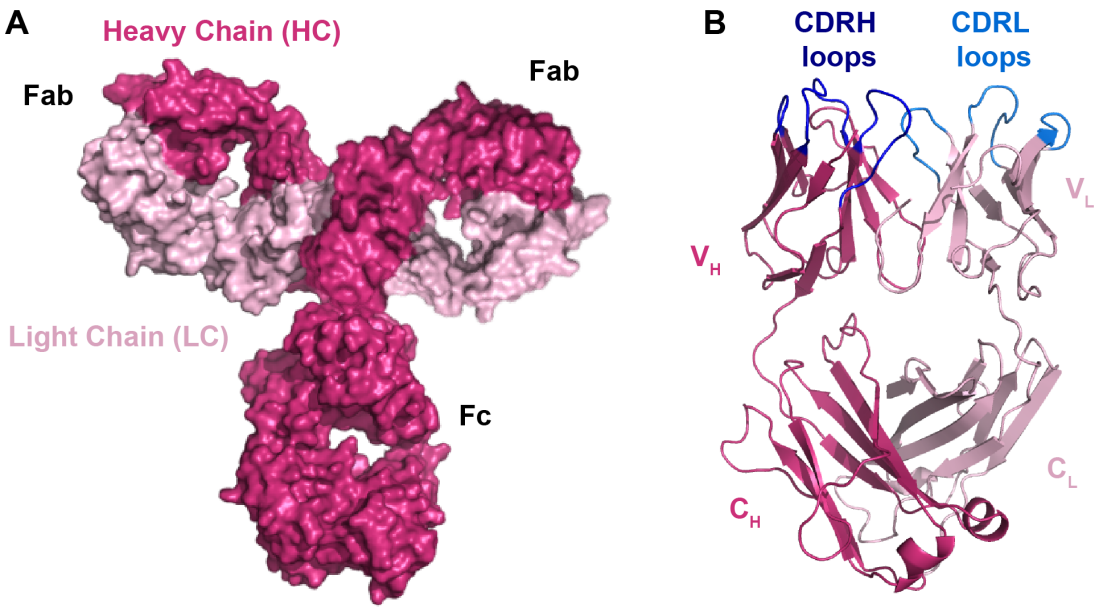

Figure 3: IgG Structure (A) The structure of an IgG with Fc and Fab arms (PDB 1IGT). The heavy and light chains are dark pink and light pink, respectively. **(B)** A Fab (PDB 1IGT) in ribbon representation with variable (V_H, V_L) and constant (C_H, C_L) domains depicted. CDRH and CDRL loops are density blue and slate blue, respectively.

Before antibodies circulate as soluble proteins in the body, they are expressed on the surface of B cells as B cell receptors (BCRs). The initial repertoire of BCRs is considered antigen-naïve and derived from germline genes. During HIV-1 infection, B cells are recruited and some (likely rare) germline B cell BCRs recognize and bind the HIV-1 Env[47]. The BCR binding stimulates the B cell to undergo clonal expansion and replication to create a clonal repertoire[42,48]. Clonal expansion is coupled with SHM. Mutations resulting from SHM can alter the binding specificity and affinity to Env. SHM that results in BCRs with higher affinity for the antigen outcompete lower affinity BCRs[42,48]. BCRs with higher affinities are selected for clonal expansion and iterative rounds of selection[42,48]. This process of clonal selection results in BCRs and secreted antibodies with increased affinities for antigen[42,48]. A schematic of affinity maturation during HIV-1 infection is presented in Figure 4.

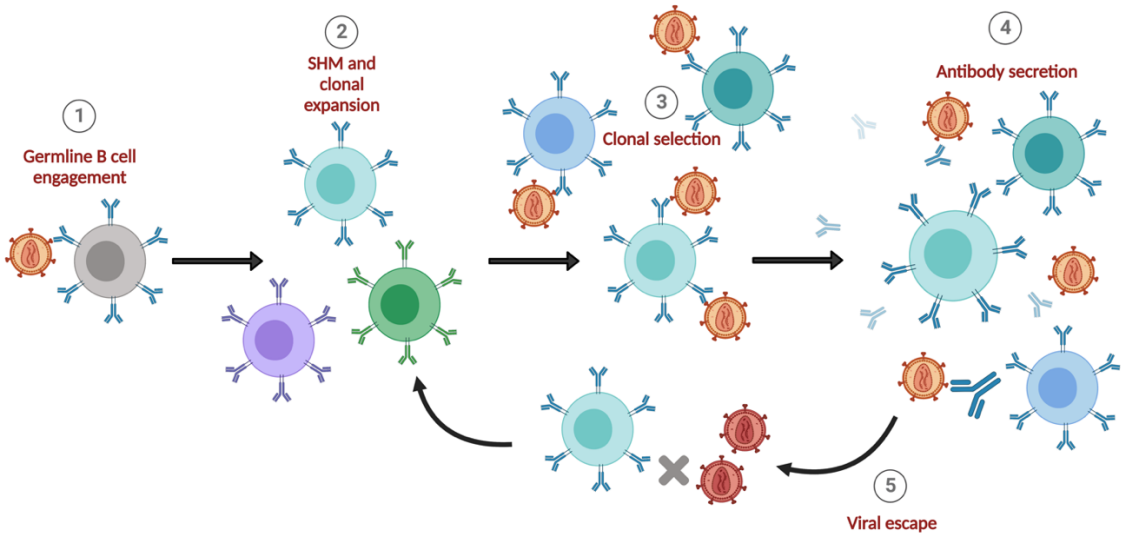

Figure 4: Schematic depicting affinity maturation during HIV-1 infection (1) Germline B cells bind HIV-1 Env which triggers (2) somatic hypermutation and clonal expansion of the B cell repertoire. (3) Clonal selection of BCRs that have high affinity interactions with Env lead to (4) B cell differentiation into plasma cells and antibody secretion. In response to antibody pressure, (5) HIV-1 mutates to evade neutralization, triggering another cycle of antibody affinity maturation. Schematic created with BioRender.

During HIV-1 infection, the rapid mutation of HIV-1 virion Envs drives antibody evolution creating a molecular arms race where antibodies and Envs are constantly battling to outcompete the other. The rate of viral mutation in most viruses is slower than HIV-1 mutation[49,50]. As a result, most viruses are not able to compete against antibody evolution. Most patients combat HIV-1 infection by creating strain-specific, or autologous, antibodies that are unable to completely eradicate all HIV-1, leading to viral escape[51,52]. Approximately 5-20% of patients create broadly neutralizing antibodies (bNAbs) capable of potent neutralization of numerous viral/HIV-1 strains; however, bNAbs do not prevent disease progression[53,54]. The relevance and characterization of bNAbs with be further discussed in

Section III: Broadly neutralizing antibodies against HIV-1. In the absence of treatment, chronic HIV-1 infection substantially depletes $CD4^+$ T cell counts, eventually resulting in AIDS[38,39].

ii. Combating HIV-1 infection: antiretroviral therapy and vaccine development

HIV-1 antiretroviral therapy

ARTs combat HIV-1 infection by blocking receptors or enzymes essential in the HIV-1 replication cycle, thereby preventing the ability of a virus to reproduce (Figure 2). Though ART is unable to cure HIV-1 infection because its genome is stably integrated into infected cells, it greatly reduces the burden of infection on the immune system, slowing AIDS progression. This makes the success of HIV-1 ARTs especially impressive—they have transformed a fatal disease into a manageable condition where patients can live a relatively normal life. Anthony Fauci, the head of the United States National Institute of Allergy and Infectious Disease, has commented on the power of ART, saying that "with collective and resolute action now and a steadfast commitment for years to come, an AIDS-free generation is indeed within reach."[55]

In 1987, the CDC approved azhidovudine (AZT), the first ART drug against HIV-1. AZT is a nucleoside reverse transcriptase inhibitor (NRTI) that prevents HIV-1 infection by inhibiting reverse transcription thereby halting the viral life cycle. AZT and several other NRTIs developed shortly after AZT induced persistent side effects, making these drugs difficult for many HIV-1 infected patients to tolerate. Additionally, studies showed these drugs only helped slow disease progression, and long-term use resulted in drug resistance due to viral mutation[56]. About ten years later, researchers developed more sophisticated highly active antiretroviral treatment (HAART) technology. HAART technology combines several antiretroviral drugs that target different parts of the viral replication cycle. The combination of two or three antiretroviral drugs leads to a sustained reduced viral load[57,58].

Lifelong chronic therapy without the interruption of treatment has been shown to reduce morbidity, prolong survival, and prevent transmission in HIV-1 infected individuals[59,60]. Today, there are over 30 HAART licensed drugs that have improved long-term use, tolerability, virologic efficacy, safety, and cost[58,61]. Treatment regimens have also been simplified for the patient by combining multiple ART drugs into a single tablet and through once-a-month injectable forms enabling individualized, optimized care[58,61].

In addition to treating active HIV-1 infection, HAART can be employed as preventative care to avert both transmission and acquisition of HIV-1. The Pivotal HIV Prevention Trials Network (HPTN) 052 studies demonstrated 96% efficacy in transmission prevention among couples where one individual was virally suppressed on HAART and the other was HIV-1 negative[41]. Several studies have since reported similar results, leading to the concept that "undetectable equals untransmissible" or "U=U"[62]. "U=U" means that patients with a viral load suppressed below the level of clinical detection through HAART treatment cannot transmit HIV-1 through sex. These observations lead to the use of HAART for pre-exposure prophylaxis (PrEP) to prevent the acquisition of HIV-1. Studies indicate that PrEP taken daily, as-prescribed, can lead up to 75-97% of HIV-1 acquisition reduction through sexual transmission among discordant couples[63–65].

Together, HAART has so far averted over 10 million AIDS-related deaths and represents an immense achievement in the treatment and prevention of a fatal disease[66].

HIV-1 Vaccine Development

Despite the successes of HAART, the gold standard of infectious disease prevention is vaccination. Vaccines have several advantages over HAART. HIV-1 treatment or prevention with HAART requires lifelong, strict adherence to medications and a huge financial burden, making HAART inaccessible for individuals in low-income countries where HIV-1 is most prevalent. The threat of drug resistance requires constant surveillance and adds to the cost of

treatment programs. Furthermore, continued and prolonged HAART is associated with loss of bone density, lipodystrophy, metabolic changes, and liver damage[67]. Alternatively, vaccines typically provide long-lasting protection, can be administered to a wide range of people, do not require life-long adherence, are not associated with long-term side effects, and are relatively cost-effective compared to HAART.

The development of an effective HIV-1 vaccine has proved a tremendous challenge. Despite the initial optimism that a vaccine could be developed within a few years of the pandemic onset, HIV-1 vaccine candidates created over the past 40 years have shown modest efficacy at best[68–70]. HIV-1 has put-forth unparalleled and unwarranted challenges for vaccine design. As discussed in Section I, Part ii. HIV-1 Pathogenesis, individuals infected with HIV-1 are unable to clear the viral infection because of stable integration of HIV-1 genomes into target cells[71]. In this way, a vaccine against HIV-1 must be able to induce an immune response that is drastically better than that which occurs during natural infection. HIV-1 vaccine development is uniquely challenging as all other vaccine development seeks to mimic natural, common immune responses rather than create an enhanced response.

HIV-1 is difficult to combat through vaccination because HIV-1 is a retrovirus, meaning that upon host infection, viral DNA is integrated into the host genome[71]. The virus creates latent reservoirs and replicates persistently throughout the lifetime of the host. An effective vaccine would have to not only clear the initial onset of infection, but also provide continuous protection from latent viral replication[72]. To date, there are no effective vaccines against retroviruses that are capable of this type of continuous protection[73,74].

Further, an effective vaccine would need to provide protection against the immense, consistently evolving genetic diversity of HIV-1. This diversity has emerged through error-prone replication machinery, genetic drift and recombination, and selective pressures leading to nine clades/subtypes (A, B, C, D, F, G, H, J, and K). Genetic diversity in nucleotides within subtypes averages 15-20% and diversity between subtypes is 25-35%[75,76]. To add to these complications, HIV-1 infections established by a single T/F virus in an individual mutate more than 10% of Env DNA within the course of infection[76]. To give context to the

vast diversity of HIV-1, estimates suggest the diversity of global influenza sequences in a given year equates to the diversity of HIV-1 sequences observed in a single individual captured at one time point[76]. Considering that influenza vaccines must be developed each year and only protect against a predicted subset of circulating strains, the idea of creating an HIV-1 vaccine that universally protects against the diversity of HIV-1 strains is daunting.

In addition to these challenges, HIV-1 has evolved to evade the host immune system by adopting low Env densities on the surface of the virus and shielding Env epitopes with glycosylation. As discussed in Section I, Part ii. HIV-1 Pathogenesis, HIV-1 virions express less than 14 Env proteins on the viral surface. Most of the Env trimers are spaced far apart to impede bivalent recognition from immunoglobulins contributing to potent neutralization[22]. Even further, each Env protein is covered by a dense glycan shield derived from host glycosylation machinery, thus serving to evade recognition by the host immune system and conceal conserved protein epitopes on Env[77–80].

Each of these characteristics provides ample challenge to researchers working to develop an effective HIV-1 vaccine. Together, these factors may make the potential of developing an effective HIV-1 seem bleak. However, decades of HIV-1 research have increased our understanding HIV-1 infection from multiple perspectives and informed our approaches to vaccine design.

II. HIV-1 Env undergoes conformational changes to infect host cells

As discussed in Section I, Part ii. HIV-1 Pathogenesis, HIV-1 Env is a Type I membrane fusion protein that undergoes dynamic conformational changes to fuse the host and viral membranes and enter host cells. Fusion is mediated by the host membrane-bound CD4 and CCR5 receptors and HIV-1 Env. Prior to receptor engagement, Env is in the prefusion, closed conformation in which the gp120 V1V2 loops occlude access to V3 loops. Upon CD4 binding to gp120, conformational changes occur that result in V1V2 loop displacement to

expose the V3 coreceptor binding loops. Engagement of the coreceptor induces conformational changes in gp41 resulting in the formation of a pre-hairpin structure in which HR1-N and HR1-C extend from HR2 towards the host membrane and the fusion peptide inserts into the host membrane[32]. From here, researchers hypothesize that receptor-bound gp120s shed from Env[81–83]. HR1 collapses onto HR2 to form the 6-helical bundle that brings the host and viral membranes together, resulting in fusion[32]. This process is depicted with a schematic in Figure 5.

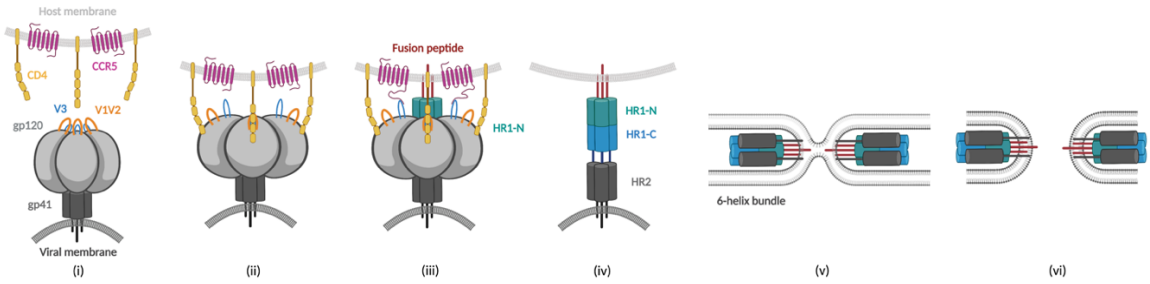

Figure 5: Schematic depicting HIV-1 Env fusion between host and viral membranes (i) HIV-1 Env membrane fusion occurs between the host membrane-bound receptors CD4 and CCR5 and the closed, prefusion Env trimer. (ii) The host CD4 receptor binds the Env CD4 binding site to induce conformational changes in gp120, including displacement of V1V2 loops and exposure of the V3 loops. (iii) These conformational changes enable binding of the CCR5 coreceptor and V3 loops that induce conformational changes in gp41 N-trimer/HR1 to form (iv) the pre-hairpin intermediate structure. In this conformation, the Env fusion peptide is embedded in the host membrane, linking the host cell and virus. (v) The pre-hairpin intermediate structure collapses to form the post-fusion six helical bundle and leads to (vi) membrane fusion. Schematic created with BioRender.

Diverse structural studies have investigated and visualized Env-mediated membrane fusion. X-ray crystallography and single particle cryo-EM have extensively characterized soluble

versions of the HIV-1 Env in the closed, prefusion[25] and the CD4-bound, open[30,31,84,85] conformations, as well as intermediate, partially open conformations[84,86–88]. Comparisons of closed and fully open conformations characterized the impressive ~40 Å displacement of gp120 V1V2 loops that enables V3 exposure[30,31,84]. Coreceptor binding has been characterized with a single particle cryo-EM structure of monomeric core gp120 complexed with CD4 and CCR5, informing a model of how HIV-1 Env transitions to the hypothesized intermediate pre-hairpin conformation[89,90]. X-ray crystallography has been used to observe the six-helical bundle that is formed by the gp41 N-trimer region composing α-helical trimeric coiled coil with three helices from the C-peptide surrounding it[91,92].

In Chapter II: DEER Spectroscopy Measurements Reveal Multiple Conformations of HIV-1 SOSIP Envelopes that Show Similarities with Envelopes on Native Virions, I describe our work that has increased the structural understanding of Env. Our methods utilized double electron-electron spectroscopy (DEER) to evaluate the conformational landscape of HIV-1 Env in solution. It revealed that DEER measurements corresponded to the prefusion, closed Env conformation described by structural biology[93]. Our findings also showed nuances of Env flexibly not captured in static cryo-EM and X-ray structures, such as gp41 elasticity and conformational heterogeneity induced by CD4 engagement[93]. This work has provided valuable information to aid our understanding of the dynamic process of Env-mediated membrane fusion.

As described, the HIV-1 Env is a homotrimer with three possible CD4 binding sites. One prevailing question related to HIV-1 membrane fusion and subsequent infection is how many CD4 receptors are required to induce gp120 conformation changes required for downstream events leading to fusion[94–98]. This information is relevant in understanding the prerequisite to initiate the fusion process and informs therapeutic designs that seek to inhibit fusion intermediates. The HIV-1 Env is a symmetrical trimer and previous structural work has shown only complexes in which CD4 is bound to all three Env protomers resulting in a symmetrically open Env[30,31]. In Chapter III: Structural characterization of HIV-1 Env trimers bound to sub-stochiometric numbers of CD4 receptors, I describe the design and structural

characterization of soluble Env constructs bound to only one or two CD4 molecules. This work is the first to investigate the structural consequences of sub-stoichiometric CD4-Env complexes.

III. Broadly neutralizing antibodies against HIV-1

As introduced in Section I, Part ii. HIV-1 Pathogenesis, in rare cases of chronic HIV-1 infection patients develop bNAbs that recognize diverse strains of HIV-1 with considerable potency. bNAb neutralization breadth and potency distinguishes it from other neutralizing antibodies. bNAb breadth refers to its ability to neutralize a wide range of genetically diverse HIV-1 subtypes. bNAb potency is the amount of bNAb needed to neutralize a particular virus, as measured by the half maximal inhibitory concentration (IC_{50}). The bNAb classification requirement includes neutralization of $\geq$ 7 clades/circulating recombinant forms (CRFs) against the 118 multi-clade pseudo irus panel and > 30% neutralization breadth with a geomean $IC_{50} \leq 3.6$ μg/ml[80].

Single cell antibody cloning techniques and advances in structural biology have allowed researchers to rapidly isolate and characterize hundreds of bNAbs[99,100]. These studies have identified conserved regions on HIV-1 Env that bNAbs consistently target. These epitopes include the V1V2 loops, V3 loop, CD4 binding site, silent face, gp120/gp41 interface, and fusion peptide (Figure 6). Due to Env's dense glycan shield, bNAbs that target these regions are often able to either accommodate or incorporate glycans into their epitopes[100,101]. Furthermore, many bNAbs require uncommon genetic features that necessitate high levels of SHM. On average, HIV-1 bNAbs contain 3-5x more mutations in variable heavy gene regions than other human antibodies that have undergone affinity maturation[102]. Some of these key mutations are located outside SHM hotspots, such as antibody framework regions and, therefore, require low-probability events to occur[103]. Nonetheless, these high levels and rare mutations have been found to be critical for recognition and neutralization[100–104].

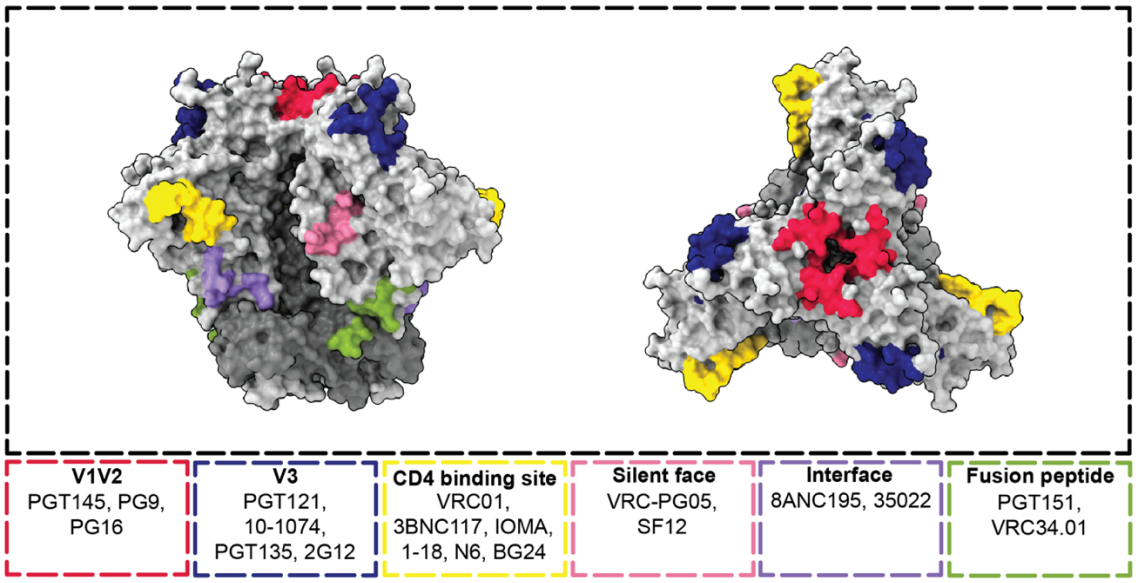

Figure 6: Broadly neutralizing antibody epitopes on HIV-1 Env Surface representation of BG505 Env SOSIP (PDB 5T3Z) represented as side (left) and top (right) views with colored patches representing epitopes for V1V2, V3, CD4 binding site, silent face, interface, and fusion peptide bNAbs. Examples of bNAbs that target each epitope are described in the boxes below.

Researchers are investigating the role of bNAbs in HIV-1 treatment and prevention. Although modern HAART has proven incredibly effective in preventing and suppressing HIV-1 viremia, adherence and long-term side effects are substantial limitations in HAART effectiveness. Therefore, research efforts have aimed to explore HAART-free therapeutics which have led to the development of passive transfer bNAb approaches[105–110]. For this treatment, individuals would receive bNAb infusions every few months to prevent and treat HIV-1 infection. For these purposes, researchers select the most broad and potent HIV-1 bNAbs to evaluate for clinical potential. First-generation approaches explored the efficacy of single bNAb therapeutics and found that monotherapy was insufficient to suppress viremia due to the frequency of pre-existing escape variants and the diversity of HIV-1 quasispecies within the host[111–113]. Recent efforts focusing on combination therapy utilize multiple bNAbs

to target different epitopes have revealed improved efficacy[105,108]. A recent phase I clinical trial investigating the safety, tolerability, and efficacy of two bNAbs including serum half-life extending mutations, 3BNC117 and 10-1074, resulted in complete suppression of plasma viremia for up to 43 weeks providing guidance for the next generation of bNAb therapeutics[108]. However, the optimal combination of bNAbs and the number of bNAbs necessary for protection and suppression remains a central question[106,110].

In addition to the potential use of bNAbs for therapeutics, HIV-1 bNAbs currently serve to inform vaccine design efforts. This methodology has been coined, "reverse vaccinology 2.0." whereby antibodies are utilized to inform vaccine development with high resolution structures of antibody-antigen complexes providing information regarding antigen recognition and enabling structure-based immunogen design. This work has been made possible through advances in cloning human B cells to derive antibody sequences from which to produce bNAbs for characterization, the development of soluble forms of HIV-1 Env-based antigens, and structural biology. In 2009, robust methods were put forth to clone memory B cells from HIV-1 infected patient blood that either bound the HIV-1 Env antigen or showed neutralization activity, revolutionizing the ability to rapidly identify bNAbs[99,101,114].

Researchers developed the first soluble HIV-1 Env antigen in 1998 in the form of a gp120 core monomer that has truncated flexible variable loops[115,116]. This construct enabled the first structural characterization of antigen complexes with HIV-1 neutralizing antibodies[115,116]. In 2013, researchers developed SOSIP.664, a soluble form of the trimeric HIV-1 Env composed of gp120 and gp41 subunits[117]. The SOSIP.664 includes the gp120 and gp41 ectodomains, where gp41 is truncated after residue 664 and incorporated stabilizing mutations I559P and a disulfide bond to link gp120 and gp41, resulting in a soluble, prefusion stabilized Env. Methods to isolate bNAbs and development of soluble Env constructs, in combination with technical advances in single particle cryo-EM, have fueled a revolution of structural characterization of bNAb:antigen complexes[118–120]. The abundance of structural information of HIV-1 antigen recognition has enabled structure-based design of gp120 and SOSIP.664-

based immunogens. Chapter IV: How Antibodies Recognize Pathogenic Viruses: Structural Correlates of Antibody Neutralization of HIV-1, SARS-CoV-2, and Zika, includes a review of how approaches in structural and molecular biology have enabled and contributed to our understanding of antibody recognition of viruses, including HIV-1. In Chapter V: Comparing methods for immobilizing HIV-1 SOSIPs in ELISAs that evaluate antibody binding, I share a technical evaluation of binding assays that evaluated bNAb binding to HIV-1 Env and identified preferred methods to ensure reliable data.

i. bNAbs against the CD4 binding site epitope

As discussed in Section I, Part ii. HIV-1 Pathogenesis, HIV-1 Env engagement with CD4 triggers the first step of viral entry and subsequent infection. This region presents a site of vulnerability for antibody neutralization as it must remain accessible for receptor binding and conserved among viral strains to maintain its function. bNAbs that target this epitope employ a logical mechanism of neutralization, namely, through the steric interference of Env with its host receptor. However, the CD4bs is composed of a recessed pocket that can easily accommodate the CD4 receptor but is a more challenging target for the bulky Fab fragments of IgGs[115]. This epitope is further obstructed through the presence of N-linked glycans that provide physical barriers to the recessed binding pocket. Despite these intrinsic challenges, during natural infection the human immune system can raise bNAbs against the CD4bs that are among the most broad and potent[121–127].

There are two distinct mechanisms that bNAbs access the CD4bs. One way is via CDRH3-dominated recognition whereby the major contacts are mediated between the Fab CDRH3 loop and CD4bs loop of Env (Figure 7). In the other mechanism, bNAb recognition occurs by mimicking CD4 and is V_H gene restricted. For these bNAbs, V_H domains approach the CD4bs at a similar pose as CD4 and use their CDRH2 loop and framework residues to engage the CD4bs loop[121,128]. CD4-mimetic recognition is divided into three classes: VRC01-class,

IOMA-class (both V_H1-2 gene derived), and the V_H1-46 gene derived class (Figure 7)[121,122,126,129,130].

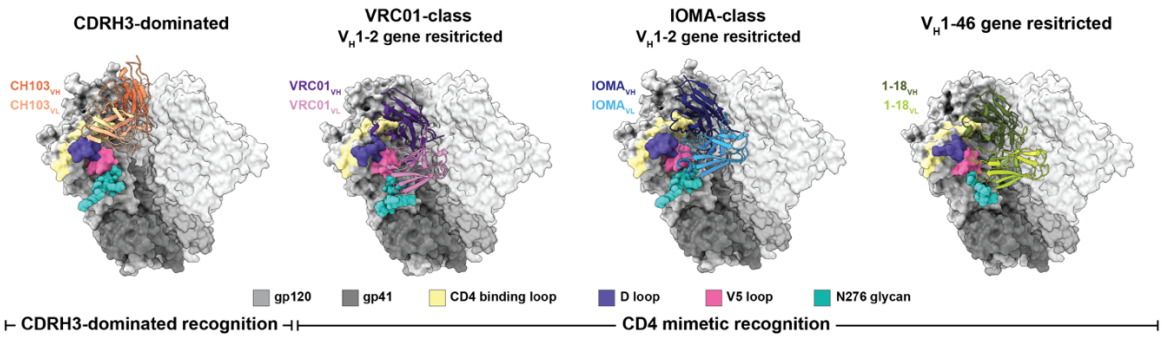

Figure 7: Classification of CD4bs bNAbs CD4bs bNAbs are categorized by the mechanism of CD4bs recognition. They fall into two classes: CDRH3-dominated and CD4 mimetic recognition. CD4-mimetic bNAbs fall into three subclasses: VRC01 class (V_H1-2 gene restricted), IOMA class (V_H1-2 gene restricted), and the V_H1-46 gene restricted. Surface representation of Env SOSIPs bound to examples of bNAbs for each class included: CH103 (PDB 4JAN), VRC01 (PDB 6V8X), IOMA (PDB 5T3Z), and 1-18 (PDB 6UDJ). CD4bs features on Env gp120 are depicted and include the CD4 binding loop, D loop, V5 loop, and N276 glycan.

The distinguishing factor that separates the two V_H1-2 gene-derived bNAb subclasses is related to aspects of the antibodylight chain. The VRC01-class is characterized by a five amino acid CDRL3, which is a rare feature, occurring in ~1% of human light chain genes[129]. The discreet length of the CDRL3 is critical to stabilize the antibody V_H-V_L interface through interactions with CDRH3 and CDRH2 residues and prevent steric clashes with the gp120 D loop[121,122,129]. On the other hand, IOMA-class V_H1-2 bNAbs contain a more normal length CDRL3 (8 residues) that is displaced away from the D loop, towards the V5 loop, to be accommodated[126,130]. Both subclasses contain either a shortened or flexible CDRL1 that is necessary to accommodate the obtrusive $N276_{gp120}$ glycan[126,129,130].

In addition to light chain differences in V_H1-2 gene-derived bNAbs, characteristics in the heavy chain further distinguish VRC01 and IOMA subclasses. The VRC01-class of V_H1-2 derived bNAbs contains what has been identified as signature residues in the heavy chain ($Trp50_{HC}$, $Asn58_{HC}$, $Arg71_{HC}$, and a hydrophobic residue at position 100_{HC}) that interact with conserved residues in the CD4bs epitope and correlate with remarkable neutralization potency[129]. The IOMA-class does not utilize these signature residues in the same manner as the VRC01-class. The IOMA-class contains $Trp50_{HC}$ but it does not make contacts with gp120[126]. The IOMA-class also mutated the $Asn58_{HC}$ signature residue to Lys and interacts with different gp120 residues compared to the VRC01-class[126]. And, instead of utilizing a hydrophobic residue at position $100B_{HC}$, IOMA-class bNAbs use a counterpart residue, $W100F_{HC}$ to interact with gp120[126]. The differences between the mechanisms that V_H1-2 gene-derived bNAbs interact with gp120 and utilize the residues described may explain why IOMA-class bNAbs are considerably less broad and potent compared to the VRC01-class.

V_H1-46 gene and V_H1-2 genes are closely related and bNAbs derived from these genes share some common features for CD4bs recognition[99,100,121]. For example, the V_H1-46 class has a normal length CDRL3 like the IOMA-class[129]. The V_H1-46 class also lacks VRC01-class signature residues Trp50, Asn58, and a hydrophobic residue at position 100B, but contains $Arg71_{HC}$[129]. Until recently V_H1-46 bNAbs were not thought to be as potent as the V_H1-2 class; however, the isolation of one of the most broad and potent CD4bs bNAbs, 1-18, that is V_H1-46-derived, changed this perspective[123]. 1-18 contains a CDRH1 insertion and makes substantial Env inter-protomer contacts that facilitates its impressive neutralization profile unseen in other V_H1-46 bNAbs. It remains to be determined if V_H1-46 bNAbs with similar characteristics to 1-18 can be isolated from other HIV-1 infected donors.

ii. Immunogen design strategies targeting the elicitation of V_H1-2 class CD4bs bNAbs

The germline targeting approach to HIV-1 immunogen design originated from observations that inferred germline (iGL) versions of HIV-1 bNAbs did not have detectable binding to HIV-1 Envs that were sufficiently recognized by the mature counterpart bNAbs[131–133]. This

knowledge led researchers to engineer Env-based immunogens that could specifically bind a subset of B cells expressing iGLs with high affinity that were known to develop into bNAbs. This initial immunogen is considered the "prime" immunogen and is meant to activate precursor B cells[134]. Subsequent boosting immunogens incorporate more native-like Env features to guide maturation and induce mutations that lead to bNAb development[134].

The germline targeting approach has primarily been utilized for elicitation of CD4bs bNAbs, particularly for the V_H1-2 gene-derived classes. V_H1-2 class bNAbs are derived from specific germline genes that are well characterized and known to encode signature residues that confer neutralization potency and breadth, making them a rational target of the germline targeting approach[129,135]. To date, several V_H1-2 class-targeting prime immunogens have been developed and tested with different boosting strategies providing a wealth of information to inform the efficacy and evolution of this approach.

gp120-based germline-targeting CD4bs immunogens

The first HIV-1 vaccine immunogens were composed of monomeric gp120 subunits. Since most bNAb responses are against gp120, the rationale in this design was to focus the immune response to such epitopes by removing gp41 and the trimeric interfaces. This design was adopted for two germline-targeting CD4bs immunogens: eOD-GT8 and 426c core (or TM4ΔV1-3). eOD-GT8 was created through iterative deep mutational screening and yeast display[136,137]. This immunogen is composed of the engineered outer domain (eOD) of gp120 in the HxB2 Clade B strain background and contains 21 point mutations found to confer VRC01-class precursor engagement. It also has removed CD4bs glycans at positions $N276_{gp120}$, $N386_{gp120}$, and $N463_{gp120}$[136,137]. These mutations result in binding to VRC01-class iGLs with extremely high affinity (dissociation constants, K_Ds, in the nM to pM range)[138].

A multimeric version eOD-GT8 that displays 60 copies of this protein on a self-assembling nanoparticle (eOD-GT8 60mer) has been evaluated in the context of prime and prime-boost studies in multiple animal models[127,137–140]. These studies revealed that this platform could selectively engage VRC01-class naïve B cells and these precursors could be matured to have

limited breadth[127,137–140]. In 2018, a Phase I human clinical trial set forth to evaluate if the eOD-GT8 60mer could prime VRC01-class naïve B cells in humans and found that there was a robust priming of VRC01-class naïve B cells in all vaccine recipients[135,141]. These results were the first to validate the HIV-1 germline targeting approach in humans representing a notable milestone. The next steps in the development of this immunogen and vaccine strategy involve maturing these precursors to bNAbs capable of protection, which will be a considerable challenge[142,143].

426c core is another gp120-based germline-targeting, VRC01-class immunogen. It is based on the gp120 sequence of the clade C isolate 426c[144]. This immunogen contains both the inner and outer gp120 domains, and has $N276_{gp120}$, $N460_{gp120}$, and $N463_{gp120}$ glycans removed along with variable loops 1-3[144]. Deletions of the variable loops were shown to confer better access for VRC01-class iGLs to the CD4bs[144]. A multimerized version of 426c core followed by a boost with a HxB2 core that contained native glycans was evaluated in mouse studies and found to elicit cross-reactive VRC01-like antibodies capable of $N276_{gp120}$ glycan accommodation, as well as autologous tier 2 neutralizing activities[145]. A phase I trial to evaluate the safety and immunogenicity for this priming immunogen is currently in progress[135].

Env-based germline-targeting CD4bs immunogens

Another strategy for germline-targeting immunogen design involves using the entire HIV-1 trimeric Env as a template. Since our understanding of the differences in the epitopes presented on both gp120 monomer and native trimer has been better understood through the wealth of structural information, the principle in this type of approach is that a more native-like antigen that maintains the trimeric Env structure and more native CD4bs epitope could be engineered through structure-based design to effectively engage target precursors. Maintaining native Env features may be advantageous in recapitulating natural infection and bNAb development. Furthermore, the Env-based approach enables targeting of multiple epitopes within a single immunogen.

The first immunogen to implement this approach is called BG505 SOSIP GT1. This construct is based on BG505 SOSIP.664 and incorporates germline targeting mutations to both the V2 apex and CD4bs epitopes[146]. In the CD4bs, BG505 SOSIP GT1 contains two amino acid mutations in gp120 (T278R and G471S) that confer interactions with VRC01-class precursors and glycans removed at positions $N197_{gp120,}$ $N276_{gp120}$, $N386_{gp120}$, and $N462_{gp120}$[146]. These mutations resulted from observations of HIV-1 antibody:Env complexes and structure-guided design. Immunization experiments in mice that evaluated a BG505 SOSIP GT1 prime showed engagement of VRC01-class precursors. A slightly modified version of this immunogen, BG505 SOSIP GT1.1, is currently being assessed in a Phase 1 clinical trial[135]. These results compared with that from the eOD-GT8 60mer clinical results will provide an interesting comparison of different germline-targeting immunogen design strategies. In Chapter VI: HIV-1 CD4-binding site germline antibody–Env structures inform vaccine design, I describe the structural characterization of an inferred germline V_H1-2 CD4bs antibody bound to BG505 SOSIP GT1 that informs further iterations of structure-based design of this immunogen.

Finally, my colleagues in the Bjorkman lab have recently described a new avenue for germline-targeting immunogen design—one that seeks to elicit IOMA-class bNAbs instead of VRC01-class[147] The hypothesis is that the IOMA-class of CD4bs bNAbs have features that might be easier to elicit than VRC01-class bNAbs that require generally higher levels of somatic mutation, a difficult-to-achieve mechanism to accommodate Env's $N276_{gp120}$ N-glycan, and rare 5-residue CDRL3s[147]. IOMA-class targeting immunogens, IGT1 and IGT2, were created through iterative rounds of yeast display screening. They are both based on the 426c SOSIP.664 sequence background[147]. IGT1 and IGT2 have glycans removed at positions $N276_{gp120}$, $N460_{gp120}$, and $N463_{gp120}$ and contain amino acids changes T278R, D279N, and V430P. IGT1 contains V5 amino acid mutations T460S, T461Q, and N463E[147]. V5 mutations for IGT2 are T460A, T461L, and N463P as well as G471S[147]. The sequence differences in IGT1 and IGT2 results in 30μM and 0.5 μM affinity, respectively, to IOMA-iGL[147].

In this design, it was hypothesized that having multiple germline-targeting immunogens with different affinities for precursors could better shepherd bNAb development in early stages[147]. These immunogens were multimerized on a nanoparticle platform and evaluated in sequential immunization regimens in several different animal models[147]. These strategies resulted in epitope-specific responses with heterologous neutralization, and cloned antibodies were shown to overcome neutralization roadblocks including $N276_{gp120}$ glycan accommodation[147]. Chapter VII: Engineering IOMA for optimal CD4 binding site features informs vaccine design, describes work that sought to inform IOMA immunogen design, by probing how different features of this class of antibodies contribute to neutralization potency and breadth. Figure 8 summarizes comparisons between gp120- and Env-based CD4bs germline-targeting immunogens.

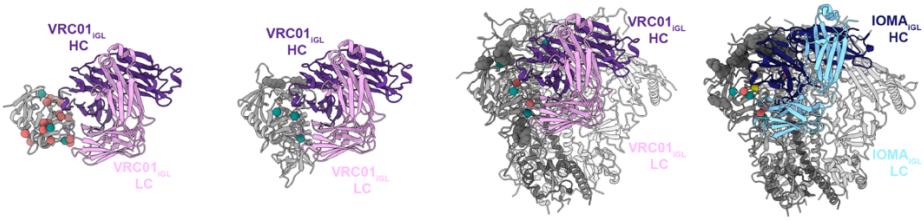

	eOD-GT8	426c core	BG505 SOSIP GT1	IGT1/2
Env component	outer domain	gp120	Env trimer: gp120/gp41	Env trimer: gp120/gp41
Strain background Clade: Tier:	HxB2 B 1	426c C 2	BG505 A 2	426c C 2
CD4bs target	VRC01-class	VRC01-class	VRC01-class	IOMA-class
Mutations Point mutations:	D27Q, N30Y, E34N, S35T, E36V, G41S, M45W, L63F, E78V, F80W, T81R, D92N, F127Y, Q136P, I144F, T146N, N159D, D165N, D170N	N/A	T278R, G471S	IGT1: T278R, D279N, V430P., T460S, T461Q, N463E IGT2: T278R, D279N, V430P, T460A, T461L, N463P, G471S
Glycan deletions:	$N276_{gp120}$, $N386_{gp120}$, $N463_{gp120}$	$N276_{gp120}$, $N460_{gp120}$, $N463_{gp120}$	$N197_{gp120}$, $N276_{gp120}$, $N386_{gp120}$, $N462_{gp120}$	$N276_{gp120}$, $N460_{gp120}$, $N463_{gp120}$

Figure 8: A Comparison of CD4bs germline targeting immunogens A comparison of eOD-GT8 (PDB 5IDL), 426c core (PDB 5FA2), BG505 SOSIP GT1 (PDB 5W6D), and IGT1/2 (PDB 6MYY) CD4bs germline targeting immunogens based on Env component, strain background, and germline targeting mutations.

IV. Scope of Work

Structural biology has enabled researchers to exceed the limitations of the naked eye and visualize living material from something as infinitesimal as single atoms that make up cells to intricate tissues composed of many hundreds of cells. In this work, we leverage structural biology to examine the 3D architecture of the HIV-1 Env glycoprotein and complexes of Env bound to bNAbs derived from human patients. The first focus of this thesis will report on characterizing the conformational changes of HIV-1 Env. The Env glycoprotein is a highly advanced fusion machine that undergoes dynamic rearrangements in response to host receptor engagement to enable fusion and subsequent infection. Structural biology has greatly illuminated the mechanisms that drive this process. Chapter II describes the use of DEER spectroscopy to probe the conformation changes of soluble Env proteins in solution and compares these results to static structures of Env. In Chapter III, we report high resolution single-particle cryo-EM structures of HIV-1 Env bound to sub-stoichiometric numbers of its host receptor, CD4. These structures reveal the conformational consequences of sub-optimal receptor engagement and sheds light on whether fusion is possible under these circumstances.

The second focus of this thesis examines Env from the perspective of the host immune system by describing the structural characterization of bNAbs that target the Env CD4bs epitope. Chapter IV broadly introduces this topic by reviewing how structures of antibodies bound to viral proteins reveal the binding mechanisms that lead to viral neutralization. In Chapter V, we introduce how assays that measure antibody binding to HIV-1 Env, and inform the interpretation of Env-bNAb structures, must consider the unintentional triggering of undesired Env conformations to avoid unreliable results. Finally, in Chapters VI and VII, we present projects that involve the characterization and engineering of two classes of CD4bs bNAbs. This work delineates the features of these bNAbs that accrue to confer breadth and potency and inform the design of vaccines that seek to elicit them.

Collectively, this thesis presents a robust structural investigation of HIV-1 Env from the fundamental perspective of Env as a fusion protein and from the perspective of Env as an

immune target. Our conclusions elucidate the structural, conformational, and antigenic landscape of Env and inform the development of an effective HIV-1 vaccine.

V. References

1.Kaposi's Sarcoma and Pneumocystis Pneumonia Among Homosexual Men — New York City and California. 5 (2020).

2.*Current Trends Update on Acquired Immune Deficiency Syndrome (AIDS) --United States*. https://www.cdc.gov/mmwr/preview/mmwrhtml/00001163.htm (1982).

3. Fauci, A. S. HIV and AIDS: 20 years of science. *Nat Med* **9**, 839–843 (2003).

4. *Current Trends Prevention of Acquired Immune Deficiency Syndrome (AIDS): Report of Inter-Agency Recommendations*. 101–3 https://www.cdc.gov/mmwr/preview/mmwrhtml/00001257.htm (1983).

5.Francis, D., Curran, J. & Essex, M. Epidemie Aequired Immune Defieiency Syndrome: Epidemiologie Evidence for a Transmissible Agent. *JNCI: Journal of the National Cancer Institute* **71**, 5–9 (1983).

6. Raju, T. The Nobel Chronicles. *The Lancet* **354**, (1999).

7. Gallo, R. C. The Early Years of HIV/AIDS. *Science* **298**, 1728–1730 (2002).

8. Montagnier, L. A History of HIV Discovery. *Science* **298**, 1727–1728 (2002).

9.Levy, J. A. *et al.* Isolation of Lymphocytopathic Retroviruses from San Francisco Patients with AIDS. *Science* **225**, 840–842 (1984).

10.Barré-Sinoussi, F. *et al.* Isolation of a T-Lymphotropic Retrovirus from a Patient at Risk for Acquired Immune Deficiency Syndrome (AIDS). *Science* **220**, 868–871 (1983).

11.Dwyer-Lindgren, L. *et al.* Mapping HIV prevalence in sub-Saharan Africa between 2000 and 2017. *Nature* **570**, 189–193 (2019).

12.Joseph, S. B., Swanstrom, R., Kashuba, A. D. M. & Cohen, M. S. Bottlenecks in HIV-1 transmission: insights from the study of founder viruses. *Nat Rev Microbiol* **13**, 414–425 (2015).

13.Keele, B. F. *et al.* Identification and characterization of transmitted and early founder virus envelopes in primary HIV-1 infection. *Proc. Natl. Acad. Sci. U.S.A.* **105**, 7552–7557 (2008).

14.Parrish, N. F. *et al.* Phenotypic properties of transmitted founder HIV-1. *Proc. Natl. Acad. Sci. U.S.A.* **110**, 6626–6633 (2013).

15.Fischer, W. *et al.* Transmission of Single HIV-1 Genomes and Dynamics of Early Immune Escape Revealed by Ultra-Deep Sequencing. *PLoS ONE* **5**, e12303 (2010).

16.Lee, H. Y. *et al.* Modeling sequence evolution in acute HIV-1 infection. *Journal of Theoretical Biology* **261**, 341–360 (2009).

17.Salazar-Gonzalez, J. F. *et al.* Deciphering Human Immunodeficiency Virus Type 1 Transmission and Early Envelope Diversification by Single-Genome Amplification and Sequencing. *J Virol* **82**, 3952–3970 (2008).

18.Russell, E. S. *et al.* The Genetic Bottleneck in Vertical Transmission of Subtype C HIV-1 Is Not Driven by Selection of Especially Neutralization-Resistant Virus from the Maternal Viral Population. *J Virol* **85**, 8253–8262 (2011).

19.Sagar, M., Wu, X., Lee, S. & Overbaugh, J. Human Immunodeficiency Virus Type 1 V1-V2 Envelope Loop Sequences Expand and Add Glycosylation Sites over the Course of Infection, and These Modifications Affect Antibody Neutralization Sensitivity. *J Virol* **80**, 9586–9598 (2006).

20.Ping, L.-H. *et al.* Comparison of Viral Env Proteins from Acute and Chronic Infections with Subtype C Human Immunodeficiency Virus Type 1 Identifies Differences in

Glycosylation and CCR5 Utilization and Suggests a New Strategy for Immunogen Design. *J Virol* **87**, 7218–7233 (2013).

21.Parker, Z. F. *et al.* Transmitted/Founder and Chronic HIV-1 Envelope Proteins Are Distinguished by Differential Utilization of CCR5. *J Virol* **87**, 2401–2411 (2013).

22.Klein, J. S. & Bjorkman, P. J. Few and Far Between: How HIV May Be Evading Antibody Avidity. *PLoS Pathog* **6**, e1000908-6 (2010).

23. Sakuragi, J. Morphogenesis of the Infectious HIV-1 Virion. *Front. Microbio.* **2**, (2011).

24.Prabakaran, P., Dimitrov, A. S., Fouts, T. R. & Dimitrov, D. S. Structure and Function of the HIV Envelope Glycoprotein as Entry Mediator, Vaccine Immunogen, and Target for Inhibitors. in *Advances in Pharmacology* vol. 55 33–97 (Elsevier, 2007).

25.Ward, A. B. & Wilson, I. A. The HIV-1 envelope glycoprotein structure: nailing down a moving target. *Immunological Reviews* **275**, 21–32 (2017).

26.Doms, R. W. & Moore, J. P. HIV-1 Membrane Fusion: Targets of Opportunity. *The Journal of Cell Biology* **151**, 5 (2000).

27.Briggs, J. A. G. Structural organization of authentic, mature HIV-1 virions and cores. *The EMBO Journal* **22**, 1707–1715 (2003).

28.Campbell, E. M. & Hope, T. J. HIV-1 capsid: the multifaceted key player in HIV-1 infection. *Nat Rev Microbiol* **13**, 471–483 (2015).

29.Toccafondi, E., Lener, D. & Negroni, M. HIV-1 Capsid Core: A Bullet to the Heart of the Target Cell. *Front. Microbiol.* **12**, 652486 (2021).

30.Ozorowski, G. *et al.* Open and closed structures reveal allostery and pliability in the HIV-1 envelope spike. *Nature Publishing Group* **547**, 360–363 (2017).

31.Wang, H. *et al.* Cryo-EM structure of a CD4-bound open HIV-1 envelope trimer reveals structural rearrangements of the gp120 V1V2 loop. *Proc. Natl. Acad. Sci. U.S.A.* **113**, E7151–E7158 (2016).

32. Harrison, S. C. Viral membrane fusion. *Virology* **479–480**, 498–507 (2015).

33.Hu, W.-S. & Hughes, S. H. HIV-1 Reverse Transcription. *Cold Spring Harbor Perspectives in Medicine* **2**, a006882–a006882 (2012).

34.Craigie, R. & Bushman, F. D. HIV DNA Integration. *Cold Spring Harbor Perspectives in Medicine* **2**, a006890–a006890 (2012).

35.Kirchhoff, F. HIV Life Cycle: Overview. in *Encyclopedia of AIDS* (eds. Hope, T. J., Stevenson, M. & Richman, D.) 1–9 (Springer New York, 2013). doi:10.1007/978-1-4614-9610-6_60-1.

36.Sundquist, W. I. & Krausslich, H.-G. HIV-1 Assembly, Budding, and Maturation. *Cold Spring Harbor Perspectives in Medicine* **2**, a006924–a006924 (2012).

37.Cuevas, J. M., Geller, R., Garijo, R., López-Aldeguer, J. & Sanjuán, R. Extremely High Mutation Rate of HIV-1 In Vivo. *PLoS Biol* **13**, e1002251 (2015).

38.*The Stages of HIV Infection*. https://hivinfo.nih.gov/understanding-hiv/fact-sheets/stages-hiv-infection#:~:text=Acute%20HIV%20infection%20is%20the,and%20spreads%20throughout%20the%20body. (2021).

39.Deeks, S. G., Overbaugh, J., Phillips, A. & Buchbinder, S. HIV infection. *Nat Rev Dis Primers* **1**, 15035 (2015).

40.Cohen, M. S., Gay, C. L., Busch, M. P. & Hecht, F. M. The Detection of Acute HIV Infection. *J INFECT DIS* **202**, S270–S277 (2010).

41.Cohen, M. S. *et al.* Prevention of HIV-1 Infection with Early Antiretroviral Therapy. *N Engl J Med* **365**, 493–505 (2011).

42.Kenneth, M., Weaver, C. & Janeway, C. *Janeway's Immunobiology*. (Garland Science, 2017).

43.Seidman, J. G. & Leder, P. The arrangement and rearrangement of antibody genes. *Nature* **276**, 790–795 (1978).

44.Roth, D. B. V(D)J Recombination: Mechanism, Errors, and Fidelity. *Microbiol Spectr* **2**, 2.6.18 (2014).

45.Patten, P. A. *et al.* The Immunological Evolution of Catalysis. *Science* **271**, 1086–1091 (1996).

46. Davis, M. M. T-cell antigen receptor genes and T-cell recognition. 8 (1988).

47.Fera, D. *et al.* Affinity maturation in an HIV broadly neutralizing B-cell lineage through reorientation of variable domains. *Proc. Natl. Acad. Sci. U.S.A.* **111**, 10275–10280 (2014).

48.Wabl, M. & Steinberg, C. Affinity maturation and class switching. *Current Opinion in Immunology* **8**, 89–92 (1996).

49.Fischer, W. *et al.* HIV-1 and SARS-CoV-2: Patterns in the evolution of two pandemic pathogens. *Cell Host & Microbe* **29**, 1093–1110 (2021).

50.Sanjuán, R., Nebot, M. R., Chirico, N., Mansky, L. M. & Belshaw, R. Viral Mutation Rates. *J Virol* **84**, 9733–9748 (2010).

51.Wei, X. *et al.* Antibody neutralization and escape by HIV-1. *Nature* **422**, 307–312 (2003).

52.Richman', D. D. HIV EVOLUTION AND ESCAPE. 15.

53.Doria-Rose, N. A. *et al.* Frequency and Phenotype of Human Immunodeficiency Virus Envelope-Specific B Cells from Patients with Broadly Cross-Neutralizing Antibodies. *J Virol* **83**, 188–199 (2009).

54.Binley, J. M. *et al.* Profiling the Specificity of Neutralizing Antibodies in a Large Panel of Plasmas from Patients Chronically Infected with Human Immunodeficiency Virus Type 1 Subtypes B and C. *J Virol* **82**, 11651–11668 (2008).

55.Fauci, A. S. & Folkers, G. K. Toward an AIDS-Free Generation. *JAMA* **308**, 343 (2012).

56.Wainberg, M. A., Brenner, B. G. & Turner, D. Changing Patterns in the Selection of Viral Mutations among Patients Receiving Nucleoside and Nucleotide Drug Combinations Directed against Human Immunodeficiency Virus Type 1 Reverse Transcriptase. *Antimicrob Agents Chemother* **49**, 1671–1678 (2005).

57.Gulick, R. M. *et al.* Treatment with Indinavir, Zidovudine, and Lamivudine in Adults with Human Immunodeficiency Virus Infection and Prior Antiretroviral Therapy. *N Engl J Med* **337**, 734–739 (1997).

58.Cihlar, T. & Fordyce, M. Current status and prospects of HIV treatment. *Current Opinion in Virology* **18**, 50–56 (2016).

59.Vittinghoff, E. *et al.* Combination Antiretroviral Therapy and Recent Declines in AIDS Incidence and Mortality. *J INFECT DIS* **179**, 717–720 (1999).

60.Palella, F. J., Loveless, M. O. & Holmberg, S. D. Declining Morbidity and Mortality among Patients with Advanced Human Immunodeficiency Virus Infection. *The New England Journal of Medicine* 8 (1998).

61.Quinn, T. C. Forty years of AIDS: a retrospective and the way forward. *Journal of Clinical Investigation* **131**, e154196 (2021).

62.Eisinger, R. W., Dieffenbach, C. W. & Fauci, A. S. HIV Viral Load and Transmissibility of HIV Infection: Undetectable Equals Untransmittable. *JAMA* **321**, 451 (2019).

63.Stenger, M. Maximizing the Benefits of HIV Preexposure Prophylaxis. *Topics in Antiviral Medicine* **25**, (2018).

64.Molina, J.-M. *et al.* On-Demand Preexposure Prophylaxis in Men at High Risk for HIV-1 Infection. *N Engl J Med* **373**, 2237–2246 (2015).

65.Baeten, J. M. *et al.* Antiretroviral Prophylaxis for HIV Prevention in Heterosexual Men and Women. *N Engl J Med* **367**, 399–410 (2012).

66.Forsythe, S. S. *et al.* Twenty Years Of Antiretroviral Therapy For People Living With HIV: Global Costs, Health Achievements, Economic Benefits. *Health Affairs* **38**, 1163–1172 (2019).

67.Powderly, W. Long-term Exposure to Lifelong Therapies. *JAIDS Journal of Acquired Immune Deficiency Syndromes* **29**, (2002).

68.Esparza, J. A brief history of the global effort to develop a preventive HIV vaccine. *Vaccine* **31**, 3502–3518 (2013).

69.Kim, J., Vasan, S., Kim, J. H. & Ake, J. A. Current approaches to HIV vaccine development: a narrative review. *J Int AIDS Soc.* **24**, (2021).

70.Hsu, D. C. & O'Connell, R. J. Progress in HIV vaccine development. *Human Vaccines & Immunotherapeutics* **13**, 1018–1030 (2017).

71.Rios, A. Fundamental challenges to the development of a preventive HIV vaccine. *Current Opinion in Virology* **29**, 26–32 (2018).

72.Shapiro, S. Z. Clinical Development of Candidate HIV Vaccines: Different Problems for Different Vaccines. *AIDS Research and Human Retroviruses* **30**, 325–329 (2014).

73.Gallo, R. C. Human retroviruses in the second decade: A personal perspective. *Nat Med* **1**, 753–759 (1995).

74.Gallo, R. C. Human retroviruses after 20 years: a perspective from the past and prospects for their future control: Gallo · Human retroviruses in 2002 − a perspective. *Immunological Reviews* **185**, 236–265 (2002).

75.Hemelaar, J., Gouws, E., Ghys, P. D. & Osmanov, S. Global and regional distribution of HIV-1 genetic subtypes and recombinants in 2004. *AIDS* **20**, W13–W23 (2006).

76.Korber, B. *et al.* Evolutionary and immunological implications of contemporary HIV-1 variation. *British Medical Bulletin* **58**, 19–42 (2001).

77.Crispin, M., Ward, A. B. & Wilson, I. A. Structure and Immune Recognition of the HIV Glycan Shield. *Annu. Rev. Biophys.* **47**, 499–523 (2018).

78.Landais, E. & Moore, P. L. Development of broadly neutralizing antibodies in HIV-1 infected elite neutralizers. *Retrovirology* **15**, 61 (2018).

79.Doores, K. J. The HIV glycan shield as a target for broadly neutralizing antibodies. *FEBS J* **282**, 4679–4691 (2015).

80.Griffith, S. A. & McCoy, L. E. To bnAb or Not to bnAb: Defining Broadly Neutralising Antibodies Against HIV-1. *Front. Immunol.* **12**, 708227 (2021).

81.Moore, J. P., McKeating, J. A., Weiss, R. A. & Sattentau, Q. J. Dissociation of gp120 from HIV-1 Virions Induced by Soluble CD4. *Science* **250**, 1139–1142 (1990).

82.Ruprecht, C. R. *et al.* MPER-specific antibodies induce gp120 shedding and irreversibly neutralize HIV-1. *Journal of Experimental Medicine* **208**, 439–454 (2011).

83.Li, Y. *et al.* Mechanism of Neutralization by the Broadly Neutralizing HIV-1 Monoclonal Antibody VRC01. *J Virol* **85**, 8954–8967 (2011).

84.Yang, Z., Wang, H., Liu, A. Z., Gristick, H. B. & Bjorkman, P. J. Asymmetric opening of HIV-1 Env bound to CD4 and a coreceptor-mimicking antibody. *Nat Struct Mol Biol* **26**, 1167–1175 (2019).

85.Jette, C. A. *et al.* Cryo-EM structures of HIV-1 trimer bound to CD4-mimetics BNM-III-170 and M48U1 adopt a CD4-bound open conformation. *Nat Commun* **12**, 1950 (2021).

86.Wang, H., Barnes, C. O., Yang, Z., Nussenzweig, M. C. & Bjorkman, P. J. Partially Open HIV-1 Envelope Structures Exhibit Conformational Changes Relevant for Coreceptor Binding and Fusion. *Cell Host and Microbe* **24**, 579-592.e4 (2018).

87.Saphire, E. O. *et al.* Crystal Structure of a Neutralizing Human IgG Against HIV-1: A Template for Vaccine Design. *Science* **293**, 1155–1159 (2001).

88.Yang, Z. *et al.* Neutralizing antibodies induced in immunized macaques recognize the CD4-binding site on an occluded-open HIV-1 envelope trimer. *Nat Commun* **13**, 732 (2022).

89.Shaik, M. M. *et al.* Structural basis of coreceptor recognition by HIV-1 envelope spike. *Nature* 1–24 (2018) doi:10.1038/s41586-018-0804-9.

90.Chan, D. C. & Kim, P. S. HIV Entry and Its Inhibition. *Cell* **93**, 681-684, (1998).

91.Chan, D. C., Fass, D., Berger, J. M. & Kim, P. S. Core Structure of gp41 from the HIV Envelope Glycoprotein. *Cell* **89**, 263–273 (1997).

92.Weissenhorn, W. Atomic structure of the ectodomain from HIV-1 gp4. 5 (1997).

93.Stadtmueller, B. M. *et al.* DEER Spectroscopy Measurements Reveal Multiple Conformations of HIV-1 SOSIP Envelopes that Show Similarities with Envelopes on Native Virions. *Immunity* 1–27 (2018) doi:10.1016/j.immuni.2018.06.017.

94.Yang, X., Kurteva, S., Ren, X., Lee, S. & Sodroski, J. Subunit Stoichiometry of Human Immunodeficiency Virus Type 1 Envelope Glycoprotein Trimers during Virus Entry into Host Cells. *J Virol* **80**, 4388–4395 (2006).

95.Salzwedel, K. & Berger, E. A. Complementation of diverse HIV-1 Env defects through cooperative subunit interactions: a general property of the functional trimer. *Retrovirology* **6**, 75 (2009).

96.Brandenberg, O. F., Magnus, C., Regoes, R. R. & Trkola, A. The HIV-1 Entry Process: A Stoichiometric View. *Trends in Microbiology* **23**, 763–774 (2015).

97.Chen, B. Molecular Mechanism of HIV-1 Entry. *Trends in Microbiology* **27**, 878–891 (2019).

98.Ma, X. & Mothes, W. HIV-1 Env trimer opens through an asymmetric intermediate in which individual protomers adopt distinct conformations. 1–18 (2018) doi:10.7554/eLife.34271.001.

99.Scheid, J. F. *et al.* Broad diversity of neutralizing antibodies isolated from memory B cells in HIV-infected individuals. *Nature* **458**, 636–640 (2009).

100.West, A. P. *et al.* Structural Insights on the Role of Antibodies in HIV-1 Vaccine and Therapy. *Cell* **156**, 633–648 (2014).

101.McCoy, L. E. & Burton, D. R. Identification and specificity of broadly neutralizing antibodies against HIV. *Immunol Rev* **275**, 11–20 (2017).

102.Tiller, T. *et al.* Autoreactivity in Human IgG+ Memory B Cells. *Immunity* **26**, 205–213 (2007).

103.Klein, F. *et al.* Somatic Mutations of the Immunoglobulin Framework Are Generally Required for Broad and Potent HIV-1 Neutralization. *Cell* **153**, 126–138 (2013).

104.Kwong, P. D. & Mascola, J. R. HIV-1 Vaccines Based on Antibody Identification, B Cell Ontogeny, and Epitope Structure. *Immunity* **48**, 855–871 (2018).

105.Gaebler, C. *et al.* Prolonged viral suppression with anti-HIV-1 antibody therapy. *Nature* **606**, 368–374 (2022).

106.Hsu, D. C., Mellors, J. W. & Vasan, S. Can Broadly Neutralizing HIV-1 Antibodies Help Achieve an ART-Free Remission? *Front. Immunol.* **12**, 710044 (2021).

107.Bar-On, Y. *et al.* Safety and antiviral activity of combination HIV-1 broadly neutralizing antibodies in viremic individuals. *Nat Med* **24**, 1701–1707 (2018).

108.Sneller, M. C. *et al.* Combination anti-HIV antibodies provide sustained virological suppression. *Nature* **606**, 375–381 (2022).

109.Julg, B. *et al.* Safety and antiviral activity of triple combination broadly neutralizing monoclonal antibody therapy against HIV-1: a phase 1 clinical trial. *Nat Med* **28**, 1288–1296 (2022).

110.Walsh, S. R. & Seaman, M. S. Broadly Neutralizing Antibodies for HIV-1 Prevention. *Front. Immunol.* **12**, 712122 (2021).

111.Caskey, M. *et al.* Antibody 10-1074 suppresses viremia in HIV-1-infected individuals. *Nat Med* **23**, 185–191 (2017).

112.Caskey, M. *et al.* Viraemia suppressed in HIV-1-infected humans by broadly neutralizing antibody 3BNC117. *Nature* **522**, 487–491 (2015).

113.Corey, L. *et al.* Two Randomized Trials of Neutralizing Antibodies to Prevent HIV-1 Acquisition. *N Engl J Med* **384**, 1003–1014 (2021).

114.Scheid, J. F. *et al.* A method for identification of HIV gp140 binding memory B cells in human blood. *Journal of Immunological Methods* **343**, 65–67 (2009).

115.Kwong, P. D. *et al.* Structure of an HIV gp120 envelope glycoprotein in complex with the CD4 receptor and a neutralizing human antibody. *Nature* **393**, 648–659 (1998).

116.Wyatt, R. *et al.* The antigenic structure of the HIV gp120 envelope glycoprotein. *Nature* **393**, 705–711 (1998).

117.Sanders, R. W. *et al.* A Next-Generation Cleaved, Soluble HIV-1 Env Trimer, BG505 SOSIP.664 gp140, Expresses Multiple Epitopes for Broadly Neutralizing but Not Non-Neutralizing Antibodies. *PLoS Pathog* **9**, e1003618-20 (2013).

118.Mak, J. & de Marco, A. Recent advances in retroviruses via cryo-electron microscopy. *Retrovirology* **15**, 23 (2018).

119.Rivera-Calzada, A. & Carroni, M. Editorial: Technical Advances in Cryo-Electron Microscopy. *Front. Mol. Biosci.* **6**, 72 (2019).

120.Abernathy, M. E., Dam, K.-M. A., Esswein, S. R., Jette, C. A. & Bjorkman, P. J. How Antibodies Recognize Pathogenic Viruses: Structural Correlates of Antibody Neutralization of HIV-1, SARS-CoV-2, and Zika. *Viruses* **13**, 2106 (2021).

121.Zhou, T. *et al.* Structural Repertoire of HIV-1-Neutralizing Antibodies Targeting the CD4 Supersite in 14 Donors. *Cell* **161**, 1280–1292 (2015).

122.Zhou, T. *et al.* Multidonor Analysis Reveals Structural Elements, Genetic Determinants, and Maturation Pathway for HIV-1 Neutralization by VRC01-Class Antibodies. *Immunity* **39**, 245–258 (2013).

123.Schommers, P. *et al.* Restriction of HIV-1 Escape by a Highly Broad and Potent Neutralizing Antibody. *Cell* **180**, 471-489.e22 (2020).

124.Barnes, C. O. *et al.* A naturally arising broad and potent CD4-binding site antibody with low somatic mutation. *BioRxiv* 51 (2022) doi:https://www.biorxiv.org/content/10.1101/2022.03.16.484662v1.

125.Umotoy, J. *et al.* Rapid and Focused Maturation of a VRC01-Class HIV Broadly Neutralizing Antibody Lineage Involves Both Binding and Accommodation of the N276-Glycan. *Immunity* **51**, 141-154.e6 (2019).

126.Gristick, H. B. *et al.* Natively glycosylated HIV-1 Env structure reveals new mode for antibody recognition of the CD4-binding site. *Nature Publishing Group* **23**, 906–915 (2016).

127.Huang, J. *et al.* Identification of a CD4-Binding-Site Antibody to HIV that Evolved Near-Pan Neutralization Breadth. *Immunity* **45**, 1108–1121 (2016).

128.Liao, H.-X. *et al.* Co-evolution of a broadly neutralizing HIV-1 antibody and founder virus. *Nature* **496**, 469–476 (2013).

129.West Jr, A. P. Structural basis for germ-line gene usage of a potent class of antibodies targeting the CD4-binding site of HIV-1 gp120. *PNAS* 1–8 (2012) doi:10.1073/pnas.1208984109/-/DCSupplemental.

130.van Schooten, J. *et al.* Identification of IOMA-class neutralizing antibodies targeting the CD4-binding site on the HIV-1 envelope glycoprotein. *Nat Commun* **13**, 4515 (2022).

131.Xiao, X. *et al.* Germline-like predecessors of broadly neutralizing antibodies lack measurable binding to HIV-1 envelope glycoproteins: Implications for evasion of immune responses and design of vaccine immunogens. *Biochemical and Biophysical Research Communications* **390**, 404–409 (2009).

132.Hoot, S. *et al.* Recombinant HIV Envelope Proteins Fail to Engage Germline Versions of Anti-CD4bs bNAbs. *PLoS Pathog* **9**, e1003106 (2013).

133.Sliepen, K. *et al.* Binding of inferred germline precursors of broadly neutralizing HIV-1 antibodies to native-like envelope trimers. *Virology* **486**, 116–120 (2015).

134.Stamatatos, L., Pancera, M. & McGuire, A. T. Germline-targeting immunogens. *Immunol Rev* **275**, 203–216 (2017).

135.Lee, J. H. & Crotty, S. HIV vaccinology: 2021 update. *Seminars in Immunology* **51**, 101470 (2021).

136.Jardine, J. *et al.* Rational HIV Immunogen Design to Target Specific Germline B Cell Receptors. *Science* **340**, 711–716 (2013).

137.Jardine, J. G. *et al.* HIV-1 broadly neutralizing antibody precursor B cells revealed by germline-targeting immunogen. *Science* **351**, 1458–1463 (2016).

138.Jardine, J. G. *et al.* Priming a broadly neutralizing antibody response to HIV-1 using a germline-targeting immunogen. *Science* **349**, 156–161 (2015).

139.Chen, X. *et al.* Vaccination induces maturation in a mouse model of diverse unmutated VRC01-class precursors to HIV-neutralizing antibodies with >50% breadth. *Immunity* **54**, 324-339.e8 (2021).

140.Huang, D. *et al.* B cells expressing authentic naive human VRC01-class BCRs can be recruited to germinal centers and affinity mature in multiple independent mouse models. *Proc Natl Acad Sci USA* **117**, 22920–22931 (2020).

141.Venkatesan, P. Preliminary phase 1 results from an HIV vaccine candidate trial. *The Lancet Microbe* **2**, e95 (2021).

142.Haynes, B. F. & Burton, D. R. Developing an HIV vaccine. *Science* **355**, 1129–1130 (2017).

143.Andrabi, R., Bhiman, J. N. & Burton, D. R. Strategies for a multi-stage neutralizing antibody-based HIV vaccine. *Current Opinion in Immunology* **53**, 143–151 (2018).

144.McGuire, A. T. *et al.* Specifically modified Env immunogens activate B-cell precursors of broadly neutralizing HIV-1 antibodies in transgenic mice. *Nat Commun* **7**, 10618 (2016).

145.Parks, K. R. *et al.* Overcoming Steric Restrictions of VRC01 HIV-1 Neutralizing Antibodies through Immunization. *CellReports* **29**, 3060-3072.e7 (2019).

146.Medina-Ramírez, M. *et al.* Design and crystal structure of a native-like HIV-1 envelope trimer that engages multiple broadly neutralizing antibody precursors in vivo. *J Exp Med* **214**, 2573–2590 (2017).

147.Gristick, H. B. *et al.* CD4-binding site immunogens elicit heterologous anti-HIV-1 neutralizing antibodies in transgenic and wildtype animals. *Submitted* (2022).

Chapter II

DEER SPECTROSCOPY MEASUREMENTS REVEAL MULTIPLE CONFORMATIONS OF HIV-1 SOSIP ENVELOPES THAT SHOW SIMILARITIES WITH ENVELOPES ON NATIVE VIRIONS

Stadtmueller, B.M., Bridges, M.D., **Dam, K.A.**, Lerch, M.T., Huey-Tubman, K.E., Hubbell, W.L., & Bjorkman, P.J. DEER Spectroscopy Measurements Reveal Multiple Conformations of HIV-1 SOSIP Envelopes that Show Similarities with Envelopes on Native Virions. *Immunity*, *49*(2), 235-246 (2018). https://doi.org/10.1016/j.immuni.2018.06.017

Graphical Abstract

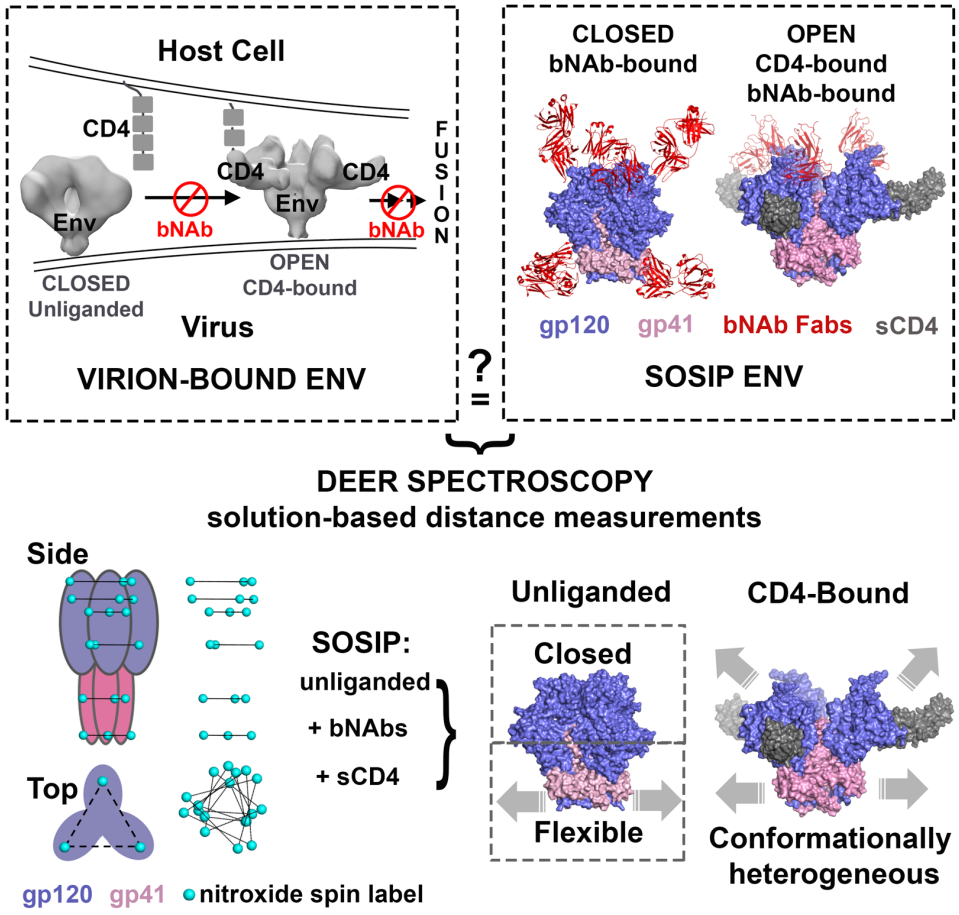

Abstract

HIV-1 Envelope (Env) mediates viral–host membrane fusion after binding host-receptor CD4 and coreceptor. Soluble envelopes (SOSIPs), designed to mimic prefusion conformational states of virion-bound envelopes, are proposed immunogens for eliciting neutralizing antibodies, yet only static structures are available. To evaluate conformational landscapes of ligand-free, CD4-bound, inhibitor-bound, and antibody-bound SOSIPs, we measured inter-subunit distances throughout spin-labeled SOSIPs using double electron-electron resonance (DEER) spectroscopy and compared results to soluble and virion-bound Env structures, and single-molecule Förster resonance energy transfer (smFRET)-derived dynamics of virion-bound Envs. Unliganded SOSIP measurements were consistent with closed, neutralizing antibody-bound structures and shielding of non-neutralizing epitopes, demonstrating homogeneity at Env apex, increased flexibility near Env base, and no evidence for the intra-subunit flexibility near Env apex suggested by smFRET. CD4 binding increased inter-subunit distances and heterogeneity, consistent with rearrangements required for coreceptor binding. Results suggest similarities between SOSIPs and virion-bound Envs and demonstrate DEER's relevance for immunogen design.

Introduction

Developing a vaccine against HIV-1 requires understanding the structure and dynamics of envelope (Env) glycoproteins on virions and in soluble forms being developed as immunogens (Sanders and Moore, 2017). HIV-1 Env, a trimer of gp120-gp41 heterodimers, mediates entry into target cells by gp120 binding to the host receptor CD4, which initiates conformational changes that allow recognition of the coreceptor CCR5, resulting in gp41 rearrangements that promote fusion between the target cell and viral membranes (Ward and Wilson, 2017). Low-resolution reconstructions of Env trimers on HIV-1 virions derived by cryo-electron tomography (cryo-ET) revealed distinct Env conformations including an unliganded, closed structure in which adjacent gp120 subunits interacted to form the trimer apex and a soluble CD4 (sCD4)-bound, open conformation in which the gp120 subunits were displaced and outwardly rotated to disrupt the trimer apex (Liu et al., 2008). Subsequent crystallographic and cryo-EM structures of soluble native-like Env trimers lacking membrane and cytoplasmic domains and including stabilizing mutations (SOSIPs) (Sanders et al., 2013) in complex with broadly neutralizing antibodies (bNAbs) resulted in higher-resolution Env structures of the closed Env conformation, revealing interactions of the gp120 V1V2 motifs at the trimer apex that shield the coreceptor binding site on V3 (Ward and Wilson, 2017) (Figure 1A,B). Consistent with cryo-ET structures of open virion-bound Envs (Liu et al., 2008), single-particle cryo-EM structures of sCD4-bound SOSIPs demonstrated rotation and displacement of gp120s, an ~40Å movement of V1V2 to the sides of Env trimer to reveal V3, and smaller rearrangements of gp41 (Ozorowski et al., 2017; Wang et al., 2016) (Figure 1A,B).

The dynamics of HIV-1 Envs on virions has been characterized by single-molecule fluorescence resonance energy transfer (smFRET) studies, in which donor and acceptor fluorophores were placed in loops within V1 and V4 of a gp120 monomer in virion-bound Env trimers, allowing for intra-subunit motions within single Env trimers to be monitored over time (Ma et al., 2018; Munro et al., 2014; Munro and Lee, 2018; Munro and Mothes, 2015). These studies suggested that virion-bound Envs transition between three primary states (States 1, 2, and 3), with State 1 (low FRET ground state with large intra-dye distances) predominating in the absence of added ligands. Transitions to State 3 (medium FRET state

with intermediate intra-dye distances) were induced by the addition of sCD4 plus the coreceptor-mimicking antibody 17b after populating State 2 (high FRET state with short intra-dye distances) (Ma et al., 2018; Munro et al., 2014). Addition of bNAbs or a small molecule inhibitor of HIV-1 entry, BMS-626529 (Li et al., 2013), stabilized the low-FRET ground state, with differential effects on the intermediate- and high-FRET states (Munro et al., 2014). There is currently no correlation between atomic resolution Env structures and the smFRET-defined states, resulting in a gap in understanding the relationship between Env molecular structure and dynamics. In addition, the development of SOSIP Envs as potential immunogens (Sanders and Moore, 2017) requires assessment of whether their unliganded structures faithfully represent the conformation(s) adopted by virion-bound Envs that would be encountered in a natural infection.

To evaluate the structure and conformational flexibility of SOSIP Envs in solution, we used double electron-electron resonance (DEER) spectroscopy to probe free and liganded SOSIP Envs spin-labeled with a nitroxide free radical. DEER measures the dipolar interaction between electron spin pairs and can be analyzed to give an interspin distance distribution in the range of 17-80Å (Jeschke, 2012). The populations of distances recorded reflect molecular motion in solution, providing a snapshot of protein dynamics and conformational heterogeneity. The largest peak amplitude defines the most probable distance in a DEER distribution and provides information on the dominant structural state in the population, while multiple peaks indicate conformational heterogeneity and peak widths are related to the internal flexibility of each conformation and the attached spin label (Hubbell et al., 2000; Hubbell et al., 2013). The accuracy of peak distance and width decrease as a function of interspin distance; 17–65Å distances can be assigned with confidence, whereas distances >65Å are detected with less accuracy (e.g., +/-10Å) (Jeschke, 2012).

Here we report DEER-derived inter-subunit distances and heterogeneity in unliganded SOSIP Envs and their complexes with sCD4, bNAbs, and a small molecule inhibitor. We also report an intra-subunit measurement between spin labels at positions similar to where dyes were introduced in smFRET studies of virion-bound Envs (Ma et al., 2018; Munro et al., 2014). These results inform models of Env dynamics relevant to developing SOSIP

immunogens and to understanding conformational changes in Env-mediated membrane fusion.

RESULTS

We chose to investigate two well-characterized SOSIP trimers, the clade A BG505 (Sanders et al., 2013) and clade B B41 (Pugach et al., 2015), because these SOSIP Envs have been characterized structurally in closed and sCD4-bound open states (Ozorowski et al., 2017; Wang et al., 2016) and both are being developed as immunogens (Sanders et al., 2015). For each DEER experiment we used site-directed spin labeling (Hubbell et al., 2013) to introduce a single cysteine into a gp120-gp41 protomer of the BG505 or B41 SOSIPs and then covalently attached a nitroxide spin label bearing the "V1" side chain (Khramtsov et al., 1989) (indicated as an asterisk,*) (Figure S1A). Once attached, the V1 spin label is about the size of an amino acid side chain and contributes limited width to DEER distance distributions (Toledo Warshaviak et al., 2013) (Figure S1A, B). This approach results in the attachment of three spin labels per trimer, which form the vertices of an equilateral triangle if located in a symmetric portion of Env (Figure 1B), or the vertices of an isosceles or scalene triangle if located in a region that lacks 3-fold symmetry and/or adopts multiple conformations. Accordingly, DEER measurements were expected to result in one distance corresponding to the sides of an equilateral triangle or ≥2 distances corresponding to the sides of an asymmetric triangle or equilateral triangles of different sizes.

We selected spin labeling sites from solvent-exposed residues in defined secondary structures (□-strand or □-helix; not loops) in the following Env structural motifs in the apex or base regions: (*i*) (apex) gp120 V1V2, which mediates inter-subunit contacts that form the apex of closed Env trimers and repositions upon Env binding to sCD4 (Wang et al., 2016); (*ii*) (apex) gp120 V3, which is shielded by V1V2 in the closed Env conformation and is exposed to provide coreceptor-binding sites upon Env binding to sCD4 (Ward and Wilson, 2017); (*iii)* (apex) gp120 bridging sheet at the base of V1V2, which undergoes structural rearrangements upon CD4 binding that stabilize open conformations (Ozorowski et al., 2017;

Wang et al., 2016); (*iv*) (base) gp120 inner domain, which interacts with gp41 (Ward and Wilson, 2017); and *(v)* (base) gp41, portions of which undergo conformational changes upon binding to sCD4 (Ozorowski et al., 2017) (Figure 1A,B).

To evaluate the positions of spin labeling sites among published structures, we measured inter-subunit C□ distances from crystal and cryo-EM structure coordinates and determined a mean distance and standard deviation for each site (Figure 1C). Measurements included seven closed Envs (six SOSIPs (Ward and Wilson, 2017) and one native (non-SOSIP) Env (Lee et al., 2016), each complexed with one or more bNAb Fabs), B41 SOSIP bound to the CD4 binding site (CD4bs) bNAb b12 (B41-b12 complex) (Ozorowski et al., 2017), BG505 SOSIP bound to sCD4, the CD4-induced (CD4i) coreceptor-mimicking antibody 17b, and the gp120-gp41 interface bNAb 8ANC195 (BG505-sCD4-17b-8ANC195 complex) (Wang et al., 2016), and B41 SOSIP bound to sCD4 and 17b (B41-sCD4-17b complex) (Ozorowski et al., 2017). For closed Envs structures, the mean inter-subunit distance standard deviations were ~1Å or less, with the exception of residue 657 in gp41, whose position was different in two structures (pdb codes 5U70 and 5U7M), resulting in a 2.8Å standard deviation (Figure 1C). We used these coordinate-derived measurements as references to compare with DEER-derived distances, noting that a coordinate-derived C□-C□ measurement and an experimental DEER distance may differ by several Ångstrom yet represent the same structure because V1 side chain rotamers could contribute to the DEER distance (Figure S1B).

V1V2 measurements correspond to closed and open Env structures.

To evaluate Env flexibility and heterogeneity in V1V2, which forms the closed trimer apex and is repositioned upon CD4 binding, we spin-labeled BG505 □-strand residue 173 to make BG505-173*. Distance distributions calculated from DEER spectra for unliganded BG505-173* revealed a most probable distance peak at 38Å, with a full width at half maximum (FWHM) of ~10Å broadening to ≥15Å at its base (Figure 2A, S2), consistent with C□-C□ measurements of closed Env structures (mean = 36Å) (Figure 1C) and suggesting 3-fold

symmetry and detectable, but limited, structural heterogeneity. Unliganded B41-173* also exhibited a most probable distance at 38Å, similar to the BG505-173* peak, albeit with a reduced FWHM and a lower probability shoulder in the 29–35Å range, indicative of structural homogeneity in V1V2 (Figure 2D, S2D).

The addition of sCD4 to BG505-173* and B41-173* induced a large reduction of interspin pairs, suggesting that the majority of 173* spin labels moved beyond the ~80Å limit of DEER detection, consistent with cryo-EM structures of sCD4-bound SOSIP Envs in which V1V2 is displaced to the sides of Env trimer and in which the three copies of residue 173 are separated by ~110Å)(Ozorowski et al., 2017; Wang et al., 2018; Wang et al., 2016) (Figure 2A,D; S2). We also detected a small heterogeneous population (<10% of total) of short (~25Å) and long (>65Å) interspin distance peaks for both samples (Figure 2A,D), which may reflect defined structures in a sCD4-bound conformation.

The V3 region is rigid when closed and flexible when CD4-bound.

We investigated the conformational flexibility of V3, the binding site for coreceptor, which is buried beneath V1V2 in closed structures and exposed upon CD4 binding (Ward and Wilson, 2017), by spin labeling BG505 residue 306 (Figure 1). DEER distributions for unliganded BG505-306* exhibited a narrow peak at 40Å with a <5Å FWHM (Figure 2B), indicating that the unliganded BG505 Env structure is 3-fold symmetric and rigid with respect to V3. Upon binding to sCD4, a decrease in interspin signal indicated that some spin labels moved out of range, while a smaller population exhibited a peak at 65Å (Figure 2B). B41-306* and B41-306*–sCD4 distance distributions yielded similar results, with a narrow distribution at 38Å for unliganded samples and increased heterogeneity characterized by a broad peak centered at 65Å upon the addition of sCD4 (Figure 2E). These results are consistent with closed and sCD4-bound Env structures: the inter-subunit distance separating residue 306 C□ atoms in closed bNAb-bound Env (Pancera et al., 2014) is 37Å, and residue 306 is either disordered (BG505-sCD4-17b-8ANC195) or separated by 78Å (B41-sCD4-17b) in sCD4-bound Env structures (Ozorowski et al., 2017; Wang et al., 2016) (Figure 1C).

The ~13Å difference in inter-subunit distances between B41-306*-sCD4 DEER measurements (65Å) and the B41-sCD4-17b cryo-EM structure (78Å) suggests that the B41-sCD4 complex can adopt shorter inter-subunit distances between V3 loops in the absence of 17b Fab, which may stabilize a larger inter-subunit separation though interactions near residue 306.

Conformational heterogeneity in the gp120 bridging sheet increases upon CD4 binding.

We next labeled residue 202 in the gp120 □3 strand that becomes part of the bridging sheet upon sCD4 binding (Ozorowski et al., 2017; Wang et al., 2016). Distance distributions for unliganded BG505-202* revealed a most probable distance at 24Å with a ~10Å FWHM (Figure 2C), consistent with closed bNAb-bound Env structures (Figure 1C). Adding sCD4 to BG505-202* broadened the FWHM to 20Å with an overall 50Å span; it also shifted most probable distances, resulting in peaks at 36Å and 42Å (Figure 2C). The B41-202* and BG505-202* distance distributions were essentially superimposable, and the B41-202*–sCD4 distance distribution also showed that addition of sCD4 increased conformational heterogeneity, including a new peak at 44Å (Figure 2F). The emergence of long distance peaks upon sCD4 binding is consistent with residue 202 C□ atoms being separated by 48Å (BG505-sCD4-17b-8ANC195) or 64Å (B41-sCD4-17b) in sCD4-bound Env structures (Ozorowski et al., 2017; Wang et al., 2016) (Figure 1C), and the existence of multiple distances suggests the existence of sCD4-bound conformations that have not been observed in X-ray and cryo-EM Env structures.

The gp120 inner domain exhibits conformational heterogeneity.

To study the gp120 inner domain, a region near the middle of Env trimer that contacts neighboring gp120 subunits and the gp41 subunit in the same protomer (Ward and Wilson, 2017), we spin-labeled gp120 residue 106. Unliganded BG505-106* distance distributions exhibited a 27Å most probable distance (Figure 2G), consistent with C□-C□ distances

measured in bNAb-bound BG505 crystal structures (30Å) (Figure 1C). We also observed a population of lower probability (~25%) peaks at 35Å, 40Å, 50Å, and 60Å, indicating conformational heterogeneity in the inner domain of unliganded SOSIP Env (Figure 2G). The addition of sCD4 induced a distance distribution shift in which peaks at 40Å, 48Å, and 60Å were populated, with the 48Å peak being the most probable. These results are consistent with residue 106 C□ atoms being separated by 46Å (BG505-sCD4-17b-8ANC195) or 51Å (B41-sCD4-17b) in sCD4-bound Env structures (Ozorowski et al., 2017; Wang et al., 2016) (Figure 1C) and also suggest the presence of sCD4-bound conformations in the inner domain of unliganded Env (Figure 2G). B41-106* exhibited a similar distance distribution to its BG505-106* counterparts when unliganded and sCD4-bound (Figure 2J). However, unliganded B41-106* appeared more homogeneous, with a larger population of the dominant peak corresponding to closed Env structures.

The gp41 base exhibts conformational flexibility.

We also spin-labeled gp41 residues 542 and 657 towards or at the base of the SOSIP trimer (Figure 1C). Unliganded BG505-542* exhibited a broad multimodal distance distribution (Figure 2H), with the shortest distance peak (26Å) consistent with closed Env structures (Figure 1C). The addition of sCD4 had relatively little effect on the overall heterogeneity of BG505-542* distribution (Figure 2H). Notably, the most probable peak at ~34Å that appeared in both liganded and sCD4-bound BG505-542* is consistent with distance measurements in sCD4-bound Env structures (Ozorowski et al., 2017; Wang et al., 2016) in which residue 542 C□ atoms are separated by 34Å (BG505-sCD4-17b-8ANC195) or 35Å (B41-sCD4-17b) (Figure 1C), suggesting the presence of sCD4-bound conformation(s) in unliganded gp41.

Distance distributions for unliganded BG505-657* showed a narrow peak at 22Å with a shoulder at 27Å and a ~10Å FWHM (Figure 2I), consistent with the 26Å measured distance in closed Env structures (Figure 1C). BG505-657* incubated with sCD4 exhibited a similar distribution, characterized by peaks at 25Å and 32Å (Figure 2i). In contrast, B41-657*

exhibited a broad multimodal distribution with multiple peaks ranging from 20–65Å, and the addition of sCD4 resulted in few changes other than minor differences in relative peak heights (Figure 2K). While the unliganded BG505-657* data were consistent with bNAb-bound closed trimer structures (26 +/- 2.8Å mean inter-subunit distance separating residue 657 C□ atoms), the BG505-657*–sCD4, B41-657*, and B41-657*–sCD4 data exhibited heterogeneity characterized by distances longer than those measured in CD4-bound Env structures (Figure 1C; 2I,K).

bNAbs and inhibitors have differential effects on SOSIP Env conformations.

To investigate how bNAb and small molecule ligands influence Env conformations, we collected DEER spectra for spin-labeled Envs following incubation with the CD4-binding site (CD4bs) bNAbs b12 (Burton et al., 1991) or 3BNC117 (Scheid et al., 2011), the small molecule HIV-1 entry inhibitor BMS-626529 (Li et al., 2013), and the gp41 fusion peptide-binding bNAb N123-VRC34.01 (Kong et al., 2016) (hereafter VRC34) (Figure 3-5; S3-S5).

b12 binding to virion-bound and SOSIP Envs stabilizes an open conformation of gp120 subunits and rearrangements in gp41 (Liu et al., 2008; Ozorowski et al., 2017), similar to changes observed upon sCD4 binding, although the ~40Å V1V2 movement and rearrangement of the gp120 bridging sheet that results from CD4 binding (Wang et al., 2016) does not occur in b12-bound Env (Ozorowski et al., 2017) (Figure 3A). By contrast, binding of VRC01-class CD4bs bNAbs such as 3BNC117 does not alter closed SOSIP structures (Lee et al., 2017; Stewart-Jones et al., 2016). We collected DEER data for b12 complexes with BG505-173*, B41-173*, BG505-202*, BG505-306*, B41-306*, and B41-657*, and 3BNC117 complexes with BG505-173* and B41-173* (Figure 3; S3).

Binding of b12 altered distance distributions associated with most sites. The BG505-173*–b12 and B41-173*–b12 DEER distributions showed new peaks at 55Å and 62Å, respectively (Figure 3B,E), consistent with the B41-b12 cryo-EM structure in which the C□-C□ distance between the three copies of residue 175 is 67Å (173 is disordered in this structure) (Figure 3A). The addition of b12 had minimal effects on BG505-306*, but increased the

heterogeneity of B41-306*, as evidenced by the broader distribution surrounding the 38Å peak that was observed in unliganded B41-306* (25Å FWHM for b12-bound B41-306*; 10Å FWHM for unliganded B41-306*) (Figure 3C,F). This result suggests that upon b12 binding, B41 residue 306 can adopt conformations other than that observed in the cryo-EM structure in which the C□-C□ separation distance is 51Å. For BG505-202*, b12 binding resulted in a multimodal distribution with a range of longer-distance peaks spanning ~31–57Å (Figure 3D). Similar to unliganded B41-657*, the B41-657*–b12 DEER data exhibited a multimodal distribution spanning ~30Å; however, the B41-657*–b12 most probable distances were shifted from their unliganded counterparts, suggesting that b12 binding to V1V2 resulted in rearrangements at the base of Env (Figure 3G).

By contrast with the b12 results, incubation of BG505-173* and B41-173* with 3BNC117 Fab revealed distance distributions indistinguishable from their unliganded counterparts, indicating that 3BNC117 binding did not alter the conformation of V1V2 (Figure 3I,J), consistent with a BG505 SOSIP-3BNC117 structure (Lee et al., 2017) (Figure 3H).

BMS-626529 is a small molecule HIV entry inhibitor (Li et al., 2013) that prevents CD4 binding by interacting with gp120 through an induced pocket involving bridging sheet residues located near the inner domain (Pancera et al., 2017) (Figure 4A). The crystal structure of a bNAb-bound BG505–BMS-626529 complex (Pancera et al., 2017) (Figure 4A), although superimposable with other bNAb-BG505 complexes except for differences in the C-terminal helix near gp41 residue 657, showed BMS-626529 binding gp120 near an inner domain helix that contains gp120 residue 106. Consistent with the crystal structure, addition of BMS-626529 did not markedly influence the distance distribution of BG505-173*, although the FWHM narrowed by ~5Å (Figure 4B, S4) suggesting reduced heterogeneity. BMS-626529 also altered the unliganded BG505-106* distance distribution in a manner suggesting reduced heterogeneity, in this case changing both long and short distance peaks (Figure 4C).

To explore how the fusion peptide-binding bNAb VRC34 (Kong et al., 2016) (Figure 5A) affects Env conformations, we collected DEER data for BG505-202*–VRC34 and BG505-657*–VRC34 complexes in the presence and absence of sCD4 (Figure 5, S5). The distance

distribution of BG505-202* incubated with VRC34 Fab was similar to unliganded BG505-202*, both exhibiting a 22Å most probable distance (Figure 5B). For the BG505-202*–VRC34–sCD4 complex, the distance distribution was broader than the distribution for unliganded BG505-202* (FWHM ~15Å compared to ~10Å for unliganded), yet narrower than the B505-202*–sCD4 distributions and characterized by a new peak at 32Å (Figure 5C). These results suggest that VRC34 inhibited some, but not all, sCD4-induced movements in the gp120 bridging sheet, and that BG505-SOSIP-VRC34-sCD4 complexes adopt conformations that have not been observed in X-ray or cryo-EM structures.

In contrast to the similarities between the BG505-202* and BG505-202*–VRC34 distance distributions (Figure 5B), the BG505-657*–VRC34 distance distribution showed differences from unliganded BG505-657* even in the absence of sCD4, exhibiting a second most probable distance at 30Å in addition to the 22Å most probable distance in both VRC34-bound and unliganded BG505-657* (Figure 5D). The BG505-657*–VRC34–sCD4 distance distribution showed only minor differences compared to BG505-657*–VRC34, suggesting few effects in gp41 following sCD4 addition to an Env-VRC34 complex (Figure 5E). The addition of VRC34 to B41-657*, which exhibited a broad multimodal distribution when unliganded (Figure 2K), increased the population of a short-distance peak at 22Å (Figure 5F). The B41-657*–VRC34–sCD4 distance distribution showed only minor differences compared to B41-657*–VRC34, but was distinct from B41-657* + sCD4 (Figure 5G). Taken together, these results are consistent with VRC34 inhibiting CD4-induced conformational changes that expose the coreceptor binding site (Kong et al., 2016) and suggest that VRC34 can limit mobility in B41 gp41.

Intra-subunit flexibility between SOSIP V1V2 and V4 is limited and contrasts with smFRET results.

To characterize conformational states within a single Env subunit and compare with smFRET studies of virion-bound Envs (Ma et al., 2018; Munro et al., 2014), we produced BG505 variants in which each gp120 included two spin-labeled sites: 173* (in V1V2) and

394* (in □18 strand immediately upstream of V4) (Figure 6A). This resulted in Env trimers with six spin labels, which include inter-subunit distances between the three copies of each spin label, and both inter- and intra- subunit distances between 173* and 394* (Figure 6A, S6). Based on measurements between C□ atoms in closed Env structures (Ward and Wilson, 2017), we expected five possible distances, two of which (394* inter-subunit distances and one of the 173*–394* inter-subunit distances) should be >80Å and thus undetectable in DEER experiments) (Figure 6A). Indeed, there was no detectable DEER signal in BG505-394* (Figure S6), and distance distributions from BG505-173*+394* variants exhibited three peaks, one at 38Å, which overlapped with the BG505-173* distributions, a peak at 50Å, corresponding to the measured 173*-394* intra-subunit distance (mean=49Å), and a peak at 62Å, corresponding to the 173*-394* inter-subunit distance (mean=61Å) (Figure 6B, S6). The close match between the BG505-173*+394* distance distribution and SOSIP Env structures (Figure 6A,B), combined with the lack of additional peaks that would indicate asymmetry and/or additional conformations, suggest that BG505 SOSIP exists in a single, symmetric conformation with respect to distances between the V1V2 and V4 regions.

Discussion

HIV-1 SOSIP Envs (Sanders et al., 2013), are being evaluated as potential immunogens to elicit anti-HIV-1 bNAbs (Escolano et al., 2016; Medina-Ramirez et al., 2017; Steichen et al., 2016). SOSIPs were designed to mimic the closed, prefusion state of virion-bound HIV-1 Envs in order to induce relevant immune responses in humans (Sanders and Moore, 2017), thus understanding their structures compared with virion Env trimers and evaluating their conformation(s) is critical for vaccine design, interpreting results from clinical trials, and understanding dynamics related to Env functions in receptor recognition and membrane fusion.

Here we investigated SOSIP conformations in solution using DEER spectroscopy, comparing results to static crystal and cryo-EM structures of SOSIP and non-SOSIP Env trimers (Ward and Wilson, 2017), low resolution cryo-ET structures of virion-bound Envs

(Liu et al., 2008), and smFRET studies of Env dynamics on viruses (Ma et al., 2018; Munro et al., 2014) (Figure 7). We note that within the ~20Å resolution limitation of the cryo-ET structures (Liu et al., 2008), the distinct closed and open conformations of Envs on HIV-1 virions superimpose with higher-resolution structures of analogous SOSIP Env conformations (Harris et al., 2011). DEER distance distributions were consistent with coordinate measurements of closed (bNAb-bound) and open sCD4-bound SOSIP Env structures demonstrating that (*i*) unliganded SOSIP Envs resemble closed bNAb-bound SOSIP structures, (*ii*) SOSIPs can adopt relevant receptor-bound conformations, and (*iii*) DEER measurements can be used as reporters of structural changes and conformational landscapes in SOSIP Envs. Given the similarity of SOSIP and virion-bound Env structures, the DEER results can be extended to allow speculation about viral Env dynamics that are relevant to recognition by antibodies and Env's function in fusion between the viral and host membranes.

DEER measurements of unliganded BG505 and B41 SOSIPs at the trimer apex (V1V2 173*, bridging sheet 202*, and V3 306*) were consistent with bNAb-bound SOSIP structures to within a few Ångstroms, confirming that cryo-EM and X-ray structures faithfully report the dominant solution conformation of SOSIP Envs at the trimer apex. The DEER distributions were relatively narrow, suggesting minimal conformational heterogeneity and/or flexibility in the trimer apex. Indeed, the remarkably narrow BG505-306* distribution indicated a highly rigid structure and tight 3-fold symmetry. On virions, 3-fold symmetry at a closed Env trimer apex is likely important to prevent exposing the coreceptor binding site on V3 prior to engagement with a host CD4 receptor (Ward and Wilson, 2017); thus SOSIPs reproduce this presumed functional property of virion Envs. In addition, these results demonstrate the ability of DEER to detect potential V3 region exposure, thereby providing a means to guide design of immunogens that do not expose non-neutralizing antibody epitopes.

DEER measurements at sites distal from the trimer apex (gp120 inner domain 106*, gp41 542*, and gp41 657*) were also consistent with bNAb-bound SOSIP structures, but the distributions were broader and multimodal compared with the narrow distributions of apex measurements. Thus, motifs at the Env base are conformationally heterogeneous and sample conformations that are not apparent in closed structures. Heterogeneity was pronounced for

B41-657*, suggesting more flexibility in B41's trimer base than the base of BG505, consistent with reports that B41 SOSIP is more flexible than BG505 (Pugach et al., 2015). However, our apex measurements indicated that B41 flexibility excluded its trimer apex.

Conformational heterogeneity associated with measurements distal from the apex could arise from local flexibility and/or deviations from 3-fold symmetry. Notably, structurally-uncharacterized distances overlapped with distances that were populated upon the addition of sCD4, suggesting that regions of the gp120 inner domain and gp41 transiently sample sCD4-bound conformations when unliganded, but that conformational heterogeneity is not transferred to the apex in the absence of sCD4. If this property of SOSIP Envs extends to virion Envs, decoupling between the Env base and apex may prevent membrane perturbations from triggering apex opening until CD4 engagement.

CD4 binding repositions V1V2 towards the side of the trimer while rotating gp120 subunits outward and triggering changes in gp41; however, most of V1V2 and V3 are disordered in sCD4-bound cryo-EM structures (Ozorowski et al., 2017; Wang et al., 2016). Consistent with these large-scale conformational changes, the addition of sCD4 to SOSIP Envs in DEER experiments shifted the most probable distances in all spin-labeled Env motifs near the trimer apex. In motifs that are ordered in sCD4-bound structures, the most probable DEER distances were in agreement with structures; however, all distributions were broad and multimodal, indicating a high level of conformational heterogeneity in sCD4-bound complexes. Observed distances that do not correspond to sCD4-bound Env structures could represent heterogeneous, but defined, positions that were in disordered regions of cryo-EM structures of sCD4-bound Envs (Ozorowski et al., 2017; Wang et al., 2016). Heterogeneity could also be explained by increased flexibility among individual motifs and/or deviations from 3-fold symmetry in Env trimer during or after sCD4 binding. For example, in sCD4-bound complexes, short distance peaks could arise from sub-stoichiometric sCD4 binding, which could induce asymmetric Env conformations characterized by displaced motifs (e.g., V1V2 or V3) in a sCD4-bound protomer adjacent to unbound "closed" motifs in an unliganded protomer. Additional evidence supporting the existence of asymmetric Env conformations was recently provided by smFRET experiments showing that individual Env protomers on

native virions adopt distinct conformations during sCD4-induced trimer opening (Ma et al., 2018).

The open sCD4-bound B41 SOSIP structure showed conformational changes in gp41 compared with closed bNAb-bound SOSIP structures (Ozorowski et al., 2017), although their magnitudes were smaller than the sCD4-induced displacements of the gp120 subunit and V1V2 region (Wang et al., 2016). The most probable distances for DEER measurements of SOSIPs with labels in gp41 in the presence of sCD4 were generally consistent with cryo-EM structures (Ozorowski et al., 2017; Wang et al., 2016). However, DEER measurements exhibited heterogeneity in the presence and absence of sCD4, with relatively minor changes upon addition of sCD4.

Comparing DEER measurements on bNAb-bound complexes with bNAb-bound Env structures (Ward and Wilson, 2017) validated and extended static structural results. DEER experiments examining the effects of the CD4bs bNAb b12 were consistent with the cryo-EM structure of a B41-b12 complex, which revealed b12 interactions with the CD4bs and V1V2 that stabilized an open Env conformation distinct from sCD4-bound complexes (Ozorowski et al., 2017). It was postulated that this conformation arises in part from b12 capturing a transient conformation (Ozorowski et al., 2017; Tran et al., 2012). However, DEER experiments showed no evidence that the V1V2, bridging sheet, or V3 regions of unliganded BG505 or B41 SOSIP Envs sampled b12-bound conformations transiently. Together with observations that BG505-173*–b12 and B41-173*–b12 distance distributions exhibited a peak that was not present in unliganded B41-173* distance distributions, our results suggest that the b12-bound Env conformation arises from an induced-fit mechanism rather than from capturing a transient Env conformation in equilibrium with the closed state. The emergent long-distance peaks associated with b12 binding were more populated in B41-173* than BG505-173* measurements, and addition of b12 induced greater heterogeneity in B41-306* than in BG505-306*, suggesting that Env apex displacements were easier to induce in B41 than BG505.

By contrast to the b12 bNAb, addition of the CD4bs bNAb 3BNC117 or the fusion-peptide binding bNAb VRC34 had only minor effects on SOSIP conformations. However, the

observation that DEER spectroscopy detected changes upon binding of VRC34 and showed that VRC34 inhibited some sCD4-induced conformational changes illustrates the sensitivity of DEER to investigate uncharacterized Env structures and effects of bNAb binding.

To address how data describing Env conformational heterogeneity relate to molecular structures, we compared results from DEER and smFRET, methods that provide distinct information related to protein structure and dynamics (Jeschke, 2012; Roy et al., 2008). DEER spectroscopy yields direct distance measurements up to ~80Å and detects the probability of different polypeptide chain backbone conformations that reflect local, domain, and global movements in molecules in a population by measuring between small and rigid labels located in defined secondary structures (Jeschke, 2012). In contrast, smFRET is a single molecule technique that records millisecond to minute time scale changes in the relative positions of large, flexible probes separated by up to ~80Å (Roy et al., 2008). The FRET signal is proportional to the distance between the dipole moments of the probes and can be correlated with domain and global movements; however, because the probes adopt unknown orientations relative to the polypeptide chain backbone, smFRET provides indirect distance information associated with conformational transition(s) (i.e., potential changes in FRET states may not be directly correlated with distance changes between the polypeptide chain backbones in the labeled sites). In both DEER and smFRET experiments, probe locations affect the results and interpretation of data. For example, smFRET studies of labeled virion-bound Envs described FRET changes between donor and acceptor dyes located in the V1 and V4 regions of a single protomer within each Env trimer (Figure 7A) (Munro et al., 2014) (i.e., intra-protomer changes), thus reporting on potential changes between two positions at or near the apex of an Env protomer. By contrast, DEER experiments reported here measured inter-protomer distances between three labels at six locations within soluble Env trimers as well as an intra-protomer V1V2–V4 distance. With these differences in mind, we attempted to integrate our DEER results using SOSIP Envs with smFRET studies conducted on virion-bound Envs (Ma et al., 2018; Munro et al., 2014), combining structural data derived from crystallographic studies of closed Envs (Ward and Wilson, 2017), single-particle cryo-EM structures of sCD4-bound Envs (Ozorowski et al.,

2017; Wang et al., 2016), and cryo-ET structures of both conformations on virions (Liu et al., 2008).

The smFRET studies reporting three states for the V1–V4 distance on virion Envs used labels attached to peptide linkers inserted at V1 residue 136 and V4 residue 400 (Ma et al., 2018; Munro et al., 2014), which are separated by ~48Å in closed Env structures (measured in pdb 5CEZ (Garces et al., 2015) between C□ atoms of residues 136 and 398; residue 400 is disordered). If changes in dye positions correlate directly with distance changes between V1 and V4, then State 1 represents the longest intra-protomer dye distance, with States 2 and 3 representing short and intermediate distances, respectively. The BG505-173*+394* DEER distances were consistent with closed Env structures in which residue 173 (in V1) and residue 394 (adjacent to V4) are separated by 49Å, and assuming a closed trimer apex as seen in Env structures (Ward and Wilson, 2017) and confirmed by inter-subunit DEER measurements, 49Å is likely the smallest distance that can separate residues 173 and 394; i.e., steric constraints should prevent shorter distances separating V1 and V4. If so, then existing SOSIP (Ward and Wilson, 2017) and non-SOSIP (Lee et al., 2016) Env structures must represent the smFRET state with the shortest intra-dye distance; i.e., State 2.

The observation that smFRET State 3 was populated from State 2 upon the addition of sCD4 (Ma et al., 2018; Munro et al., 2014) suggests State 3 represents sCD4-bound conformation(s), which presumably correspond to the CD4-bound open conformation observed in cryo-EM structures of sCD4-bound SOSIPs (Ozorowski et al., 2017; Wang et al., 2016) and cryo-ET structures of sCD4-bound Envs on viruses (Liu et al., 2008), which are equivalent within the ~20Å resolution limitation of the cryo-ET-derived structures (Harris et al., 2011). The intermediate FRET associated with State 3 is consistent with (*i*) the increased distance between V1 and V4 in sCD4-bound Env structures resulting from V1V2 displacement from the trimer apex (Wang et al., 2016), (*ii*) an ~72Å V1–V4 distance measured between residues 136 and 400 in a sCD4-bound SOSIP Env structure (Wang et al., 2016) including a molecular dynamics model for the displaced V1V2 (Yokoyama et al., 2016), and (*iii*) the appearance of long inter-subunit distances (>70Å) in BG505-173*–sCD4 and B41-173*–sCD4 DEER experiments. The lower FRET signal associated with State 1 indicates an increase in the distance between probes in V1 and V4 compared with the State

3 inter-probe distance, suggesting that V1 and V4 are separated by larger distances in State 1 Envs than in CD4-bound Envs. This possibility is difficult to reconcile with the constraints of a closed trimer apex that buries the coreceptor binding site.

Intra-subunit DEER measurements between V1V2 residue 173 and V4 residue 394, which approximate the positions of smFRET dyes inserted into V1 and V4 (Figure 7A), suggested a single predominant state for the closed BG505 SOSIP apex, rather than the three states interpreted from the smFRET studies of unliganded virion-bound Envs (Munro et al., 2014). This DEER result was consistent with closed SOSIP (Ward and Wilson, 2017) and non-SOSIP (Lee et al., 2016) Env structures, as well as the closed, unliganded Env conformation on virions (Liu et al., 2008), and revealed no evidence for distinct conformational states with respect to the V1V2 – V4 distance in the absence of sCD4 as suggested by smFRET (Ma et al., 2018; Munro et al., 2014). Although this difference could relate to different V1–V4 conformational landscapes in SOSIPs compared with virion Envs, some of the discrepancy could result from size, hydrophobicity, and/or flexibility differences in DEER and smFRET labels.

Although our experiments showed no evidence of multiple states with respect to V1V2–V4 separation distances, DEER detected multiple inter-subunit distances in gp41 and neighboring regions of the gp120 inner domain of unliganded SOSIPs, suggesting conformational plasticity distal from the apex. If these results can be extended to virion-bound Envs, both smFRET State 1 and State 2 could be characterized by a closed apex, but distinguishable by differences towards the Env base. Thus movements distal to the apex might be sensed by the smFRET V4 probe, which is large and flexible enough to extend below the trimer apex and whose position could be altered by ligands that affect the stability of this region and/or by the SOSIP substitutions. Indeed, DEER experiments detected multiple states of unliganded SOSIPs in Env regions below the apex, perhaps analogous to the multiple states of virion-bound Env detected by smFRET (Ma et al., 2018; Munro et al., 2014). One way to more directly compare results from smFRET and DEER experiments would be to perform smFRET studies on SOSIPs labeled in multiple locations with smaller and less flexible dyes. Another possibility, conducting DEER experiments on spin-labeled virion Envs, is not yet feasible because the concentrations of properly folded, spin-labeled

Env likely achievable in virions is insufficient for DEER measurements using currently-available technology.

In conclusion, the DEER results reported here provide previously-unavailable information, not detectable in cryo-EM and X-ray structures, which map regions of low (apex) and high (base) structural heterogeneity in SOSIP Envs currently being evaluated as immunogens. DEER measurements uncovered evidence for multiple conformations in the SOSIP Env base and demonstrated decoupling between the base and apex, indicating that SOSIP immunogens do not expose non-neutralizing apex epitopes (e.g., V3), which if extended to virion-bound Envs, would prevent membrane perturbations from triggering Env apex opening until CD4 engagement. Thus DEER measurements are informative for evaluating the conformational stability of immunogens and understanding the metastable, closed pre-fusion state of HIV-1 Env. When combined with measurements in the presence of sCD4, which revealed receptor-bound conformations in V1V2, V3, and the trimer base not seen in sCD4-bound cryo-EM structures (Ozorowski et al., 2017; Wang et al., 2016), DEER can be used to map conformational changes required for coreceptor binding and fusion between the viral and host cell membranes. Our results also demonstrated strain-specific differences in Env conformations and degrees to which bNAb and inhibitor binding alter the Env conformational landscape. This information is important for better understanding viral fusion, how we might inhibit this process to combat HIV-1 infection, and for identifying conformational differences that distinguish the most effective immunogens.

Methods

Key Resource Table

REAGENT or RESOURCE	SOURCE	IDENTIFIER
Chemicals, Peptides, and Recombinant Proteins		
kifunensine	GlycoSyn	Cat#FC-034
tris(2-carboxyethyl)phosphine (TCEP)	Pierce	Cat#20491
bis(2,2,5,5-tetramethyl-3-imidazoline-1-oxyl-4-il)-disulfide	Enzo	Cat# ALX-430-102-M010
Deuterium oxide, 99.9 atom % D	Sigma-Aldrich	Cat#151882-10x0.6ML
BG505 SOSIP.664 v3.2 (A501C, T605C, I559P, R6, ΔMPER, I535M, L543N)	Bjorkman Lab	GenBank: ABA61516 and DQ208458; Sanders et al., 2013; de Taeye et al., 2015.
BG505 SOSIP.664 v3.2 (Y173C)	This paper	N/A
BG505 SOSIP.664 v3.2 (S306C)	This paper	N/A
BG505 SOSIP.664 v3.2 (T202C)	This paper	N/A
BG505 SOSIP.664 v3.2 (T106C)	This paper	N/A
BG505 SOSIP.664 v3.2 (T394C)	This paper	N/A
BG505 SOSIP.664 v3.2 (R542C)	This paper	N/A
BG505 SOSIP.664 v3.2 (E657C)	This paper	N/A
BG505 SOSIP.664 v3.2 (Y173C; T394C)		
B41 SOSIP.664 v4.2 (A501C, T605C, I559P, R6, ΔMPER, I535M, L543Q, L543N, A316W, H66R)	Bjorkman Lab	GenBank:EU576114; Pugach et al., 2015; de Taeye et al., 2015
B41 SOSIP.664 v4.2 (Y173C)	This paper	N/A
B41 SOSIP.664 v4.2 (S306C)	This paper	N/A
B41 SOSIP.664 v4.2 (T202C)	This paper	N/A
B41 SOSIP.664 v4.2 (E106C)	This paper	N/A
B41 SOSIP.664 v4.2 (R542C)	This paper	N/A
B41 SOSIP.664 v4.2 (E657C)	This paper	N/A
2G12 IgG	Bjorkman Lab	See recombinant DNA
sCD4	Bjorkman Lab	See recombinant DNA
b12 Fab	Bjorkman Lab	See recombinant DNA
3BNC117 Fab	Bjorkman Lab	See recombinant DNA
BMS-626529	APExBIO	Cat#A3253
VRC34.01 Fab	Bjorkman Lab	See recombinant DNA
Critical Commercial Assays		
QuikChange II Site-Directed Mutagenesis Kit	Agilent	Cat#200524
Experimental Models: Cell Lines		
HEK293-6E	National Research Council of Canada	License#11565
Expi293-F	ThermoFisher	Cat#A14635
Recombinant DNA		
pTT5 mammalian expression vector (used to express all BG505 SOSIP variants and all ligands described above)	National Research Council of Canada	N/A
pIPP4 mammalian expression vector (used to express all B41 SOSIP variants and all ligands described above)	John Moore Laboratory	Weill Cornell Medical College
2G12 IgG light chain in pTT5	Bjorkman Lab	Buchacher et al., 1994
2G12 IgG heavy chain in pTT5	Bjorkman Lab	Buchacher et al., 1994
b12 Fab light chain in pTT5	Bjorkman Lab	Burton et al., 1991
b12 Fab heavy chain in pTT5	Bjorkman Lab	Burton et al., 1991

(*Continued on next page*)

Continued

REAGENT or RESOURCE	SOURCE	IDENTIFIER
3BNC117 Fab light chain in pTT5	Bjorkman Lab	GenBank: HE584538.1
3BNC117 Fab heavy chain in pTT5	Bjorkman Lab	GenBank: HE584537.1
VRC34.01 Fab light chain in pTT5	Bjorkman Lab	Kong et al., 2016
VRC34.01 Fab heavy chain in pTT5	Bjorkman Lab	Kong et al., 2016
sCD4 D1D2 in pTT5	Bjorkman Lab	NCBI Reference Sequence: NM_000616.4
Software and Algorithms		
Multiscale Modeling of Macromolecules (MMM)	Polyhach et al., 2011	http://www.epr.ethz.ch/software/mmm-older-versions.html
Pymol	Schrödinger, 2011	RRID:SCR_000305
LongDistances v.593	Christian Altenbach	http://www.biochemistry.ucla.edu/biochem/Faculty/Hubbell/
GraphPad Prism	GraphPad	RRID:SCR_002798
Other		
2.0/2.4 mm borosilicate capillary	Vitrocom, Mountain Lakes, NJ	Cat#S102
1.4/1.7 mm (i.d./o.d.) quartz capillary	Vitrocom, Mountain Lakes, NJ	Cat#CV1518Q
Recirculating/closed-loop helium cryocooler and compressor	Cold Edge Technologies, Allentown, PA	N/A
Elexsys 580 spectrometer	Bruker	N/A
E5106400 cavity resonator	Bruker	N/A
TWT amplifier	Applied Engineering Systems, Fort Worth, TX	N/A
Arbitrary waveform generator	Bruker	N/A
HiLoad 16/600 Superdex 200 pg column	GE Healthcare	Cat#28989335
HiTrap Q HP, 5 mL column	GE Healthcare	Cat#17115401
Bio-Spin P-6 Gel columns	Bio-Rad	Cat#7326228
Superose 6 10/300 GL column	GE Healthcare	Cat#17517201
2G12 5 ml column made in-house using using NHS-activated HP resin and 2G12 IgG	GE Healthcare	Cat#17071601
Crystal Structure of the BG505 SOSIP gp140 HIV-1 Env trimer in Complex with an early putative precursor of the PGT121 family at 3.0 Angstrom	RCSB Protein Data Bank	5CEZ
Crystal Structure of HIV-1 BG505 SOSIP.664 Prefusion Env Trimer Bound to Small Molecule HIV-1 Entry Inhibitor BMS-626529 in Complex with Human Antibodies PGT122 and 35O22 at 3.8 Angstrom	RCSB Protein Data Bank	5U7O
Crystal Structure of HIV-1 BG505 SOSIP.664 Prefusion Env Trimer Bound to Small Molecule HIV-1 Entry Inhibitor BMS-378806 in Complex with Human Antibodies PGT122 and 35O22 at 3.8 Angstrom	RCSB Protein Data Bank	5U7M
Cryo-EM model of B41 SOSIP.664 in complex with soluble CD4 (D1-D2) and fragment antigen binding variable domain of 17b	RCSB Protein Data Bank	5VN3
3.5 Angstrom Crystal Structure of a Fully and Natively Glycosylated BG505 SOSIP.664 HIV-1 Env Trimer in Complex with the Broadly Neutralizing Antibodies IOMA and 10-1074	RCSB Protein Data Bank	5T3Z
Crystal Structure of HIV-1 BG505 SOSIP.664 Prefusion Env Trimer in Complex with V3 Loop-targeting Antibody PGT122 Fab and Fusion Peptide-targeting Antibody VRC34.01 Fab	RCSB Protein Data Bank	5I8H

(*Continued on next page*)

Continued

REAGENT or RESOURCE	SOURCE	IDENTIFIER
Crystal Structure at 3.7 A Resolution of Glycosylated HIV-1 Clade A BG505 SOSIP.664 Prefusion Env Trimer with Four Glycans (N197, N276, N362, and N462) removed in Complex with Neutralizing Antibodies 3H+109L and 35O22	RCSB Protein Data Bank	5V7J
Ectodomain of cleaved wild type JR-FL EnvdCT trimer in complex with PGT151 Fab	RCSB Protein Data Bank	5FUU
Cryo-EM structure of a BG505 Env-sCD4-17b-8ANC195 complex	RCSB Protein Data Bank	5THR
Cryo-EM model of B41 SOSIP.664 in complex with fragment antigen binding variable domain of b12	RCSB Protein Data Bank	5VN8
BG505 SOSIP.664 trimer in complex with broadly neutralizing HIV antibody 3BNC117	RCSB Protein Data Bank	5V8M
3.9 Angstrom Crystal Structure of a Fully and Natively Glycosylated BG505 SOSIP.664 HIV-1 Env Trimer in Complex with the Broadly Neutralizing Antibodies IOMA and 10-1074	RCSB Protein Data Bank	5T3X
Molecular Structure of Unliganded Native HIV-1 gp120 trimer: Spike region	Electron Microscopy Data Bank	EMD-5019
Molecular Structure of the Native HIV-1 gp120 trimer bound to CD4 and 17b: Spike region	Electron Microscopy Data Bank	EMD-5020

Protein expression, purification, and spin labeling

Genes encoding BG505 SOSIP.664 v3.2 (in vector pTT5; National Research Council of Canada) and B41 SOSIP.664 v4.2 (in vector pIPP4; John Moore Laboratory - Weill Cornell Medical College), soluble clade A and clade B gp140 trimers, respectively (de Taeye et al., 2015; Pugach et al., 2015; Sanders et al., 2013), including the 'SOS' substitutions ($A501C_{gp120}$, $T605C_{gp41}$), the 'IP' substitution ($I559P_{gp41}$), the *N*-linked glycan sequence at residue 332_{gp120} ($T332N_{gp120}$), an enhanced gp120-gp41 cleavage site (REKR to RRRRRR), and a stop codon after residue 664_{gp41} (Env numbering according to HX nomenclature), were modified to include cysteine residues at single defined positions by site-directed mutagenesis. Modified SOSIPs were expressed in transiently-transfected HEK293-6E cells (National Research Council of Canada) or Expi-293-F cells (ThermoFisher) in the presence of 5 μM kifunensine and purified by 2G12 immunoaffinity chromatography, ion exchange chromatography, and size exclusion chromatography (SEC) as previously described (Scharf et al., 2015). Introduction of cysteines did not alter SEC migration (data not shown). The protein ligands, bNAb Fabs and sCD4 domains 1 and 2, were purified from supernatants of

transiently-transfected HEK293-6E cells as described (Scharf et al., 2015). The HIV-1 attachment inhibitor BMS-626529 was purchased from APExBIO.

SOSIP Nitroxide spin labeling

Purified SOSIP Envs were concentrated to ~100 μM (gp120-gp41 protomer concentration) in Tris-buffered saline (TBS) pH 7.4 and diluted 2x in buffer containing TBS, 40 mM EDTA, and tris(2-carboxyethyl)phosphine (TCEP), resulting in a final solution with a 2x molar excess of TCEP relative to each target cysteine residue. After a 1 hour incubation at room temperature, TCEP was removed using a desalting column (Biorad) and the resulting protein solution was incubated with a 5 molar excess of bis(2,2,5,5-tetramethyl-3-imidazoline-1-oxyl-4-il)-disulfide, which yields the V1 nitroxide side chain, for 3-5 hours at room temperature and overnight at 4˚ C. Excess spin label was removed using Superose 6 SEC. Elution profiles of spin-labeled variants were superimposable with those recorded prior to spin labeling (data not shown). To further assess the effects of introducing cysteines into SOSIP Envs, we used a thermofluor dye-binding assay (Lavinder et al., 2009) to compare the melting temperatures of unmodified BG505 and B41 SOSIP proteins before and after TCEP reduction to the melting temperatures of their counterpart cysteine variants used for DEER experiments. The thermofluor-derived melting temperatures for cysteine-modified and TCEP-treated BG505 and B41 variants were within 2˚C of the melting temperatures derived using this assay for wild type BG505 (melting temperature = 68˚C) and B41 (melting temperature = 58˚C) SOSIP proteins (data not shown). Proteins were exchanged into deuterated solvent to increase the nitroxide spin-spin relaxation times, thus allowing longer times of data collection (El Mkami and Norman, 2015). Incubations of SOSIPs with bNAb, sCD4, and/or small molecule ligands were conducted for ≥20 hrs, and samples for DEER were maintained at 4˚ C until being flash frozen. Deuterium-exchanged proteins and protein complexes were flash frozen in DEER capillaries within 48 hours of spin labeling to minimize dissociation of the V1 spin label.

Pulsed DEER Spectroscopy

For pulsed DEER spectroscopy, a 15-30 µL sample of ~25-150 µM spin-labeled protein in a deuterated buffer solution containing 20% glycerol was placed in a 1.4/1.7 mm (i.d./o.d.) quartz capillary jacketed in a 2.0/2.4 mm borosilicate capillary (Vitrocom, Mountain Lakes, NJ) and then flash frozen in liquid nitrogen. Sample temperature was maintained at 50 K by a recirculating/closed-loop helium cryocooler and compressor system (Cold Edge Technologies, Allentown, PA). Four-pulse Q-band DEER experiments were conducted on a Bruker Elexsys 580 spectrometer fitted with a E5106400 cavity resonator. Pulse lengths were optimized via nutation experiment but ranged from 12 to 22 ns (π/2) and 24 to 44 ns (π); pulses were amplified with a TWT amplifier (Applied Engineering Systems, Fort Worth, TX). Observer frequency was set to a spectral position 2 G downfield of the low and central resonance intersection point, and the pump envelope frequency was a 50 MHz-wide square-chirp pulse (generated by a Bruker arbitrary waveform generator) set 70 MHz downfield from the observer frequency. Dipolar data were analyzed using LongDistances v.593, a custom program written by Christian Altenbach in LabVIEW (National Instruments); software available online (http://www.biochemistry.ucla.edu/biochem/Faculty/Hubbell/) and described elsewhere (Fleissner et al., 2009). Processing of dipolar evolution data (Figure S2-S6) yields distance probability distributions that reflect all interacting spins in the 15-80Å range (Jeschke, 2012). Each distribution was normalized to total area and depth of modulation (DOM), as indicated by solid lines in the distributions (Figure 2-6). For ease of visualization of peak distances and FWHMs, we also normalized liganded data sets to the maximum amplitude of their unliganded counterpart (dotted lines in Figure 2-6). Distance distributions shown in figures were made using Prism (GraphPad) and associated molecular structure figures were made using Pymol (Schrödinger, 2011).

Dipolar evolution data for mock-labeled BG505 and B41 SOSIP proteins (purified proteins containing no introduced cysteines that were subjected to the V1 labeling procedure) did not exhibit signals above background (data not shown).

Modeling potential V1 nitroxide rotamers and fitting structures to EM maps

To investigate how nitroxide side chain rotamers contributed to DEER measurements, we compared inter-subunit C□-C□ distances (derived from measurements in Env structures from the Protein Data Bank) with inter-subunit V1 nitroxide radicals modeled into the same structures. The Multiscale Modeling of Macromolecules (MMM) program (Polyhach et al., 2011) (http://www.epr.ethz.ch/software/mmm-older-versions.html) was used to model positions of V1 rotamers at each target site. Structures of BG505 and B41 SOSIPS (pdb codes 5CEZ, 5VN8, 5VN3) were used as templates. Each target residue was mutated to cysteine using Pymol (Schrödinger, 2011). V1 spin labels were modeled onto resulting structures using MMM, generating a library of potential rotamers at each site that were used in simulations of DEER distance distributions. We used the most probable rotamer identified by MMM to measure distances between nitroxide radical atoms using Pymol (Schrödinger, 2011). For these measurements, we assumed that the probability of V1 side chains adopting a given rotamer was equivalent in all three protomers of homotrimeric Env. The analysis demonstrated consistency between C□-C□, V1 label - V1 label, and experimentally-determined DEER distances (Figure S1B). Thus differences in V1 rotamers are likely to contribute minimally to experimental DEER distance distributions.

To assess the similarity between atomic resolution structures and EM maps derived by cryo-ET/subtomogram averaging and to make associated figures, SOSIP Env structures (closed, pdb 5T3X (Gristick et al., 2016) and CD4-17b-bound, pdb 5VN3 (Ozorowski et al., 2017)) were fit to the EM density maps of virion-bound Envs (unliganded EMDB 5019 and CD4-17b-bound EMDB 5020 respectively) (Liu et al., 2008) using UCSF Chimera (Pettersen et al., 2004). N-glycans at Env residues 186, 137, 339, 398, 411 and 462 (disordered in 5T3X) were modeled as Man8. Coordinates and EM density for Fabs were omitted for clarity.

Acknowledgements

We thank J. Vielmetter, H. Gao and the Caltech Protein Expression Center for producing proteins, J. Keeffe and A. Voll for cloning assistance, M.E. Abernathy and H. Wang for

making chemical structure and ET map figures, respectively, M. Murphy for assistance with other figures, C. Altenbach for advice on DEER acquisition and analysis, and members of the Bjorkman laboratory for critical reading of the manuscript. B.M.S. was supported by a Caltech Baxter Senior Post-doctoral fellowship. This research was supported by the NIH Grant HIVRAD P01 AI100148 (P.J.B.), the Bill and Melinda Gates Foundation [CAVD Grant OPP1124068 (P.J.B.)], the Jules Stein Professorship Endowment and NIH Grants R01 EY05216, T33 EY07026 and 5P41EB001980.

Author Contributions

B.M.S. and P.J.B. designed the study; B.M.S., M.D.B, M.T.L. and W.L.H. designed DEER experiments and analyzed data; B.M.S. designed and produced spin-labeled proteins with assistance from K.M.D. and K.H.T.; M.D.B. collected and processed DEER data; B.M.S. and P.J.B. wrote the manuscript with contributions from all authors.

Declaration of Interests

The authors declare no competing interests.

References

Bartesaghi, A., Merk, A., Borgnia, M.J., Milne, J.L., and Subramaniam, S. (2013). Prefusion structure of trimeric HIV-1 envelope glycoprotein determined by cryo-electron microscopy. Nat Struct Mol Biol *20*, 1352-1357.

Buchacher, A., Predl, R., Strutzenberger, K., Steinfellner, W., Trkola, A., Purtscher, M., Gruber, G., Tauer, C., Steindl, F., Jungbauer, A.*, et al.* (1994). Generation of human monoclonal antibodies against HIV-1 proteins; electrofusion and Epstein-Barr virus transformation for peripheral blood lymphocyte immortalization. AIDS Res Hum Retroviruses *10*, 359-369.

Burton, D.R., Barbas, C.F., 3rd, Persson, M.A., Koenig, S., Chanock, R.M., and Lerner, R.A. (1991). A large array of human monoclonal antibodies to type 1 human immunodeficiency virus from combinatorial libraries of asymptomatic seropositive individuals. Proc Natl Acad Sci USA *88*, 10134-10137.

de Taeye, S.W., Ozorowski, G., Torrents de la Pena, A., Guttman, M., Julien, J.P., van den Kerkhof, T.L., Burger, J.A., Pritchard, L.K., Pugach, P., Yasmeen, A.*, et al.* (2015). Immunogenicity of Stabilized HIV-1 Envelope Trimers with Reduced Exposure of Non-neutralizing Epitopes. Cell *163*, 1702-1715.

El Mkami, H., and Norman, D.G. (2015). EPR Distance Measurements in Deuterated Proteins. Methods Enzymol *564*, 125-152.

Escolano, A., Steichen, J.M., Dosenovic, P., Kulp, D.W., Golijanin, J., Sok, D., Freund, N.T., Gitlin, A.D., Oliveira, T., Araki, T.*, et al.* (2016). Sequential Immunization Elicits Broadly Neutralizing Anti-HIV-1 Antibodies in Ig Knockin Mice. Cell *166*, 1445-1458 e1412.

Fleissner, M.R., Brustad, E.M., Kalai, T., Altenbach, C., Cascio, D., Peters, F.B., Hideg, K., Peuker, S., Schultz, P.G., and Hubbell, W.L. (2009). Site-directed spin labeling of a genetically encoded unnatural amino acid. Proc Natl Acad Sci U S A *106*, 21637-21642.

Garces, F., Lee, J.H., de Val, N., Torrents de la Pena, A., Kong, L., Puchades, C., Hua, Y., Stanfield, R.L., Burton, D.R., Moore, J.P.*, et al.* (2015). Affinity Maturation of a Potent Family of HIV Antibodies Is Primarily Focused on Accommodating or Avoiding Glycans. Immunity *43*, 1053-1063.

Gristick, H.B., von Boehmer, L., West, A.P., Jr., Schamber, M., Gazumyan, A., Golijanin, J., Seaman, M.S., Fatkenheuer, G., Klein, F., Nussenzweig, M.C.*, et al.* (2016). Natively glycosylated HIV-1 Env structure reveals new mode for antibody recognition of the CD4-binding site. Nat Struct Mol Biol *23*, 906-915.

Harris, A., Borgnia, M.J., Shi, D., Bartesaghi, A., He, H., Pejchal, R., Kang, Y.K., Depetris, R., Marozsan, A.J., Sanders, R.W.*, et al.* (2011). Trimeric HIV-1 glycoprotein gp140 immunogens and native HIV-1 envelope glycoproteins display the same closed and open quaternary molecular architectures. Proc Natl Acad Sci U S A *108*, 11440-11445.

Hubbell, W.L., Cafiso, D.S., and Altenbach, C. (2000). Identifying conformational changes with site-directed spin labeling. Nature Struct Biol *7*, 735-739.

Hubbell, W.L., Lopez, C.J., Altenbach, C., and Yang, Z. (2013). Technological advances in site-directed spin labeling of proteins. Curr Opin Struct Biol *23*, 725-733.

Jeschke, G. (2012). DEER distance measurements on proteins. Annu Rev Phys Chem *63*, 419-446.

Khramtsov, V.V., Yelinova, V.I., Weiner, L.M., Berezina, T.A., Martin, V.V., and Volodarsky, L.B. (1989). Quantitative determination of SH groups in low- and high-molecular-weight compounds by an electron spin resonance method. Anal Biochem *182*, 58-63.

Kong, R., Xu, K., Zhou, T., Acharya, P., Lemmin, T., Liu, K., Ozorowski, G., Soto, C., Taft, J.D., Bailer, R.T.*, et al.* (2016). Fusion peptide of HIV-1 as a site of vulnerability to neutralizing antibody. Science *352*, 828-833.

Lavinder, J.J., Hari, S.B., Sullivan, B.J., and Magliery, T.J. (2009). High-throughput thermal scanning: a general, rapid dye-binding thermal shift screen for protein engineering. J Am Chem Soc *131*, 3794-3795.

Lee, J.H., Andrabi, R., Su, C.Y., Yasmeen, A., Julien, J.P., Kong, L., Wu, N.C., McBride, R., Sok, D., Pauthner, M.*, et al.* (2017). A Broadly Neutralizing Antibody Targets the Dynamic HIV Envelope Trimer Apex via a Long, Rigidified, and Anionic beta-Hairpin Structure. Immunity *46*, 690-702.

Lee, J.H., Ozorowski, G., and Ward, A.B. (2016). Cryo-EM structure of a native, fully glycosylated, cleaved HIV-1 envelope trimer. Science *351*, 1043-1048.

Li, Z., Zhou, N., Sun, Y., Ray, N., Lataillade, M., Hanna, G.J., and Krystal, M. (2013). Activity of the HIV-1 attachment inhibitor BMS-626529, the active component of the prodrug BMS-663068, against CD4-independent viruses and HIV-1 envelopes resistant to other entry inhibitors. Antimicrobial agents and chemotherapy *57*, 4172-4180.

Liu, J., Bartesaghi, A., Borgnia, M.J., Sapiro, G., and Subramaniam, S. (2008). Molecular architecture of native HIV-1 gp120 trimers. Nature *455*, 109-113.

Ma, X., Lu, M., Gorman, J., Terry, D.S., Hong, X., Zhou, Z., Zhao, H., Altman, R.B., Arthos, J., Blanchard, S.C.*, et al.* (2018). HIV-1 Env trimer opens through an asymmetric intermediate in which individual protomers adopt distinct conformations. Elife *7*.

Medina-Ramirez, M., Garces, F., Escolano, A., Skog, P., de Taeye, S.W., Del Moral-Sanchez, I., McGuire, A.T., Yasmeen, A., Behrens, A.J., Ozorowski, G.*, et al.* (2017). Design and crystal structure of a native-like HIV-1 envelope trimer that engages multiple broadly neutralizing antibody precursors in vivo. J Exp Med *214*, 2573-2590.

Munro, J.B., Gorman, J., Ma, X., Zhou, Z., Arthos, J., Burton, D.R., Koff, W.C., Courter, J.R., Smith, A.B., 3rd, Kwong, P.D.*, et al.* (2014). Conformational dynamics of single HIV-1 envelope trimers on the surface of native virions. Science *346*, 759-763.

Munro, J.B., and Lee, K.K. (2018). Probing Structural Variation and Dynamics in the HIV-1 Env Fusion Glycoprotein. Curr HIV Res *16*, 5-12.

Munro, J.B., and Mothes, W. (2015). Structure and Dynamics of the Native HIV-1 Env Trimer. J Virol *89*, 5752-5755.

Ozorowski, G., Pallesen, J., de Val, N., Lyumkis, D., Cottrell, C.A., Torres, J.L., Copps, J., Stanfield, R.L., Cupo, A., Pugach, P.*, et al.* (2017). Open and closed structures reveal allostery and pliability in the HIV-1 envelope spike. Nature *547*, 360-363.

Pancera, M., Lai, Y.T., Bylund, T., Druz, A., Narpala, S., O'Dell, S., Schon, A., Bailer, R.T., Chuang, G.Y., Geng, H.*, et al.* (2017). Crystal structures of trimeric HIV envelope with entry inhibitors BMS-378806 and BMS-626529. Nat Chem Biol *13*, 1115-1122.

Pancera, M., Zhou, T., Druz, A., Georgiev, I.S., Soto, C., Gorman, J., Huang, J., Acharya, P., Chuang, G.Y., Ofek, G.*, et al.* (2014). Structure and immune recognition of trimeric pre-fusion HIV-1 Env. Nature *514*, 455-461.

Pettersen, E.F., Goddard, T.D., Huang, C.C., Couch, G.S., Greenblatt, D.M., Meng, E.C., and Ferrin, T.E. (2004). UCSF Chimera--a visualization system for exploratory research and analysis. J Comput Chem *25*, 1605-1612.

Polyhach, Y., Bordignon, E., and Jeschke, G. (2011). Rotamer libraries of spin labelled cysteines for protein studies. Phys Chem Chem Phys *13*, 2356-2366.

Pugach, P., Ozorowski, G., Cupo, A., Ringe, R., Yasmeen, A., de Val, N., Derking, R., Kim, H.J., Korzun, J., Golabek, M.*, et al.* (2015). A native-like SOSIP.664 trimer based on an HIV-1 subtype B env gene. J Virol *89*, 3380-3395.

Roy, R., Hohng, S., and Ha, T. (2008). A practical guide to single-molecule FRET. Nat Methods *5*, 507-516.

Sanders, R.W., Derking, R., Cupo, A., Julien, J.P., Yasmeen, A., de Val, N., Kim, H.J., Blattner, C., de la Pena, A.T., Korzun, J.*, et al.* (2013). A next-generation cleaved, soluble

HIV-1 Env Trimer, BG505 SOSIP.664 gp140, expresses multiple epitopes for broadly neutralizing but not non-neutralizing antibodies. PLoS Pathog *9*, e1003618.

Sanders, R.W., and Moore, J.P. (2017). Native-like Env trimers as a platform for HIV-1 vaccine design. Immunol Rev *275*, 161-182.

Sanders, R.W., van Gils, M.J., Derking, R., Sok, D., Ketas, T.J., Burger, J.A., Ozorowski, G., Cupo, A., Simonich, C., Goo, L.*, et al.* (2015). HIV-1 neutralizing antibodies induced by native-like envelope trimers. Science.

Scharf, L., Wang, H., Gao, H., Chen, S., McDowall, A.W., and Bjorkman, P.J. (2015). Broadly Neutralizing Antibody 8ANC195 Recognizes Closed and Open States of HIV-1 Env. Cell *162*, 1379-1390.

Scheid, J.F., Mouquet, H., Ueberheide, B., Diskin, R., Klein, F., Olivera, T.Y., Pietzsch, J., Fenyo, D., Abadir, A., Velinzon, K.*, et al.* (2011). Sequence and Structural Convergence of Broad and Potent HIV Antibodies That Mimic CD4 Binding. Science *333*, 1633-1637.

Schrödinger, L. (2011). The PyMOL Molecular Graphics System (The PyMOL Molecular Graphics System).

Steichen, J.M., Kulp, D.W., Tokatlian, T., Escolano, A., Dosenovic, P., Stanfield, R.L., McCoy, L.E., Ozorowski, G., Hu, X., Kalyuzhniy, O.*, et al.* (2016). HIV Vaccine Design to Target Germline Precursors of Glycan-Dependent Broadly Neutralizing Antibodies. Immunity *45*, 483-496.

Stewart-Jones, G.B.E., Soto, C., Lemmin, T., Chuang, G.-Y., Druz, A., Kong, R., Thomas, P.V., Wagh, K., Zhou, T., Behrens, A.-J.*, et al.* (2016). Trimeric HIV-1-Env Structures Define Glycan Shields from Clades A, B, and G. Cell *165*, 813-826.

Toledo Warshaviak, D., Khramtsov, V.V., Cascio, D., Altenbach, C., and Hubbell, W.L. (2013). Structure and dynamics of an imidazoline nitroxide side chain with strongly hindered internal motion in proteins. J Magn Reson *232*, 53-61.

Tran, E.E., Borgnia, M.J., Kuybeda, O., Schauder, D.M., Bartesaghi, A., Frank, G.A., Sapiro, G., Milne, J.L., and Subramaniam, S. (2012). Structural mechanism of trimeric HIV-1 envelope glycoprotein activation. PLoS Pathog *8*, e1002797.

Wang, H., Barnes, C.O., Yanga, Z., Nussenzweig, M.C., and Bjorkman, P.J. (2018). Partially-open HIV-1 Envelope Structures Define Conformational Changes Required for Coreceptor Binding and Fusion. Submitted.

Wang, H., Cohen, A.A., Galimidi, R.P., Gristick, H.B., Jensen, G.J., and Bjorkman, P.J. (2016). Cryo-EM structure of a CD4-bound open HIV-1 envelope trimer reveals structural rearrangements of the gp120 V1V2 loop. Proc Natl Acad Sci U S A *113*, E7151-E7158.

Ward, A.B., and Wilson, I.A. (2017). The HIV-1 envelope glycoprotein structure: nailing down a moving target. Immunol Rev *275*, 21-32.

Yokoyama, M., Nomaguchi, M., Doi, N., Kanda, T., Adachi, A., and Sato, H. (2016). In silico Analysis of HIV-1 Env-gp120 Reveals Structural Bases for Viral Adaptation in Growth-Restrictive Cells. Front Microbiol *7*, 110.

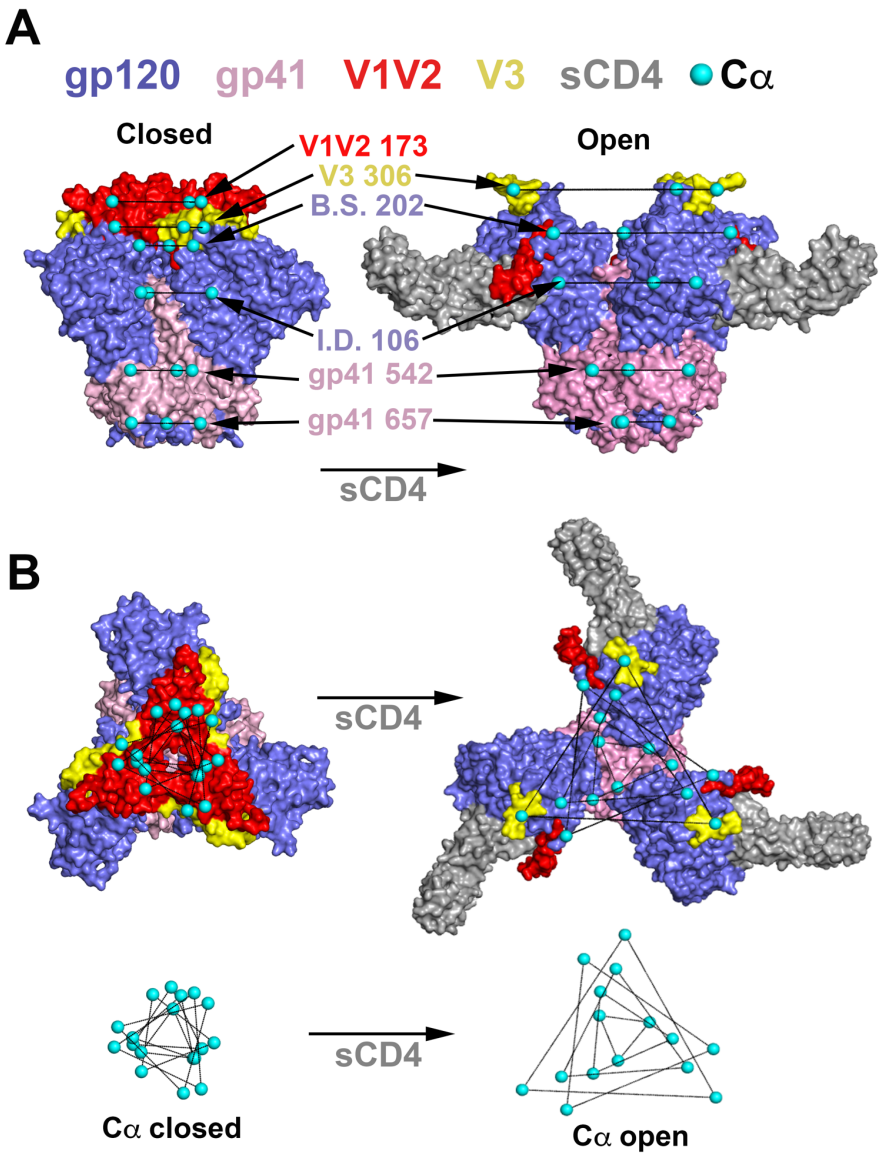

C

Residue Position	Closed Cα-Cα (Å)	Open BG505-sCD4 Cα-Cα (Å)	Open B41-sCD4 Cα-Cα (Å)
V1V2 173	36 +/- 1.1	-	-
V3 306	37 +/- 0.6	-	78 +/- 0.3
B.S. 202	21 +/- 0.6	48 +/- 0.7	64 +/- 0.2
I.D. 106	30 +/- 0.2	46 +/- 0.4	51 +/- 0.1
gp41 542	25 +/- 0.8	34 +/- 0.5	35 +/- 0.1
gp41 657	26 +/- 2.8	24 +/- 0.9	20 +/- 0.2

Figure 1. Inter-subunit distances between target site Cα atoms.

(A) Side-view molecular surface representations of a closed bNAb-bound BG505 (pdb 5CEZ; PGT121 precursor and 35O22 Fabs not shown) and an open B41-sCD4 complex (pdb 5VN3; 17b Fab not shown). Spin-label site Cα atoms shown as cyan spheres. B.S.=bridging sheet; I.D.=inner domain. One of three copies of V1V2 and two of three bound sCD4s are visible. (B) Top view of structures shown in (A) and overlay of spin-label site Cα atoms on closed and open Env structures to illustrate changes upon sCD4 binding. (C) Table listing Env motifs, residue numbers, and measured inter-subunit distances. For closed Envs, each distance is presented as the mean and standard deviation for measurements of SOSIP Env trimers (pdbs 5CEZ, 5T3Z, 5I8H, 5V7J, 5U7M, 5U7O) and a native (non-SOSIP) Env trimer (pdb 5FUU). For open, sCD4-bound Envs, each distance is presented as the mean and standard deviation for the three inter-subunit distances in BG505+sCD4 (pdb 5THR) and B41+sCD4 (pdb 5VN3) structures. Dashes indicate disordered residues for which inter-subunit distances cannot be measured. See also Figure S1.

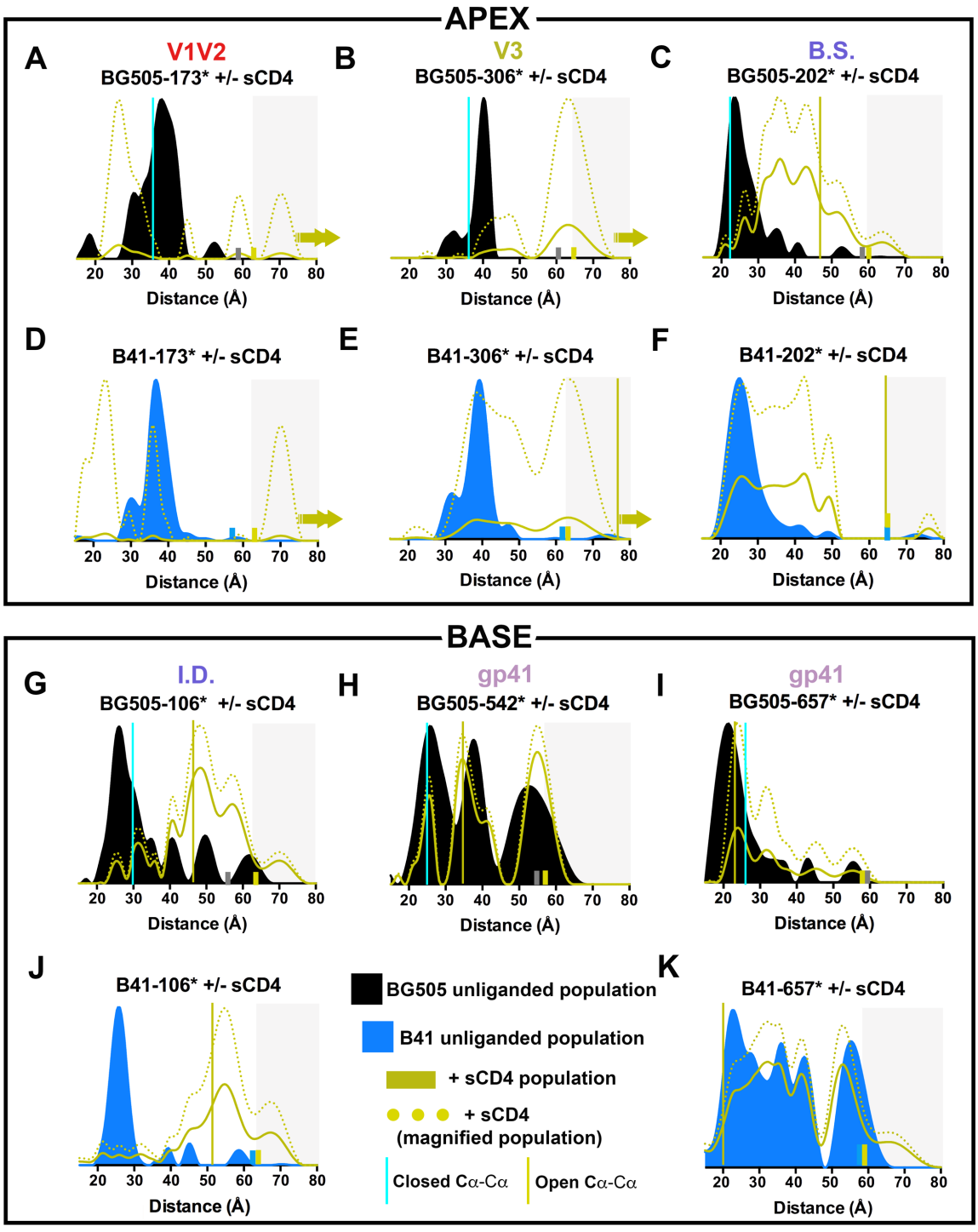
APEX
A
V1V2
BG505-173* +/- sCD4
B
V3
BG505-306* +/- sCD4
C
B.S.
BG505-202* +/- sCD4
D
B41-173* +/- sCD4
E
B41-306* +/- sCD4
F
B41-202* +/- sCD4
Distance (Å)
BASE
G
I.D.
BG505-106* +/- sCD4
H
gp41
BG505-542* +/- sCD4
I
gp41
BG505-657* +/- sCD4
J
B41-106* +/- sCD4
K
B41-657* +/- sCD4
BG505 unliganded population
B41 unliganded population
+ sCD4 population
+ sCD4
(magnified population)
Closed Cα-Cα
Open Cα-Cα

Figure 2. DEER detects conformational changes between unliganded and sCD4-bound Envs. (A-F) Distance distributions for spin labels at Env apex in unliganded and sCD4-bound BG505 and B41 Envs. (G-J) Distributions for spin labels at Env base in unliganded and sCD4-bound BG505 and B41 Envs. The heights of solid colored distributions (BG505 unliganded, B41 unliganded, +sCD4) were normalized for total distribution area scaled by the depth of modulation (DOM) (Figure S2) to reflect the fraction of total spin pairs within the DEER detection limit, and thus, monitor changes in the detectable populations at each distance. For sCD4-bound samples, the heights of dotted distributions were scaled to the amplitude of the unliganded sample, providing a magnified population to facilitate visualization of peak distances and FWHMs. Vertical lines indicate the mean inter-subunit distance (Figure 1) for each site in structures of closed Env (cyan lines) and in open sCD4-bound Envs (yellow lines). Small bars (grey, unliganded BG505; blue, unliganded B41; yellow, Env plus sCD4) indicate the limit of reliable distance measurements for each dataset; populations not reliably determined are indicated by a grey background. Upon the addition of sCD4, the number of spin pairs in the detection range decreased sharply in some samples (highlighted by arrows in liganded populations) as spins moved beyond the detection range; the distance distribution shown is only for the populations within the detection range. For BG505-173*–sCD4 and B41-173*–sCD4, two arrows indicate that ~90% of the spins moved out of range to longer distances. See also Figure S2.

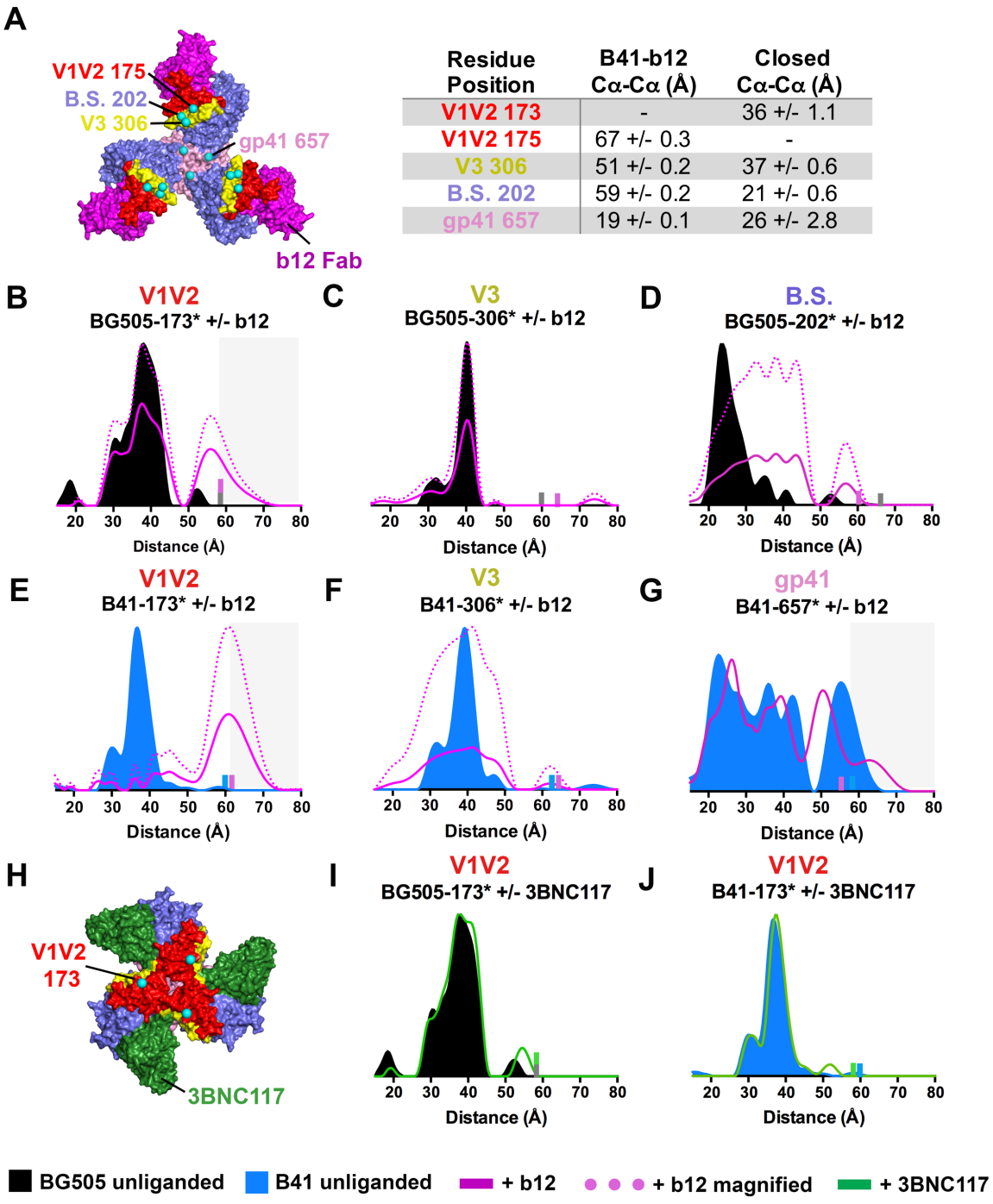

Residue Position	B41-b12 Cα-Cα (Å)	Closed Cα-Cα (Å)
V1V2 173	-	36 +/- 1.1
V1V2 175	67 +/- 0.3	-
V3 306	51 +/- 0.2	37 +/- 0.6
B.S. 202	59 +/- 0.2	21 +/- 0.6
gp41 657	19 +/- 0.1	26 +/- 2.8

Figure 3. CD4bs bNAbs induce distinct structural changes. (A) Left: Structure of a B41-b12 complex (pdb 5VN8) with b12 V_H-V_L in magenta and the positions of spin-labeled sites overlaid as cyan spheres. Right: Measured inter-subunit distances separating the indicated residues in b12-bound and closed structures. Each distance is presented as the mean and standard deviation from multiple measurements as described in the Figure 1C legend. (B-G) Distance distributions for labeled BG505 (panels B-D) and labeled B41 (panels E-G) Envs in the presence and absence of b12. (H) Structure of a BG505-3BNC117 complex (pdb 5V8M) with 3BNC117 V_H-V_L shown in green and the positions of spin-labeled sites overlaid as cyan spheres. (I-J) Distance distributions for unliganded and 3BNC117-bound Envs for BG505-173* (panel I) and B41-173* (panel J). Small bars (grey, BG505 unliganded; blue, B41 unliganded; magenta, Env plus b12; green, Env plus 3BC117) indicate the limit of reliable distance measurements for each dataset; populations not reliably determined are indicated by a grey background. Distributions were normalized and shown as described in the Figure 2 legend. See also Figure S3.

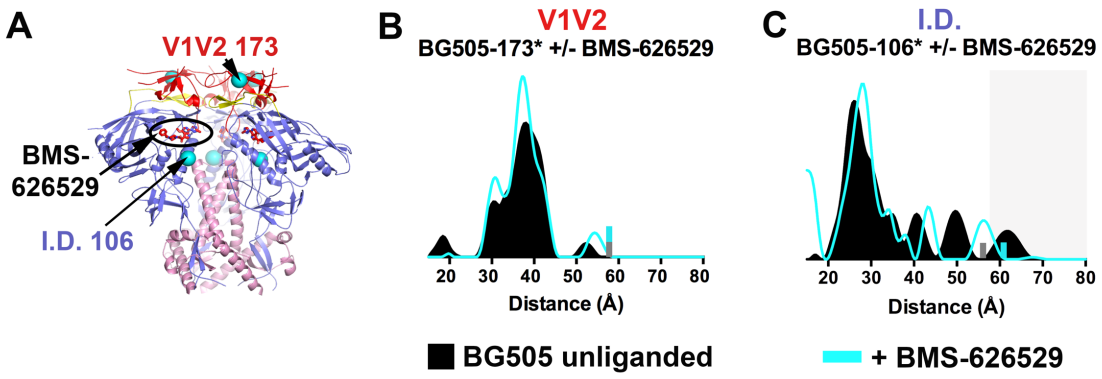

Figure 4. Small molecule inhibitor BMS-626529. (A) BG505–BMS-626529 structure (pdb 5U7O; PGT122 and 35O22 Fabs not shown) showing the BMS-626529 binding sites (one site indicated) with the positions of spin-labeled sites overlaid as cyan spheres. (B-C) Distance distributions for BG505-173* (panel B) and BG505-106* (panel C) in the presence and absence of BMS-626529. Small bars (grey, BG505 unliganded; cyan, Env plus BMS-626529) indicate the limit of reliable distance measurements for each dataset; populations not reliably determined are indicated by a grey background. Distance distributions were normalized as described in Figure 2 legend. See also Figure S4.

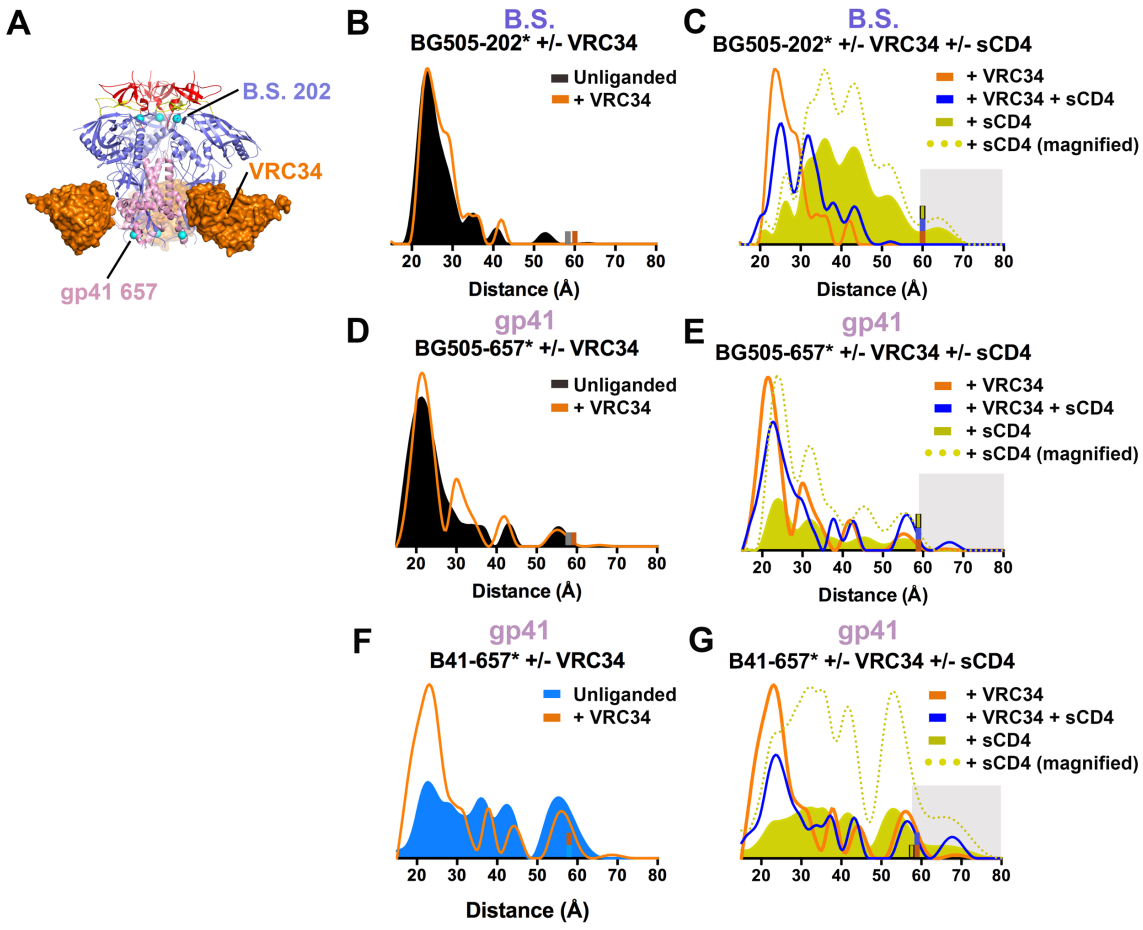
A
B.S. 202
VRC34
gp41 657
B
B.S.
BG505-202* +/- VRC34
Unliganded
+ VRC34
Distance (Å)
C
B.S.
BG505-202* +/- VRC34 +/- sCD4
+ VRC34
+ VRC34 + sCD4
+ sCD4
+ sCD4 (magnified)
Distance (Å)
D
gp41
BG505-657* +/- VRC34
Unliganded
+ VRC34
Distance (Å)
E
gp41
BG505-657* +/- VRC34 +/- sCD4
+ VRC34
+ VRC34 + sCD4
+ sCD4
+ sCD4 (magnified)
Distance (Å)
F
gp41
B41-657* +/- VRC34
Unliganded
+ VRC34
Distance (Å)
G
gp41
B41-657* +/- VRC34 +/- sCD4
+ VRC34
+ VRC34 + sCD4
+ sCD4
+ sCD4 (magnified)
20 30 40 50 60 70 80

Figure 5. Effects of bNAb VRC34. (A) BG505-VRC34 crystal structure (pdb 5I84; PGT122 Fab not shown) with spin-labeled sites overlaid as cyan spheres. (B-E) Distance distributions for BG505-202* (panels B,C) and BG505-657* (panels D,E) and B41-657* (panels F,G) . Panels B, D, F show distance distributions for labeled BG505 or B41 in the presence and absence of VRC34. Panels C, E, F show distance distributions for labeled Env-VRC34 complexes in the presence and absence of sCD4 and comparisons to distributions for labeled Env-sCD4 complexes from Figure 2. Small bars (grey, BG505 unliganded; blue, B41 unliganded; orange, Env plus VRC34; blue, Env plus VRC34 and sCD4; yellow, Env plus sCD4) indicate the limit of reliable distance measurements for each dataset; populations not reliably determined are indicated by a grey background. Distance distributions for BG505-sCD4 are shown for comparison. Distance distributions were normalized as described in the Figure 2 legend and magnified distributions (dotted line; scaled to the amplitude of the unliganded sample) are shown for sCD4 only-containing samples to facilitate comparison of peak distances among samples. See also Figure S5.

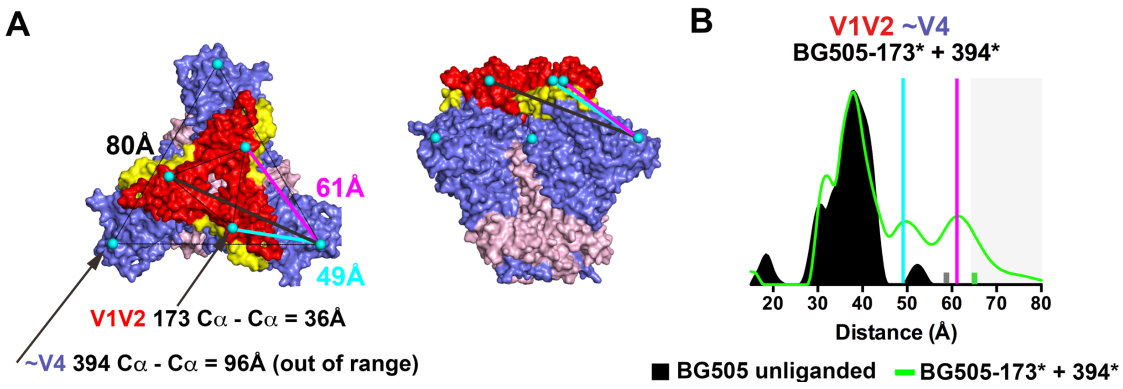

Figure 6. Intra-protamer V1-V4 distance measurements reveal one distance. A) Closed BG505 structure (pdb 5CEZ) colored as in Figure 1 with spin-labeled sites (three 173* labels in V1V2 and three 394* labels in the □-strand preceding V4) overlaid as cyan spheres. A single set of possible 173*–394* distances are drawn as colored lines between a residue 394 C□ atom in one protomer and the three residue 173 C□ atoms in the trimer. The analogous distances measured from the other two residue 394 C□ atoms are equivalent in closed Env structures. Distances shown on the figure are the mean of measurements from the seven closed Env structures used for inter-subunit measurements in Figure 1C. Standard deviations for these measurements were under 1Å. (B) DEER distance distributions for unliganded BG505-173* and unliganded BG505-173*+394*. The positions of the 49Å and the 61Å distances shown in panel A are shown as cyan and magenta lines, respectively on the distance distribution. Measurements on BG505-394* did not produce detectable signal (Supplementary Figure 6), indicating that spin labels were out of DEER range. Small bars (grey, BG505-173* unliganded; green, BG505-173* + 394* unliganded) indicate the limit of reliable distance measurements for each dataset; populations not reliably determined are indicated by a grey background. BG505-173* and BG505-173* + 394* distributions were scaled to the same amplitude because they were independent protein variants. See also Figure S6.

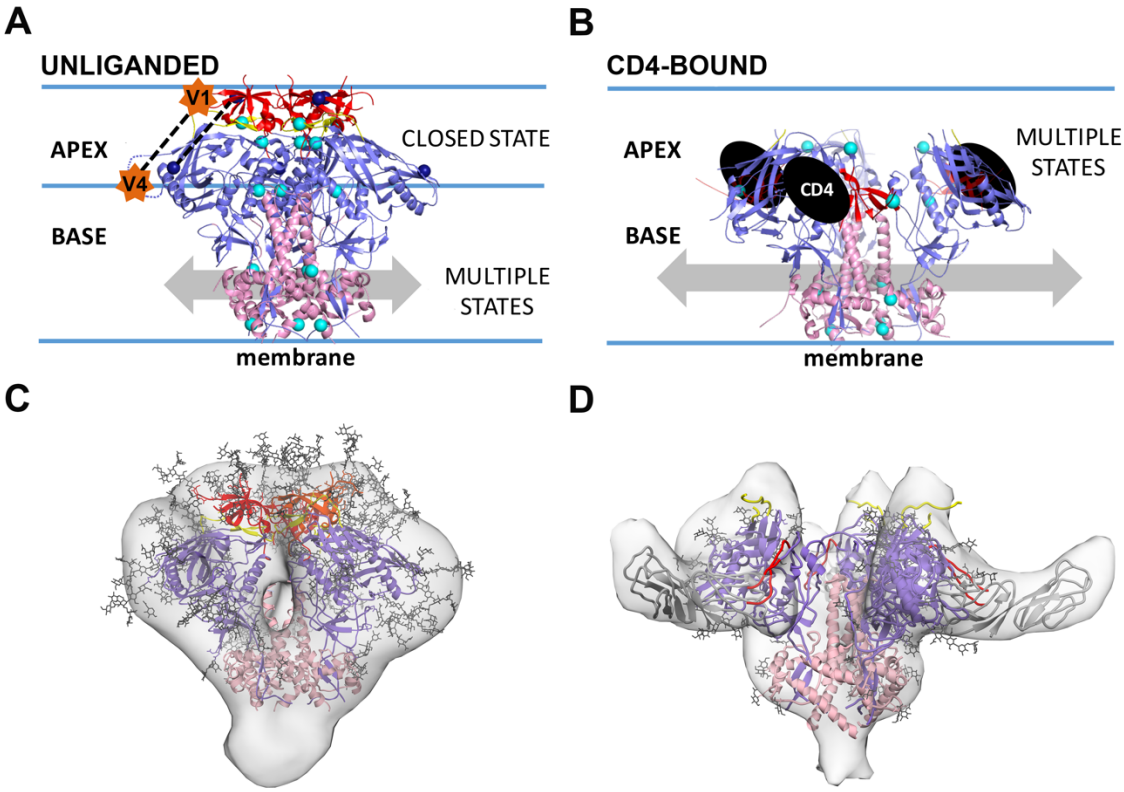

Figure 7. Model for Env conformational dynamics. (A) Unliganded SOSIP Envs are characterized by a closed, three-fold symmetric and homogeneous apex conformation and heterogeneous base conformations. Spin label locations for inter-subunit DEER experiments are shown as cyan spheres; spin labels used to measure an intra-subunit distance (V1V2 173* to ~V4 394*; Figure 6) are navy blue and connected by a dotted line. The approximate locations of residues 136 (in V1) and 400 (V4; disordered in SOSIP structures) where peptide linkers were inserted to attach smFRET dyes that evaluated intra-subunit dynamics (Munro et al., 2014) are shown as orange stars connected by a dotted line. (B) The sCD4-bound SOSIP is characterized by open heterogeneous conformations at the apex and the base. (C) Comparison of closed SOSIP Env structure (cartoon representation with N-glycans depicted as sticks (pdb 5T3X) and EM density map of virion-bound unliganded Env (EMDB 5019) derived by cryo-ET/subtomogram averaging. (D) Comparison of open B41 SOSIP complexed with sCD4 and 17b (pdb 5VN3) and EM density map of open virion-bound Env complexed with sCD4 plus 17b (EMDB 5020). Coordinates and EM density for 17b Fabs were omitted for clarity. The central cavities in the virion-bound EM density maps in panels

C and D are artifacts of the low resolution (~20Å) of the cryo-ET structures (Bartesaghi et al., 2013).

Supplemental Information

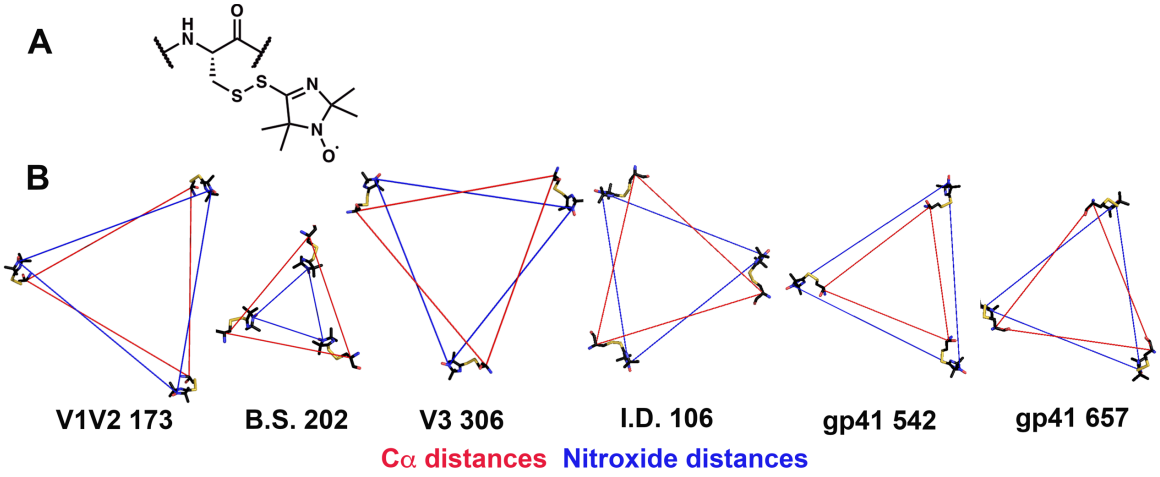

Target Site	MMM # Predicted V1 Nitroxide Rotamers	MMM Predicted DEER Distance (Å)	Nitroxide Distance (Å) (most probable rotamer)	Cα- Cα Distance (Å) (pdb: 5CEZ)	Cα- Cα Distance (Å) (pdbs: 5CEZ, 5T3Z, 5I8H, 5V7J, 5FUU, 5U7M, 5U7O)
V1V2 173	3	36	37	36	36 ± 1.1
B.S. 202	1	12	13	21	21 ± 0.6
V3 306	16	37	36	36	37 ± 0.6
I.D. 106	10	30	29	29	30 ± 0.2
gp41 542	13	34	36	25	25 ± 0.8
gp41 657	17	31	30	27	26 ± 2.8

C

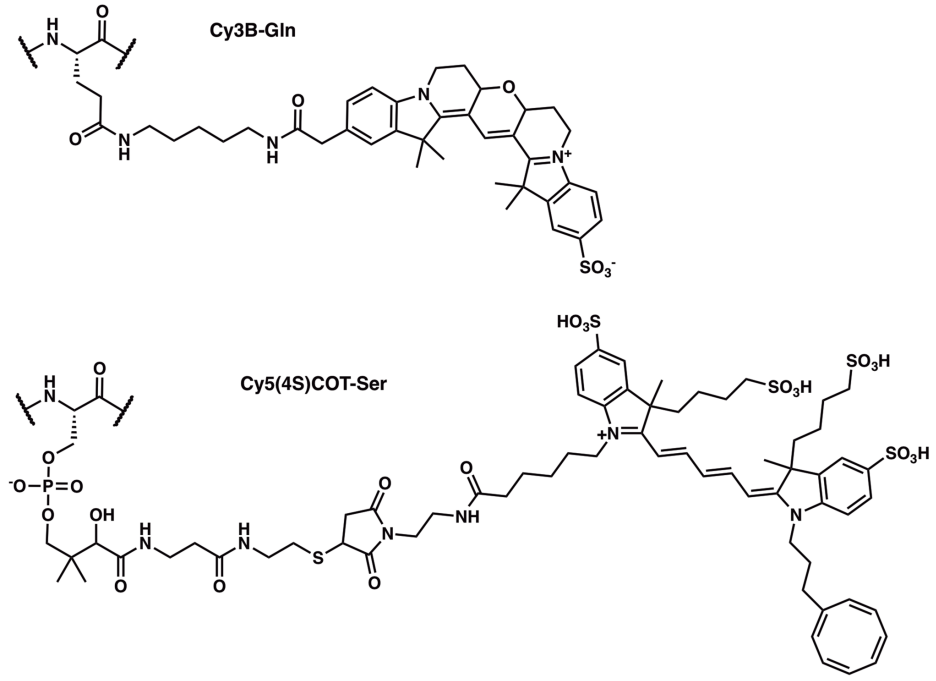

Supplemental Figure 1, related to Figure 1. Chemical structures of labels used for DEER and smFRET. (A) The V1 nitroxide side chain attached to a polypeptide backbone cysteine residue. (B) Top: Measurements of target sites from a closed BG505 structure (pdb code 5CEZ), in which the V1 nitroxide side chain was computationally attached using MMM (Polyhach et al., 2011). The measurements between C□ atoms (red lines) and nitroxide radicals (blue lines) are indicated for each target site. Bottom: Table summarizing the number of V1 rotamers identified by MMM, the most probable distance for each site predicted in a DEER simulation, and the radical-radical atom distance between each site for the most probable V1 rotamer, the C□-C□ distance between each site measured in pdb 5CEZ and the average distance and standard deviation measured in seven pdbs (5CEZ, 5T3Z, 5I8H, 5V7J, 5FUU, 5U7M, 5U7O). All predictions agree within 2-3 Å with measured backbone C□ distances except for site 202 in which case the BG505-202* DEER data were consistent with the C□-C□ distance (Figure 1, 2). (C) Donor and acceptor smFRET probes attached to a Gln within a peptide linker inserted at residue 136 in V1 (top) and a Ser within a peptide linker inserted at residue 400 in V4 (bottom) in virion-bound Envs (Munro et al., 2014). The COT (1,3,5,7 cyclooctatetraene) moiety adds hydrophobicity to the V4 probe.

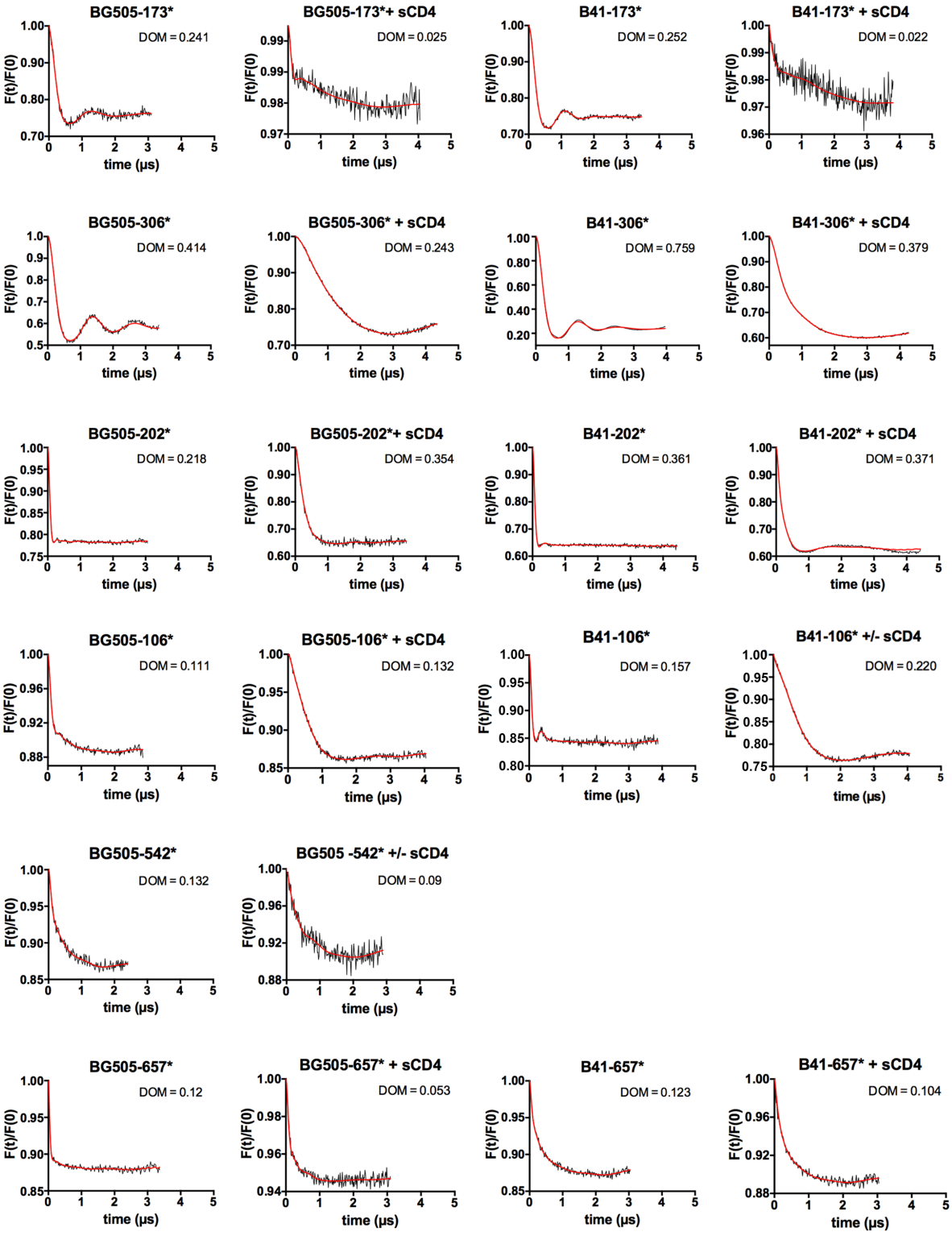
BG505-173*
DOM = 0.241
BG505-173*+ sCD4
DOM = 0.025
B41-173*
DOM = 0.252
B41-173* + sCD4
DOM = 0.022
BG505-306*
DOM = 0.414
BG505-306* + sCD4
DOM = 0.243
B41-306*
DOM = 0.759
B41-306* + sCD4
DOM = 0.379
BG505-202*
DOM = 0.218
BG505-202*+ sCD4
DOM = 0.354
B41-202*
DOM = 0.361
B41-202* + sCD4
DOM = 0.371
BG505-106*
DOM = 0.111
BG505-106* + sCD4
DOM = 0.132
B41-106*
DOM = 0.157
B41-106* +/- sCD4
DOM = 0.220
BG505-542*
DOM = 0.132
BG505 -542* +/- sCD4
DOM = 0.09
BG505-657*
DOM = 0.12
BG505-657* + sCD4
DOM = 0.053
B41-657*
DOM = 0.123
B41-657* + sCD4
DOM = 0.104
F(t)/F(0)
time (µs)

Supplementary Figure 2, related to Figure 2. Background corrected dipolar evolution data for SOSIP Envs and SOSIP Envs incubated with sCD4. Background corrected dipolar evolution data (black traces) for each indicated sample with fits to data shown in red. An important feature of the dipolar evolution function is the depth of modulation (DOM). For given instrumental settings, the DOM is proportional to the number of interacting spin pairs that lie within the detectable distance limit of the DEER experiment. The vertical axis of each plot in the figure is scaled to show details and the quality of fit; the DOM is the full amplitude of change on the vertical axis. The maximum DOM for a quantitatively labeled trimer was ~80% for the instrument and settings used in these experiments. Distance distributions obtained from analysis of low DOM data (<10%) are implicitly less reliable. Low DOM and can be attributed to a small equilibrium population within the detectable distance limit or can indicate low spin labeling efficiency. In situations in which the addition of a ligand to a labeled Env causes a dramatic drop in DOM depth (e.g., sCD4 added to BG505-173* or B41-173*), the DOM drop strongly suggests that the majority of spin pairs moved out of the detectable range in the presence of ligand. Data with large DOM can be problematic in tri-radical systems such as the labeled Env trimers studied here because, for a rigid and completely-labeled system of three interacting spins, in addition to a single major peak in the distribution observed at a distance corresponding to the legs of the equilateral triangle representing the three labels, a smaller "ghost peak" will also appear at a distance ~80% of the real peak[1]. The ghost peak amplitude becomes insignificant for trimers that have low labeling efficiency and thus low DOM (<~0.50), but the major peak remains unchanged in position. Thus, under-labeling of the sample simplifies the analysis. The labeling efficiency high enough to observe ghost peaks in only two cases reported here: B41-306* (Fig. 2E, ~31 Å) and B41-306* + b12 (Fig 3F, broad shoulder to peak ~20-30 Å).

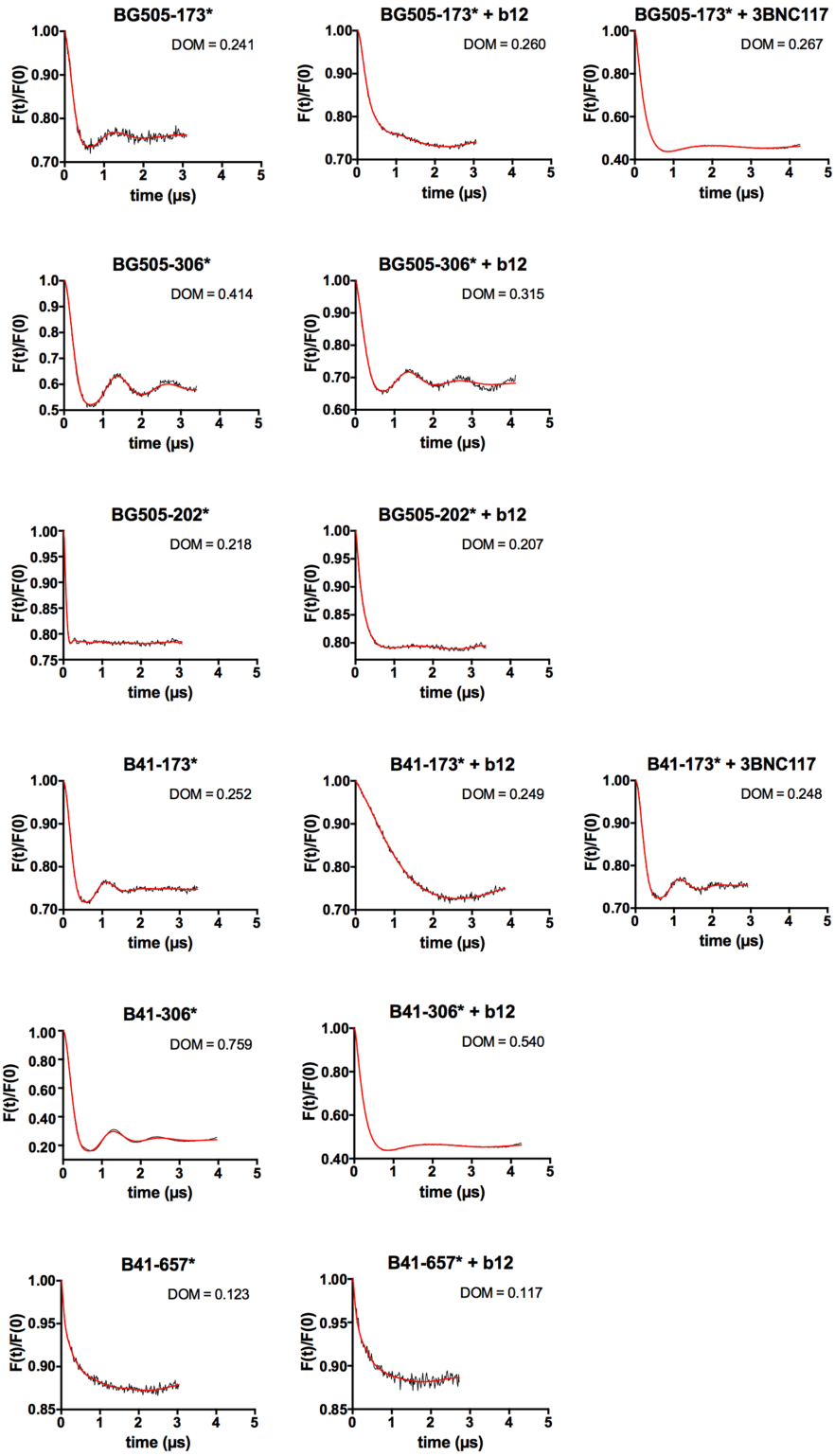
BG505-173*
DOM = 0.241
BG505-173* + b12
DOM = 0.260
BG505-173* + 3BNC117
DOM = 0.267
BG505-306*
DOM = 0.414
BG505-306* + b12
DOM = 0.315
BG505-202*
DOM = 0.218
BG505-202* + b12
DOM = 0.207
B41-173*
DOM = 0.252
B41-173* + b12
DOM = 0.249
B41-173* + 3BNC117
DOM = 0.248
B41-306*
DOM = 0.759
B41-306* + b12
DOM = 0.540
B41-657*
DOM = 0.123
B41-657* + b12
DOM = 0.117
F(t)/F(0)
time (µs)

Supplemental Figure 3, related to Figure 3. Background corrected dipolar evolution data for SOSIP Env incubated with CD4bs bNAbs. Dipolar evolution data (black traces) for all trimer measurements shown in Figure 3 with fits to data shown in red. A potential ghost peak is observed in panel F between 20-30 Å. See Supplemental Figure 2 legend for discussion of DOM and ghost peaks.

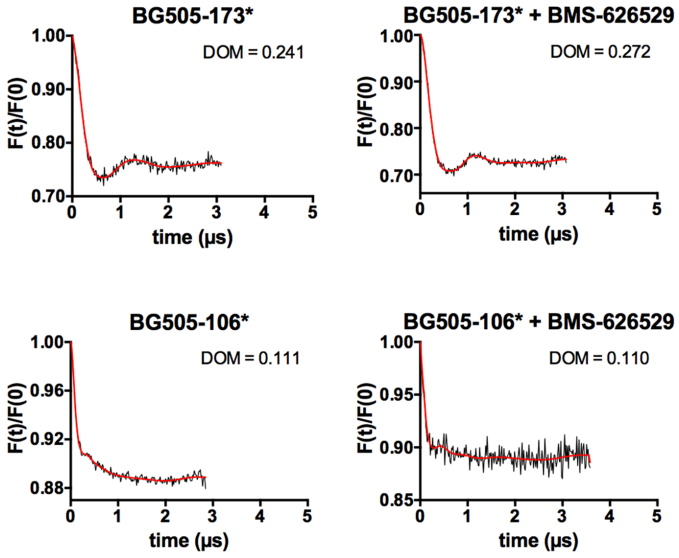

Supplemental Figure 4, related to Figure 4. Background corrected dipolar evolution data for SOSIP Env incubated with the small molecule inhibitor BMS-626529. Dipolar evolution data (black traces) for all trimer measurements shown in Figure 4 with fits to data shown in red. See Supplemental Figure 2 legend for a discussion of DOM.

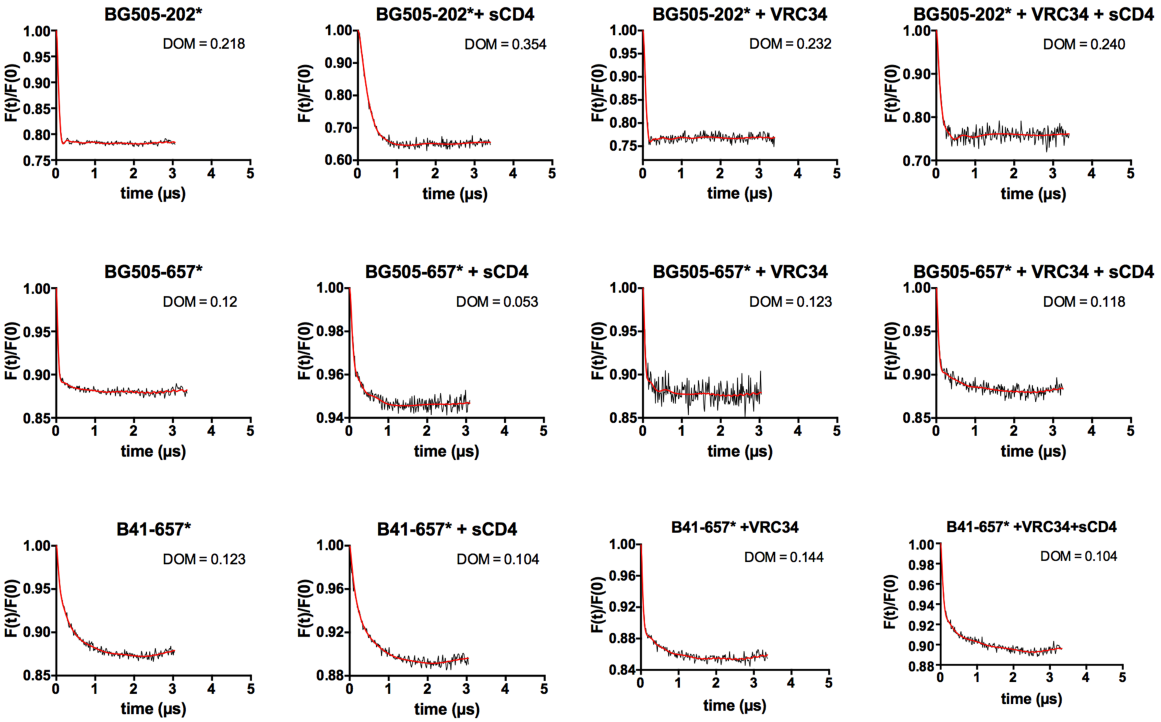

Supplemental Figure 5, related to Figure 5. Background corrected dipolar evolution data for SOSIP Env incubated with VRC34 and/or sCD4. Dipolar evolution data (black traces) for all trimer measurements shown in Figure 5 with fits to data shown in red. See Supplemental Figure 2 legend for a discussion of DOM.

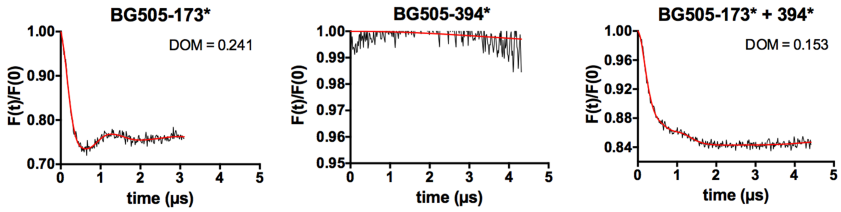

Supplemental Figure 6, related to Figure 6. Background corrected dipolar evolution data for BG505-173*+394*, Dipolar evolution data (black traces) for all trimer measurements shown in Figure 6 with fits to data shown in red. See Supplemental Figure 2 legend for a discussion of DOM.

Chapter III

STRUCTURAL CHARACTERIZATION OF HIV-1 ENV HETEROTRIMERS BOUND TO ONE OR TWO CD4 RECEPTORS REVEALS INTERMEDIATE ENV CONFORMATIONS

Dam, K. A.*, Fan, C.*, Yang, Z., & Bjorkman, P. J. (2023). Structural characterization of HIV-1 Env heterotrimers bound to one or two CD4 receptors reveals intermediate Env conformations. *In Review & bioRxiv*. 2023.01.27.525985. https://doi.org/10.1101/2023.01.27.525985

**These authors contributed equally.*

Summary

HIV-1 envelope (Env) exhibits distinct conformational changes in response to host receptor (CD4) engagement. Env, a trimer of gp120/gp41 heterodimers, has been structurally characterized in a closed, prefusion conformation with closely associated gp120s and coreceptor binding sites on gp120 V3 hidden by V1V2 loops, and in fully-saturated CD4-bound open Env conformations with changes including outwardly rotated gp120s and displaced V1V2 loops. To investigate changes resulting from sub-stoichiometric CD4 binding, we solved 3.4Å and 3.9Å single-particle cryo-EM structures of soluble, native-like Envs bound to one or two CD4 molecules. The majority of Env trimers bound to one CD4 adopted the closed, prefusion Env state, with a minority exhibiting a heterogeneous partially open Env conformation. When bound to two CD4s, the CD4-bound gp120s exhibited an open Env conformation including a four-stranded gp120 bridging sheet and displaced gp120 V1V2 loops that expose the coreceptor sites on V3. The third gp120 adopted an intermediate, occluded-open state that included gp120 outward rotation but maintained the prefusion, three-stranded gp120 bridging sheet and showed only partial V1V2 displacement and V3 exposure. We conclude that the majority of engagements with one CD4 molecule was insufficient to stimulate CD4-induced conformational changes, while binding two CD4 molecules led to Env opening in CD4-bound protomers only. Together, these results illuminate HIV-1 Env intermediate conformations and illustrate the structural plasticity of HIV-1 Env.

The HIV-1 envelope (Env) glycoprotein, a heavily glycosylated homotrimer containing gp120 and gp41 subunits, mediates entry into host cells to initiate infection[1]. On the surface of virions, Env adopts a closed, prefusion conformation similar to that observed in soluble, native-like Env trimer ectodomains[2–5]. The viral entry process is initiated when gp120s bind to the host receptor, CD4, at the CD4-binding site (CD4bs) located distal to the Env apex on the sides of each of the three gp120s[6–10]. This triggers conformational changes in gp120 that expose the gp120 V3 coreceptor binding site that is occluded in the prefusion conformation beneath gp120 V1V2 loops[6–10]. Coreceptor binding results in further conformational changes that lead to insertion of the gp41 fusion peptide into the host cell membrane and fusion of viral and host membranes[1,10].

X-ray crystallography and single particle cryo-electron microscopy (cryo-EM) structures have characterized soluble versions of HIV-1 Envs[11] in closed, prefusion[2,3], CD4-bound open[6,7,10], and intermediate, partially-open conformations[6,8,12]. Multiple studies have demonstrated that the native-like soluble Envs (SOSIPs)[11] used for structural studies resemble virion-bound Envs, suggesting these conformations are relevant to the viral Env entry process[4,5,11,13–15]. The closed, prefusion Env conformation is characterized by gp120 V1V2 loops interacting around the trimer apex, thereby shielding the coreceptor binding sites on the V3 loops[2,3,16]. Structures of CD4-bound open Env trimers revealed receptor-induced changes in which the gp120 subunits rotated outwards, the V1V2 loops were displaced from the apex by ~40 Å to the sides of Env, and the coreceptor binding site on each V3 was exposed and became mostly disordered[6–10] (Supplementary Movie 1). This process also

converted the closed, prefusion conformation three-stranded gp120 bridging sheet composed of the β20, β21, and β3 β-strands[2] to a four-stranded antiparallel β-sheet in which strand β2, whose residues are located in a proximal helix in the closed prefusion formation, intercalated between strands β21 and β3[2,6–8]. Intermediate Env conformations include occluded open[6,12] and partially open conformations[8,17]. In the occluded open conformation observed in trimer complexes with the CD4bs antibody b12[6] and with similar antibodies raised in vaccinated non-human primates[12], the gp120 subunits were outwardly rotated from the central trimer axis as in CD4-bound open conformations, but V1V2 displacement and V3 exposure did not occur and the prefusion three-stranded gp120 sheet was maintained[6,12]. In partially open Env conformations, CD4 binding led to the characteristic CD4-induced structural changes in gp120 but subsequent binding of the gp120-gp41 interface antibody 8ANC195 led to partial closure of the gp120s[8].

A prevailing enigma regarding Env conformational changes and the role of CD4 in initiating the fusion process concerns whether the gp120/gp41 protomers that form the Env trimer behave cooperatively or independently during receptor-induced transformations. This information would reveal how many CD4 receptor and CCR5 coreceptor molecules are needed to engage each Env trimer to induce fusion and further elucidate Env function as it relates to virus infectivity, thereby informing the design of entry inhibitors and mechanisms of antibody neutralization and fusion. To illuminate the role of receptor stoichiometry in CD4-induced conformational changes in HIV-1 Env, we designed soluble Env heterotrimers that can bind only one or only two CD4 receptors for comparisons with Env homotrimers binding either zero CD4s (closed, prefusion trimers) or three CD4s (fully-saturated CD4-

bound open trimers). Using single-particle cryo-EM, we solved structures of one or two CD4s bound to the clade A BG505 trimer[11] to 3.4 and 3.9 Å, respectively. We found that binding one CD4 primarily resulted in a closed, prefusion Env conformation that showed only subtle indications of CD4-induced changes. Binding two CD4 molecules induced an asymmetric, partially open Env conformation in which the gp120 subunits resembled open (for the CD4-bound protomers) and occluded-open (for the unliganded protomer) conformations, while the three gp41 subunits were structurally different from each other. Together, these results illustrate intermediate Env conformations and inform our understanding of the events that lead to HIV-1 fusion.

Results

Design and validation of heterotrimer Env constructs

A soluble heterotrimer Env that can bind only one CD4 receptor, termed HT1, was generated by co-expressing plasmids encoding BG505 SOSIP.664[11,18] bearing a D368R mutation that eliminates CD4 binding[19,20] and an affinity-tagged mutant BG505 SOSIP.664 at a 20:1 ratio (Extended Data Fig. 1a). For HT2, which binds only two CD4 receptors, plasmids encoding BG505 SOSIP.664 and a tagged BG505-D368R SOSIP.664 were co-expressed in a 20:1 ratio (Extended Data Fig. 1a). Assuming random assembly, 13% of the Env population would be composed of the desired singly-tagged heterotrimer and less than 1% would contain dually- and triply-tagged trimers[21]. For both constructs, immunoaffinity column purification resulted in purified tagged heterotrimers (Extended Data Fig. 1a).

To validate the design and purification of BG505-HT1 and BG505-HT2, we performed enzyme-linked immunosorbent assays (ELISAs) to compare binding of soluble CD4 to heterotrimeric Envs and to homotrimeric BG505 (both wildtype and D368R mutant) Envs (Extended Data Fig. 1b). As expected, wildtype BG505 exhibited the highest level of CD4 binding, BG505-D368R showed only limited CD4 binding at high concentrations, and BG505-HT1 and -HT2 showed intermediate levels of CD4 binding, with more binding to -HT2 than to -HT1.

BG505-HT1 bound to one CD4 adopts a closed, prefusion Env trimer conformation

We used single-particle cryo-EM to solve structures of BG505-HT1 heterotrimer in the presence of CD4 (Fig. 1a, Extended Data Fig. 2). Three classes of HT1 heterotrimer were recovered: class I (132,550 particles; 3.4 Å resolution), with density for one bound CD4, class II (68,508 particles; 4.2 Å resolution), with strong density for one bound CD4 and weak density for a second bound CD4, and class III (260,558 particles; 3.2 Å resolution), with no density corresponding to bound CD4 molecules. The weak density for a second bound CD4 in the class II reconstruction suggests that this map represents an average of HT1 Envs in different conformations bound to one or two CD4 molecules, with one CD4-bound Envs likely in the majority. Because of heterogeneity of the class II reconstruction and the lack of bound CD4 in the class III reconstruction, we fit CD4 and Env trimer coordinates only to the class I CD4-HT1 reconstruction.

Despite CD4 recognition of the CD4bs of one gp120 protomer, the class I Env trimer maintained the prefusion, closed conformation with V1V2 loops at the Env apex and V3

loops shielded beneath V1V2[2,3,11] (Fig. 1b; Supplementary Movie 1), suggesting that interactions of a soluble Env trimer with one CD4 molecule are predominantly insufficient to trigger conformational changes that lead to Env opening[6–8]. The ability of CD4 to bind to a closed Env conformation was previously observed in a low-resolution structure of CD4 bound to a homotrimeric SOSIP that included mutations to prevent Env opening[22], whereas the HT1 heterotrimer used for the structural studies reported here did not include mutations that lock Env into a closed, prefusion conformation.

We next compared interactions in the CD4bs of the CD4-bound protomer of the class I CD4-HT1 complex with the CD4bs in the gp120 of a CD4-bound open BG505 trimer (PDB 6CM3) by calculating the surface area on gp120 buried by CD4 (buried surface area; BSA) (Fig. 1c,d). The BSA within the CD4bs was comparable for CD4-HT1 (class I) and CD4-BG505 gp120s but for gp120s in the CD4-BG505 Env complex, V1V2 displacement led to an additional ~200 A^2 of BSA on gp120 (Fig. 1c,d), which was previously shown to stabilize the CD4-induced, open Env conformation[6,7]. These comparisons suggest that the Env-CD4 interface remains largely unchanged during CD4 engagement, the primary difference in the CD4-bound open structure is the displacement of V1V2 from the Env apex to the side of gp120 where it makes additional contacts with CD4.

CD4-induced Env conformational changes are triggered, at least in part, by insertion of $Phe43_{CD4}$ into a conserved, hydrophobic cavity (the Phe43 cavity) on gp120[6–8,23,24]. Small molecule CD4 mimetics such as BNM-III-170 and M48U1 insert hydrophobic entities into the $Phe43_{CD4}$ cavity, thereby competing with CD4 binding and inducing Env opening[9,25–30].

Some CD4bs broadly neutralizing antibodies (bNAbs) also mimic $Phe43_{CD4}$ interactions by inserting a hydrophobic residue at antibody heavy chain (HC) position 54 into the Phe43 cavity on gp120. However, by contrast to the conformational effects of CD4 and selected small mimetic inhibitors on Env conformation, CD4bs bNAbs with a hydrophobic HC residue 54 stabilize the prefusion, closed Env conformation when bound to trimeric Env[31–35].

To examine the consequences of insertion of $Phe43_{CD4}$ into a single gp120 Phe43 cavity in the class I CD4-HT1 complex, we compared the structural landscape of the Phe43 cavity in the gp120s of two symmetric Env trimer complexes: the CD4bs bNAb 1-18 bound to a closed, prefusion conformation BG505[33] and CD4 bound to an open, fully-saturated CD4-bound BG505 trimer[8] (Fig. 1e). We identified and compared the positions of conserved residues in the region, some of which have been characterized to undergo rearrangements during CD4-induced Env opening[7,23]. Residues in the CD4 binding loop ($E370_{gp120}$, $V371_{gp120}$) along with $T257_{gp120}$ and exit loop ($G473_{gp120}$, $M475_{gp120}$) residues maintained analogous positions in the one CD4-bound HT1 (class I), zero CD4-bound closed, and three CD4-bound open trimers (Fig. 1e). However, subtle differences in the gp120 β20/β21 loop were observed. For example, in the 1-18–BG505 complex, the $N425_{gp120}$ side chain pointed away from $Phe54_{1\text{-}18\ HC}$, while the $M426_{gp120}$ side chain pointed towards $Phe54_{1\text{-}18\ HC}$ and the planes of the $W427_{gp120}$ side chain and $Phe54_{1\text{-}18\ HC}$ side chain were parallel. By contrast, in the CD4-BG505 open complex, the $N425_{gp120}$ side chain pointed upward from the Phe43 cavity ceiling, the $M426_{gp120}$ side chain pointed away from $Phe43_{CD4}$, and the $W427_{gp120}$ side chain was perpendicular to the $Phe43_{CD4}$ side chain. The CD4-HT1 (class I) complex showed

an intermediate orientation of gp120 β20/β21 loop residues, with the $N425_{gp120}$ and $M426_{gp120}$ side chains adopting positions similar to their positions in the CD4-BG505 complex, while the $W427_{gp120}$ side chain adopted a position similar to that in the 1-18–BG505 complex. This suggests that, while the overall conformation of the Env trimer in the CD4-HT1 (class I) complex represented a closed prefusion Env, the gp120 Phe43 cavity showed indications of structural changes consistent with CD4 binding.

BG505-HT2 bound to two CD4s adopts an asymmetric, open Env conformation

To structurally characterize BG505-HT2 complexed with CD4, we collected single particle cryo-EM data and recovered three classes that resembled Env-CD4 complexes (Extended Data Fig. 3). Class I (92,660 particles; 3.9 Å resolution) contained a BG505 heterotrimer with two CD4-bound protomers and one unliganded protomer (Extended Data Fig. 3). Class II (48,577 particles; 3.8 Å resolution), which was similar to the CD4-HT1 (class I) structure, contained a BG505 trimer bound to a single CD4 (Extended Data Fig. 3e). Class III (28,548 particles; 6.4 Å resolution) was poorly resolved (Extended Data Fig. 3), with one Env protomer showing clear density indicative of CD4 binding, while the adjacent protomer showed less defined CD4 density, and density for the third, unliganded protomer extended from the Env gp120 across the trimer apex, appearing to contact the adjacent CD4-bound protomer. Further interpretation was prevented by the limited resolution. Subsequent analyses of the BG505 CD4-HT2 complex were confined to the 3.9 Å class I structure.

We compared the class I two CD4-bound HT2 structure to other Env conformations by quantifying gp120 rearrangements using measurements of inter-protomer distances between

the C□ atoms of conformationally-characteristic Env residues (Fig. 2a,b). The relationship between the HT2 gp120 protomers that bound CD4 resembled a typical CD4-induced open conformation, with V1V2 loops displaced from the Env apex to the sides of gp120 and the V3 loops exposed (Fig. 2a), consistent with increased inter-protomer distances between these protomers compared to closed[33], occluded-open[12], and partially open[8] Env conformations (Fig. 2b). The unliganded HT2 protomer did not show V1V2 and V3 loop movement to the extent observed in the CD4-bound protomers. Instead, the V1V2 and V3 loops were displaced as a rigid body from the Env apex, as observed in the protomers of the homotrimeric occluded-open Env conformation (Fig. 2a)[12]. Asymmetry of the HT2 Env with two bound CD4s was demonstrated by variable inter-protomer distances: the measured distance between the two CD4-bound gp120s (protomers A and B) were consistent with the open, CD4-bound Env conformation, by contrast to distances between the CD4-bound gp120s and the unliganded gp120 (protomer C), which were slightly smaller than distances between CD4-bound gp120s. Thus, the HT2 Env adopted an asymmetric conformation in which the distance to the central trimer axis was smaller in the unliganded protomer than in the CD4-bound protomers (Fig. 2b; Supplementary Movie 1).

Since a hallmark of CD4-induced gp120 structural changes is the transition of the three-stranded β-sheet to a four-stranded antiparallel bridging sheet[6–8,10], we next examined the β-sheet conformations in the CD4-HT2 (class I) complex. The β-sheet conformations observed in the CD4-HT2 (class I) complex differed: CD4-bound protomers A and B included the four-stranded bridging sheet observed in CD4-bound open Env trimer structures[6–8], whereas the unliganded gp120 in protomer C contained a three-stranded sheet resembling its

counterpart gp120s in closed and occluded open conformations[12,33] (Fig. 2c). In summary, the binding of two CD4s to BG505-HT2 resulted in an asymmetric and partially open Env trimer composed of two CD4-bound, open conformation gp120s and one unliganded gp120 in an occluded-open conformation.

To address the generality of the effects of Env interactions with sub-stoichiometric numbers of CD4s, we prepared HT2 heterotrimers for the clade B B41 SOSIP.664[36] (Extended Data Fig. 1a), obtaining a 4.1 Å cryo-EM density map of B41-HT2 bound to two CD4 molecules (Extended Data Fig. 4). Fitting the CD4-BG505 HT2 structure into the density map for CD4-B41 HT2 showed agreement in the overall structural features, including V1V2 displacement of CD4-bound protomers and partial outward gp120 rotation of the unliganded protomer (Extended Data Fig. 4).

In addition, we solved 4.2 Å and 3.8 Å single-particle cryo-EM structures of CD4 complexes with BG505 HT1 and HT2 plus 17b[37], a CD4-induced antibody that recognizes the exposed coreceptor binding site on V3[6–9] (Extended Data Fig. 5). For both complexes, the Envs showed three bound 17b Fabs and three bound CD4 molecules and adopted an open conformation, as indicated by density for V1V2 that was displaced to the sides of gp120 on each protomer (Extended Data Fig. 5). Superimposition of CD4-17b-HT1 and -HT2 density maps with the cryo-ET/subtomogram averaged map of membrane-bound BaL Env bound to CD4 and 17b[5] show similarities in the orientations of Env gp120s, CD4 molecules, and 17b Fabs (Extended Data Fig. 5i). However, the poor local map densities surrounding the Fab-gp120 and CD4 interfaces in the single-particle reconstructions with HT1 and HT2

heterotrimers prevented building of reliable atomic models. Although low resolution, these structures can be interpreted by assuming that the BG505 Env is in equilibrium between closed and open conformations, with the equilibrium generally favoring the closed, prefusion conformation, and with transitions to the open conformation in the absence of CD4 binding sampled less frequently. The structural results suggest that the binding of CD4 to an unmutated CD4 binding site on a gp120 occurs first, enabling subsequent exposure of the V3 loop and binding to 17b Fab in those protomers. Disruption to the prefusion trimer apex through V1V2 displacement likely allows the remaining, unliganded gp120 protomer(s) in the heterotrimer to sample open conformations more frequently, thereby enabling 17b binding. Once the gp120-17b interaction occurs, gp120 could adopt an open conformation with displaced V1V2 loops and become trapped in this state. CD4 could then make contacts with the displaced V1V2, allowing CD4 binding to that protomer. This interaction could overcome the unfavorable effects of the D368R mutation, which otherwise would hinder or prevent CD4 binding to the protomer containing that mutation.

gp41 conformational changes are mediated by gp120 conformations in CD4-bound heterotrimer Env structures

HIV-1 gp41 subunits are responsible for fusion events between host and viral membranes to enable infection[1,38,39]. Prefusion gp41 is composed of a long HR1 helix that extends from beneath the gp120 apex, an HR2 helix that surrounds the N-termini of the HR1 coils, and the fusion peptide (FP) and fusion peptide proximal region (FPPR) located between the HR1 and HR2 helices[1,38,40]. CD4 binding leads to compacting of the C-termini of the HR1 ($HR1_c$) helices, triggering formation of a pre-hairpin intermediate in which HR1 extends away from

HR2 and the viral membrane[1,38,40]. These movements lead to the formation of compact FPPR helices and the transition of the fusion peptides from □-helices that are shielded in hydrophobic environments to solvent-exposed disordered loops[1,10,38,40].

Previous studies suggested that changes in Env gp120 conformation are correlated with changes in gp41, suggesting cooperativity between the gp120 and gp41 subunits[6–8,10]. Indeed, in closed and CD4-saturated open Env conformations, gp41 subunits undergo the characterized CD4-induced changes described above (Fig. 3a). Closed Env trimers contain gp41s with a disordered $HR1_C$, a helical FP, and an FPPR bent helix, while the gp41 subunits in open Env conformations contain a helical $HR1_C$, disordered FP, and straight helical FPPR (Fig. 3b). This pattern is also evident in the class I CD4-HT1 complex, in which despite engagement of one CD4, each of the three gp120 and gp41 subunits mostly retain closed, prefusion conformations (Fig. 3a). The only deviation from the closed gp41 conformation in the class I HT1 heterotrimer is a disordered FP in all protomers (Fig. 3b).

In the class I CD4-HT2 complex, individual gp41 subunits adopted distinct conformations despite the near identical conformations of the two CD4-bound gp120s (Fig. 3a,b). The gp41 in CD4-bound protomer A revealed a slanted HR1 helix, a short helical $HR1_C$, a disordered FP, and a bent helical FPPR (Fig. 3b). The other CD4-bound gp120 in protomer B contained contrasting elements in gp41: the HR1 and $HR1_C$ helices were erect (HR1) or fully extended ($HR1_C$), consistent with CD4-induced structural changes (Fig. 3b). By contrast, the FP and FPPR resembled their conformations in closed Envs (Fig. 3b). Despite protomer C being unliganded, its gp41 most resembled the CD4-induced gp41 conformation, with a helical

$HR1_c$, disordered FP, and a helical FPPR (Fig. 3b). Together, these results demonstrate that individual gp41 subunits can adopt different, distinct conformations in the context of a two CD4-bound Env.

A potential link between gp120 and gp41 Env conformations involves the gp120 α0 region. During Env trimer opening, the $HR1_c$ extension displaces the α0 disordered loop located above $HR1_c$ in the prefusion conformation and forms a stable α-helix that caps the neighboring gp41 HR1 helix (Fig. 3c)[6,9,10]. In the class I CD4-HT1 complex, the α0 loops resembled those in the prefusion conformation, whereas the α0 conformations in the CD4-HT2 complex were variable (Fig. 3a,c). Despite only a partial extension of $HR1_c$ in CD4-bound protomer A of the class I HT2 heterotrimer, the gp120 α0 helix was formed and displaced towards the protomer C $HR1_c$, where it was stabilized through interactions with the short disordered protomer C $HR1_c$ tip (Fig. 3c). Similarly, for CD4-bound protomer B, $HR1_c$ extension occurred to form a gp120 α0 helix that interacted with its neighboring protomer A $HR1_c$ (Fig. 3c). In unliganded protomer C, the gp120 α0 region remained in the prefusion disordered loop conformation despite extension of its $HR1_c$ (Fig. 3c). The loop conformation was likely accommodated because protomer C gp120 does not undergo the full outwards displacement from the Env trimer axis. However, partial outwards rotation of protomer C's gp120 still enabled interactions with the neighboring protomer B $HR1_c$ (Fig. 3c). These inter-protomer interactions between gp120s and gp41s in CD4-HT2 rationalize why each gp41 subunit adopted a distinct conformation, suggesting that formation of the α0 helix is dependent of CD4 occupancy and likely drives gp41 conformational changes.

CD4-bound soluble and membrane-bound Env trimers exhibit similar conformations

Cryo-electron tomography (cryo-ET) and sub-tomogram averaging was used to determine the conformations of membrane-bound Envs complexed with sub-stoichiometric numbers of membrane-bound CD4s[41]. We can therefore compare our higher resolution soluble CD4–soluble heterotrimer Env structures with structures of CD4-Env complexes investigated under more physiological conditions.

Rigid body fitting of the class I CD4-HT1 model into the cryo-ET/sub-tomogram averaged density of a one CD4-bound Env trimer showed major differences (Extended Data Fig. 6a). Unlike the closed Env conformation observed for the soluble CD4-HT1 complex (Fig. 1a), the membrane-bound Env adopted a partially open conformation in response to engagement with a single CD4 in which the CD4-bound protomer appeared to undergo CD4-induced conformational changes consistent with V1V2 displacement (Extended Data Fig. 6a)[41]. However, the single-particle cryo-EM derived heterogeneous class II CD4-HT1 complex reconstruction (Extended Data Fig. 2c) superimposed well with the cryo-ET/subtomogram averaged density for the one CD4-bound Env trimer[41] (Extended Data Fig. 6b), consistent with the ability of soluble and membrane-bound Envs to adopt similar conformations upon binding of a single CD4.

In addition, the two CD4-bound membrane-embedded and soluble Envs exhibited similar conformations. Rigid body fitting of the soluble CD4-HT2 (class I) structure into the corresponding cryo-ET/sub-tomogram averaged CD4-Env density showed alignment of bound CD4s and Env gp120s (Fig. 4a,b). The displaced V1V2 loops in the CD4-HT2 CD4-

bound protomers A and B were clearly matched with density from membrane-embedded Env (Fig. 4c,d), and the partial outward gp120 rotation described in unliganded protomer C in the soluble CD4-Env structure (Fig. 2a,b) also aligned with density for the unliganded protomer in the membrane-bound Env (Fig. 4e). However, the V1V2 and V3 densities were not resolved in the cryo-ET map[41] likely due to flexibility of this region, limiting our comparisons of the V1V2 and V3 regions of the unliganded protomer in membrane-bound Env and soluble Env (Fig. 4e).

Discussion

HIV-1 Env trimers on virions are likely to encounter multiple CD4 receptors on the surface of target cells. However, experimental studies have yet to definitively address whether one, two, or all three CD4 binding sites on each trimer must be occupied to induce the characterized structural rearrangements in Env (e.g., V1V2 displacement and gp120 rotation) that expose the coreceptor binding site. In addition, the degree of cooperativity between Env protomers upon binding to CD4 had not been investigated structurally. The characterization of a non-neutralizing antibody isolated from an immunized macaque that mimicked FP interactions with a single gp41 per trimer, thereby rendering one FP per trimer inactive[42], implies that not all protomers in each Env trimer are required for virus-host cell membrane fusion. Consistent with this conclusion, fusion and infectivity studies that incorporated Env mutations resulting in defective CD4, coreceptor, and fusion activity in individual protomers of Env heterotrimers[43–46] suggested that Env entry does not require that each subunit in an individual trimer be competent in performing all functions[43–45]. However, the effects of sub-stoichiometric binding of CD4 in these experiments were complicated by the necessity that

Env protomers with different defective mutations were randomly assembled as homotrimeric and heterotrimer Envs that were compared for fusion and infectivity with homotrimeric controls[43–45]. In addition, neither of these types of experiments included structural characterizations to examine the conformational effects of sub-stoichiometric CD4 interactions with individual Env trimers. Thus, our single-particle cryo-EM investigation of Env heterotrimers binding one or two CD4s, together with the accompanying cryo-ET visualization of the native HIV-1 virions and membrane-bound CD4[41], adds to our knowledge of Env structures, which was previously limited to closed, prefusion Env conformations with either no bound CD4s or three CD4s bound to fully-saturated open Env trimers[2–9,41].

By engineering soluble Env heterotrimers with either one or two wildtype CD4 binding sites, we solved single-particle cryo-EM structures of Env trimers with sub-stoichiometric numbers of bound CD4s at sufficient resolutions to monitor CD4-induced changes to gp120 and gp41 subunits. We found that binding of one CD4 to the dominant class I 3D reconstruction of CD4-HT1 resulted in minor structural changes to a native-like soluble Env trimer in the closed, prefusion state; for example, we did not observe opening of any of the gp120 subunits of the trimer or the accompanying changes in the CD4-bound gp120 that result from CD4 associating with gp120 in CD4-bound open trimers[6–10] (in particular, changes resulting from insertion of $Phe43_{CD4}$ into a gp120 hydrophobic cavity, which facilitates induced changes such as V1V2 displacement in CD4-bound gp120 subunits of fully-saturated open Env trimers[6–8,23,24], were minor). By contrast, the one CD4-bound conformation of membrane-bound Env trimer revealed by cryo-ET/sub-tomogram averaging

showed a partially open conformation in which the CD4-bound protomer appeared to undergo CD4-induced conformational changes[41]. This conformation aligned well with a second CD4-HT1 cryo-EM reconstruction, a subdominant heterogeneous class that also showed partial Env opening.

The class I single-particle cryo-EM CD4-HT1 and the cryo-ET structures of one CD4-bound Env trimers may represent different conformational intermediates involved with engagement of a single CD4, with the closed trimer conformation likely preceding the more open conformation (Fig. 5). Several factors could contribute to the observation of these different one CD4-bound Env trimer conformations: (*i*) Differences in the Env clade being investigated (tier 2 BG505 for single-particle cryo-EM versus tier 1B BaL for cryo-ET), with tier 2 viruses being more resistant to neutralization and likely also CD4-induced changes than tier 1[47]. (*ii*) The increased ability of membrane-bound CD4 compared with soluble CD4 to engage and then dissociate from Envs over the course of an incubation, thus perhaps leading to visualization in the cryo-ET experiments of one CD4-bound Envs that had recently bound two CD4s. (*iii*) SOSIP substitutions that stabilize the prefusion, closed conformation (including the interprotomer disulfide, I556P, A316W)[11,18] could prevent CD4-induced structural changes when only one CD4 is bound. (*iv*) The CD4-HT1 complex solved by single-particle cryo-EM was prepared at 4°C, whereas the analogous cryo-ET sample was incubated at room temperature – the lower temperature incubation perhaps contributing to observation of the closed trimer conformational state with one CD4 bound that likely precedes a more open trimer conformation (Fig. 5). Although the cryo-ET one CD4-bound open Env structure differed from the predominant one CD4-bound closed heterotrimer

structure (CD4-HT1 class I), the heterogeneous class II CD4-HT1 single-particle cryo-EM reconstruction superimposed well with the one CD4-bound cryo-ET Env density, thus suggesting the ability of the SOSIP HT1 Env to adopt a more open conformation in response to primarily binding a single CD4.

The single-particle cryo-EM and cryo-ET structures of two CD4-bound Env trimers were remarkably consistent, such that both showed two protomers in CD4-bound open conformations and the remaining unbound protomer in a conformation resembling an occluded open Env protomer (Fig. 4)[12]. These results provide further evidence of native-like soluble SOSIP Env trimers resembling their virion-bound counterparts[4,5], both in the closed, prefusion conformation and in various CD4-bound conformations that adopt different conformations compared with unliganded Env trimers. Thus, this and the accompanying cryo-ET study[41], together with previous Env structures, complete a description of the conformations of HIV-1 Env trimers at each stage of engaging CD4, starting with no bound receptors to the final conformation with three bound receptors (Fig, 5; Supplementary Movie 1).

The ability to confirm single-particle soluble Env heterotrimer conformations that include residue-level details using lower-resolution Env trimer structures derived by cryo-ET under more physiological conditions[41] lends confidence to the proposed order of structural transitions induced by CD4 binding (Fig. 5; Supplementary Movie 1). The single-particle cryo-EM structures also include the first descriptions of details of CD4-induced structural changes in gp120 and gp41, including cooperative inter-subunit structural transitions. These

results reveal intermediate Env conformations that expand our understanding of receptor-induced structural changes preceding host and viral membrane fusion, thereby informing the design of therapeutics to block HIV-1 infection.

Methods

Protein expression and purification

SOSIP.664v4 Env constructs included the following stabilizing mutations: introduced cysteines 501C and 605C (SOS), I559P (IP), A316W, and the furin cleavage site mutated to six arginine residues (6R)[11,18]. SOSIPs with D7324 tags included a GSAPTKAKRRVVQREKR sequence after residue 664 in the gp41 ectodomain[11]. The D368R mutation was encoded in Envs to impair CD4 binding[19,48–50]. Genes encoding tagged and untagged SOSIP.664 Env homotrimers were expressed by transient transfection of Expi293 cells (ThermoFisher). Env heterotrimers were purified from co-transfections involving a 20:1 expression plasmid DNA ratio of untagged to tagged Env constructs: a 20:1 ratio of Env-D368R:Env-D7324 (HT1) and a 20:1 plasmid of Env:Env- D368R-D7324 (HT2). Trimeric Envs were purified from cell supernatants by PGT145 immunoaffinity chromatography and size-exclusion chromatography (SEC) using a Superose 6 10/300 column (Cytiva)[11,51]. Tagged Env homotrimers and heterotrimers (HT1 and HT2) were further purified using JR-52 immunoaffinity chromatography as described[11].

Genes encoding CD4 D1D2 (domains 1 and 2) and D1-D4 (domains 1-4) with C-terminal 6x-His or StrepII tags were transiently transfected using the Expi293 expression system (ThermoFisher)[7]. CD4 proteins were purified using Ni^{2+}-NTA (Cytiva) or Strep-Tactin XT (IBA Life Sciences) affinity columns, followed by SEC using a Superdex 200 10/300 column (Cytiva).

The Fab from the CD4i antibody 17b[37] was expressed by transient transfection using expression vectors encoding the LC and a C-terminally tagged HC portion of the Fab using the Expi293 expression system (ThermoFisher)[7]. Fab was purified from cell supernatants by Ni^{2+}-NTA (Cytiva) chromatography followed by SEC using a Superdex 200 10/300 column (Cytiva).

D7324 capture ELISA

ELISAs were performed as described[9,12,52]. Briefly, 5 µg/mL of JR-52 IgG[11] (kind gift of James Robinson, Tulane University) was coated on Corning Costar high-binding 96-well plates in 0.1 M $NaHCO_3$ (pH 9.6). Plates were incubated overnight at 4 °C. After washing, plates were blocked with 3% BSA in TBS-T (20 mM Tris, 150 mM NaCl, 0.1% Tween-20) for 1 hour at room temperature. Blocking buffer was removed and D7324-tagged Envs were applied to plates at 5 µg/mL in 3% BSA in TBS-T. Plates were incubated for 1 hour at room temperature, and then buffer was removed. For some experiments, 6x-His tagged CD4 was serially diluted in 3% BSA in TBS-T at a top concentration of 100 µg/mL, added to plates, and incubated for 4 hours at room temperature. The CD4 solution was removed and plates were washed with TBS-T, twice. A horseradish peroxidase (HRP) labeled secondary against the His tag (Genscript) was added at a 1:5,000 dilution in 3% BSA in TBS-T. Plates were incubated for 30 minutes, and then washed with TBS-T three times. Colorimetric detection of CD4 binding was accomplished using Ultra TMB-ELISA Substrate Solution (ThermoFisher Scientific) and quenching with 1.0 N HCl. Absorption was measured at 450 nm. Two independent biological replicates (n = 2) were performed for all assays.

Assembly of protein complexes and cryo-EM sample preparation

The D1-D4 version of CD4 was chosen instead of CD4 D1D2 for structural studies with BG505 HT1 and HT2 to increase particle size. HT1-CD4 and HT2-CD4 complexes were prepared by incubating purified Env heterotrimers with a 1.1x molar excess of CD4 D1-D4 overnight at 4 °C. We attempted CD4-Env incubations at different temperatures (namely 37°C and room temperature) and found that overnight incubation at 4 °C produced the most favorable particle quality when frozen on cryo-EM grids. For HT1-CD4-17b and HT2-CD4-17b complexes, 17b Fab was added prior to grid freezing at a 1.1x molar excess and incubated at 4 °C for 30 minutes. QuantiFoil 300 mesh 1.2/1.3 grids (Electron Microscopy Sciences, Hatfield, PA) were glow discharged with PELCO easiGLOW (Ted Pella, Redding, CA) for 1 min at 20 mA. Fluorinated octylmaltoside solution (Anatrace, Maumee, OH) was added to the protein complex to a final concentration of 0.02% (w/v), and 3 μL of the complex/detergent mixture was applied to glow-discharged grids. A Mark IV Vitrobot (Thermo Fisher Scientific, Waltham, MA) was used to blot grids for 3 seconds with 0 blot force using Whatman No.1 filter paper and 100% humidity at room temperature. Grids were plunge-frozen and vitrified in 100% liquid ethane.

Cryo-EM sample preparation and data collection

Single particle cryo-EM datasets for HT1-CD4, HT2-CD4, HT1-CD4-17b, and HT2-CD4-17b were collected on a 300 keV Titan Krios (Thermo Fisher Scientific, Waltham, MA) cryo-electron microscope equipped with a K3 direct electron detector camera (Gatan, Pleasanton, CA) using SerialEM[53] automated data collection software. Movies were recorded with 40 frames at a total dosage of 60 $e^-/Å^2$ using a 3×3 beam image shift pattern with 3 exposures

per hole in the super resolution mode, a defocus range of −1 to −3 μm, and pixel size of 0.416 Å.

Data were processed using cryoSPARC[54]. Patch motion correction was applied to each dataset with a binning factor of 2, followed by Patch CTF to estimate CTF parameters. The blob picker with a diameter of 100 to 230 Å was used to pick particles. Particles were extracted and then 2D classified. Particle classes representing the expected complex were selected and used for *ab initio* modeling. The *ab initio* models and corresponding particles that represented the expected complex underwent subsequent rounds of heterogeneous, homogeneous, and non-uniform refinement.

Model building and refinement of cryo-EM structures

The model coordinates for BG505 HT1-CD4 (class I) were generated by fitting the following reference coordinate files into cryo-EM density using UCSF ChimeraX[55]: BG505 gp120 monomer (PDB 6UDJ), gp41 monomer (PDB 6UDJ), and CD4 D1D2 (PDB 5U1F). For the BG505 HT2-CD4 (class I) reconstruction, the initial coordinates included BG505 gp120 CD4-bound monomer (PDB 7LOK), BG505 gp120 unliganded monomer (PDB 7TFN), gp41 monomer (PDB 6UDJ), and CD4 D1D2 (PDB 5VN3). Domains 3 and 4 of CD4 D1-D4 were not modeled due to potential flexibility between CD4 domains 2 and 3. Initial BG505 HT-CD4 models and N-linked glycans were manually refined using Coot[56]. Iterative rounds of whole-complex refinements using Phenix (phenix.real_space_refine)[57,58] and Coot[56] were then performed to generate the final models.

Structural analyses

Structure figures were created with PyMol (Schrödinger LLC) and UCSF ChimeraX[55]. BSA was calculated using PDBePISA[59] using a 1.4 Å probe. gp120 BSA was calculated for protein components of gp120 without including glycan coordinates. Due to the low resolution of complexes, interactions were assigned tentatively using the following criteria: hydrogen bonds were assigned as pairwise interactions less than 6.0 Å and with an A-D-H angle >90°, and van der Waals interactions were assigned as distances between atoms that were less than 6.0 Å.

Acknowledgements

We thank W. Mothes and W. Li, and Z. Qin (Yale University) for sharing cryo-ET data, J. Vielmetter, A. Rorick, K. Storm, and the Protein Expression Center in the Beckman Institute at Caltech for expression assistance, and J.E. Robinson (Tulane University) for the JR-52 antibody. Electron microscopy was performed in the Caltech Cryo-EM Center with assistance from S. Chen, and A. DeLaitsch for comments on the manuscript. This work was supported by the NIH U54 AI170856 (P.J.B.), National Institute of Allergy and Infectious Diseases (NIAID) Grant HIVRAD P01 AI100148 (to P.J.B.), and the Bill and Melinda Gates Foundation Collaboration for AIDS Vaccine Discovery (CAVD) grant INV-002143 (P.J.B.). The contents of this publication are solely the responsibility of the authors and do not necessarily represent the official views of NIAID or NIH.

Author contributions

K.A.D., C.F., and P.J.B. designed the research. K.A.D. designed Env constructs, performed protein purification, and conducted ELISAs. C.F. collected structural data. Z.Y. created Supplementary Movie 1. K.A.D., C.F., Z.Y., and P.J.B. analyzed results. K.A.D. and P.J.B. wrote the manuscript with input from co-authors.

Competing interests

The authors declare that there are no competing interests.

Data availability

The cryo-EM maps and atomic structures have been deposited in the PDB and/or Electron Microscopy Data Bank (EMDB) under accession codes 8FYI [http://doi.org/ 10.2210/pdb8fyi/pdb] and EMD- 29579 [https://www.ebi.ac.uk/pdbe/entry/emdb/EMD-29579] for CD4-BG505 HT1 (class I), EMD-40437 [https://www.ebi.ac.uk/pdbe/entry/emdb/EMD-40437] for CD4-BG505 HT1 (class II), EMD-40438 [https://www.ebi.ac.uk/pdbe/entry/emdb/EMD-40438] for BG505 HT1 (class III), 8FYJ [http://doi.org/ 10.2210/pdb8fyj/pdb] and EMD-29580 [https://www.ebi.ac.uk/pdbe/entry/emdb/EMD-29580] for CD4-BG505 HT2 (class I), EMD- 29581 [https://www.ebi.ac.uk/pdbe/entry/emdb/EMD-29581] for CD4-BG505 HT2 (class II), EMD- 29582 [https://www.ebi.ac.uk/pdbe/entry/emdb/EMD-29582] for CD4-BG505 HT2 (class III), EMD-29601 [https://www.ebi.ac.uk/pdbe/entry/emdb/EMD-29601] for CD4-B41 HT2, EMD-29583 [https://www.ebi.ac.uk/pdbe/entry/emdb/EMD-29583] for

CD4-17b-BG505 HT1, and EMD-29584 [https://www.ebi.ac.uk/pdbe/entry/emdb/EMD-29584] for CD4-17b-BG505 HT2.

References

1. Harrison, S. C. Viral membrane fusion. *Virology* **479–480**, 498–507 (2015).
2. Lyumkis, D. *et al.* Cryo-EM Structure of a Fully Glycosylated Soluble Cleaved HIV-1 Envelope Trimer. *Science* **342**, 1484–1490 (2013).
3. Julien, J.-P. *et al.* Crystal Structure of a Soluble Cleaved HIV-1 Envelope Trimer. *Science* **342**, 1477–1483 (2013).
4. Liu, J., Bartesaghi, A., Borgnia, M. J., Sapiro, G. & Subramaniam, S. Molecular architecture of native HIV-1 gp120 trimers. *Nature* **455**, 109–113 (2008).
5. Li, Z. *et al.* Subnanometer structures of HIV-1 envelope trimers on aldrithiol-2-inactivated virus particles. *Nat. Struct. Mol. Biol.* **27**, 726–734 (2020).
6. Ozorowski, G. *et al.* Open and closed structures reveal allostery and pliability in the HIV-1 envelope spike. *Nat. Publ. Group* **547**, 360–363 (2017).
7. Wang, H. *et al.* Cryo-EM structure of a CD4-bound open HIV-1 envelope trimer reveals structural rearrangements of the gp120 V1V2 loop. *Proc. Natl. Acad. Sci. U. S. A.* **113**, E7151–E7158 (2016).
8. Wang, H., Barnes, C. O., Yang, Z., Nussenzweig, M. C. & Bjorkman, P. J. Partially Open HIV-1 Envelope Structures Exhibit Conformational Changes Relevant for Coreceptor Binding and Fusion. *Cell Host Microbe* **24**, 579-592.e4 (2018).
9. Jette, C. A. *et al.* Cryo-EM structures of HIV-1 trimer bound to CD4-mimetics BNM-III-170 and M48U1 adopt a CD4-bound open conformation. *Nat. Commun.* **12**, 1950 (2021).

10. Yang, Z., Wang, H., Liu, A. Z., Gristick, H. B. & Bjorkman, P. J. Asymmetric opening of HIV-1 Env bound to CD4 and a coreceptor-mimicking antibody. *Nat. Struct. Mol. Biol.* **26**, 1167–1175 (2019).
11. Sanders, R. W. *et al.* A Next-Generation Cleaved, Soluble HIV-1 Env Trimer, BG505 SOSIP.664 gp140, Expresses Multiple Epitopes for Broadly Neutralizing but Not Non-Neutralizing Antibodies. *PLoS Pathog.* **9**, e1003618-20 (2013).
12. Yang, Z. *et al.* Neutralizing antibodies induced in immunized macaques recognize the CD4-binding site on an occluded-open HIV-1 envelope trimer. *Nat. Commun.* **13**, 732 (2022).
13. Stadtmueller, B. M. *et al.* DEER Spectroscopy Measurements Reveal Multiple Conformations of HIV-1 SOSIP Envelopes that Show Similarities with Envelopes on Native Virions. *Immunity* 1–27 (2018) doi:10.1016/j.immuni.2018.06.017.
14. Pan, J., Peng, H., Chen, B. & Harrison, S. C. Cryo-EM Structure of Full-length HIV-1 Env Bound With the Fab of Antibody PG16. *J. Mol. Biol.* **432**, 1158–1168 (2020).
15. Harris, A. *et al.* Trimeric HIV-1 glycoprotein gp140 immunogens and native HIV-1 envelope glycoproteins display the same closed and open quaternary molecular architectures. *Proc. Natl. Acad. Sci.* **108**, 11440–11445 (2011).
16. Gristick, H. B. *et al.* Natively glycosylated HIV-1 Env structure reveals new mode for antibody recognition of the CD4-binding site. *Nat. Publ. Group* **23**, 906–915 (2016).
17. Scharf, L. *et al.* Broadly Neutralizing Antibody 8ANC195 Recognizes Closed and Open States of HIV-1 Env. *Cell* 1–13 (2018) doi:10.1016/j.cell.2015.08.035.

18. de Taeye, S. W. *et al.* Immunogenicity of Stabilized HIV-1 Envelope Trimers with Reduced Exposure of Non-neutralizing Epitopes. *Cell* **163**, 1702–1715 (2015).
19. Sanders, R. W. *et al.* HIV-1 neutralizing antibodies induced by native-like envelope trimers. *Science* **349**, aac4223 (2015).
20. Olshevsky, U. *et al.* Identification of individual human immunodeficiency virus type 1 gp120 amino acids important for CD4 receptor binding. *J. Virol.* **64**, 5701–5707 (1990).
21. Lu, M. *et al.* Associating HIV-1 envelope glycoprotein structures with states on the virus observed by smFRET. *Nature* **15**, 690–21 (2019).
22. Liu, Q. *et al.* Quaternary contact in the initial interaction of CD4 with the HIV-1 envelope trimer. *Nat. Struct. Mol. Biol.* **24**, 370–378 (2017).
23. Prévost, J. *et al.* The HIV-1 Env gp120 Inner Domain Shapes the Phe43 Cavity and the CD4 Binding Site. *mBio* **11**, e00280-20 (2020).
24. Kwong, P. D. *et al.* Structure of an HIV gp120 envelope glycoprotein in complex with the CD4 receptor and a neutralizing human antibody. *Nature* **393**, 648–659 (1998).
25. Huang, C. *et al.* Scorpion-Toxin Mimics of CD4 in Complex with Human Immunodeficiency Virus gp120. *Structure* **13**, 755–768 (2005).
26. Stricher, F. *et al.* Combinatorial Optimization of a CD4-Mimetic Miniprotein and Cocrystal Structures with HIV-1 gp120 Envelope Glycoprotein. *J. Mol. Biol.* **382**, 510–524 (2008).

27. Vita, C. *et al.* Rational engineering of a miniprotein that reproduces the core of the CD4 site interacting with HIV-1 envelope glycoprotein. *Proc. Natl. Acad. Sci.* **96**, 13091–13096 (1999).

28. Melillo, B. *et al.* Small-Molecule CD4-Mimics: Structure-Based Optimization of HIV-1 Entry Inhibition. *ACS Med. Chem. Lett.* **7**, 330–334 (2016).

29. Haim, H. *et al.* Soluble CD4 and CD4-Mimetic Compounds Inhibit HIV-1 Infection by Induction of a Short-Lived Activated State. *PLoS Pathog.* **5**, e1000360 (2009).

30. Courter, J. R. *et al.* Structure-Based Design, Synthesis and Validation of CD4-Mimetic Small Molecule Inhibitors of HIV-1 Entry: Conversion of a Viral Entry Agonist to an Antagonist. *Acc. Chem. Res.* **47**, 1228–1237 (2014).

31. West Jr, A. P. Structural basis for germ-line gene usage of a potent class of antibodies targeting the CD4-binding site of HIV-1 gp120. *PNAS* 1–8 (2012) doi:10.1073/pnas.1208984109/-/DCSupplemental.

32. Huang, J. *et al.* Identification of a CD4-Binding-Site Antibody to HIV that Evolved Near-Pan Neutralization Breadth. *Immunity* **45**, 1108–1121 (2016).

33. Schommers, P. *et al.* Restriction of HIV-1 Escape by a Highly Broad and Potent Neutralizing Antibody. *Cell* **180**, 471-489.e22 (2020).

34. Barnes, C. O. *et al.* A naturally arising broad and potent CD4-binding site antibody with low somatic mutation. *Sci. Adv.* **8**, eabp8155 (2022).

35. Zhou, T. *et al.* Structural Basis for Broad and Potent Neutralization of HIV-1 by Antibody VRC01. *Science* **329**, 811–817 (2010).

36. Pugach, P. *et al.* A Native-Like SOSIP.664 Trimer Based on an HIV-1 Subtype B *env* Gene. *J. Virol.* **89**, 3380–3395 (2015).

37. Sullivan, N. *et al.* CD4-Induced Conformational Changes in the Human Immunodeficiency Virus Type 1 gp120 Glycoprotein: Consequences for Virus Entry and Neutralization. *J. Virol.* **72**, 4694–4703 (1998).
38. Chan, D. C. & Kim, P. S. HIV Entry and Its Inhibition. *Cell* **93**, 681-684, (1998).
39. Chan, D. C., Fass, D., Berger, J. M. & Kim, P. S. Core Structure of gp41 from the HIV Envelope Glycoprotein. *Cell* **89**, 263–273 (1997).
40. Ladinsky, M. S. *et al.* Electron tomography visualization of HIV-1 fusion with target cells using fusion inhibitors to trap the pre-hairpin intermediate. *eLife* **9**, e58411 (2020).
41. Li, W. *et al. Asymmetric HIV-1 envelope trimers bound to one and two CD4 molecules are intermediates during membrane binding*. http://biorxiv.org/lookup/doi/10.1101/2022.12.23.521843 (2022) doi:10.1101/2022.12.23.521843.
42. Abernathy, M. E. *et al.* Antibody elicited by HIV-1 immunogen vaccination in macaques displaces Env fusion peptide and destroys a neutralizing epitope. *Npj Vaccines* **6**, 126 (2021).
43. Yang, X., Kurteva, S., Ren, X., Lee, S. & Sodroski, J. Subunit Stoichiometry of Human Immunodeficiency Virus Type 1 Envelope Glycoprotein Trimers during Virus Entry into Host Cells. *J. Virol.* **80**, 4388–4395 (2006).
44. Salzwedel, K. & Berger, E. A. Complementation of diverse HIV-1 Env defects through cooperative subunit interactions: a general property of the functional trimer. *Retrovirology* **6**, 75 (2009).

45. Salzwedel, K. & Berger, E. A. Cooperative subunit interactions within the oligomeric envelope glycoprotein of HIV-1: Functional complementation of specific defects in gp120 and gp41. *Proc. Natl. Acad. Sci.* **97**, 12794–12799 (2000).

46. Khasnis, M. D., Halkidis, K., Bhardwaj, A. & Root, M. J. Receptor Activation of HIV-1 Env Leads to Asymmetric Exposure of the gp41 Trimer. *PLOS Pathog.* **12**, e1006098 (2016).

47. Seaman, M. S. *et al.* Tiered Categorization of a Diverse Panel of HIV-1 Env Pseudoviruses for Assessment of Neutralizing Antibodies. *J. Virol.* **84**, 1439–1452 (2010).

48. Li, Y. *et al.* Broad HIV-1 neutralization mediated by CD4-binding site antibodies. *Nat. Med.* **13**, 1032–1034 (2007).

49. Umotoy, J. *et al.* Rapid and Focused Maturation of a VRC01-Class HIV Broadly Neutralizing Antibody Lineage Involves Both Binding and Accommodation of the N276-Glycan. *Immunity* **51**, 141-154.e6 (2019).

50. Ma, X. & Mothes, W. HIV-1 Env trimer opens through an asymmetric intermediate in which individual protomers adopt distinct conformations. *eLife* **7:e34271**, 1–18 (2018).

51. Cupo, A. *et al.* Optimizing the production and affinity purification of HIV-1 envelope glycoprotein SOSIP trimers from transiently transfected CHO cells. *PLOS ONE* **14**, e0215106 (2019).

52. Dam, K.-M. A., Mutia, P. S. & Bjorkman, P. J. Comparing methods for immobilizing HIV-1 SOSIPs in ELISAs that evaluate antibody binding. *Sci. Rep.* **12**, 11172 (2022).

53. Mastronarde, D. N. SerialEM: A Program for Automated Tilt Series Acquisition on Tecnai Microscopes Using Prediction of Specimen Position. *Microsc. Microanal.* **9**, 1182–1183 (2003).

54. Punjani, A., Rubinstein, J. L., Fleet, D. J. & Brubaker, M. A. cryoSPARC: algorithms for rapid unsupervised cryo-EM structure determination. *Nat. Methods* **14**, 290–296 (2017).

55. Goddard, T. D. *et al.* UCSF ChimeraX: Meeting modern challenges in visualization and analysis: UCSF ChimeraX Visualization System. *Protein Sci.* **27**, 14–25 (2018).

56. Emsley, P., Lohkamp, B., Scott, W. G. & Cowtan, K. Features and development of *Coot*. *Acta Crystallogr. D Biol. Crystallogr.* **66**, 486–501 (2010).

57. Adams, P. D. *et al. PHENIX* : a comprehensive Python-based system for macromolecular structure solution. *Acta Crystallogr. D Biol. Crystallogr.* **66**, 213–221 (2010).

58. Afonine, P. V. *et al.* Real-space refinement in *PHENIX* for cryo-EM and crystallography. *Acta Crystallogr. Sect. Struct. Biol.* **74**, 531–544 (2018).

59. Krissinel, E. & Henrick, K. Inference of Macromolecular Assemblies from Crystalline State. *J. Mol. Biol.* **372**, 774–797 (2007).

60. Kyte, J. & Doolittle, R. F. A simple method for displaying the hydropathic character of a protein. *J. Mol. Biol.* **157**, 105–132 (1982).

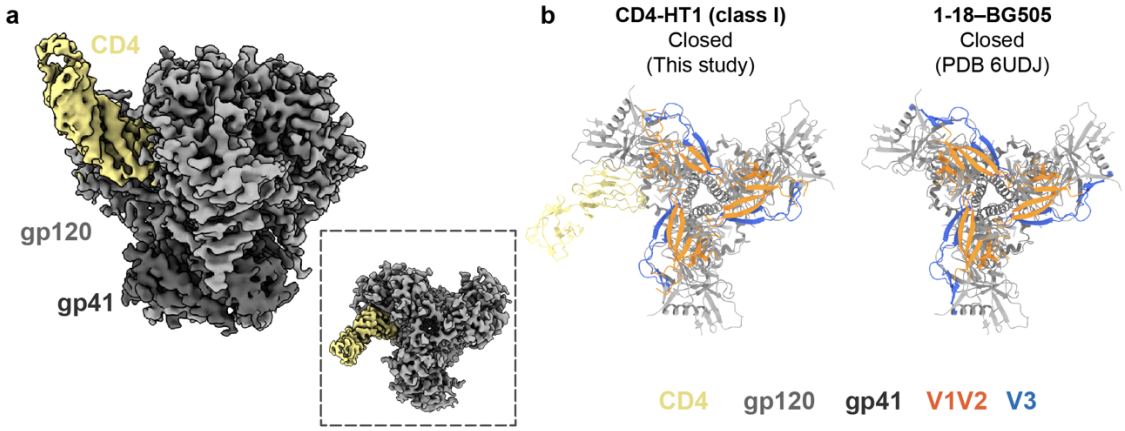

c

Surface area (Å²) buried on gp120 by CD4

gp120 Motif	CD4-HT1 (class I)	CD4-BG505
V1V2	0	192
$T257_{gp120}$	1	4
D Loop	161	192
CD4 binding loop	258	237
β20/β21	191	221
β23	95	99
V5 loop	38	25
β24	19	20
Exit loop	101	84
Alpha 5	25	21
Total	889	1095

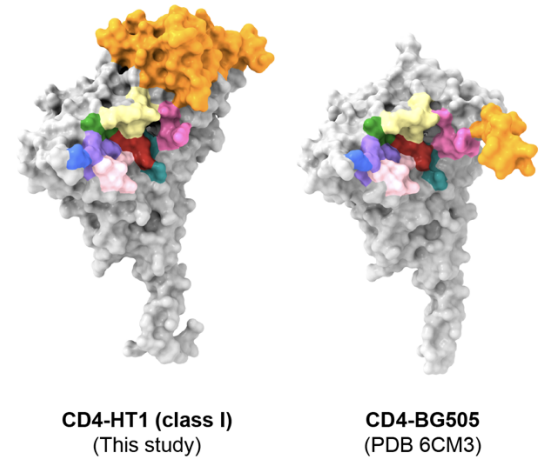

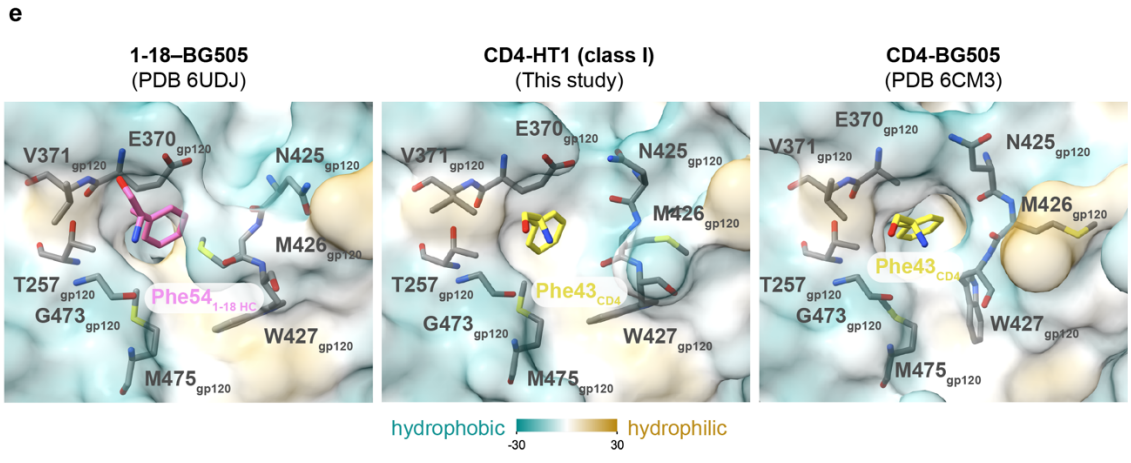

Fig. 1: 3.4 Å cryo-EM structure of BG505-HT1 bound to one CD4 reveals closed, pre-fusion Env conformation

a, Side view of the 3.4 Å CD4-HT1 (class I) density map. Inset: top-down view. **b,** Top-down cartoon representations of CD4-HT1 (class I) and 1-18–BG505 (PDB 6UDJ) structures with gp120 V1V2 and V3 loops highlighted. **c,** Table summarizing BSA on gp120 from CD4 binding for CD4-HT1 (class I) and CD4-BG505 (PDB 6CM3) complexes. **d,** Surface representation comparisons of CD4-HT1 (class I) and CD4-BG505 (PDB 6CM3). **e,** Surface representations depicting hydrophobicity (Kyte-Doolittle scale[60]) for 1-18–BG505 (PDB 6UDJ), CD4-HT1 (class I), and CD4-BG505 (PDB 6CM3) overlaid with stick representations of gp120 residues within the Phe43 cavity.

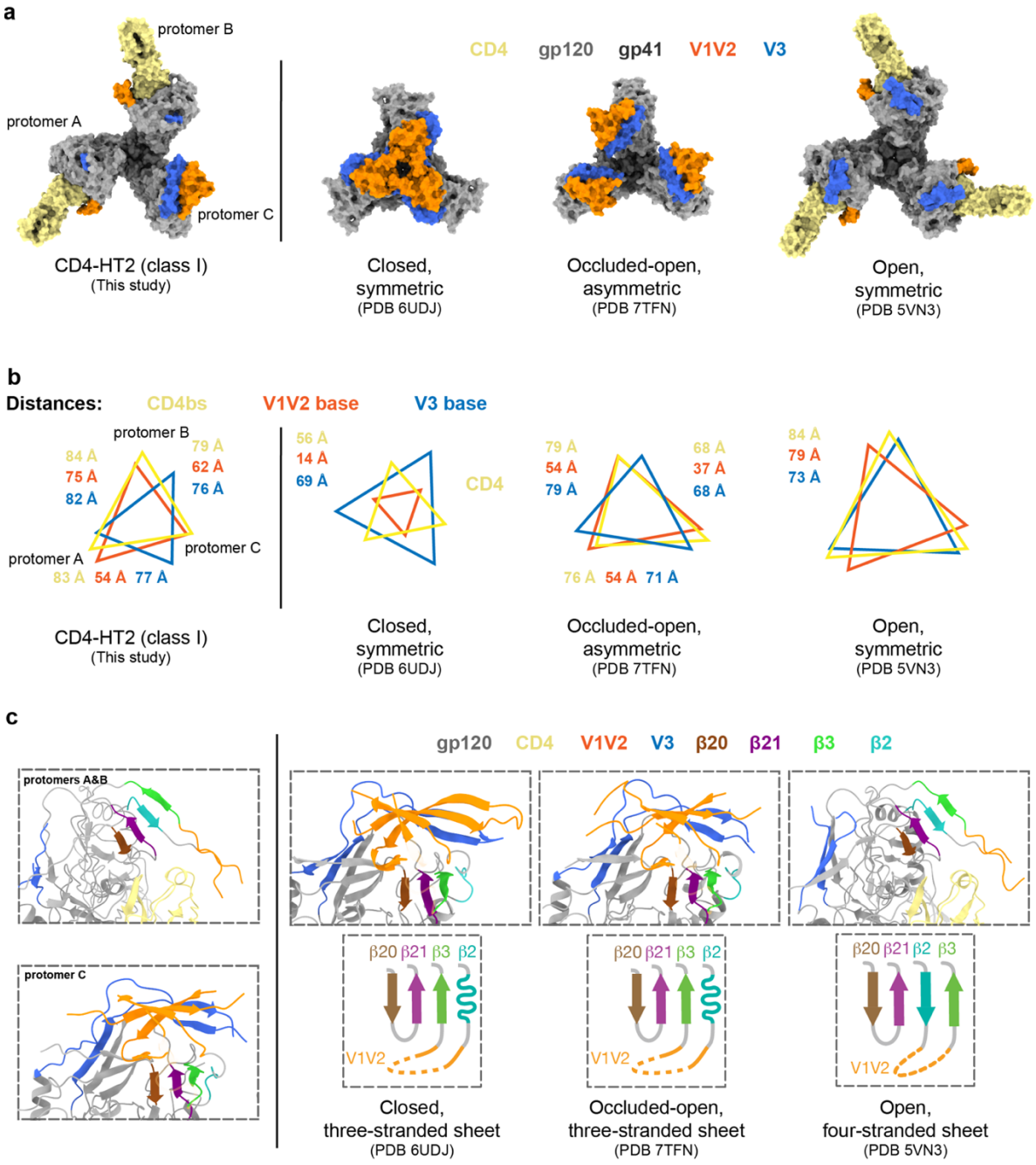
a
protomer B
protomer A
protomer C
CD4
gp120
gp41
V1V2
V3
CD4-HT2 (class I)
(This study)
Closed,
symmetric
(PDB 6UDJ)
Occluded-open,
asymmetric
(PDB 7TFN)
Open,
symmetric
(PDB 5VN3)
b
Distances:
CD4bs
V1V2 base
V3 base
protomer B
84 Å
75 Å
82 Å
79 Å
62 Å
76 Å
protomer A
protomer C
83 Å
54 Å
77 Å
56 Å
14 Å
69 Å
CD4
79 Å
54 Å
79 Å
68 Å
37 Å
68 Å
76 Å
54 Å
71 Å
84 Å
79 Å
73 Å
CD4-HT2 (class I)
(This study)
Closed,
symmetric
(PDB 6UDJ)
Occluded-open,
asymmetric
(PDB 7TFN)
Open,
symmetric
(PDB 5VN3)
c
gp120
CD4
V1V2
V3
β20
β21
β3
β2
protomers A&B
protomer C
β20 β21 β3 β2
V1V2
β20 β21 β3 β2
V1V2
β20 β21 β2 β3
V1V2
Closed,
three-stranded sheet
(PDB 6UDJ)
Occluded-open,
three-stranded sheet
(PDB 7TFN)
Open,
four-stranded sheet
(PDB 5VN3)

Fig. 2: 3.9 Å cryo-EM structure of BG505-HT2 bound to two CD4 molecules reveals an asymmetric open Env conformation

a, Top-down views of surface depictions of CD4-HT2 (class I), an Env in a prefusion conformation (PDB 6UDJ), Env in the occluded-open conformation (PDB 7TFN), and the CD4-bound open conformation of Env (PDB 5VN3). **b,** Inter-protomer distance measurements between reference residues for the base of the V3 loop ($H330_{gp120}$), the base of the V1/V2 loop ($P124_{gp120}$), and the CD4bs ($D/R368_{gp120}$) for CD4-HT2 (class I), an Env in a prefusion conformation (PDB 6UDJ), Env in the occluded-open conformation (PDB 7TFN), and the CD4-bound open conformation of Env (PDB 5VN3). **c,** Cartoon representations of the gp120 bridging sheet motif for CD4-HT2 (class I), an Env in a prefusion conformation (PDB 6UDJ), Env in an occluded-open conformation (PDB 7TFN), and the CD4-bound open conformation of Env (PDB 5VN3).

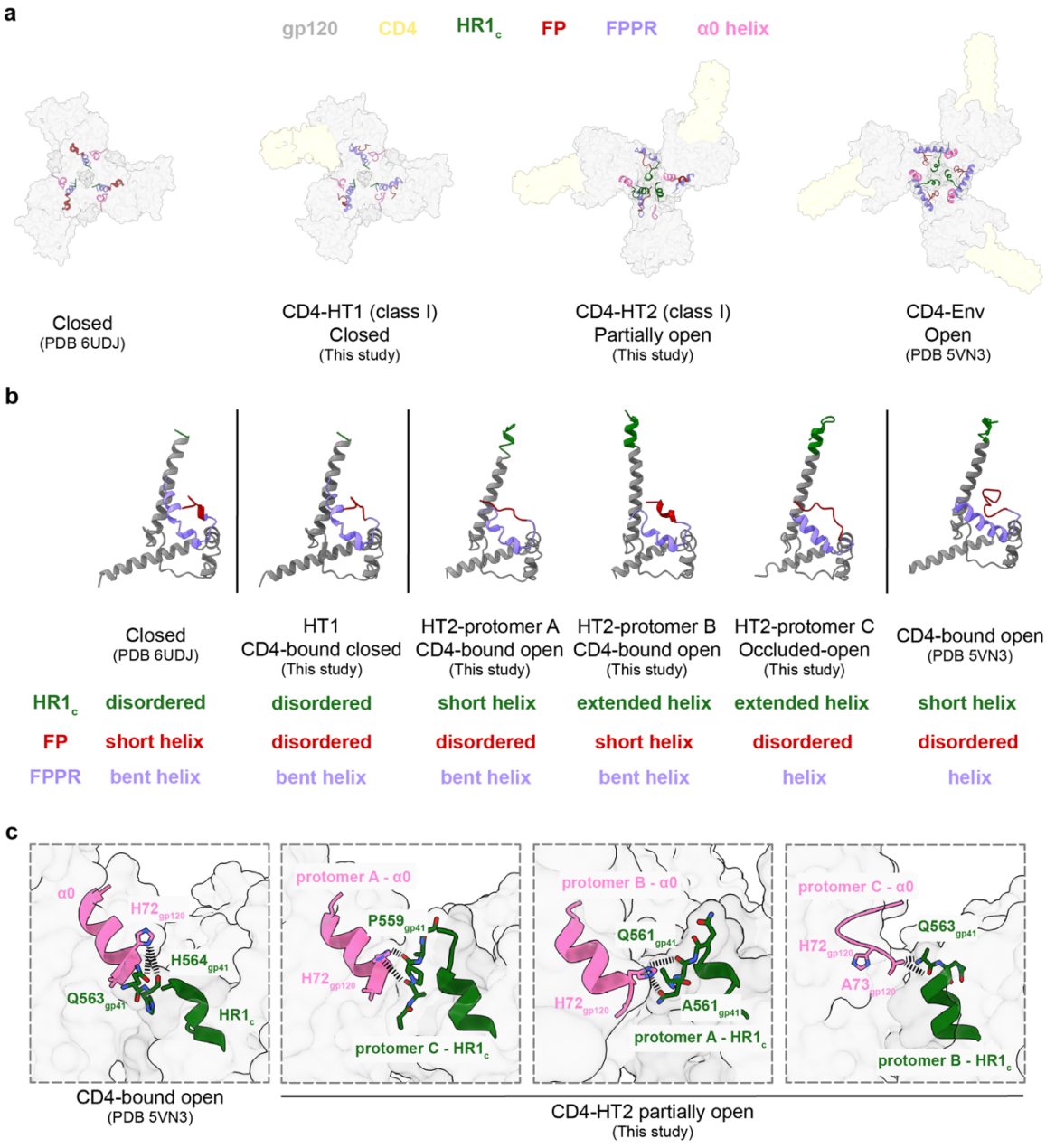
a
gp120
CD4
HR1c
FP
FPPR
α0 helix
Closed
(PDB 6UDJ)
CD4-HT1 (class I)
Closed
(This study)
CD4-HT2 (class I)
Partially open
(This study)
CD4-Env
Open
(PDB 5VN3)
b
Closed
(PDB 6UDJ)
HT1
CD4-bound closed
(This study)
HT2-protomer A
CD4-bound open
(This study)
HT2-protomer B
CD4-bound open
(This study)
HT2-protomer C
Occluded-open
(This study)
CD4-bound open
(PDB 5VN3)
HR1c
disordered
disordered
short helix
extended helix
extended helix
short helix
FP
short helix
disordered
disordered
short helix
disordered
disordered
FPPR
bent helix
bent helix
bent helix
bent helix
helix
helix
c
α0
H72gp120
H564gp41
Q563gp41
HR1c
protomer A - α0
P559gp41
H72gp120
protomer C - HR1c
protomer B - α0
Q561gp41
H72gp120
A561gp41
protomer A - HR1c
protomer C - α0
Q563gp41
H72gp120
A73gp120
protomer B - HR1c
CD4-bound open
(PDB 5VN3)
CD4-HT2 partially open
(This study)

Fig. 3: Conformational changes in gp41 were coordinated with gp120 conformation in CD4-bound heterotrimers

a, Top-down views of surface representations of Envs from closed (PDB 6UDJ), CD4-HT1 (class I), CD4-HT2 (class I), and CD4-Env (PDB 5VN3) structures with gp41 structural elements ($HR1_C$, FP, FPPR, α0 helix) depicted in cartoon representations. **b,** Cartoon representations of gp41 subunits from closed (PDB 6UDJ), CD4-HT1 (class I), CD4-HT2 (class I) (protomers a-c), and CD4-Env (PDB 5VN3) structures with colored gp41 ($HR1_C$, FP, FPPR, α0 helix) structural elements. **c,** Cartoon representations of the α0 helix and $HR1_C$ for CD4-Env (PDB 5VN3) and CD4-HT2 (class I) (protomers a-c) with stick representations of selected amino acids. Black dashed connecting lines indicate gp120-gp41 interactions within 6.0 Å.

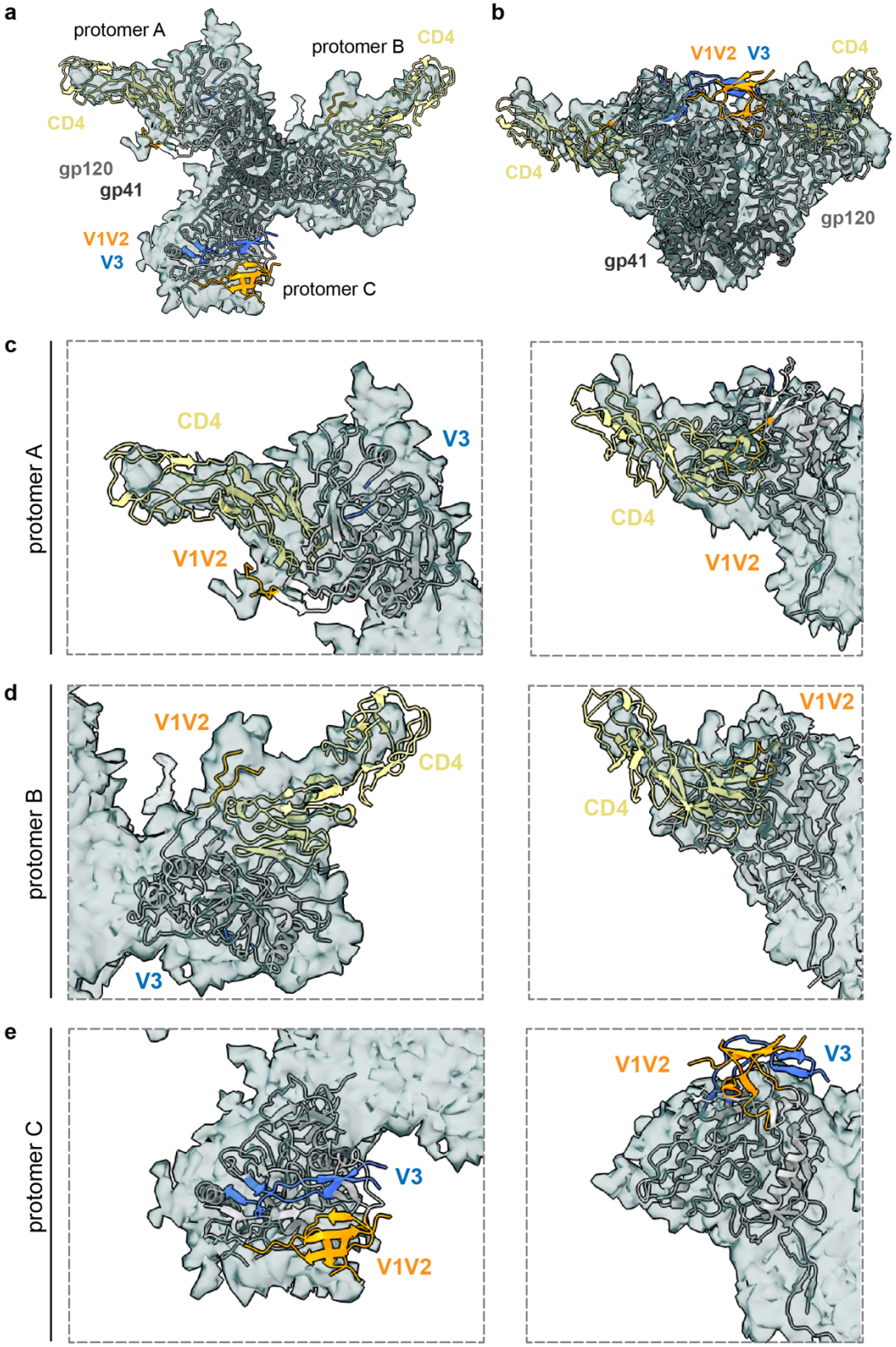
a
protomer A
protomer B
CD4
CD4
gp120
gp41
V1V2
V3
protomer C
b
V1V2
V3
CD4
CD4
gp120
gp41
c
protomer A
CD4
V3
V1V2
CD4
V1V2
d
protomer B
V1V2
CD4
V3
CD4
V1V2
e
protomer C
V3
V1V2
V1V2
V3

Fig. 4: The CD4-HT2 heterotrimer resembles a two CD4-bound membrane-bound Env

a, Top-down and **b**, side views of a cartoon representation of the CD4-HT2 (class I) structure fit into density (gray mesh) of a two CD4-bound Env derived from cryo-ET/sub-tomogram averaging[41]. Close-ups of **c,** protomer A, **d,** protomer B, and **e,** protomer C from top-down and side views depicted in **a,** and **b**, respectively.

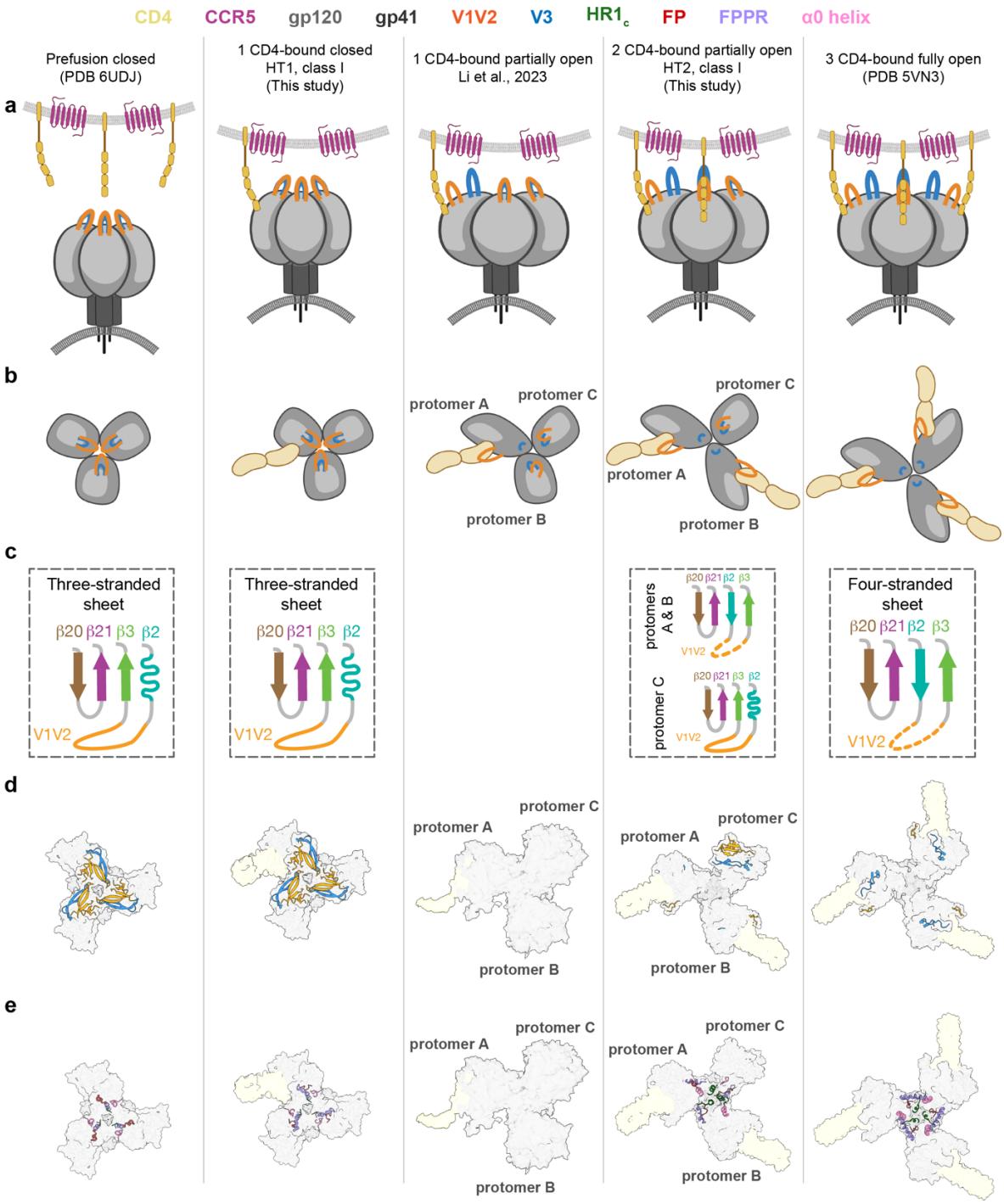
CD4
CCR5
gp120
gp41
V1V2
V3
HR1c
FP
FPPR
α0 helix
Prefusion closed (PDB 6UDJ)
1 CD4-bound closed HT1, class I (This study)
1 CD4-bound partially open Li et al., 2023
2 CD4-bound partially open HT2, class I (This study)
3 CD4-bound fully open (PDB 5VN3)
a
b
c
d
e
protomer A
protomer B
protomer C
Three-stranded sheet
Four-stranded sheet
β20 β21 β3 β2
V1V2
protomers A & B
protomer C

Fig. 5: Overview of Env receptor-induced conformational changes that lead to coreceptor binding and fusion

Summary of Env conformational changes, including Envs in prefusion, closed (PDB 6UDJ), one CD4-bound closed (CD4-HT1, class I), one CD4-bound open (cryo-ET), two CD4-bound partially open (CD4-HT2, class I), and three-CD4 bound (PDB 5VN3) conformations. The CD4-HT1 class II cryo-EM reconstruction was similar to the partially open Env conformation observed by cryo-ET for one CD4-bound Env but coordinates were not modeled due to heterogeneity. Schematics were generated using BioRender. Depictions for each Env conformation include: Env schematics in **a,** side and **b,** top-down views, **c,** diagrams describing □-sheet conformations observed in Env gp120s, **d,** surface representations of structures for each Env conformation with cartoon representations of V1V2 and V3 loops and **e,** gp41 structural features.

Extended Data

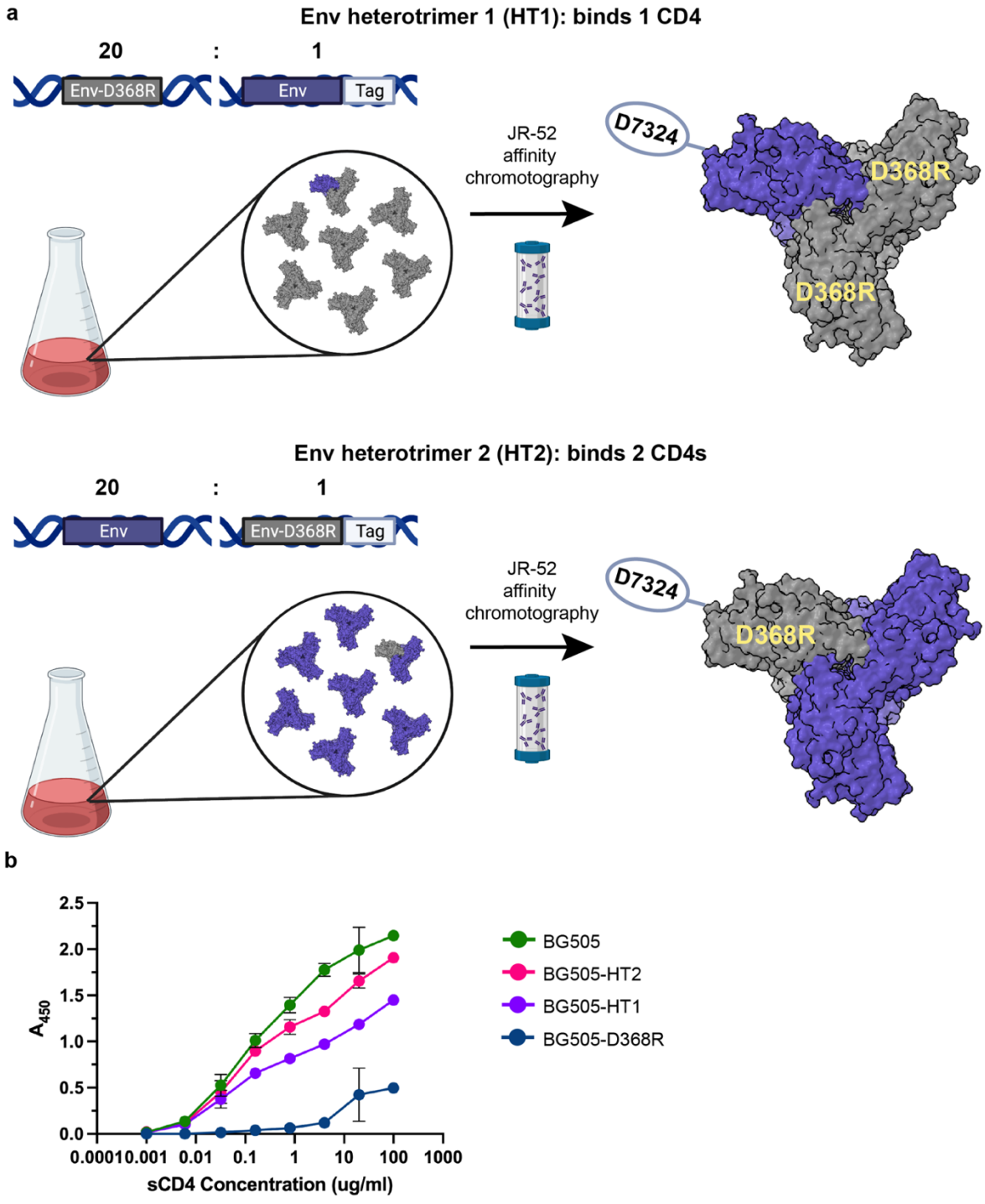

Extended Data Fig. 1: Design and validation of soluble HIV-1 Env heterotrimer constructs

a, Methods used to create soluble HT1 and HT2 HIV-1 Env heterotrimers. A 20:1 transfection ratio of untagged and D7324-tagged Env expression plasmids, one of which encoded the D368R CD4 knockout mutation in gp120, was co-transfected to produce two predominant populations: untagged trimers and singly tagged trimers. Transfection supernatants were harvested and Env proteins purified by JR-52 immunoaffinity chromatography (as described), resulting in the HT1 and HT2 heterotrimers. **b,** ELISA comparing CD4 binding of BG505, BG505-HT2, BG505-HT1, and BG505-D368R. Values are shown as mean ± s.d. of two individual biological replicates (n=2). Error bars are not visible for data points where bars are smaller than the size of the symbol representing the mean value.

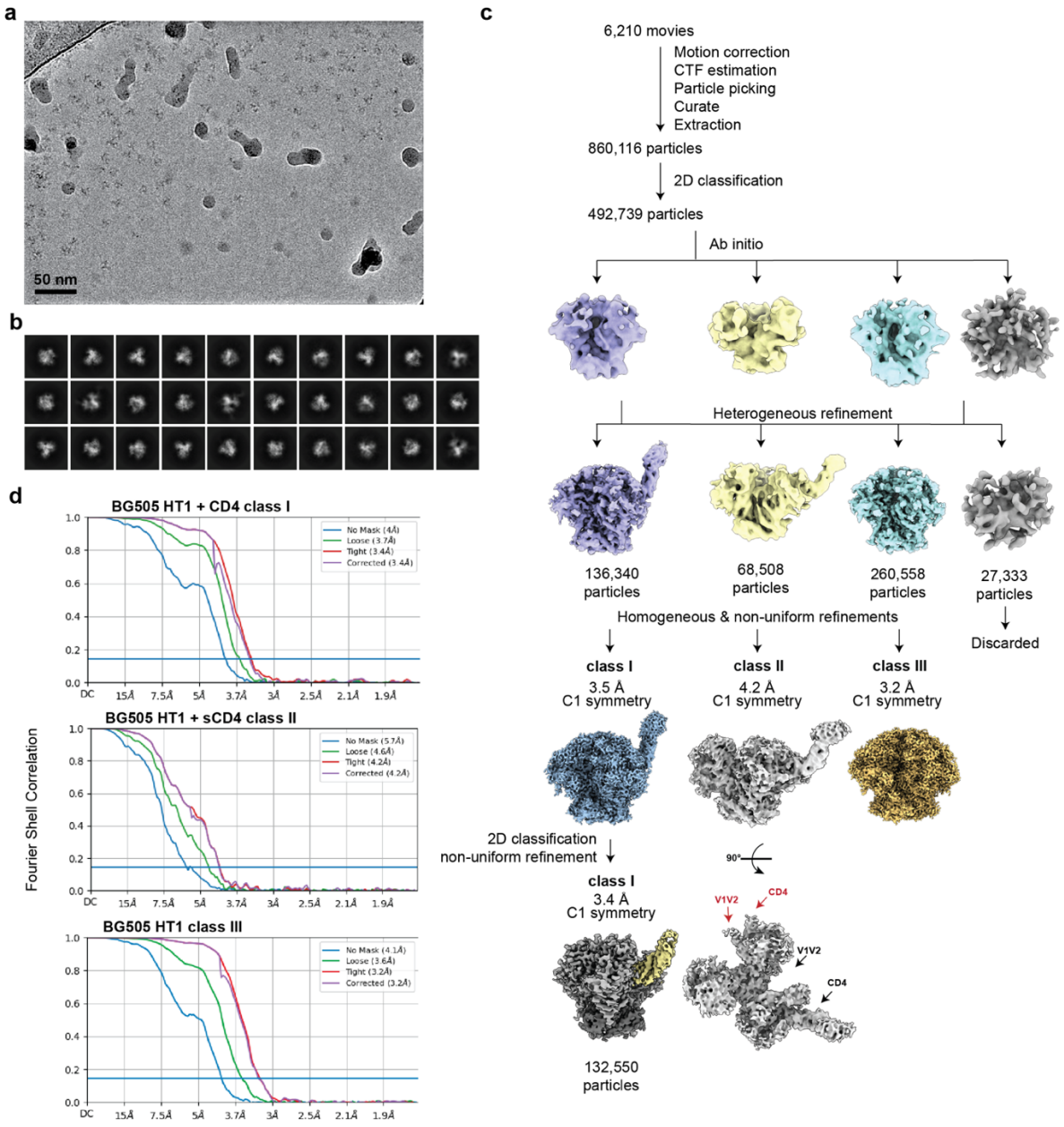
a
50 nm
b
c
6,210 movies
Motion correction
CTF estimation
Particle picking
Curate
Extraction
860,116 particles
2D classification
492,739 particles
Ab initio
Heterogeneous refinement
136,340 particles
68,508 particles
260,558 particles
27,333 particles
Discarded
Homogeneous & non-uniform refinements
class I
3.5 Å
C1 symmetry
class II
4.2 Å
C1 symmetry
class III
3.2 Å
C1 symmetry
2D classification
non-uniform refinement
90°
class I
3.4 Å
C1 symmetry
V1V2
CD4
V1V2
CD4
132,550 particles
d
BG505 HT1 + CD4 class I
No Mask (4Å)
Loose (3.7Å)
Tight (3.4Å)
Corrected (3.4Å)
BG505 HT1 + sCD4 class II
No Mask (5.7Å)
Loose (4.6Å)
Tight (4.2Å)
Corrected (4.2Å)
BG505 HT1 class III
No Mask (4.1Å)
Loose (3.6Å)
Tight (3.2Å)
Corrected (3.2Å)
Fourier Shell Correlation
DC
15Å
7.5Å
5Å
3.7Å
3Å
2.5Å
2.1Å
1.9Å

Extended Data Fig. 2: Cryo-EM data processing and validation for BG505-HT1 in complex with CD4

a, Representative micrograph and **b**, representative 2D classes for the CD4-BG505 HT1 complex. **c**, Workflow of single particle cryo-EM data processing. Class I shows one CD4 bound to a closed, prefusion conformation of HT1. Class II shows density for one CD4 molecule bound to HT1 and weak density for an additional bound CD4 (red arrow). The class II density map may represent an average of HT1 Envs bound to one or two CD4 molecules. We were unable to further separate these particles into different subclasses. Class III resembles an unliganded, closed prefusion Env trimer. **d**, Fourier shell correlation (FSC) plots of the final reconstructions for CD4-BG505 HT1 classes I, II, and III.

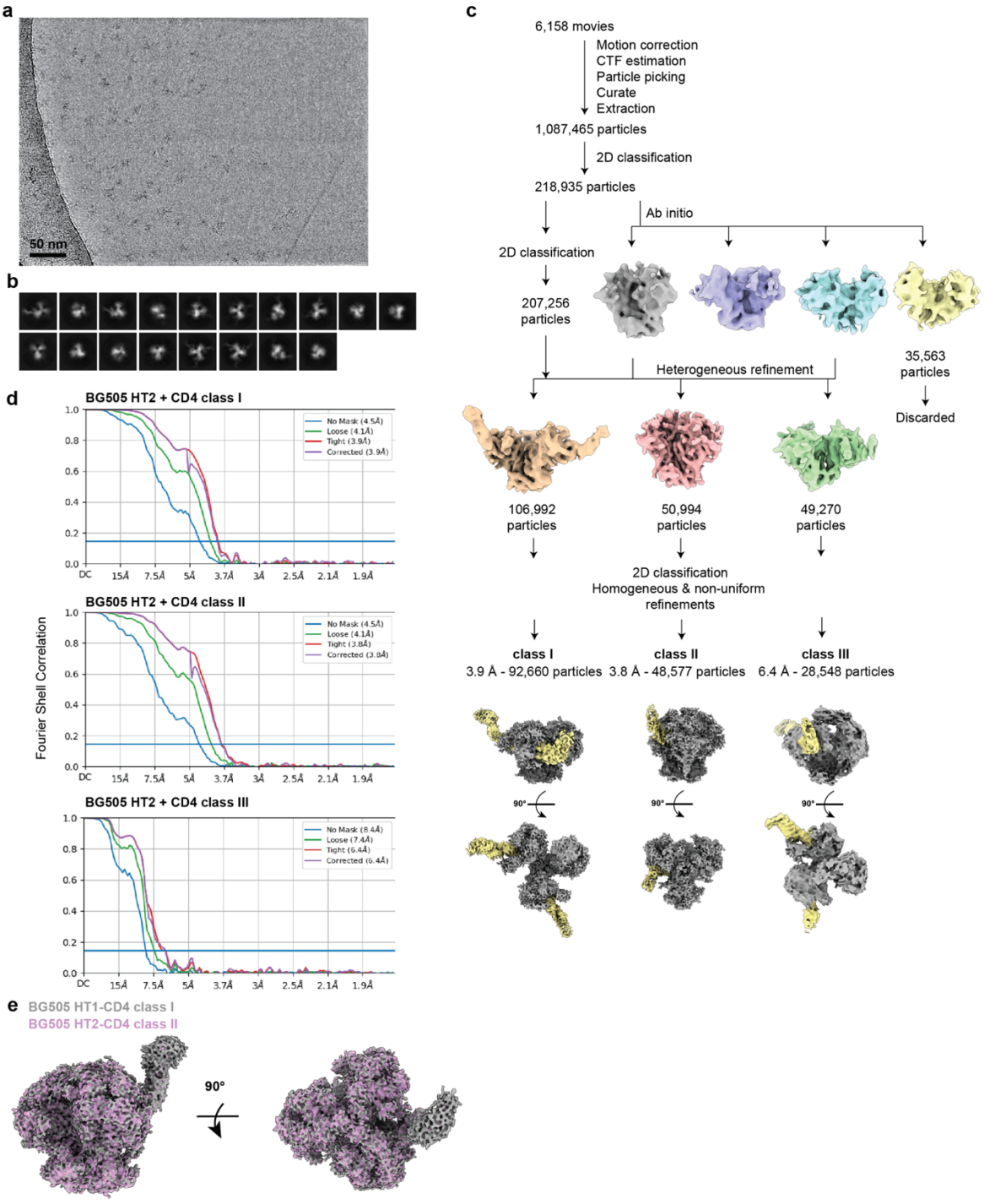
a
50 nm
b
c
6,158 movies
Motion correction
CTF estimation
Particle picking
Curate
Extraction
1,087,465 particles
2D classification
218,935 particles
Ab initio
2D classification
207,256 particles
Heterogeneous refinement
35,563 particles
Discarded
106,992 particles
50,994 particles
49,270 particles
2D classification
Homogeneous & non-uniform refinements
class I
3.9 Å - 92,660 particles
class II
3.8 Å - 48,577 particles
class III
6.4 Å - 28,548 particles
90°
d
BG505 HT2 + CD4 class I
No Mask (4.5Å)
Loose (4.1Å)
Tight (3.9Å)
Corrected (3.9Å)
BG505 HT2 + CD4 class II
No Mask (4.5Å)
Loose (4.1Å)
Tight (3.8Å)
Corrected (3.8Å)
BG505 HT2 + CD4 class III
No Mask (8.4Å)
Loose (7.4Å)
Tight (6.4Å)
Corrected (6.4Å)
Fourier Shell Correlation
DC
15Å
7.5Å
5Å
3.7Å
3Å
2.5Å
2.1Å
1.9Å
e
BG505 HT1-CD4 class I
BG505 HT2-CD4 class II
90°

Extended Data Fig. 3: Cryo-EM data processing and validation for BG505-HT2 in complex with CD4

a, Representative micrograph and **b**, representative 2D classes for the CD4-BG505 HT2 complex. **c**, Workflow of single particle cryo-EM data processing. **d**, Fourier shell correlation (FSC) plot of the final reconstruction for CD4-BG505 HT2 classes I, II, and III. **e**, Side and top-down views of superimposed BG505 CD4-HT1 class I and BG505 CD4-HT2 class II single-particle cryo-EM density maps. The densities for CD4 overlap extensively, thus obscuring the pink density for CD4 in the BG505 CD4-HT2 map.

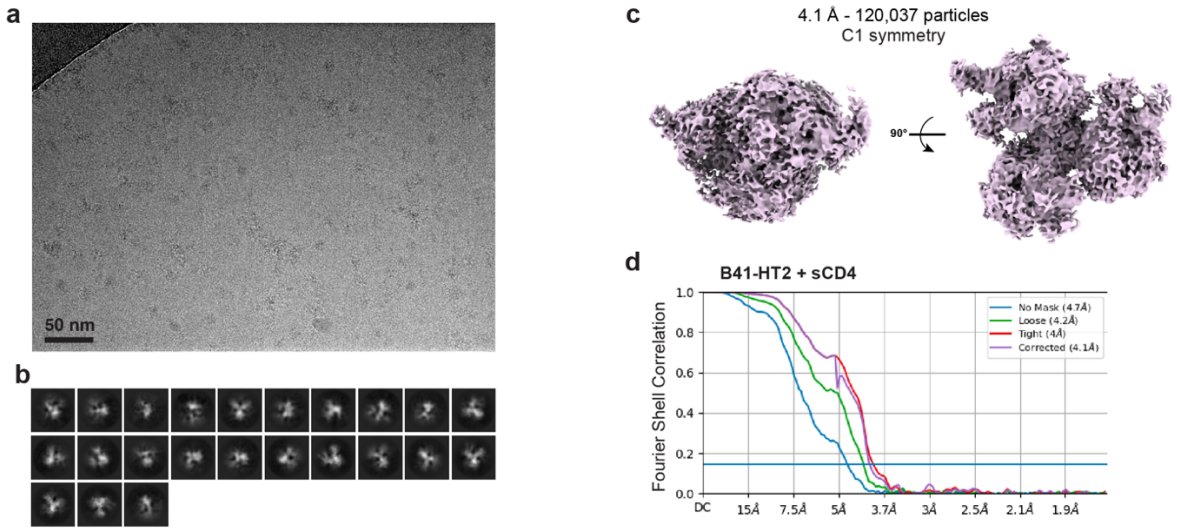
a
50 nm
b
c
4.1 Å - 120,037 particles
C1 symmetry
90°
d
B41-HT2 + sCD4
Fourier Shell Correlation
No Mask (4.7Å)
Loose (4.2Å)
Tight (4Å)
Corrected (4.1Å)
DC
15Å
7.5Å
5Å
3.7Å
3Å
2.5Å
2.1Å
1.9Å

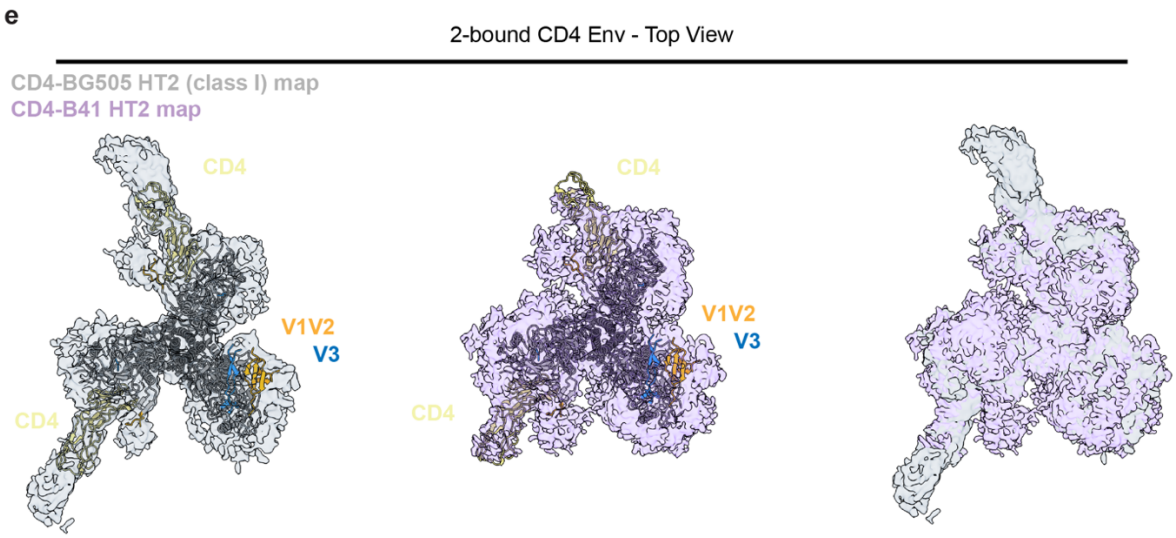
e
2-bound CD4 Env - Top View
CD4-BG505 HT2 (class I) map
CD4-B41 HT2 map
CD4
V1V2
V3
CD4
CD4
V1V2
V3
CD4

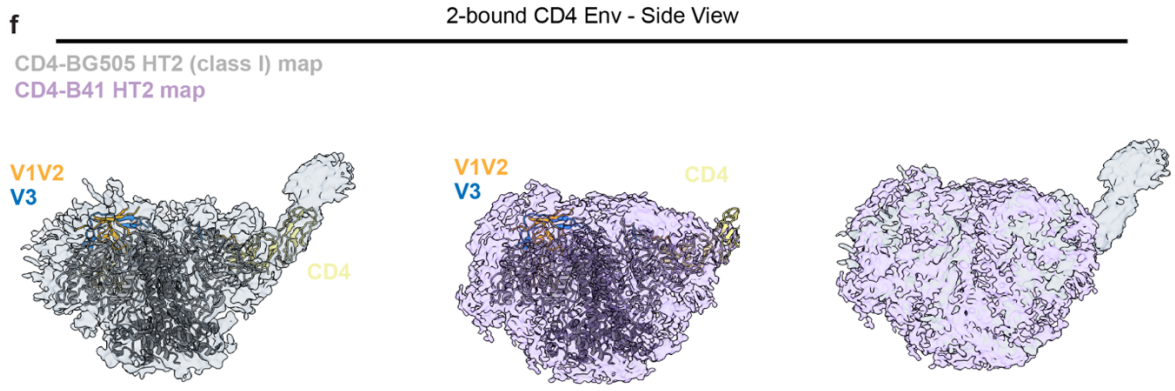
f
2-bound CD4 Env - Side View
CD4-BG505 HT2 (class I) map
CD4-B41 HT2 map
V1V2
V3
CD4
V1V2
V3
CD4

Extended Data Fig. 4: Cryo-EM data processing, validation, and interpretation for B41-HT2 in complex with CD4

a, Representative micrograph, **b**, representative 2D classes, and **c**, density map for the CD4-B41 HT2 complex. **d**, Fourier shell correlation (FSC) plot of the final reconstruction for CD4-B41 HT2. **e**, Top-down views of CD4-BG505 HT2 (class I) model fit into CD4-BG505 HT2 (class I) (left) or CD4-B41 HT2 (middle) density maps and alignment of both density maps (right). **f**, Side views of CD4-BG505 HT2 (class I) model fit into CD4-BG505 HT2 (class I) (left) or CD4-B41 HT2 (middle) density maps and alignment of both density maps (right).

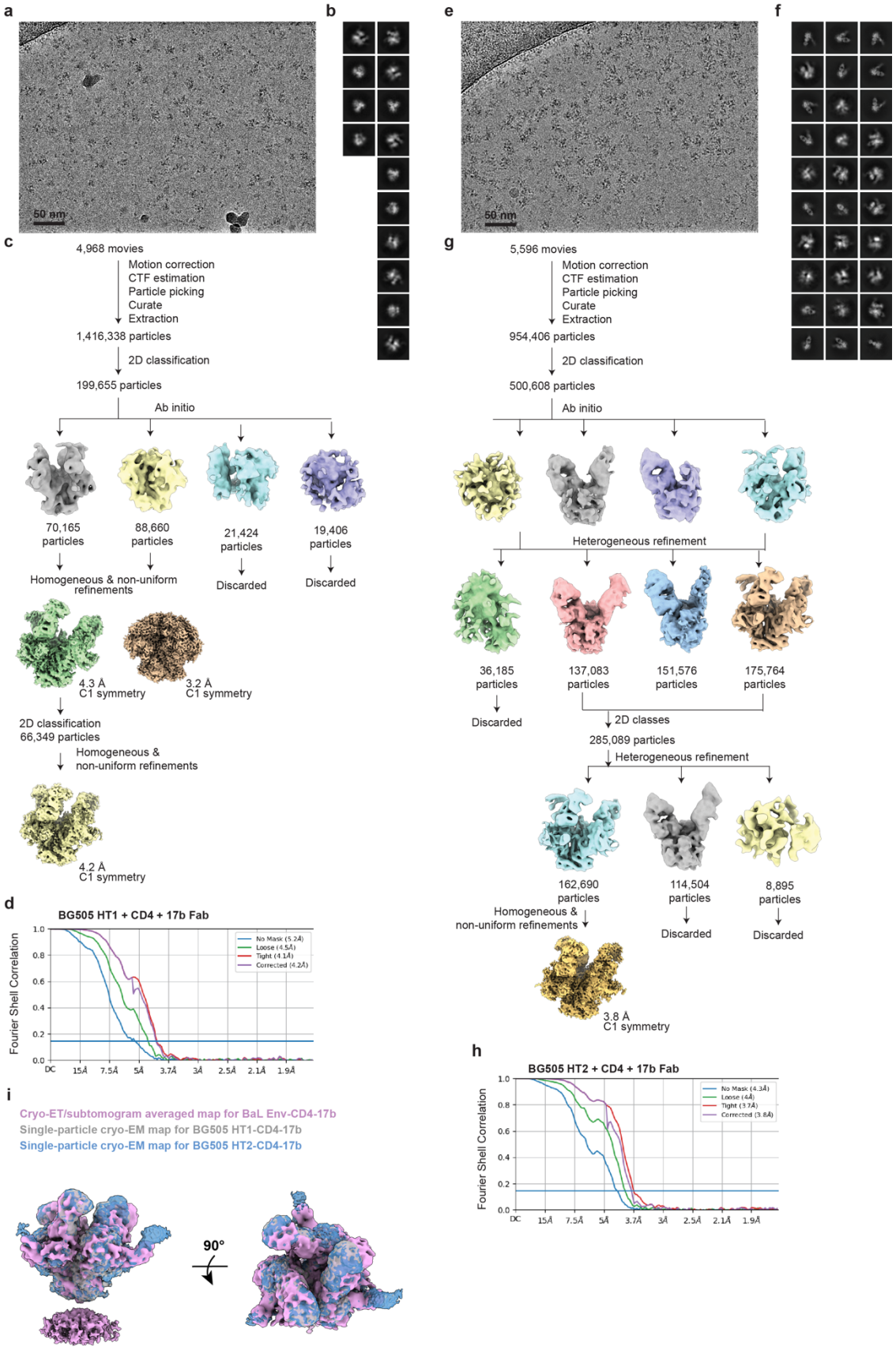
a
b
50 nm
c
4,968 movies
Motion correction
CTF estimation
Particle picking
Curate
Extraction
1,416,338 particles
2D classification
199,655 particles
Ab initio
70,165 particles
88,660 particles
21,424 particles
19,406 particles
Homogeneous & non-uniform refinements
Discarded
Discarded
4.3 Å C1 symmetry
3.2 Å C1 symmetry
2D classification 66,349 particles
Homogeneous & non-uniform refinements
4.2 Å C1 symmetry
d
BG505 HT1 + CD4 + 17b Fab
Fourier Shell Correlation
No Mask (5.2Å)
Loose (4.5Å)
Tight (4.1Å)
Corrected (4.2Å)
e
f
50 nm
g
5,596 movies
Motion correction
CTF estimation
Particle picking
Curate
Extraction
954,406 particles
2D classification
500,608 particles
Ab initio
Heterogeneous refinement
36,185 particles
137,083 particles
151,576 particles
175,764 particles
Discarded
2D classes
285,089 particles
Heterogeneous refinement
162,690 particles
114,504 particles
8,895 particles
Homogeneous & non-uniform refinements
Discarded
Discarded
3.8 Å C1 symmetry
h
BG505 HT2 + CD4 + 17b Fab
Fourier Shell Correlation
No Mask (4.3Å)
Loose (4Å)
Tight (3.7Å)
Corrected (3.8Å)
i
Cryo-ET/subtomogram averaged map for BaL Env-CD4-17b
Single-particle cryo-EM map for BG505 HT1-CD4-17b
Single-particle cryo-EM map for BG505 HT2-CD4-17b
90°

Extended Data Fig. 5: Cryo-EM data processing and validation for BG505-HT1 and BG505-HT2 in complex with CD4 and 17b Fab

a, Representative micrograph and **b**, representative 2D classes for the CD4-17b-BG505 HT1 complex. **c**, Workflow of single particle cryo-EM data processing. **d**, Fourier shell correlation (FSC) plot of the final reconstruction for CD4-17b-BG505 HT1. **e**, Representative micrograph and **f**, representative 2D classes for the CD4-17b-BG505 HT2 complex. **g**, Workflow of single particle cryo-EM data processing. **h**, Fourier shell correlation (FSC) plot of the final reconstruction for CD4-17b-BG505 HT2. **i**, Side and top-down views of CD4-17b-BG505 HT1 and CD4-17b-BG505 HT2 single-particle cryo-EM densities (both processed with C1 symmetry) superimposed with the cryo-ET/sub-tomogram averaged density map (C3 symmetry) of a CD4- and 17b-bound virion-bound BaL Env trimer (EMD-21411). Despite the single-particle cryo-EM structures being derived from heterotrimeric Envs that lack C3 symmetry and the cryo-ET structure being derived from symmetric homotrimeric Envs, the CD4-17b-Env trimer maps are similar.

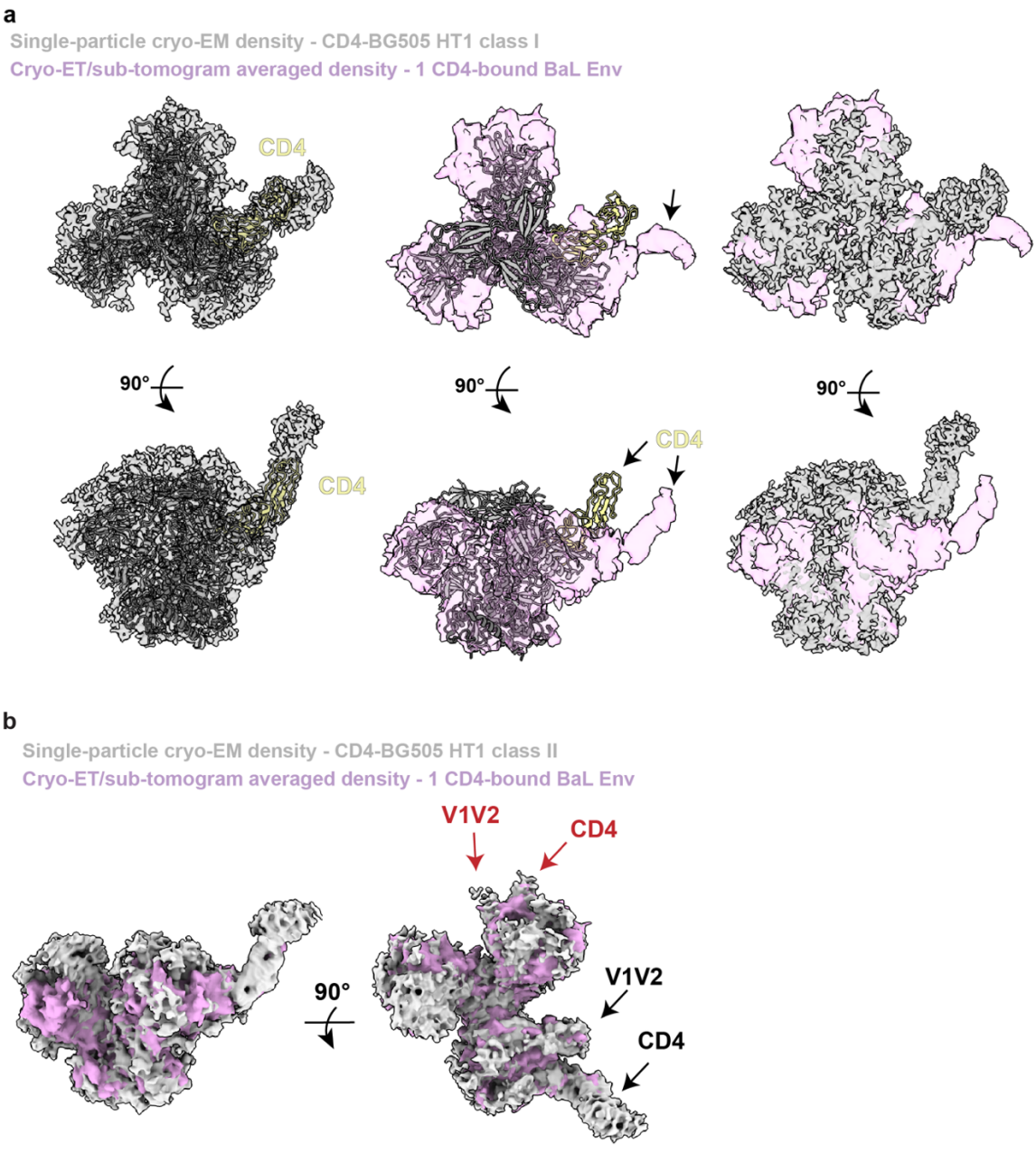
a
Single-particle cryo-EM density - CD4-BG505 HT1 class I
Cryo-ET/sub-tomogram averaged density - 1 CD4-bound BaL Env
CD4
90°
CD4
90°
CD4
90°
b
Single-particle cryo-EM density - CD4-BG505 HT1 class II
Cryo-ET/sub-tomogram averaged density - 1 CD4-bound BaL Env
V1V2
CD4
90°
V1V2
CD4

Extended Data Fig. 6: Comparisons of single particle cryo-EM densities of CD4-HT1 with one CD4-bound Env cryo-ET/sub-tomogram averaged density

a, Top-down (top) and side (bottom) views of CD4-HT1 (class I) model fit into one-CD4 bound Env from single-particle cryo-EM (left) or cryo-ET/sub-tomogram averaged (middle) density maps. Right: alignment of single-particle cryo-EM and cryo-ET/sub-tomogram averaged density maps. **b**, Side and top-down views of CD4-HT1 (class II) single-particle cryo-EM density superimposed with one-CD4 bound Env from cryo-ET/sub-tomogram averaged density map. The densities for CD4 overlap extensively, thus obscuring the pink density for CD4 in the cryo-ET map. Weak densities in the single-particle cryo-EM map for a second bound CD4 and a rearranged V1V2 in the protomer adjacent to the protomer with strong CD4 density are marked with red arrows.

Chapter IV

HOW ANTIBODIES RECOGNIZE PATHOGENIC VIRUSES: STRUCTURAL CORRELATES OF ANTIBODY NEUTRALIZATION OF HIV-1, SARS-COV-2, AND ZIKA

Abernathy*, M. E., **Dam*, K. A.,** Esswein*, S. R., Jette*, C. A. & Bjorkman, P. J. How Antibodies Recognize Pathogenic Viruses: Structural Correlates of Antibody Neutralization of HIV-1, SARS-CoV-2, and Zika. Viruses 13, 2106 (2021). https://doi.org/10.3390/v13102106

**These authors contributed equally.*

Abstract

The H1N1 pandemic of 2009-2010, MERS epidemic of 2012, Ebola epidemics of 2013-2016 and 2018-2020, Zika epidemic of 2015-2016, and COVID-19 pandemic of 2019-2021, are recent examples in the long history of epidemics that demonstrate the enormous global impact of viral infection. The rapid development of safe and effective vaccines and therapeutics has proven vital to reducing morbidity and mortality from newly emerging viruses. Structural biology methods can be used to determine how antibodies elicited during infection or vaccination target viral proteins and identify viral epitopes that correlate with potent neutralization. Here we review how structural and molecular biology approaches have contributed to our understanding of antibody recognition of pathogenic viruses, specifically HIV-1, SARS-CoV-2, and Zika. Determining structural correlates of neutralization of viruses has guided the design of vaccines, monoclonal antibodies, and small molecule inhibitors in response to the global threat of viral epidemics.

Keywords:

antibody

cryo-electron microscopy

HIV-1

SARS-CoV-2

structural biology

virus

X-ray crystallography

Zika

Introduction

Advances in structural biology in recent decades have played a key role in the determination of disease-relevant protein complexes and guided the design of new therapeutics and vaccines. An early pioneer in structural biology was the X-ray crystallographer Rosalind Franklin. While she is best known for her role in collecting the X-ray fiber diffraction patterns that revealed the 3D structure of DNA, her contributions in biologically-related fields also included insights into the structures of protein encapsulated viruses such as tobacco mosaic virus (TMV), poliovirus, and turnip yellow mosaic virus. During Franklin's studies of viruses in the 1950s, a central question was how viruses managed to build a protein shell to shield their genetic material given that only a limited number of viral capsid proteins could be encoded within a viral genome based on capsid size constraints. Franklin's X-ray analysis revealed the arrangement of the protein subunits in TMV, allowing her to create the first three-dimensional model of a virus [1–4]. Following this work, she used X-ray data to determine the position and orientation of RNA packaged inside of the rod-shaped TMV [5]. Unlike prior speculation that placed the RNA at the center of the rod, her work revealed the virus was hollow, which led to the discovery that the RNA spiraled with the helical protein capsid. This work was fundamental in understanding principles of virus structure. Franklin's contributions to the field of virology are summarized on her tombstone, which reads, "Her research and discoveries on viruses remain of lasting benefit to mankind." Together, her remarkable contributions to structural studies in three separate areas, DNA, coal, and viruses, before her death at the age of 37 make her an inspiration to future generations of structural biologists, particularly women. We are proud to follow in her footsteps to use structural biology to gain insight into viruses with the goal of providing benefits to human health.

The severe acute respiratory syndrome coronavirus (SARS-CoV) epidemic of 2002, Middle East Respiratory Syndrome (MERS) epidemic of 2012, acquired immune deficiency syndrome (AIDS) pandemic starting in 1981, the Zika virus (ZIKV) epidemic of 2015-2016, and the ongoing SARS-CoV-2/COVID-19 pandemic are examples of the enormous global burden of viruses and the urgent need for vaccine and therapeutic development. Building on

the prior contributions of early pioneers such as Rosalind Franklin, structural biologists continue to advance techniques in X-ray crystallography and cryo-electron microscopy (cryo-EM) to investigate viruses and viral proteins. We are interested in investigating antibody (Ab) recognition of viruses, which we do by solving 3D structures of viral proteins bound to Abs elicited by infection or vaccination. Understanding the structural correlates of Ab recognition of viruses is key for the development of effective monoclonal Ab therapies and vaccines (**Figure 1**).

Human immunodeficiency virus 1 (HIV-1) is responsible for the AIDS pandemic and 36 million deaths to date [6] and has long posed a challenge for vaccine development due its remarkable ability to evade the host immune response and establish latent reservoirs. HIV-1 contains a single viral protein on its surface that facilitates infection of immune cells. This protein, named Envelope or Env, is a trimer of gp120/gp41 heterodimers (Figure 2A). The gp120 portion of Env interacts with host CD4 receptors, which stimulates conformational changes that allow binding to the co-receptor, usually a host chemokine receptor called CCR5 [7]. These events trigger rearrangements in gp41 that allow fusion of the viral and host cell membranes, which is required for entry of the HIV-1 genome into the host cell [7]. In addition to small molecule anti-retroviral drug treatments to treat infected individuals, current strategies to prevent HIV-1 infection include vaccine design. Vaccine efforts seek to stimulate the evolution of broadly neutralizing Abs (bNAbs) that have been isolated in rare cases of human HIV-1 infection and are capable of broad and potent protection [8–10]. Advances in X-ray crystallography and cryo-EM have given us the invaluable opportunity to structurally characterize bNAb interactions with Env and Env conformational changes which have informed vaccine design efforts.

SARS-CoV-2, the virus responsible for the COVID-19 pandemic, has caused 4.5 million deaths and an estimated 225 million infections as of September 2021 [11]. The spike (S) proteins on the surface of SARS-CoV-2 allow it to infect host cells by binding the host cellular angiotensin-converting enzyme 2 (ACE2) receptor [12,13]. Each of the three protomers on an S protein includes two subunits, S1 and S2. The receptor binding domain (RBD) on S1 is the component that recognizes ACE2 during cell entry (Figure 2B) [13–16].

While the RBD can adopt both ‘up’ and ‘down’ conformations, it can only bind ACE2 when it is an ‘up’ conformation [14–20]. Due to the critical role of the RBD in facilitating infection, neutralizing Abs that target the RBD are an important component of the immune response against SARS-CoV-2 [21–31]. Structural biology has been instrumental in the rapid characterization and evaluation of the S protein and Abs produced in natural infection [15,21,21–33]. This work has contributed to the development of COVID-19 vaccines and monoclonal Ab (mAb) therapeutics, which have saved countless lives.

ZIKV is a mosquito-borne virus that can cause microcephaly and neurodevelopmental abnormalities in the newborns of infected mothers [34–37]. As part of the *flavivirus* genus, ZIKV shares similar features as other widespread flaviviruses such as dengue (DENV), West Nile virus (WNV), and yellow fever virus (YFV) [38–41]. Mature ZIKV has seven non-structural proteins (NS1, NS2A, NS2B, NS3, NS4A, NS4B and NS5) and three structural proteins: envelope (E), membrane (M), and capsid (C) [42–44]. The surface of ZIKV is coated by 180 copies of the E protein arranged as 90 dimers, and each E protein includes three ectodomains, EDI, EDII, and EDIII (Figure 2C) [38,42,43]. The flexible regions between the domains allows dynamic conformational changes to occur during viral entry and fusion [38,45–48]. EDII contains a conserved fusion loop (FL) peptide that becomes exposed after viral entry into cells and initiates endosomal fusion [42,43,49,50]. EDIII is thought to be important for receptor binding during infection, and consequently, is an important target for neutralizing Abs [51–56]. There is not yet a safe and effective vaccine against ZIKV that is universally available.

Here we review how approaches in structural and molecular biology have increased our understanding of Ab recognition of HIV-1, SARS-CoV-2, and ZIKV. We discuss how the design of stable and soluble viral antigens amenable for structural approaches has enabled our ability to analyze complexes of viral antigens bound by the antigen binding fragment (Fab) of Abs. Use of both cryo-EM and X-ray crystallography has increased our understanding of key viral epitopes targeted by Abs and conformational changes of viral proteins necessary for infection. These structural insights, combined with analyses of the levels of somatic hypermutation found in potently neutralizing Abs, provide valuable

information for the development of effective vaccines and monoclonal Ab therapies to reduce global morbidity and mortality from epidemic/pandemic-causing viruses.

Main Body

Engineering viral surface proteins for structural studies

Structural biology techniques such as X-ray crystallography and single particle cryo-EM require samples that are stable enough to be isolated and manipulated in the laboratory. For some viruses, especially those that are symmetric, it is feasible to structurally characterize intact viruses using cryo-EM. For example, cryo-EM structures of intact, whole ZIKV have been solved with and without Fabs of Abs bound [42,43,57–62]. Viruses with pleomorphic structures (e.g., most enveloped viruses) can also be investigated structurally using cryo-electron tomography [63–65]. In order to prepare surface viral proteins of enveloped viruses for structural studies and therapeutic development, it has been necessary to produce soluble, native-like versions that are stabilized in a pre-fusion conformation that is targeted by neutralizing Abs.

Classically, the simplest way to solubilize a surface viral protein is to remove the transmembrane and cytoplasmic domains by truncation [66,67]. Truncation has also been used to produce smaller components such as single domains. Examples of truncated domains include gp120 cores of HIV-1 Env, which have the β4 and β26 strands and all flexible loops removed [68,69], coronavirus RBDs truncated at the base where the flexible hinge connects them to the rest of the S1 subunit [70,71], and the individual EDIII truncated from the rest of the ZIKV E protein [52–54,72,73]. Truncation of individual domains has been especially powerful for X-ray crystallography as crystallization is hindered by flexible regions such as loops or inter-domain linkers and hinges. Single domains are useful for solving high resolution structures of Fab-domain complexes that provide detail about the Ab interactions that may not be possible using single particle cryo-EM due to flexibility or heterogeneity of larger protein complex structures [32,52–54,72–74].

While truncated proteins have been useful in the field of structural biology, they do not necessarily reflect all aspects of the whole antigen and cannot always recapitulate the properties of a native viral protein. An extra layer of complexity exists since many viral proteins adopt distinct conformations depending on the step in the viral life cycle, requiring engineering and stabilization of the desired conformation for larger, multi-subunit complexes [43,46,47,57]. Fusion proteins such as Env and S include folded helical bundles that must extend for fusion of the viral and host cell membrane bilayers. These proteins are metastable in their pre-fusion conformation, which is usually the target of neutralizing Abs [75]. The introduction of stabilizing mutations can be helpful for preparing soluble constructs of larger, multi-subunit complexes. For example, helix-breaking proline mutations have been introduced into the central helices of fusion proteins, preventing the extension of helices required for membrane fusion [76]. In combination with an inter-subunit disulfide bond and truncation after residue 664, these mutations were introduced into HIV-1 Env to produce the pre-fusion stabilized SOSIP.664 trimers [77]. The proline helix-breaking stabilizing mutations have been successfully adapted to other viral fusion proteins including those on coronaviruses, RSV, Ebola virus, human metapneumovirus, and Lassa virus [75]. For SARS-CoV-2 S, additional prolines were introduced that further stabilize the trimer in the 6P, or 'HexaPro' version [67]. For studies of the ZIKV E protein soluble constructs of both monomeric E protein [56,78–80] and engineered disulfide-linked E protein dimers [55,81] have been designed.

Most regions of proteins have a purpose that is important to their function, particularly transmembrane regions and cytoplasmic tails [82]. Consequently, truncated and stabilized proteins used as substitutes for full-length equivalents are only useful to the extent that they are able to approximate the native state of the protein. It is essential for the engineered forms used for structural studies to be characterized with non-structural methods to confirm that they behave in a similar fashion to the native form in the context they are being studied.

Dominant Ab Epitopes on Viral Fusion Proteins

Structural analysis has facilitated identification of neutralizing epitopes on HIV-1, SARS-CoV-2 and ZIKV. Both X-ray crystallography and cryo-EM analyses of viral antigens in complex with neutralizing Ab Fabs have provided insights into mechanisms of neutralization by Abs and identified new therapeutic targets [7,32]. Neutralizing epitopes tend to be in structurally functional regions, and in many cases facilitate or hinder a structural change. In addition to neutralizing Abs, an immune response to a pathogen or vaccine can produce weakly neutralizing or non-neutralizing antibodies. which can be protective through various mechanisms such as antibody dependent cell cytotoxicity (ADCC) [83–86]. For viral fusion, there is typically a dramatic conformational change that occurs in the fusion protein to expose receptor binding sites for attachment and to insert the fusion machinery into the target membrane to undergo fusion [87]. Requiring a large conformational change is a strategy that allows viruses to hide vulnerable regions that are necessary for interactions important for viral function, such as target receptor binding. Many Abs bind in ways that can hinder or trigger fusion-necessitated conformational changes, resulting in various neutralization mechanisms [7].

HIV-1 Env Epitopes

HIV-1 Env is present on the surfaces of virions in a closed pre-fusion conformation that includes centrally located gp120 subunits and the V1/V2 and V3 variable loops interacting about the apex of the trimer, hiding the co-receptor binding site on V3 [88]. Upon binding to the host cell receptor CD4 at the CD4 binding site (CD4bs) in the gp120 subunit, the Env protein rearranges to an open state in which the gp120s are rotated outwards, the V1/V2 loop is displaced to the sides of the Env trimer, and the V3 loop is exposed, allowing access to the co-receptor binding site on V3 [89–93] (**Figure 3A**). In the CD4-bound open conformation, a 4-stranded antiparallel bridging sheet is formed by the gp120 β-strands β20, β21, β2, and β3, the gp120 subunits swing away from the central axis and rotate slightly counter-clockwise, and the gp41 HR1 helices become more ordered and extended [90–92]. In this conformation, the V3 loop is exposed and can then bind to the co-receptor, which is required for entry [93]. HIV-1 Env epitopes target some of these intermediate fusion conformations, in addition to the closed, pre-fusion structure.

The epitopes of bNAbs often include conserved functional regions that are conformationally masked in the closed, pre-fusion structure or sterically restricted by N-linked glycans [7]. In fact, in many cases, N-glycans that occlude the protein surface of Env actually become part of the Ab epitope. HIV-1 epitope targets of bNAbs can be divided into the following categories: (1) bNAbs that bind at the apex of the trimer, specifically to the V1/V2 loops that undergo a dramatic rearrangement during host receptor engagement [94–96], (2) bNAbs against the V3-glycan patch, which includes the highly conserved GDIR motif and several N-linked glycans on and around the V3 loop [97,98], (3) CD4bs bNAbs that target the host receptor binding domain [7,74,99], (4) bNAbs that only bind to Envs in a CD4-induced open state [68,89,91], (5) "silent face" bNAbs that target a glycan-rich patch on the opposite face from the CD4bs on gp120 [98,100,101], (6) bNAbs that target the gp120/gp41 interface, including those that interact with the fusion peptide [102,103], and (7) bNAbs that bind to the membrane proximal external region (MPER) on gp41 [104] (**Figure 4A**).

Each epitope presents a distinct landscape for bNAb binding and poses different challenges for Abs to overcome. For most epitopes, N-linked glycans on the heavily-glycosylated Env trimer sterically restrict access to conserved protein regions, and therefore bNAbs tend to include conserved N-linked glycans in the epitope and/or develop long complementary determining region (CDR) loops to penetrate through the glycan shield [7]. This is the case for V1/V2, V3, and silent face epitopes. For example, the V3-glycan patch epitope is defined by the V3 loop that is essential for co-receptor binding and several N-linked glycans. bNAbs that target this region, including 10-1074, PGT121, and BG18, have long, 20+ amino acid CDRH3 loops that reach through the glycan patch to bind a conserved V3 motif from gp120 residues 324-327 with the sequence GDIR [97]. These bNAbs also make important contacts with conserved glycans $Asn156_{gp120}$ and $Asn332_{gp120}$. In contrast, some bNAbs against the CD4bs require short CDR loops to accommodate an N-linked glycan in that region. CD4bs bNAb 3BNC117 has a 5-residue deletion in CDRL1 that is necessary to prevent steric clashes with the $Asn276_{gp120}$ glycan and a short, 5-amino acid CDRL3 that is essential to avoid clashes with gp120 [105]. The gp120-gp41 interface epitope is composed of protein and glycan residues in both subunits. This category includes bNAbs that target the fusion peptide

(FP), which are the highly conserved N terminal residues of gp41 responsible for burying into the host cell membrane during the fusion process of viral entry. FP bNAb VRC34.01 binds primarily to the N-terminal 8 residues of gp41 with the remainder of interactions made with $Asn88_{gp120}$ [102]. Together, these examples demonstrate the diverse epitope landscape of the HIV-1 Env trimer and how Abs develop particular features to overcome challenges posed by the dense glycan shield.

The mode of binding for bNAbs at all epitopes has been greatly illuminated by structural biology. In particular, X-ray crystallographic and cryo-EM structures of Ab:Env complexes have been essential tools to characterize which epitope newly isolated bNAbs bind, the mode of binding implemented, and to understand the context of atypical features in the sequence such as CDR lengths. The wealth of structural data has enabled structure-based design of gp120 and SOSIP-based immunogens that seek to elicit responses to particular epitopes and design small molecule drugs.

SARS-CoV-2 S Epitopes

The SARS-CoV-2 fusion machinery is the surface protein S, which is composed of three identical subunits each containing an RBD that sits at the apex of S and is attached to the rest of the subunits with a flexible hinge [14]. The RBDs are able to sample a 'down' conformation that hides the ACE2 binding site by packing it against a neighboring RBD, or an 'up' conformation, which exposes the ACE2 binding site at the tip of the RBD and is required for host receptor binding [15,32,106] (**Figure 3B**).

Abs that recognize the RBD of the SARS-CoV-2 S protein are a vital part of the neutralizing Ab response to infection and vaccination because the RBD contains the binding site for ACE2. Effective neutralization by many anti-RBD Abs is due to their ability to block the RBD from binding the host ACE2 receptor. The epitopes targeted by Abs against the RBD can be organized into four simplified classes [32]. Class 1, *VH3-53/VH3-63*-derived Abs, target epitopes overlapping with the ACE2 binding site and only bind 'up' conformation RBDs. Class 2 Abs target epitopes overlapping with the ACE2 binding site and can bind both

‘up’ and ‘down’ RBDs. Class 3 Abs target epitopes that do not overlap with the ACE2 binding site and bind both ‘up’ and ‘down’ RBDs. Finally, class 4 Abs target a cryptic surface facing the S trimer interior and only bind ‘up’ RBDs [32] (**Figure 4B**).

While the anti-SARS-CoV-2 Ab landscape has primarily focused on the RBD, a growing number of neutralizing Abs that target other regions of the S protein are being found. Neutralizing Abs that bind to the N terminal domain (NTD) [107–109] and the S2 domain [107,110–113] have been reported, indicating that the RBD is not the only site of neutralization. In addition, some of these Abs are also broadly cross-reactive to other betacoronaviruses as they target highly conserved regions of S such as the class 4 cryptic epitope on the RBD [24,114–116] or the stem helix of S2 [111–113].

ZIKV Epitopes

The E protein of ZIKV and other flaviviruses is key for facilitating cellular entry and fusion [48]. The mature structure of ZIKV displays smooth virus particles with 180 copies of the E protein arranged as 90 dimers with icosahedral symmetry, and EDIII is thought to be responsible for binding cellular receptors [43,48,117–120]. After cellular entry through receptor-mediated endocytosis, the acidic pH triggers a conformational change by which the E proteins form trimers and expose the FL on EDII for membrane fusion [121–123].

Given its role in fusion, the E protein is an important target of neutralizing Abs that effectively clear ZIKV, inhibit ZIKV infection in vitro, decrease vertical transmission, and are protective in ZIKV challenge in animal models [53–56,72,79,124,125] (**Figure 2C)**. Structural characterization of Abs that bind the ZIKV E protein have revealed multiple epitopes on the three domains: (1) the conserved FL found on EDII [56,126], (2) EDIII [52–54,72,73,127], (3) multiple domains of single E protein [79,80], (4) multiple domains spanning an E protein dimer [55,60,79,125,128,129], and (5) multiple domains spanning neighboring E dimer pairs [61,62,79,129]. Abs against the FL in EDII compose a large portion of the response to infection, and because the FL is conserved among flaviviruses, these Abs can cross-react with different flaviviruses [56,79,124–126,130]. However, many

potently-neutralizing Abs target EDIII and these Abs tend to be more specific for ZIKV than other flaviviruses [51–56,61,72,124,125,131–137] (**Figure 2C**).

Notably, some Ab epitopes characterized by crystallography are not accessible on the known cryo-EM structures of mature ZIKV [43,54,56,126] (**Figure 3C**). While cryo-EM structures show a static envelope, evidence suggests the E proteins are dynamic and sample different conformations. The phenomenon of flavivirus "breathing" may result from conformational changes of the E protein during the viral life cycle, such as during fusion. The flavivirus DENV serotype 2 (DENV2) structure showed E protein rearrangements when heated to 37°C, providing further evidence for flavivirus breathing [47,138] (**Figure 3C**). However, ZIKV maintains a smooth structure at 40°C and its breathing conformation has not yet been determined [42].

Somatic Hypermutation of Neutralizing Abs

Abs evolve to neutralize antigen targets through the process of affinity maturation. This process begins when germline-encoded B cell receptors interact with an antigen and receive signals from T cells. This activation stimulates iterative rounds of somatic hypermutation (SHM), whereby a cellular mechanism orchestrates single base pair mutations, insertions, and deletions (indels) primarily in the CDRs of Abs [139]. These mutations are random, although favorable mutations that enhance recognition of antigen are selected for in further rounds of SHM [139]. Affinity maturation can rapidly diversify the Ab repertoire, allowing for the recognition of innumerable antigens that can mutate to evade Ab recognition [140]. This arms race between distinct Abs and antigens has been monitored through structural biology, which can illuminate how SHM impacts the antigen:Ab interface. For different viral antigens, SHM plays different roles in overcoming infection.

In HIV-1 infection, SHM plays a major role in the creation of bNAbs. Human Abs that have undergone affinity maturation on average carry 15-20 nucleotide mutations in the variable heavy (V_H) gene; however, HIV-1 bNAbs include 40-100 V_H gene mutations [141]. High levels of bNAb SHM are necessary to combat a rapidly evolving antigen target in which Env

mutations are selected to evade bNAb recognition. In fact, these mutations have been deemed critical for recognition and neutralization of native viral envelopes, as unmutated germline precursors of bNAbs do not usually interact with viral Envs [142]. X-ray crystallography and cryo-EM have allowed for the characterization of bNAb SHM to understand how mutated residues interact with HIV-1 Env and confer broadly neutralizing activity and potency [7,143,144]. Structures of Env:bNAb complexes have identified individual SHMs that are critical for neutralization activity at different epitopes and have set forth criteria for predicting the capability of newly isolated bNAbs.

Furthermore, structural biology has given context to unusual bNAb characteristics brought on by SHM; namely, framework region (FWR) mutations and indels. The FWRs of an Ab variable domain are the relatively constant sequences that provide a scaffold for the more diverse CDR loops. SHMs in FWRs are often poorly tolerated as they impair the structural integrity of the Ab [145–147]. However, HIV-1 bNAbs FWR SHM has been found to be critical for breadth and potency [145]. Analysis of crystal structures of bNAbs bound to gp120s revealed that regions of FWR SHM can directly interact with the antigen to increase the binding affinity or contribute to the structural rigidity and flexibility of a Fab for optimal binding [99,145]. HIV-1 bNAbs also contain unusually high levels of SHM indels [76, 73]. Prior studies reporting sequences of Ab genes from memory B cells found between 1-3% of Ab genes contained indels [148]. For HIV-1 bNAbs, approximately 40% of bNAbs include indel mutations that range from 3-33 nucleotides in length [76, 73]. Analysis of crystal structures of bNAb:gp120 complexes found that these indels are preferentially found within 10Å of the Ab:antigen interface [149]. Indels are therefore important to optimize interactions with Env, specifically to penetrate the dense glycan shield. Thus, structural biology has aided in elucidating how unusual SHM features in HIV-1 bNAbs contribute to breadth and potency.

Unlike HIV-1 bNAbs, Abs against SARS-CoV-2 S and ZIKV E protein have much lower levels of SHM and, in fact, affinity maturation via SHM is not always required to interact with their viral antigen targets [23,54,150]. Longitudinal studies tracking Ab evolution after SARS-CoV-2 infection found 1.3 months post-infection averages of 4.2 V_H and 2.8 V_L

nucleotide mutations [151]. However, after 12 months past infection, SHM increased to approximately 15 V_H and 8 V_L nucleotide mutations [152]. Low levels of SHM have also been reported in longitudinal studies tracking ZIKV infection and comparisons of mature and germline versions of anti-ZIKV Abs [52,54,56,150, 153,154]. Inferred germline Abs have been shown to be able to bind and even weakly neutralize ZIKV [52,54,153,155]. Structural analysis of Ab:antigen complexes for SARS-CoV-2 and ZIKV suggests most SHMs are found in CDR loops and contribute to the complex interface to create optimal contacts for antigen recognition [25,32,52,54]. For both of these viruses, the relatively low levels of SHM indicate near-germline and germline Abs are readily capable of recognizing viral antigens and maturing into potently neutralizing Abs.

Structure-guided design of vaccines, small molecules inhibitors, and Ab therapeutics

Structural biology has played a pivotal role in characterizing the optimal human Ab response which vaccines and therapeutics can be designed to mimic (**Figure 1**). For many viruses, the ability to produce a cross reactive response either to many strains of the same virus or to different viruses in the same group is necessary for complete protection from disease, presenting a challenge for vaccine design [156]. Therefore, the structure-guided development of small molecules, peptides, and protein decoys as therapeutics is a complementary strategy for treating viral infection [157].

Structural biology has allowed for the advancement of structure-based vaccine design, which is considered to be one of the current avenues most likely to eventually lead to an HIV-1 vaccine after the failure of subunit vaccines [158]. bNAbs are only elicited by a small subset of the population infected with HIV-1; even so these ‘elite controllers’ still never clear the virus [159]. In fact, arguably the biggest hurdle in creating an HIV-1 vaccine is eliciting an immune response that is far better than what is observed in infected people. The vast number of HIV-1 strains means a vaccine must protect against initial infection of countless distinct viral species rather than a single, or only a few, strains. Due to the inherent difficulty of eliciting bNAbs against HIV-1, some current structure-based efforts for HIV-1 vaccine design rely on structurally characterizing bNAbs in an effort to reverse engineer an

immunogen that can elicit them, rather than the commonly-observed strain-specific, autologous neutralizing responses [158]. Structures of antigen:Ab complexes have allowed for the classification of Abs by their epitopes, which is necessary for the design of effective therapeutic monoclonal Ab cocktails [7]. In many cases, the dosing of single monoclonals is often suboptimal due to the ability of viruses to rapidly mutate. For example, in the case of HIV-1, the viral swarm inside a patient can evolve resistance mutations that make a therapy either less or not effective within days to weeks [160]. Therapeutics have also been designed to mimic an existing interaction by binding directly, such as CD4 mimetic drugs that bind into the CD4 pocket on gp120 [161,162]. As an alternative therapeutic approach, binding targets separate from canonical interaction sites can be used to inhibit function by preventing conformational changes, such as inhibitors directed at the HIV-1 Env fusion peptide [163].

In the case of SARS-CoV-2, which mutates at a lower frequency than HIV-1 but whose variants of concern are posing current problems, future efforts will need to focus on producing vaccines that are effective in the face of new variants [164,165]. Key regions of the S protein are highly conserved across the subgenus of sarbecovirus coronaviruses, of which at least three others can infect human cells: SARS-CoV, SHC014, and RaTG13 [166]. Neutralizing Abs that target the S of SARS-CoV-2 and also bind and neutralize other sarbecoviruses including SARS-CoV-2 variants of concern have been identified by several groups and have been structurally characterized [24,112–116,167,168], suggesting that an immunogen could be designed to produce a pan-sarbecovirus vaccine. Additionally, therapeutic mAb cocktails have successfully been developed for the treatment of SARS-CoV-2 [169]. Therapeutics have also been designed to mimic an existing interaction by binding directly, such as ACE2-S small protein decoys [170].

For ZIKV, design of a safe vaccine is complicated due to the similarities in structures between ZIKV and other flaviviruses. Since the structure of ZIKV is similar to that of DENV, WENV and YFV [38–41], there is concern that Abs elicited during infection with one flavivirus may cross-react with, but not neutralize, other flaviviruses during a later infection. This cross-reactive Ab recognition may worsen symptoms due to a phenomenon termed Ab-dependent enhancement (ADE), by which Ab-bound viruses can infect cells through

interactions of the Fc regions of the bound Abs with the host Fcγ receptor, resulting in infection of cells after endocytosis of the Ab-virus complex [38,130,154,171–178]. This is of particular concern for the mosquito-borne virus DENV, since it has been shown that prior DENV or ZIKV infection that results in low or intermediate Ab titers increases the risk of worsened disease severity from a subsequent DENV infection with a different serotype [38,179–187]. However, potent neutralizing Abs against ZIKV EDIII have been identified that appear to be more specific for ZIKV than other flaviviruses, suggesting ZIKV EDIII is a potential candidate for the design of a safe vaccine [51–56,61,72,124,125,131–136]. No vaccine is yet universally available for ZIKV, although both the full E protein and individual EDIII have been investigated as potential immunogens [78,135,188–194].

Conclusions

Structural biology has allowed for a deeper understanding of the immune responses to many viruses, including HIV-1, SARS-CoV-2, and ZIKV discussed here. Mutations have been engineered that stabilize surface proteins in their pre-fusion conformations for use as starting immunogens for structure-based vaccine design and as laboratory reagents that can be used to study other aspects of the elicited humoral immune response. Structures of Abs bound to these stabilized proteins have allowed for the elucidation of neutralizing epitopes on the viral surface proteins. Additionally, such structures have increased our understanding of the role of features that Abs develop in response to antigens, such as somatic hypermutation, insertions, and deletions. For targets where whole inactivated or subunit vaccines have failed, structures of viral antigens bound to elicited Abs have facilitated alternative routes for structure-based design of vaccines, small molecules therapeutics, and Ab cocktails. It is through structural biology, inspired by advancements by Rosalind Franklin, that we are able to make progress toward vaccines and Ab treatments for the viruses we study, including HIV-1, SARS-CoV-2, and ZIKV.

Methods

Biorender.com was used to produce portions of Figure 1 and Figure 2. All structure renderings were made using PyMOL ver. 2.5.0. or 1.7.6.4.

Figure 4 was produced in PyMOL by aligning the HIV-1 Env or SARS-CoV-2 S proteins of each Fab-bound structure with the structure of the viral protein depicted in the figure (Env PDB: 5T3Z, S PDB: 7K8V). Only V_HV_L domains are shown for each Ab.

Acknowledgements

Structural biology studies in our laboratory were supported by the National Institute of Allergy and Infectious Diseases (NIAID) Grant HIVRAD P01 AI100148, the Bill and Melinda Gates Foundation Collaboration for AIDS Vaccine Discovery (CAVD) grant INV-002143, a George Mason University Fast Grant GMU.SARSCOV2, an NSF GRFP (to M.E.A.), a NIH National Research Service Award Fellowship F30AI147579 (S.R.E.), NIH National Institute of General Medical Sciences Training Grant T32-GM008042 (to S.R.E.) through the University of California, Los Angeles–California Institute of Technology Medical Scientist Training Program, and the National Institutes of Health (NIH) Grant AI138938. We would also like to thank members of the Bjorkman laboratory for helpful discussions, the Caltech Merkin Institute for Translational Research for resources that enable our work, the Caltech Beckman Institute Resource Center for Transmission Electron Microscopy for support in cryo-EM projects, the Gordon and Betty Moore and Beckman Foundations for gifts to support the Molecular Observatory at Caltech that provides aid for protein crystallization, and the Stanford Synchrotron Radiation Lightsource (SSRL) that provides data collection capabilities for X-ray crystallography.

Finally, we are grateful for Rosalind Franklin's contributions to structural biology and for her brazen career as a female scientist that continues to embolden researchers, especially women.

Author Contributions

M.E.A., K.A.D., S.R.E., and C.A.J. wrote and edited this review article with critical reading and editing by P.J.B.

Conflicts of Interest

The authors declare no conflict of interest for this work.

References

1. Creager, A.N.H.; Morgan, G.J. After the Double Helix: Rosalind Franklin's Research on Tobacco Mosaic Virus. *Isis* **2008**, *99*, 239–272, doi:https://doi.org/10.1086/588626.
2. Franklin, R.E.; Klug, A. The Nature of the Helical Groove on the Tobacco Mosaic Virus Particle X-Ray Diffraction Studies. *Biochim. Biophys. Acta* **1956**, *19*, 403–416, doi:https://doi.org/10.1016/0006-3002(56)90463-2.
3. Franklin, R.E.; Holmes, K.C. The Helical Arrangement of the Protein Sub-Units in Tobacco Mosaic Virus. *Biochim. Biophys. Acta* **1956**, *21*, 405–406, doi:https://doi.org/10.1016/0006-3002(56)90043-9.
4. Franklin, R.E. X-Ray Diffraction Studies of Cucumber Virus 4 and Three Strains of Tobacco Mosaic Virus. *Biochim. Biophys. Acta* **1956**, *19*, 203–211, doi:10.1016/0006-3002(56)90421-8.
5. FRANKLIN, R.E. Structure of Tobacco Mosaic Virus: Location of the Ribonucleic Acid in the Tobacco Mosaic Virus Particle. *Nature* **1956**, *177*, 928–930, doi:10.1038/177928b0.
6. *Global HIV & AIDS Statistics Available Online: Https://Www.Unaids.Org/En/Resources/Fact-Sheet (Accessed on 13 September 2021).*;
7. West Jr, A.P.; Scharf, L.; Scheid, J.F.; Klein, F.; Bjorkman, P.J.; Nussenzweig, M.C. Structural Insights on the Role of Antibodies in HIV-1 Vaccine and Therapy. *Cell* **2014**, *156*, 633–648, doi:10.1016/j.cell.2014.01.052.
8. Gray, E.S.; Madiga, M.C.; Hermanus, T.; Moore, P.L.; Wibmer, C.K.; Tumba, N.L.; Werner, L.; Mlisana, K.; Sibeko, S.; Williamson, C.; et al. The Neutralization Breadth of HIV-1 Develops Incrementally over Four Years and Is Associated with CD4+ T Cell Decline and High Viral Load during Acute Infection. *J. Virol.* **2011**, *85*, 4828–4840, doi:10.1128/JVI.00198-11.
9. Sather, D.N.; Armann, J.; Ching, L.K.; Mavrantoni, A.; Sellhorn, G.; Caldwell, Z.; Yu, X.; Wood, B.; Self, S.; Kalams, S.; et al. Factors Associated with the Development of Cross-Reactive Neutralizing Antibodies during Human Immunodeficiency Virus Type 1 Infection. *J. Virol.* **2009**, *83*, 757–769, doi:10.1128/JVI.02036-08.
10. Doria-Rose, N.A.; Klein, R.M.; Manion, M.M.; O'Dell, S.; Phogat, A.; Chakrabarti, B.;

Hallahan, C.W.; Migueles, S.A.; Wrammert, J.; Ahmed, R.; et al. Frequency and Phenotype of Human Immunodeficiency Virus Envelope-Specific B Cells from Patients with Broadly Cross-Neutralizing Antibodies. *J. Virol.* **2009**, *83*, 188–199, doi:10.1128/JVI.01583-08.

11. COVID-19 Map Available online: https://coronavirus.jhu.edu/map.html (13 September 2021).
12. Hoffmann, M.; Kleine-Weber, H.; Schroeder, S.; Krüger, N.; Herrler, T.; Erichsen, S.; Schiergens, T.S.; Herrler, G.; Wu, N.-H.; Nitsche, A.; et al. SARS-CoV-2 Cell Entry Depends on ACE2 and TMPRSS2 and Is Blocked by a Clinically Proven Protease Inhibitor. *Cell* **2020**, *181*, 271-280.e8, doi:10.1016/j.cell.2020.02.052.
13. Lan, J.; Ge, J.; Yu, J.; Shan, S.; Zhou, H.; Fan, S.; Zhang, Q.; Shi, X.; Wang, Q.; Zhang, L.; et al. Structure of the SARS-CoV-2 Spike Receptor-Binding Domain Bound to the ACE2 Receptor. *Nature* **2020**, *581*, 215–220, doi:10.1038/s41586-020-2180-5.
14. Wrapp, D.; Wang, N.; Corbett, K.S.; Goldsmith, J.A.; Hsieh, C.-L.; Abiona, O.; Graham, B.S.; McLellan, J.S. Cryo-EM Structure of the 2019-NCoV Spike in the Prefusion Conformation. *Science* **2020**, *367*, 1260–1263, doi:10.1126/science.abb2507.
15. Walls, A.C.; Park, Y.-J.; Tortorici, M.A.; Wall, A.; McGuire, A.T.; Veesler, D. Structure, Function, and Antigenicity of the SARS-CoV-2 Spike Glycoprotein. *Cell* **2020**, *181*, 281-292.e6, doi:10.1016/j.cell.2020.02.058.
16. Kirchdoerfer, R.N.; Cottrell, C.A.; Wang, N.; Pallesen, J.; Yassine, H.M.; Turner, H.L.; Corbett, K.S.; Graham, B.S.; McLellan, J.S.; Ward, A.B. Pre-Fusion Structure of a Human Coronavirus Spike Protein. *Nature* **2016**, *531*, 118–121, doi:10.1038/nature17200.
17. Yuan, Y.; Cao, D.; Zhang, Y.; Ma, J.; Qi, J.; Wang, Q.; Lu, G.; Wu, Y.; Yan, J.; Shi, Y.; et al. Cryo-EM Structures of MERS-CoV and SARS-CoV Spike Glycoproteins Reveal the Dynamic Receptor Binding Domains. *Nat. Commun.* **2017**, *8*, 15092, doi:10.1038/ncomms15092.
18. Li, Z.; Tomlinson, A.C.; Wong, A.H.; Zhou, D.; Desforges, M.; Talbot, P.J.; Benlekbir, S.; Rubinstein, J.L.; Rini, J.M. The Human Coronavirus HCoV-229E S-Protein Structure and Receptor Binding. *eLife* **2019**, *8*, e51230, doi:10.7554/eLife.51230.
19. Walls, A.C.; Tortorici, M.A.; Bosch, B.-J.; Frenz, B.; Rottier, P.J.M.; DiMaio, F.; Rey,

F.A.; Veesler, D. Cryo-Electron Microscopy Structure of a Coronavirus Spike Glycoprotein Trimer. *Nature* **2016**, *531*, 114–117, doi:10.1038/nature16988.

20. Roy, S.; Jaiswar, A.; Sarkar, R. Dynamic Asymmetry Exposes 2019-NCoV Prefusion Spike. *J. Phys. Chem. Lett.* **2020**, *11*, 7021–7027, doi:10.1021/acs.jpclett.0c01431.
21. Brouwer, P.J.M.; Caniels, T.G.; Straten, K. van der; Snitselaar, J.L.; Aldon, Y.; Bangaru, S.; Torres, J.L.; Okba, N.M.A.; Claireaux, M.; Kerster, G.; et al. Potent Neutralizing Antibodies from COVID-19 Patients Define Multiple Targets of Vulnerability. *Science* **2020**, *369*, 643–650, doi:10.1126/science.abc5902.
22. Cao, Y.; Su, B.; Guo, X.; Sun, W.; Deng, Y.; Bao, L.; Zhu, Q.; Zhang, X.; Zheng, Y.; Geng, C.; et al. Potent Neutralizing Antibodies against SARS-CoV-2 Identified by High-Throughput Single-Cell Sequencing of Convalescent Patients' B Cells. *Cell* **2020**, *182*, 73-84.e16, doi:10.1016/j.cell.2020.05.025.
23. Kreer, C.; Zehner, M.; Weber, T.; Ercanoglu, M.S.; Gieselmann, L.; Rohde, C.; Halwe, S.; Korenkov, M.; Schommers, P.; Vanshylla, K.; et al. Longitudinal Isolation of Potent Near-Germline SARS-CoV-2-Neutralizing Antibodies from COVID-19 Patients. *Cell* **2020**, *182*, 843-854.e12, doi:10.1016/j.cell.2020.06.044.
24. Liu, H.; Wu, N.C.; Yuan, M.; Bangaru, S.; Torres, J.L.; Caniels, T.G.; van Schooten, J.; Zhu, X.; Lee, C.-C.D.; Brouwer, P.J.M.; et al. Cross-Neutralization of a SARS-CoV-2 Antibody to a Functionally Conserved Site Is Mediated by Avidity. *Immunity* **2020**, *53*, 1272-1280.e5, doi:10.1016/j.immuni.2020.10.023.
25. Robbiani, D.F.; Gaebler, C.; Muecksch, F.; Lorenzi, J.C.C.; Wang, Z.; Cho, A.; Agudelo, M.; Barnes, C.O.; Gazumyan, A.; Finkin, S.; et al. Convergent Antibody Responses to SARS-CoV-2 in Convalescent Individuals. *Nature* **2020**, *584*, 437–442, doi:10.1038/s41586-020-2456-9.
26. Rogers, T.F.; Zhao, F.; Huang, D.; Beutler, N.; Burns, A.; He, W.; Limbo, O.; Smith, C.; Song, G.; Woehl, J.; et al. Isolation of Potent SARS-CoV-2 Neutralizing Antibodies and Protection from Disease in a Small Animal Model. *Science* **2020**, *369*, 956–963, doi:10.1126/science.abc7520.
27. Seydoux, E.; Homad, L.J.; MacCamy, A.J.; Parks, K.R.; Hurlburt, N.K.; Jennewein, M.F.; Akins, N.R.; Stuart, A.B.; Wan, Y.-H.; Feng, J.; et al. Analysis of a SARS-CoV-2-Infected Individual Reveals Development of Potent Neutralizing Antibodies with

Limited Somatic Mutation. *Immunity* **2020**, *53*, 98-105.e5, doi:10.1016/j.immuni.2020.06.001.

28. Shi, R.; Shan, C.; Duan, X.; Chen, Z.; Liu, P.; Song, J.; Song, T.; Bi, X.; Han, C.; Wu, L.; et al. A Human Neutralizing Antibody Targets the Receptor-Binding Site of SARS-CoV-2. *Nature* **2020**, *584*, 120–124, doi:10.1038/s41586-020-2381-y.
29. Zost, S.J.; Gilchuk, P.; Case, J.B.; Binshtein, E.; Chen, R.E.; Nkolola, J.P.; Schäfer, A.; Reidy, J.X.; Trivette, A.; Nargi, R.S.; et al. Potently Neutralizing and Protective Human Antibodies against SARS-CoV-2. *Nature* **2020**, *584*, 443–449, doi:10.1038/s41586-020-2548-6.
30. Zost, S.J.; Gilchuk, P.; Chen, R.E.; Case, J.B.; Reidy, J.X.; Trivette, A.; Nargi, R.S.; Sutton, R.E.; Suryadevara, N.; Chen, E.C.; et al. Rapid Isolation and Profiling of a Diverse Panel of Human Monoclonal Antibodies Targeting the SARS-CoV-2 Spike Protein. *Nat. Med.* **2020**, *26*, 1422–1427, doi:10.1038/s41591-020-0998-x.
31. Pinto, D.; Park, Y.-J.; Beltramello, M.; Walls, A.C.; Tortorici, M.A.; Bianchi, S.; Jaconi, S.; Culap, K.; Zatta, F.; De Marco, A.; et al. Cross-Neutralization of SARS-CoV-2 by a Human Monoclonal SARS-CoV Antibody. *Nature* **2020**, *583*, 290–295, doi:10.1038/s41586-020-2349-y.
32. Barnes, C.O.; Jette, C.A.; Abernathy, M.E.; Dam, K.-M.A.; Esswein, S.R.; Gristick, H.B.; Malyutin, A.G.; Sharaf, N.G.; Huey-Tubman, K.E.; Lee, Y.E.; et al. SARS-CoV-2 Neutralizing Antibody Structures Inform Therapeutic Strategies. *Nature* **2020**, *588*, 682–687, doi:10.1038/s41586-020-2852-1.
33. Barnes, C.O.; West, A.P.; Huey-Tubman, K.E.; Hoffmann, M.A.G.; Sharaf, N.G.; Hoffman, P.R.; Koranda, N.; Gristick, H.B.; Gaebler, C.; Muecksch, F.; et al. Structures of Human Antibodies Bound to SARS-CoV-2 Spike Reveal Common Epitopes and Recurrent Features of Antibodies. *Cell* **2020**, *182*, 828-842.e16, doi:10.1016/j.cell.2020.06.025.
34. Suy, A.; Sulleiro, E.; Rodo, C.; Vazquez, E.; Bocanegra, C.; Molina, I.; Esperalba, J.; Sanchez-Seco, M.P.; Boix, H.; Pumarola, T.; et al. Prolonged Zika Virus Viremia during Pregnancy. *N Engl J Med* **2016**, *375*, 2611–2613, doi:10.1056/NEJMc1607580.
35. Brasil, P.; Pereira, J.P.; Moreira, M.E.; Ribeiro Nogueira, R.M.; Damasceno, L.; Wakimoto, M.; Rabello, R.S.; Valderramos, S.G.; Halai, U.A.; Salles, T.S.; et al. Zika

Virus Infection in Pregnant Women in Rio de Janeiro. *N Engl J Med* **2016**, *375*, 2321–2334, doi:10.1056/NEJMoa1602412.

36. Coyne, C.B.; Lazear, H.M. Zika Virus - Reigniting the TORCH. *Nat Rev Microbiol* **2016**, *14*, 707–715, doi:10.1038/nrmicro.2016.125.
37. Mlakar, J.; Korva, M.; Tul, N.; Popović, M.; Poljšak-Prijatelj, M.; Mraz, J.; Kolenc, M.; Resman Rus, K.; Vesnaver Vipotnik, T.; Fabjan Vodušek, V.; et al. Zika Virus Associated with Microcephaly Available online: https://www.nejm.org/doi/10.1056/NEJMoa1600651 (accessed on 18 June 2021).
38. Heinz, F.X.; Stiasny, K. The Antigenic Structure of Zika Virus and Its Relation to Other Flaviviruses: Implications for Infection and Immunoprophylaxis. *Microbiol Mol Biol Rev* **2017**, *81*, doi:10.1128/MMBR.00055-16.
39. Chang, H.-H.; Huber, R.G.; Bond, P.J.; Grad, Y.H.; Camerini, D.; Maurer-Stroh, S.; Lipsitch, M. Systematic Analysis of Protein Identity between Zika Virus and Other Arthropod-Borne Viruses. *Bull. World Health Organ.* **2017**, *95*, 517-525I, doi:10.2471/BLT.16.182105.
40. da Fonseca, N.J.; Lima Afonso, M.Q.; Pedersolli, N.G.; de Oliveira, L.C.; Andrade, D.S.; Bleicher, L. Sequence, Structure and Function Relationships in Flaviviruses as Assessed by Evolutive Aspects of Its Conserved Non-Structural Protein Domains. *Biochem. Biophys. Res. Commun.* **2017**, *492*, 565–571, doi:10.1016/j.bbrc.2017.01.041.
41. Ye, Q.; Liu, Z.-Y.; Han, J.-F.; Jiang, T.; Li, X.-F.; Qin, C.-F. Genomic Characterization and Phylogenetic Analysis of Zika Virus Circulating in the Americas. *Infect. Genet. Evol.* **2016**, *43*, 43–49, doi:10.1016/j.meegid.2016.05.004.
42. Kostyuchenko, V.A.; Lim, E.X.; Zhang, S.; Fibriansah, G.; Ng, T.S.; Ooi, J.S.; Shi, J.; Lok, S.M. Structure of the Thermally Stable Zika Virus. *Nature* **2016**, *533*, 425–8, doi:10.1038/nature17994.
43. Sirohi, D.; Chen, Z.; Sun, L.; Klose, T.; Pierson, T.C.; Rossmann, M.G.; Kuhn, R.J. The 3.8 A Resolution Cryo-EM Structure of Zika Virus. *Science* **2016**, *352*, 467–70, doi:10.1126/science.aaf5316.
44. Pierson, T.C.; Diamond, M.S. The Emergence of Zika Virus and Its New Clinical Syndromes. *Nature* **2018**, *560*, 573–581, doi:10.1038/s41586-018-0446-y.
45. Kuhn, R.J.; Dowd, K.A.; Beth Post, C.; Pierson, T.C. Shake, Rattle, and Roll: Impact of

the Dynamics of Flavivirus Particles on Their Interactions with the Host. *Virology* **2015**, *479–480*, 508–17, doi:10.1016/j.virol.2015.03.025.

46. Dowd, K.A.; DeMaso, C.R.; Pierson, T.C. Genotypic Differences in Dengue Virus Neutralization Are Explained by a Single Amino Acid Mutation That Modulates Virus Breathing. *MBio* **2015**, *6*, e01559-15, doi:10.1128/mBio.01559-15.
47. Fibriansah, G.; Ng, T.-S.; Kostyuchenko, V.A.; Lee, J.; Lee, S.; Wang, J.; Lok, S.-M. Structural Changes in Dengue Virus When Exposed to a Temperature of 37°C. *J. Virol.* **2013**, *87*, 7585–7592, doi:10.1128/JVI.00757-13.
48. Mukhopadhyay, S.; Kuhn, R.J.; Rossmann, M.G. A Structural Perspective of the Flavivirus Life Cycle. *Nat. Rev. Microbiol.* **2005**, *3*, 13–22, doi:10.1038/nrmicro1067.
49. Yu, I.M.; Zhang, W.; Holdaway, H.A.; Li, L.; Kostyuchenko, V.A.; Chipman, P.R.; Kuhn, R.J.; Rossmann, M.G.; Chen, J. Structure of the Immature Dengue Virus at Low PH Primes Proteolytic Maturation. *Science* **2008**, *319*, 1834–7, doi:10.1126/science.1153264.
50. Kuhn, R.J.; Zhang, W.; Rossmann, M.G.; Pletnev, S.V.; Corver, J.; Lenches, E.; Jones, C.T.; Mukhopadhyay, S.; Chipman, P.R.; Strauss, E.G.; et al. Structure of Dengue Virus: Implications for Flavivirus Organization, Maturation, and Fusion. *Cell* **2002**, *108*, 717–725, doi:10.1016/S0092-8674(02)00660-8.
51. Pierson, T.C.; Fremont, D.H.; Kuhn, R.J.; Diamond, M.S. Structural Insights into the Mechanisms of Antibody-Mediated Neutralization of Flavivirus Infection: Implications for Vaccine Development. *Cell Host Microbe* **2008**, *4*, 229–38, doi:10.1016/j.chom.2008.08.004.
52. Esswein, S.R.; Gristick, H.B.; Jurado, A.; Peace, A.; Keeffe, J.R.; Lee, Y.E.; Voll, A.V.; Saeed, M.; Nussenzweig, M.C.; Rice, C.M.; et al. Structural Basis for Zika Envelope Domain III Recognition by a Germline Version of a Recurrent Neutralizing Antibody. *Proc. Natl. Acad. Sci.* **2020**, doi:10.1073/pnas.1919269117.
53. Keeffe, J.R.; Van Rompay, K.K.A.; Olsen, P.C.; Wang, Q.; Gazumyan, A.; Azzopardi, S.A.; Schaefer-Babajew, D.; Lee, Y.E.; Stuart, J.B.; Singapuri, A.; et al. A Combination of Two Human Monoclonal Antibodies Prevents Zika Virus Escape Mutations in Non-Human Primates. *Cell Rep.* **2018**, *25*, 1385-1394.e7, doi:10.1016/j.celrep.2018.10.031.
54. Robbiani, D.F.; Bozzacco, L.; Keeffe, J.R.; Khouri, R.; Olsen, P.C.; Gazumyan, A.;

Schaefer-Babajew, D.; Avila-Rios, S.; Nogueira, L.; Patel, R.; et al. Recurrent Potent Human Neutralizing Antibodies to Zika Virus in Brazil and Mexico. *Cell* **2017**, *169*, 597-609.e11, doi:10.1016/j.cell.2017.04.024.

55. Barba-Spaeth, G.; Dejnirattisai, W.; Rouvinski, A.; Vaney, M.C.; Medits, I.; Sharma, A.; Simon-Loriere, E.; Sakuntabhai, A.; Cao-Lormeau, V.M.; Haouz, A.; et al. Structural Basis of Potent Zika-Dengue Virus Antibody Cross-Neutralization. *Nature* **2016**, *536*, 48–53, doi:10.1038/nature18938.
56. Dai, L.; Song, J.; Lu, X.; Deng, Y.Q.; Musyoki, A.M.; Cheng, H.; Zhang, Y.; Yuan, Y.; Song, H.; Haywood, J.; et al. Structures of the Zika Virus Envelope Protein and Its Complex with a Flavivirus Broadly Protective Antibody. *Cell Host Microbe* **2016**, *19*, 696–704, doi:10.1016/j.chom.2016.04.013.
57. Prasad, V.M.; Miller, A.S.; Klose, T.; Sirohi, D.; Buda, G.; Jiang, W.; Kuhn, R.J.; Rossmann, M.G. Structure of the Immature Zika Virus at 9 A Resolution. *Nat Struct Mol Biol* **2017**, *24*, 184–186, doi:10.1038/nsmb.3352.
58. Sevvana, M.; Long, F.; Miller, A.S.; Klose, T.; Buda, G.; Sun, L.; Kuhn, R.J.; Rossmann, M.G. Refinement and Analysis of the Mature Zika Virus Cryo-EM Structure at 3.1 Å Resolution. *Structure* **2018**, *26*, 1169-1177.e3, doi:10.1016/j.str.2018.05.006.
59. Morrone, S.R.; Chew, V.S.Y.; Lim, X.-N.; Ng, T.-S.; Kostyuchenko, V.A.; Zhang, S.; Wirawan, M.; Chew, P.-L.; Lee, J.; Tan, J.L.; et al. High Flavivirus Structural Plasticity Demonstrated by a Non-Spherical Morphological Variant. *Nat. Commun.* **2020**, *11*, 3112, doi:10.1038/s41467-020-16925-y.
60. Tyagi, A.; Ahmed, T.; Shi, J.; Bhushan, S. A Complex between the Zika Virion and the Fab of a Broadly Cross-Reactive Neutralizing Monoclonal Antibody Revealed by Cryo-EM and Single Particle Analysis at 4.1 Å Resolution. *J. Struct. Biol. X* **2020**, 100028, doi:10.1016/j.yjsbx.2020.100028.
61. Zhang, S.; Loy, T.; Ng, T.-S.; Lim, X.-N.; Chew, S.-Y.V.; Tan, T.Y.; Xu, M.; Kostyuchenko, V.A.; Tukijan, F.; Shi, J.; et al. A Human Antibody Neutralizes Different Flaviviruses by Using Different Mechanisms. *Cell Rep.* **2020**, *31*, 107584, doi:10.1016/j.celrep.2020.107584.
62. Long, F.; Doyle, M.; Fernandez, E.; Miller, A.S.; Klose, T.; Sevvana, M.; Bryan, A.; Davidson, E.; Doranz, B.J.; Kuhn, R.J.; et al. Structural Basis of a Potent Human

Monoclonal Antibody against Zika Virus Targeting a Quaternary Epitope. *Proc. Natl. Acad. Sci.* **2019**, *116*, 1591–1596, doi:10.1073/pnas.1815432116.

63. Jiang, W.; Tang, L. Atomic Cryo-EM Structures of Viruses. *Curr. Opin. Struct. Biol.* **2017**, *46*, 122–129, doi:10.1016/j.sbi.2017.07.002.
64. Luque, D.; Castón, J.R. Cryo-Electron Microscopy for the Study of Virus Assembly. *Nat. Chem. Biol.* **2020**, *16*, 231–239, doi:10.1038/s41589-020-0477-1.
65. Grünewald, K.; Cyrklaff, M. Structure of Complex Viruses and Virus-Infected Cells by Electron Cryo Tomography. *Curr. Opin. Microbiol.* **2006**, *9*, 437–442, doi:10.1016/j.mib.2006.06.016.
66. Klasse, P.J.; Depetris, R.S.; Pejchal, R.; Julien, J.-P.; Khayat, R.; Lee, J.H.; Marozsan, A.J.; Cupo, A.; Cocco, N.; Korzun, J.; et al. Influences on Trimerization and Aggregation of Soluble, Cleaved HIV-1 SOSIP Envelope Glycoprotein. *J. Virol.* **2013**, *87*, 9873–9885, doi:10.1128/JVI.01226-13.
67. Hsieh, C.-L.; Goldsmith, J.A.; Schaub, J.M.; DiVenere, A.M.; Kuo, H.-C.; Javanmardi, K.; Le, K.C.; Wrapp, D.; Lee, A.G.; Liu, Y.; et al. Structure-Based Design of Prefusion-Stabilized SARS-CoV-2 Spikes. *Science* **2020**, *369*, 1501–1505, doi:10.1126/science.abd0826.
68. Kwong, P.D.; Wyatt, R.; Robinson, J.; Sweet, R.W.; Sodroski, J.; Hendrickson, W.A. Structure of an HIV Gp120 Envelope Glycoprotein in Complex with the CD4 Receptor and a Neutralizing Human Antibody. *Nature* **1998**, *393*, 648–659, doi:10.1038/31405.
69. Diskin, R.; Marcovecchio, P.M.; Bjorkman, P.J. Structure of a Clade C HIV-1 Gp120 Bound to CD4 and CD4-Induced Antibody Reveals Anti-CD4 Polyreactivity. *Nat. Publ. Group* **2010**, *17*, 608–613, doi:10.1038/nsmb.1796.
70. Li, F. Structure of SARS Coronavirus Spike Receptor-Binding Domain Complexed with Receptor. *Science* **2005**, *309*, 1864–1868, doi:10.1126/science.1116480.
71. Du, L.; Kou, Z.; Ma, C.; Tao, X.; Wang, L.; Zhao, G.; Chen, Y.; Yu, F.; Tseng, C.-T.K.; Zhou, Y.; et al. A Truncated Receptor-Binding Domain of MERS-CoV Spike Protein Potently Inhibits MERS-CoV Infection and Induces Strong Neutralizing Antibody Responses: Implication for Developing Therapeutics and Vaccines. *PLoS ONE* **2013**, *8*, e81587, doi:10.1371/journal.pone.0081587.
72. Zhao, H.; Fernandez, E.; Dowd, K.A.; Speer, S.D.; Platt, D.J.; Gorman, M.J.; Govero,

J.; Nelson, C.A.; Pierson, T.C.; Diamond, M.S.; et al. Structural Basis of Zika Virus-Specific Antibody Protection. *Cell* **2016**, *166*, 1016–27, doi:10.1016/j.cell.2016.07.020.

73. Zhao, H.; Xu, L.; Bombardi, R.; Nargi, R.; Deng, Z.; Errico, J.M.; Nelson, C.A.; Dowd, K.A.; Pierson, T.C.; Crowe, J.E.; et al. Mechanism of Differential Zika and Dengue Virus Neutralization by a Public Antibody Lineage Targeting the DIII Lateral Ridge. *J. Exp. Med.* **2020**, *217*, doi:10.1084/jem.20191792.
74. Zhou, T.; Zhu, J.; Wu, X.; Moquin, S.; Zhang, B.; Acharya, P.; Georgiev, I.S.; Altae-Tran, H.R.; Chuang, G.-Y.; Joyce, M.G.; et al. Multidonor Analysis Reveals Structural Elements, Genetic Determinants, and Maturation Pathway for HIV-1 Neutralization by VRC01-Class Antibodies. *Immunity* **2013**, *39*, 245–258, doi:10.1016/j.immuni.2013.04.012.
75. Sanders, R.W.; Moore, J.P. Virus Vaccines: Proteins Prefer Prolines. *Cell Host Microbe* **2021**, *29*, 327–333, doi:10.1016/j.chom.2021.02.002.
76. Qiao, H.; Pelletier, S.L.; Hoffman, L.; Hacker, J.; Armstrong, R.T.; White, J.M. Specific Single or Double Proline Substitutions in the "Spring-Loaded" Coiled-Coil Region of the Influenza Hemagglutinin Impair or Abolish Membrane Fusion Activity. *J. Cell Biol.* **1998**, *141*, 1335–1347, doi:10.1083/jcb.141.6.1335.
77. Sanders, R.W.; Vesanen, M.; Schuelke, N.; Master, A.; Schiffner, L.; Kalyanaraman, R.; Paluch, M.; Berkhout, B.; Maddon, P.J.; Olson, W.C.; et al. Stabilization of the Soluble, Cleaved, Trimeric Form of the Envelope Glycoprotein Complex of Human Immunodeficiency Virus Type 1. *J VIROL* **2002**, *76*, 15.
78. Qu, P.; Zhang, W.; Li, D.; Zhang, C.; Liu, Q.; Zhang, X.; Wang, X.; Dai, W.; Xu, Y.; Leng, Q.; et al. Insect Cell-Produced Recombinant Protein Subunit Vaccines Protect against Zika Virus Infection. *Antiviral Res.* **2018**, *154*, 97–103, doi:10.1016/j.antiviral.2018.04.010.
79. Wang, Q.; Yang, H.; Liu, X.; Dai, L.; Ma, T.; Qi, J.; Wong, G.; Peng, R.; Liu, S.; Li, J.; et al. Molecular Determinants of Human Neutralizing Antibodies Isolated from a Patient Infected with Zika Virus. *Sci Transl Med* **2016**, *8*, 369ra179, doi:10.1126/scitranslmed.aai8336.
80. Dussupt, V.; Sankhala, R.S.; Gromowski, G.D.; Donofrio, G.; De La Barrera, R.A.; Larocca, R.A.; Zaky, W.; Mendez-Rivera, L.; Choe, M.; Davidson, E.; et al. Potent Zika

and Dengue Cross-Neutralizing Antibodies Induced by Zika Vaccination in a Dengue-Experienced Donor. *Nat. Med.* **2020**, *26*, 228–235, doi:10.1038/s41591-019-0746-2.

81. Slon Campos, J.L.; Marchese, S.; Rana, J.; Mossenta, M.; Poggianella, M.; Bestagno, M.; Burrone, O.R. Temperature-Dependent Folding Allows Stable Dimerization of Secretory and Virus-Associated E Proteins of Dengue and Zika Viruses in Mammalian Cells. *Sci. Rep.* **2017**, *7*, 966, doi:10.1038/s41598-017-01097-5.
82. Harrison, S.C. Viral Membrane Fusion. *Virology* **2015**, *479–480*, 498–507, doi:10.1016/j.virol.2015.03.043.
83. Ackerman, M.E.; Mikhailova, A.; Brown, E.P.; Dowell, K.G.; Walker, B.D.; Bailey-Kellogg, C.; Suscovich, T.J.; Alter, G. Polyfunctional HIV-Specific Antibody Responses Are Associated with Spontaneous HIV Control. *PLOS Pathog.* **2016**, *12*, e1005315, doi:10.1371/journal.ppat.1005315.
84. Gunn, B.M.; Yu, W.-H.; Karim, M.M.; Brannan, J.M.; Herbert, A.S.; Wec, A.Z.; Halfmann, P.J.; Fusco, M.L.; Schendel, S.L.; Gangavarapu, K.; et al. A Role for Fc Function in Therapeutic Monoclonal Antibody-Mediated Protection against Ebola Virus. *Cell Host Microbe* **2018**, *24*, 221-233.e5, doi:10.1016/j.chom.2018.07.009.
85. Lu, L.L.; Suscovich, T.J.; Fortune, S.M.; Alter, G. Beyond Binding: Antibody Effector Functions in Infectious Diseases. *Nat. Rev. Immunol.* **2018**, *18*, 46–61, doi:10.1038/nri.2017.106.
86. Saphire, E.O.; Schendel, S.L.; Gunn, B.M.; Milligan, J.C.; Alter, G. Antibody-Mediated Protection against Ebola Virus. *Nat. Immunol.* **2018**, *19*, 1169–1178, doi:10.1038/s41590-018-0233-9.
87. White, J.M.; Delos, S.E.; Brecher, M.; Schornberg, K. Structures and Mechanisms of Viral Membrane Fusion Proteins: Multiple Variations on a Common Theme. *Crit. Rev. Biochem. Mol. Biol.* **2008**, *43*, 189–219, doi:10.1080/10409230802058320.
88. Ward, A.B.; Wilson, I.A. The HIV-1 Envelope Glycoprotein Structure: Nailing down a Moving Target. *Immunol. Rev.* **2017**, *275*, 21–32, doi:10.1111/imr.12507.
89. Ozorowski, G.; Pallesen, J.; de Val, N.; Lyumkis, D.; Cottrell, C.A.; Torres, J.L.; Copps, J.; Stanfield, R.L.; Cupo, A.; Pugach, P.; et al. Open and Closed Structures Reveal Allostery and Pliability in the HIV-1 Envelope Spike. *Nature* **2017**, *547*, 360–363, doi:10.1038/nature23010.

90. Wang, H.; Barnes, C.O.; Yang, Z.; Nussenzweig, M.C.; Bjorkman, P.J. Partially Open HIV-1 Envelope Structures Exhibit Conformational Changes Relevant for Coreceptor Binding and Fusion. *Cell Host Microbe* **2018**, *24*, 579-592.e4, doi:10.1016/j.chom.2018.09.003.
91. Yang, Z.; Wang, H.; Liu, A.Z.; Gristick, H.B.; Bjorkman, P.J. Asymmetric Opening of HIV-1 Env Bound to CD4 and a Coreceptor-Mimicking Antibody. *Nat. Struct. Mol. Biol.* **2019**, *26*, 1167–1175, doi:10.1038/s41594-019-0344-5.
92. Wang, H.; Cohen, A.A.; Galimidi, R.P.; Gristick, H.B.; Jensen, G.J.; Bjorkman, P.J. Cryo-EM Structure of a CD4-Bound Open HIV-1 Envelope Trimer Reveals Structural Rearrangements of the Gp120 V1V2 Loop. *Proc. Natl. Acad. Sci. U. S. A.* **2016**, *113*, E7151–E7158, doi:10.1073/pnas.1615939113.
93. Alkhatib, G. The Biology of CCR5 and CXCR4: *Curr. Opin. HIV AIDS* **2009**, *4*, 96–103, doi:10.1097/COH.0b013e328324bbec.
94. Lee, J.H.; Andrabi, R.; Su, C.-Y.; Yasmeen, A.; Julien, J.-P.; Kong, L.; Wu, N.C.; McBride, R.; Sok, D.; Pauthner, M.; et al. A Broadly Neutralizing Antibody Targets the Dynamic HIV Envelope Trimer Apex via a Long, Rigidified, and Anionic β-Hairpin Structure. *Immunity* **2017**, *46*, 690–702, doi:10.1016/j.immuni.2017.03.017.
95. Gorman, J.; Soto, C.; Yang, M.M.; Davenport, T.M.; Guttman, M.; Bailer, R.T.; Chambers, M.; Chuang, G.-Y.; DeKosky, B.J.; Doria-Rose, N.A.; et al. Structures of HIV-1 Env V1V2 with Broadly Neutralizing Antibodies Reveal Commonalities That Enable Vaccine Design. *Nat. Struct. Mol. Biol.* **2016**, *23*, 81–90, doi:10.1038/nsmb.3144.
96. Walker, L.M.; Phogat, S.K.; Chan-Hui, P.-Y.; Wagner, D.; Phung, P.; Goss, J.L.; Wrin, T.; Simek, M.D.; Fling, S.; Mitcham, J.L.; et al. Broad and Potent Neutralizing Antibodies from an African Donor Reveal a New HIV-1 Vaccine Target. *Science* **2009**, *326*, 285–289, doi:10.1126/science.1178746.
97. Fera, D.; Lee, M.S.; Wiehe, K.; Meyerhoff, R.R.; Piai, A.; Bonsignori, M.; Aussedat, B.; Walkowicz, W.E.; Ton, T.; Zhou, J.O.; et al. HIV Envelope V3 Region Mimic Embodies Key Features of a Broadly Neutralizing Antibody Lineage Epitope. *Nat. Commun.* **2018**, *9*, 1111, doi:10.1038/s41467-018-03565-6.
98. Barnes, C.O.; Gristick, H.B.; Freund, N.T.; Escolano, A.; Lyubimov, A.Y.; Hartweger,

H.; West, A.P.; Cohen, A.E.; Nussenzweig, M.C.; Bjorkman, P.J. Structural Characterization of a Highly-Potent V3-Glycan Broadly Neutralizing Antibody Bound to Natively-Glycosylated HIV-1 Envelope. *Nat. Commun.* **2018**, *9*, 1251, doi:10.1038/s41467-018-03632-y.

99. Scheid, J.F.; Mouquet, H.; Ueberheide, B.; Diskin, R.; Klein, F.; Oliveira, T.Y.K.; Pietzsch, J.; Fenyo, D.; Abadir, A.; Velinzon, K.; et al. Sequence and Structural Convergence of Broad and Potent HIV Antibodies That Mimic CD4 Binding. *Science* **2011**, *333*, 1633–1637, doi:10.1126/science.1207227.
100. Schoofs, T.; Barnes, C.O.; Suh-Toma, N.; Golijanin, J.; Schommers, P.; Gruell, H.; West, A.P.; Bach, F.; Lee, Y.E.; Nogueira, L.; et al. Broad and Potent Neutralizing Antibodies Recognize the Silent Face of the HIV Envelope. *Immunity* **2019**, *50*, 1513-1529.e9, doi:10.1016/j.immuni.2019.04.014.
101. Zhou, T.; Zheng, A.; Baxa, U.; Chuang, G.-Y.; Georgiev, I.S.; Kong, R.; O'Dell, S.; Shahzad-ul-Hussan, S.; Shen, C.-H.; Tsybovsky, Y.; et al. A Neutralizing Antibody Recognizing Primarily N-Linked Glycan Targets the Silent Face of the HIV Envelope. *Immunity* **2018**, *48*, 500-513.e6, doi:10.1016/j.immuni.2018.02.013.
102. Xu, K.; Acharya, P.; Kong, R.; Cheng, C.; Chuang, G.-Y.; Liu, K.; Louder, M.K.; O'Dell, S.; Rawi, R.; Sastry, M.; et al. Epitope-Based Vaccine Design Yields Fusion Peptide-Directed Antibodies That Neutralize Diverse Strains of HIV-1. *Nat. Med.* **2018**, *24*, 857–867, doi:10.1038/s41591-018-0042-6.
103. Scharf, L.; Wang, H.; Gao, H.; Chen, S.; McDowall, A.W.; Bjorkman, P.J. Broadly Neutralizing Antibody 8ANC195 Recognizes Closed and Open States of HIV-1 Env. *Cell* **2018**, 1–13, doi:10.1016/j.cell.2015.08.035.
104. Caillat, C.; Guilligay, D.; Sulbaran, G.; Weissenhorn, W. Neutralizing Antibodies Targeting HIV-1 Gp41. *Viruses* **2020**, *12*, 1210, doi:10.3390/v12111210.
105. West Jr, A.P. Structural Basis for Germ-Line Gene Usage of a Potent Class of Antibodies Targeting the CD4-Binding Site of HIV-1 Gp120. **2012**, 1–8, doi:10.1073/pnas.1208984109/-/DCSupplemental.
106. Zhou, P.; Yang, X.-L.; Wang, X.-G.; Hu, B.; Zhang, L.; Zhang, W.; Si, H.-R.; Zhu, Y.; Li, B.; Huang, C.-L.; et al. A Pneumonia Outbreak Associated with a New Coronavirus of Probable Bat Origin. *Nature* **2020**, *579*, 270–273, doi:10.1038/s41586-020-2012-7.

107. Shiakolas, A.R.; Kramer, K.J.; Wrapp, D.; Richardson, S.I.; Schäfer, A.; Wall, S.; Wang, N.; Janowska, K.; Pilewski, K.A.; Venkat, R.; et al. Cross-Reactive Coronavirus Antibodies with Diverse Epitope Specificities and Fc Effector Functions. *Cell Rep. Med.* **2021**, *2*, 100313, doi:10.1016/j.xcrm.2021.100313.

108. Chi, X.; Yan, R.; Zhang, J.; Zhang, G.; Zhang, Y.; Hao, M.; Zhang, Z.; Fan, P.; Dong, Y.; Yang, Y.; et al. A Neutralizing Human Antibody Binds to the N-Terminal Domain of the Spike Protein of SARS-CoV-2. *Science* **2020**, *369*, 650–655, doi:10.1126/science.abc6952.

109. McCallum, M.; De Marco, A.; Lempp, F.A.; Tortorici, M.A.; Pinto, D.; Walls, A.C.; Beltramello, M.; Chen, A.; Liu, Z.; Zatta, F.; et al. N-Terminal Domain Antigenic Mapping Reveals a Site of Vulnerability for SARS-CoV-2. *Cell* **2021**, *184*, 2332-2347.e16, doi:10.1016/j.cell.2021.03.028.

110. Song, G.; He, W.; Callaghan, S.; Anzanello, F.; Huang, D.; Ricketts, J.; Torres, J.L.; Beutler, N.; Peng, L.; Vargas, S.; et al. Cross-Reactive Serum and Memory B-Cell Responses to Spike Protein in SARS-CoV-2 and Endemic Coronavirus Infection. *Nat. Commun.* **2021**, *12*, 2938, doi:10.1038/s41467-021-23074-3.

111. Wang, C.; van Haperen, R.; Gutiérrez-Álvarez, J.; Li, W.; Okba, N.M.A.; Albulescu, I.; Widjaja, I.; van Dieren, B.; Fernandez-Delgado, R.; Sola, I.; et al. A Conserved Immunogenic and Vulnerable Site on the Coronavirus Spike Protein Delineated by Cross-Reactive Monoclonal Antibodies. *Nat. Commun.* **2021**, *12*, 1715, doi:10.1038/s41467-021-21968-w.

112. Pinto, D.; Sauer, M.M.; Czudnochowski, N.; Low, J.S.; Tortorici, M.A.; Housley, M.P.; Noack, J.; Walls, A.C.; Bowen, J.E.; Guarino, B.; et al. Broad Betacoronavirus Neutralization by a Stem Helix-Specific Human Antibody. *Science* **2021**, eabj3321, doi:10.1126/science.abj3321.

113. Sauer, M.M.; Tortorici, M.A.; Park, Y.-J.; Walls, A.C.; Homad, L.; Acton, O.J.; Bowen, J.E.; Wang, C.; Xiong, X.; de van der Schueren, W.; et al. Structural Basis for Broad Coronavirus Neutralization. *Nat. Struct. Mol. Biol.* **2021**, *28*, 478–486, doi:10.1038/s41594-021-00596-4.

114. Lv, Z.; Deng, Y.-Q.; Ye, Q.; Cao, L.; Sun, C.-Y.; Fan, C.; Huang, W.; Sun, S.; Sun, Y.; Zhu, L.; et al. Structural Basis for Neutralization of SARS-CoV-2 and SARS-CoV by a

Potent Therapeutic Antibody. *Science* **2020**, *369*, 1505–1509, doi:10.1126/science.abc5881.

115. Starr, T.N.; Czudnochowski, N.; Liu, Z.; Zatta, F.; Park, Y.-J.; Addetia, A.; Pinto, D.; Beltramello, M.; Hernandez, P.; Greaney, A.J.; et al. SARS-CoV-2 RBD Antibodies That Maximize Breadth and Resistance to Escape. *Nature* **2021**, *597*, 97–102, doi:10.1038/s41586-021-03807-6.
116. Tortorici, M.A.; Czudnochowski, N.; Starr, T.N.; Marzi, R.; Walls, A.C.; Zatta, F.; Bowen, J.E.; Jaconi, S.; Di Iulio, J.; Wang, Z.; et al. Broad Sarbecovirus Neutralization by a Human Monoclonal Antibody. *Nature* **2021**, *597*, 103–108, doi:10.1038/s41586-021-03817-4.
117. Lee, E.; Lobigs, M. Substitutions at the Putative Receptor-Binding Site of an Encephalitic Flavivirus Alter Virulence and Host Cell Tropism and Reveal a Role for Glycosaminoglycans in Entry. *J. Virol.* **2000**, *74*, 8867–8875, doi:10.1128/JVI.74.19.8867-8875.2000.
118. Watterson, D.; Kobe, B.; Young, P.R.Y. 2012 Residues in Domain III of the Dengue Virus Envelope Glycoprotein Involved in Cell-Surface Glycosaminoglycan Binding. *J. Gen. Virol. 93*, 72–82, doi:10.1099/vir.0.037317-0.
119. Chu, J.J.H.; Rajamanonmani, R.; Li, J.; Bhuvanakantham, R.; Lescar, J.; Ng, M.-L.Y. 2005 Inhibition of West Nile Virus Entry by Using a Recombinant Domain III from the Envelope Glycoprotein. *J. Gen. Virol. 86*, 405–412, doi:10.1099/vir.0.80411-0.
120. Bhardwaj, S.; Holbrook, M.; Shope, R.E.; Barrett, A.D.T.; Watowich, S.J. Biophysical Characterization and Vector-Specific Antagonist Activity of Domain III of the Tick-Borne Flavivirus Envelope Protein. *J. Virol.* **2001**, *75*, 4002–4007, doi:10.1128/JVI.75.8.4002-4007.2001.
121. Modis, Y.; Ogata, S.; Clements, D.; Harrison, S.C. Structure of the Dengue Virus Envelope Protein after Membrane Fusion. *Nature* **2004**, *427*, 313–9, doi:10.1038/nature02165.
122. Stiasny, K.; Allison, S.L.; Marchler-Bauer, A.; Kunz, C.; Heinz, F.X. Structural Requirements for Low-PH-Induced Rearrangements in the Envelope Glycoprotein of Tick-Borne Encephalitis Virus. *J. Virol.* **1996**, *70*, 8142–8147, doi:10.1128/JVI.70.11.8142-8147.1996.

123. Stiasny, K.; Bressanelli, S.; Lepault, J.; Rey, F.A.; Heinz, F.X. Characterization of a Membrane-Associated Trimeric Low-PH-Induced Form of the Class II Viral Fusion Protein E from Tick-Borne Encephalitis Virus and Its Crystallization. *J. Virol.* **2004**, *78*, 3178–3183, doi:10.1128/JVI.78.6.3178-3183.2004.

124. Stettler, K.; Beltramello, M.; Espinosa, D.A.; Graham, V.; Cassotta, A.; Bianchi, S.; Vanzetta, F.; Minola, A.; Jaconi, S.; Mele, F.; et al. Specificity, Cross-Reactivity, and Function of Antibodies Elicited by Zika Virus Infection. *Science* **2016**, *353*, 823–6, doi:10.1126/science.aaf8505.

125. Sapparapu, G.; Fernandez, E.; Kose, N.; Bin, C.; Fox, J.M.; Bombardi, R.G.; Zhao, H.; Nelson, C.A.; Bryan, A.L.; Barnes, T.; et al. Neutralizing Human Antibodies Prevent Zika Virus Replication and Fetal Disease in Mice. *Nature* **2016**, *540*, 443–447, doi:10.1038/nature20564.

126. Deng, Y.-Q.; Dai, J.-X.; Ji, G.-H.; Jiang, T.; Wang, H.-J.; Yang, H.; Tan, W.-L.; Liu, R.; Yu, M.; Ge, B.-X.; et al. A Broadly Flavivirus Cross-Neutralizing Monoclonal Antibody That Recognizes a Novel Epitope within the Fusion Loop of E Protein. *PLOS ONE* **2011**, *6*, e16059, doi:10.1371/journal.pone.0016059.

127. Wang, J.; Bardelli, M.; Espinosa, D.A.; Pedotti, M.; Ng, T.-S.; Bianchi, S.; Simonelli, L.; Lim, E.X.Y.; Foglierini, M.; Zatta, F.; et al. A Human Bi-Specific Antibody against Zika Virus with High Therapeutic Potential. *Cell* **2017**, *171*, 229-241.e15, doi:10.1016/j.cell.2017.09.002.

128. Rouvinski, A.; Guardado-Calvo, P.; Barba-Spaeth, G.; Duquerroy, S.; Vaney, M.-C.; Kikuti, C.M.; Navarro Sanchez, M.E.; Dejnirattisai, W.; Wongwiwat, W.; Haouz, A.; et al. Recognition Determinants of Broadly Neutralizing Human Antibodies against Dengue Viruses. *Nature* **2015**, *520*, 109–113, doi:10.1038/nature14130.

129. Zhang, S.; Kostyuchenko, V.A.; Ng, T.S.; Lim, X.N.; Ooi, J.S.; Lambert, S.; Tan, T.Y.; Widman, D.G.; Shi, J.; Baric, R.S.; et al. Neutralization Mechanism of a Highly Potent Antibody against Zika Virus. *Nat Commun* **2016**, *7*, 13679, doi:10.1038/ncomms13679.

130. Dejnirattisai, W.; Jumnainsong, A.; Onsirisakul, N.; Fitton, P.; Vasanawathana, S.; Limpitikul, W.; Puttikhunt, C.; Edwards, C.; Duangchinda, T.; Supasa, S.; et al. Cross-Reacting Antibodies Enhance Dengue Virus Infection in Humans. *Science* **2010**, *328*, 745–748, doi:10.1126/science.1185181.

131. Oliphant, T.; Engle, M.; Nybakken, G.E.; Doane, C.; Johnson, S.; Huang, L.; Gorlatov, S.; Mehlhop, E.; Marri, A.; Chung, K.M.; et al. Development of a Humanized Monoclonal Antibody with Therapeutic Potential against West Nile Virus. *Nat. Med.* **2005**, *11*, 522–530, doi:10.1038/nm1240.

132. Wang, L.; Wang, R.; Wang, L.; Ben, H.; Yu, L.; Gao, F.; Shi, X.; Yin, C.; Zhang, F.; Xiang, Y.; et al. Structural Basis for Neutralization and Protection by a Zika Virus-Specific Human Antibody. *Cell Rep.* **2019**, *26*, 3360-3368.e5, doi:10.1016/j.celrep.2019.02.062.

133. Yu, L.; Wang, R.; Gao, F.; Li, M.; Liu, J.; Wang, J.; Hong, W.; Zhao, L.; Wen, Y.; Yin, C.; et al. Delineating Antibody Recognition against Zika Virus during Natural Infection. *JCI Insight* **2017**, *2*, doi:10.1172/jci.insight.93042.

134. Wahala, W.M.P.B.; Kraus, A.A.; Haymore, L.B.; Accavitti-Loper, M.A.; de Silva, A.M. Dengue Virus Neutralization by Human Immune Sera: Role of Envelope Protein Domain III-Reactive Antibody. *Virology* **2009**, *392*, 103–113, doi:10.1016/j.virol.2009.06.037.

135. Slon-Campos, J.L.; Dejnirattisai, W.; Jagger, B.W.; López-Camacho, C.; Wongwiwat, W.; Durnell, L.A.; Winkler, E.S.; Chen, R.E.; Reyes-Sandoval, A.; Rey, F.A.; et al. A Protective Zika Virus E-Dimer-Based Subunit Vaccine Engineered to Abrogate Antibody-Dependent Enhancement of Dengue Infection. *Nat. Immunol.* **2019**, *20*, 1291–1298, doi:10.1038/s41590-019-0477-z.

136. Watanabe, S.; Chan, K.W.K.; Wang, J.; Rivino, L.; Lok, S.-M.; Vasudevan, S.G. Dengue Virus Infection with Highly Neutralizing Levels of Cross-Reactive Antibodies Causes Acute Lethal Small Intestinal Pathology without a High Level of Viremia in Mice. *J. Virol.* **2015**, *89*, 5847–5861, doi:10.1128/JVI.00216-15.

137. Heinz, F.X.; Stiasny, K. Flaviviruses and Flavivirus Vaccines. *Vaccine* **2012**, *30*, 4301–4306, doi:10.1016/j.vaccine.2011.09.114.

138. Zhang, X.; Sheng, J.; Plevka, P.; Kuhn, R.J.; Diamond, M.S.; Rossmann, M.G. Dengue Structure Differs at the Temperatures of Its Human and Mosquito Hosts. *Proc. Natl. Acad. Sci.* **2013**, *110*, 6795–6799, doi:10.1073/pnas.1304300110.

139. Victora, G.D.; Nussenzweig, M.C. Germinal Centers. *Annu. Rev. Immunol.* **2012**, *30*, 429–457, doi:10.1146/annurev-immunol-020711-075032.

140. Milstein, C.; Neuberger, M.S. Maturation of the Immune Response. In *Advances in Protein Chemistry*; Richards, F.M., Eisenberg, D.E., Kim, P.S., Eds.; Academic Press, 1996; Vol. 49, pp. 451–485 ISBN 0065-3233.

141. Tiller, T.; Tsuiji, M.; Yurasov, S.; Velinzon, K.; Nussenzweig, M.C.; Wardemann, H. Autoreactivity in Human IgG+ Memory B Cells. 9.

142. Davenport, T.M.; Gorman, J.; Joyce, M.G.; Zhou, T.; Soto, C.; Guttman, M.; Moquin, S.; Yang, Y.; Zhang, B.; Doria-Rose, N.A.; et al. Somatic Hypermutation-Induced Changes in the Structure and Dynamics of HIV-1 Broadly Neutralizing Antibodies. *Structure* **2016**, *24*, 1346–1357, doi:10.1016/j.str.2016.06.012.

143. Klein, F.; Mouquet, H.; Dosenovic, P.; Scheid, J.F.; Scharf, L.; Nussenzweig, M.C. Antibodies in HIV-1 Vaccine Development and Therapy. *Science* **2013**, *341*, 1199–1204, doi:10.1126/science.1241144.

144. Kwong, P.D.; Mascola, J.R. HIV-1 Vaccines Based on Antibody Identification, B Cell Ontogeny, and Epitope Structure. *Immunity* **2018**, *48*, 855–871, doi:10.1016/j.immuni.2018.04.029.

145. Klein, F.; Diskin, R.; Scheid, J.F.; Gaebler, C.; Mouquet, H.; Georgiev, I.S.; Pancera, M.; Zhou, T.; Incesu, R.-B.; Fu, B.Z.; et al. Somatic Mutations of the Immunoglobulin Framework Are Generally Required for Broad and Potent HIV-1 Neutralization. *Cell* **2013**, *153*, 126–138, doi:10.1016/j.cell.2013.03.018.

146. Wagner, S.D.; Milstein, C.; Neuberger, M.S. Codon Bias Targets Mutation. *Nature* **1995**, *376*, 732–732, doi:10.1038/376732a0.

147. Reynaud, C.-A.; Garcia, C.; Hein, W.R.; Weill, J.-C. Hypermutation Generating the Sheep Immunoglobulin Repertoire Is an Antigen-Independent Process. *Cell* **1995**, *80*, 115–125, doi:10.1016/0092-8674(95)90456-5.

148. Briney, B.S.; Willis, J.R.; Crowe, J.E. Location and Length Distribution of Somatic Hypermutation-Associated DNA Insertions and Deletions Reveals Regions of Antibody Structural Plasticity. *Genes Immun.* **2012**, *13*, 523–529, doi:10.1038/gene.2012.28.

149. Kepler, T.B.; Liao, H.-X.; Alam, S.M.; Bhaskarabhatla, R.; Zhang, R.; Yandava, C.; Stewart, S.; Anasti, K.; Kelsoe, G.; Parks, R.; et al. Immunoglobulin Gene Insertions and Deletions in the Affinity Maturation of HIV-1 Broadly Reactive Neutralizing Antibodies. *Cell Host Microbe* **2014**, *16*, 304–313, doi:10.1016/j.chom.2014.08.006.

150. Niu, X.; Yan, Q.; Yao, Z.; Zhang, F.; Qu, L.; Wang, C.; Wang, C.; Lei, H.; Chen, C.; Liang, R.; et al. Longitudinal Analysis of the Antibody Repertoire of a Zika Virus-Infected Patient Revealed Dynamic Changes in Antibody Response. *Emerg. Microbes Infect.* **2020**, *9*, 111–123, doi:10.1080/22221751.2019.1701953.

151. Gaebler, C.; Wang, Z.; Lorenzi, J.C.C.; Muecksch, F.; Finkin, S.; Tokuyama, M.; Cho, A.; Jankovic, M.; Schaefer-Babajew, D.; Oliveira, T.Y.; et al. Evolution of Antibody Immunity to SARS-CoV-2. *Nature* **2021**, *591*, 639–644, doi:10.1038/s41586-021-03207-w.

152. Wang, Z.; Muecksch, F.; Schaefer-Babajew, D.; Finkin, S.; Viant, C.; Gaebler, C.; Hoffmann, H.-H.; Barnes, C.O.; Cipolla, M.; Ramos, V.; et al. Naturally Enhanced Neutralizing Breadth against SARS-CoV-2 One Year after Infection. *Nature* **2021**, *595*, 426–431, doi:10.1038/s41586-021-03696-9.

153. Magnani, D.M.; Silveira, C.G.T.; Rosen, B.C.; Ricciardi, M.J.; Pedreno-Lopez, N.; Gutman, M.J.; Bailey, V.K.; Maxwell, H.S.; Domingues, A.; Gonzalez-Nieto, L.; et al. A Human Inferred Germline Antibody Binds to an Immunodominant Epitope and Neutralizes Zika Virus. *PLoS Negl Trop Dis* **2017**, *11*, e0005655, doi:10.1371/journal.pntd.0005655.

154. Rogers, T.F.; Goodwin, E.C.; Briney, B.; Sok, D.; Beutler, N.; Strubel, A.; Nedellec, R.; Le, K.; Brown, M.E.; Burton, D.R.; et al. Zika Virus Activates de Novo and Cross-Reactive Memory B Cell Responses in Dengue-Experienced Donors. *Sci Immunol* **2017**, *2*, doi:10.1126/sciimmunol.aan6809.

155. Gao, F.; Lin, X.; He, L.; Wang, R.; Wang, H.; Shi, X.; Zhang, F.; Yin, C.; Zhang, L.; Zhu, J.; et al. Development of a Potent and Protective Germline-like Antibody Lineage against Zika Virus in a Convalescent Human. *bioRxiv* **2019**, 661918, doi:10.1101/661918.

156. Kennedy, R.B. Current Challenges in Vaccinology. *Front. Immunol.* **2020**, *11*, 18.

157. Narkhede, Y.B.; Gonzalez, K.J.; Strauch, E.-M. Targeting Viral Surface Proteins through Structure-Based Design. *Viruses* **2021**, *13*, 1320, doi:10.3390/v13071320.

158. Burton, D.R. What Are the Most Powerful Immunogen Design Vaccine Strategies?: Reverse Vaccinology 2.0 Shows Great Promise. *Cold Spring Harb. Perspect. Biol.* **2017**, *9*, a030262, doi:10.1101/cshperspect.a030262.

159. Gebara, N.Y.; Kamari, V.E.; Rizk, N. HIV-1 Elite Controllers: An Immunovirological Review and Clinical Perspectives. 4.

160. Caskey, M.; Schoofs, T.; Gruell, H.; Settler, A.; Karagounis, T.; Kreider, E.F.; Murrell, B.; Pfeifer, N.; Nogueira, L.; Oliveira, T.Y.; et al. Antibody 10-1074 Suppresses Viremia in HIV-1-Infected Individuals. *Nat Med* **2017**, *23*, 185–191, doi:10.1038/nm.4268.

161. Courter, J.R.; Madani, N.; Sodroski, J.; Schön, A.; Freire, E.; Kwong, P.D.; Hendrickson, W.A.; Chaiken, I.M.; LaLonde, J.M.; Smith, A.B. Structure-Based Design, Synthesis and Validation of CD4-Mimetic Small Molecule Inhibitors of HIV-1 Entry: Conversion of a Viral Entry Agonist to an Antagonist. *Acc. Chem. Res.* **2014**, *47*, 1228–1237, doi:10.1021/ar4002735.

162. Vita, C.; Drakopoulou, E.; Vizzavona, J.; Rochette, S.; Martin, L.; Ménez, A.; Roumestand, C.; Yang, Y.-S.; Ylisastigui, L.; Benjouad, A.; et al. Rational Engineering of a Miniprotein That Reproduces the Core of the CD4 Site Interacting with HIV-1 Envelope Glycoprotein. *Proc. Natl. Acad. Sci. U. S. A.* **1999**, *96*, 13091–13096.

163. Ozorowski, G.; Torres, J.L.; Santos-Martins, D.; Forli, S.; Ward, A.B. A Strain-Specific Inhibitor of Receptor-Bound HIV-1 Targets a Pocket near the Fusion Peptide. *Cell Rep.* **2020**, *33*, 108428, doi:10.1016/j.celrep.2020.108428.

164. Fischer, W.; Giorgi, E.E.; Chakraborty, S.; Nguyen, K.; Bhattacharya, T.; Theiler, J.; Goloboff, P.A.; Yoon, H.; Abfalterer, W.; Foley, B.T.; et al. HIV-1 and SARS-CoV-2: Patterns in the Evolution of Two Pandemic Pathogens. *Cell Host Microbe* **2021**, *29*, 1093–1110, doi:10.1016/j.chom.2021.05.012.

165. Hastie, K.M.; Li, H.; Bedinger, D.; Schendel, S.L.; Dennison, S.M.; Li, K.; Rayaprolu, V.; Yu, X.; Mann, C.; Zandonatti, M.; et al. Defining Variant-Resistant Epitopes Targeted by SARS-CoV-2 Antibodies: A Global Consortium Study. *Science* **2021**, doi:10.1126/science.abh2315.

166. Letko, M.; Marzi, A.; Munster, V. Functional Assessment of Cell Entry and Receptor Usage for SARS-CoV-2 and Other Lineage B Betacoronaviruses. *Nat. Microbiol.* **2020**, *5*, 562–569, doi:10.1038/s41564-020-0688-y.

167. Jette, C.A.; Cohen, A.A.; Gnanapragasam, P.N.P.; Muecksch, F.; Lee, Y.E.; Huey-Tubman, K.E.; Schmidt, F.; Hatziioannou, T.; Bieniasz, P.D.; Nussenzweig, M.C.; et al. Broad Cross-Reactivity across Sarbecoviruses Exhibited by a Subset of COVID-19

Donor-Derived Neutralizing Antibodies. *Cell Rep.* **2021**, 109760, doi:10.1016/j.celrep.2021.109760.

168. Wec, A.Z.; Wrapp, D.; Herbert, A.S.; Maurer, D.P.; Haslwanter, D.; Sakharkar, M.; Jangra, R.K.; Dieterle, M.E.; Lilov, A.; Huang, D.; et al. Broad Neutralization of SARS-Related Viruses by Human Monoclonal Antibodies. *Science* **2020**, *369*, 731–736, doi:10.1126/science.abc7424.
169. Taylor, P.C.; Adams, A.C.; Hufford, M.M.; de la Torre, I.; Winthrop, K.; Gottlieb, R.L. Neutralizing Monoclonal Antibodies for Treatment of COVID-19. *Nat. Rev. Immunol.* **2021**, *21*, 382–393, doi:10.1038/s41577-021-00542-x.
170. Linsky, T.W.; Vergara, R.; Codina, N.; Nelson, J.W.; Walker, M.J.; Su, W.; Barnes, C.O.; Hsiang, T.-Y.; Esser-Nobis, K.; Yu, K.; et al. De Novo Design of Potent and Resilient HACE2 Decoys to Neutralize SARS-CoV-2. *Science* **2020**, *370*, 1208–1214, doi:10.1126/science.abe0075.
171. Bardina, S.V.; Bunduc, P.; Tripathi, S.; Duehr, J.; Frere, J.J.; Brown, J.A.; Nachbagauer, R.; Foster, G.A.; Krysztof, D.; Tortorella, D.; et al. Enhancement of Zika Virus Pathogenesis by Preexisting Antiflavivirus Immunity. *Science* **2017**, *356*, 175–180, doi:10.1126/science.aal4365.
172. Harrison, S.C. Immunogenic Cross-Talk between Dengue and Zika Viruses. *Nat Immunol* **2016**, *17*, 1010–2, doi:10.1038/ni.3539.
173. Priyamvada, L.; Quicke, K.M.; Hudson, W.H.; Onlamoon, N.; Sewatanon, J.; Edupuganti, S.; Pattanapanyasat, K.; Chokephaibulkit, K.; Mulligan, M.J.; Wilson, P.C.; et al. Human Antibody Responses after Dengue Virus Infection Are Highly Cross-Reactive to Zika Virus. *Proc Natl Acad Sci U A* **2016**, *113*, 7852–7, doi:10.1073/pnas.1607931113.
174. Vaughn, D.W.; Green, S.; Kalayanarooj, S.; Innis, B.L.; Nimmannitya, S.; Suntayakorn, S.; Endy, T.P.; Raengsakulrach, B.; Rothman, A.L.; Ennis, F.A.; et al. Dengue Viremia Titer, Antibody Response Pattern, and Virus Serotype Correlate with Disease Severity. *J. Infect. Dis.* **2000**, *181*, 2–9, doi:10.1086/315215.
175. Halstead, S.B. Neutralization and Antibody-Dependent Enhancement of Dengue Viruses. *Adv Virus Res* **2003**, *60*, 421–67.
176. Dejnirattisai, W.; Supasa, P.; Wongwiwat, W.; Rouvinski, A.; Barba-Spaeth, G.;

Duangchinda, T.; Sakuntabhai, A.; Cao-Lormeau, V.M.; Malasit, P.; Rey, F.A.; et al. Dengue Virus Sero-Cross-Reactivity Drives Antibody-Dependent Enhancement of Infection with Zika Virus. *Nat Immunol* **2016**, *17*, 1102–8, doi:10.1038/ni.3515.

177. Wahala, W.M.; Silva, A.M. The Human Antibody Response to Dengue Virus Infection. *Viruses* **2011**, *3*, 2374–95, doi:10.3390/v3122374.
178. Alwis, R. de; Williams, K.L.; Schmid, M.A.; Lai, C.-Y.; Patel, B.; Smith, S.A.; Crowe, J.E.; Wang, W.-K.; Harris, E.; Silva, A.M. de Dengue Viruses Are Enhanced by Distinct Populations of Serotype Cross-Reactive Antibodies in Human Immune Sera. *PLOS Pathog.* **2014**, *10*, e1004386, doi:10.1371/journal.ppat.1004386.
179. Nisalak, A.; Clapham, H.E.; Kalayanarooj, S.; Klungthong, C.; Thaisomboonsuk, B.; Fernandez, S.; Reiser, J.; Srikiatkhachorn, A.; Macareo, L.R.; Lessler, J.T.; et al. Forty Years of Dengue Surveillance at a Tertiary Pediatric Hospital in Bangkok, Thailand, 1973–2012. *Am. J. Trop. Med. Hyg.* **2016**, *94*, 1342–1347, doi:10.4269/ajtmh.15-0337.
180. SANGKAWIBHA, N.; ROJANASUPHOT, S.; AHANDRIK, S.; VIRIYAPONGSE, S.; JATANASEN, S.; SALITUL, V.; PHANTHUMACHINDA, B.; HALSTEAD, S.B. RISK FACTORS IN DENGUE SHOCK SYNDROME: A PROSPECTIVE EPIDEMIOLOGIC STUDY IN RAYONG, THAILAND: I. THE 1980 OUTBREAK. *Am. J. Epidemiol.* **1984**, *120*, 653–669, doi:10.1093/oxfordjournals.aje.a113932.
181. Katzelnick, L.C.; Narvaez, C.; Arguello, S.; Mercado, B.L.; Collado, D.; Ampie, O.; Elizondo, D.; Miranda, T.; Carillo, F.B.; Mercado, J.C.; et al. Zika Virus Infection Enhances Future Risk of Severe Dengue Disease. *Science* **2020**, *369*, 1123–1128, doi:10.1126/science.abb6143.
182. Halstead, S.B. In Vivo Enhancement of Dengue Virus Infection in Rhesus Monkeys by Passively Transferred Antibody. *J. Infect. Dis.* **1979**, *140*, 527–533, doi:10.1093/infdis/140.4.527.
183. Waggoner, J.J.; Katzelnick, L.C.; Burger-Calderon, R.; Gallini, J.; Moore, R.H.; Kuan, G.; Balmaseda, A.; Pinsky, B.A.; Harris, E. Antibody-Dependent Enhancement of Severe Disease Is Mediated by Serum Viral Load in Pediatric Dengue Virus Infections. *J. Infect. Dis.* **2020**, *221*, 1846–1854, doi:10.1093/infdis/jiz618.
184. Katzelnick, L.C.; Gresh, L.; Halloran, M.E.; Mercado, J.C.; Kuan, G.; Gordon, A.; Balmaseda, A.; Harris, E. Antibody-Dependent Enhancement of Severe Dengue Disease

in Humans. *Science* **2017**, *358*, 929–932, doi:10.1126/science.aan6836.

185. Salje, H.; Cummings, D.A.T.; Rodriguez-Barraquer, I.; Katzelnick, L.C.; Lessler, J.; Klungthong, C.; Thaisomboonsuk, B.; Nisalak, A.; Weg, A.; Ellison, D.; et al. Reconstruction of Antibody Dynamics and Infection Histories to Evaluate Dengue Risk. *Nature* **2018**, *557*, 719–723, doi:10.1038/s41586-018-0157-4.
186. Cattarino, L.; Rodriguez-Barraquer, I.; Imai, N.; Cummings, D.A.T.; Ferguson, N.M. Mapping Global Variation in Dengue Transmission Intensity. *Sci. Transl. Med.* **2020**, *12*, doi:10.1126/scitranslmed.aax4144.
187. Faria, N.R.; Quick, J.; Claro, I.M.; Thézé, J.; de Jesus, J.G.; Giovanetti, M.; Kraemer, M.U.G.; Hill, S.C.; Black, A.; da Costa, A.C.; et al. Establishment and Cryptic Transmission of Zika Virus in Brazil and the Americas. *Nature* **2017**, *546*, 406–410, doi:10.1038/nature22401.
188. Yang, C.; Zeng, F.; Gao, X.; Zhao, S.; Li, X.; Liu, S.; Li, N.; Deng, C.; Zhang, B.; Gong, R. Characterization of Two Engineered Dimeric Zika Virus Envelope Proteins as Immunogens for Neutralizing Antibody Selection and Vaccine Design. *J. Biol. Chem.* **2019**, *294*, 10638–10648, doi:10.1074/jbc.RA119.007443.
189. Cimica, V.; Williams, S.; Adams-Fish, D.; McMahon, C.; Narayanan, A.; Rashid, S.; Stedman, T.T. Zika Virus-Like Particle (VLP) Vaccine Displaying Envelope (E) Protein CD Loop Antigen Elicits Protective and Specific Immune Response in a Murine Model. *Biochem. Biophys. Res. Commun.* **2020**, *529*, 805–811, doi:10.1016/j.bbrc.2020.05.161.
190. Tai, W.; Chen, J.; Zhao, G.; Geng, Q.; He, L.; Chen, Y.; Zhou, Y.; Li, F.; Du, L. Rational Design of Zika Virus Subunit Vaccine with Enhanced Efficacy. *J. Virol.* **2019**, *93*, e02187-18, doi:10.1128/JVI.02187-18.
191. Shanmugam, R.K.; Ramasamy, V.; Shukla, R.; Arora, U.; Swaminathan, S.; Khanna, N. Pichia Pastoris-Expressed Zika Virus Envelope Domain III on a Virus-like Particle Platform: Design, Production and Immunological Evaluation. *Pathog. Dis.* **2019**, *77*, doi:10.1093/femspd/ftz026.
192. Yang, M.; Lai, H.; Sun, H.; Chen, Q. Virus-like Particles That Display Zika Virus Envelope Protein Domain III Induce Potent Neutralizing Immune Responses in Mice. *Sci. Rep.* **2017**, *7*, 7679, doi:10.1038/s41598-017-08247-9.
193. Espinosa, D.; Mendy, J.; Manayani, D.; Vang, L.; Wang, C.; Richard, T.; Guenther, B.;

Aruri, J.; Avanzini, J.; Garduno, F.; et al. Passive Transfer of Immune Sera Induced by a Zika Virus-Like Particle Vaccine Protects AG129 Mice Against Lethal Zika Virus Challenge. *EBioMedicine* **2018**, *27*, 61–70, doi:10.1016/j.ebiom.2017.12.010.

194. Cabral-Miranda, G.; Lim, S.M.; Mohsen, M.O.; Pobelov, I.V.; Roesti, E.S.; Heath, M.D.; Skinner, M.A.; Kramer, M.F.; Martina, B.E.E.; Bachmann, M.F. Correction: Zika Virus-Derived E-DIII Protein Displayed on Immunologically Optimized VLPs Induces Neutralizing Antibodies without Causing Enhancement of Dengue Virus Infection. Vaccines 2019, 7, 72. *Vaccines* **2020**, *8*, 94, doi:10.3390/vaccines8010094.

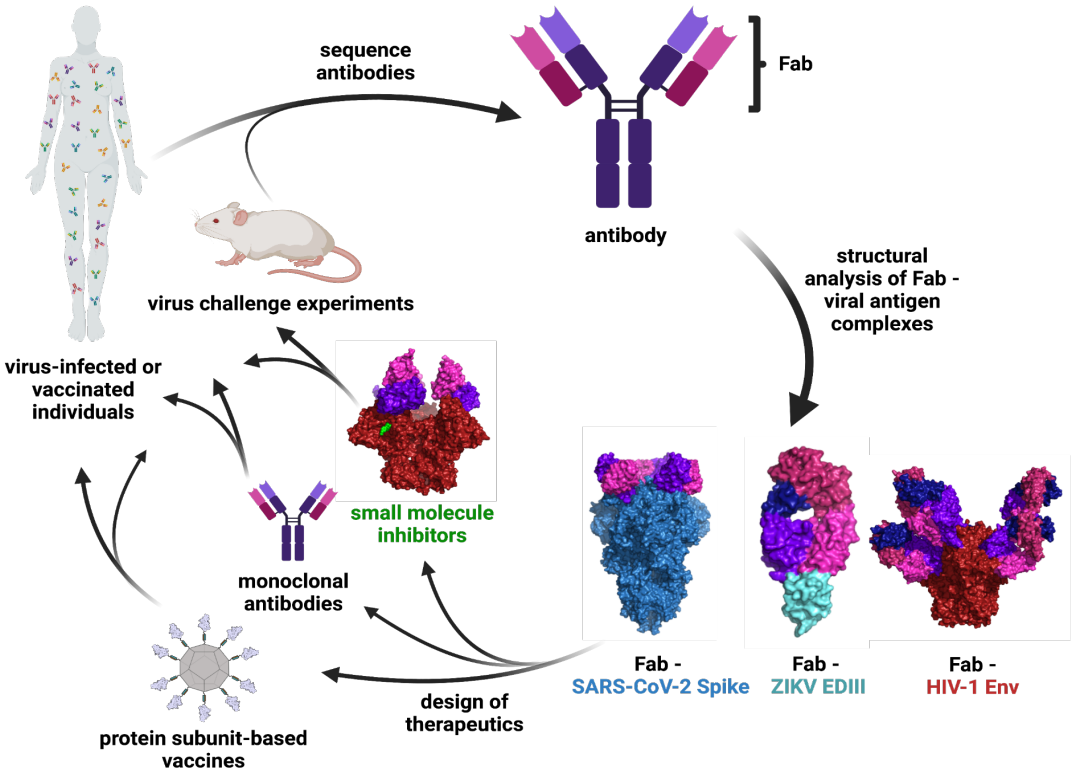

Figure 1: Schematic of Ab characterization and therapeutic development.

The binding epitopes of Abs isolated from infected or vaccinated individuals or animal studies are determined through structural analysis of Fab - viral antigen complexes. These structures inform the design of vaccines, monoclonal Abs, and small molecule therapeutics that can be tested in clinical trials and animal models. Surface representations are shown for the following structures: Fab - SARS-CoV-2 S (PDB 7K90), Fab - ZIKV EDIII (PDB 5VIG), Fab - HIV-1 Env (PDB 5T3Z), and small molecule inhibitor - HIV-1 Env (PDB 7LO6).

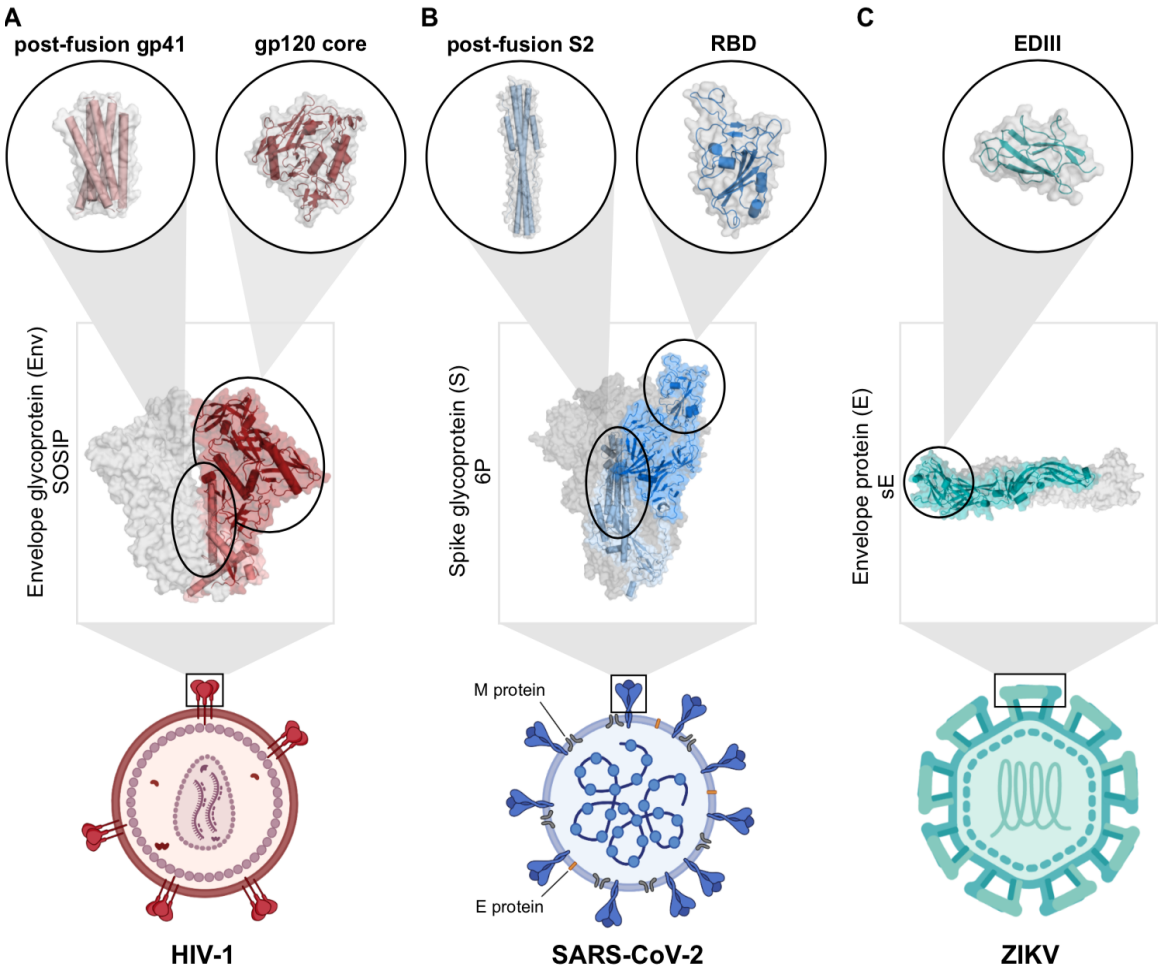

Figure 2: Structural targets of HIV-1, SARS-CoV-2, and ZIKV.

(A) Cartoon HIV-1 virion with a closed, pre-fusion Env protein structure highlighted (PDB: 6UDJ). Circles show crystal structures of the postfusion gp41 bundle (left, PDB: 1AIK) and gp120 core (right, PDB: 5F4P).

(B) Cartoon SARS-CoV-2 virion with S protein (blue), M protein (grey), and E protein (orange). The closed, pre-fusion S protein structure with one 'up' RBD (blue subunit) and two 'down' RBDs (grey subunits) is shown in the box (PDB: 7K8V). Circles show postfusion S2 helices (left, PDB: 6LXT) and RBD (right, PDB: 7K8M) structures.

(C) Cartoon ZIKV virion with E protein (teal). The soluble E (sE) protein dimer structure is shown in the box with one E protein highlighted (PDB: 5JHM).The EDIII structure is shown in the circle (PDB: 6UTA).

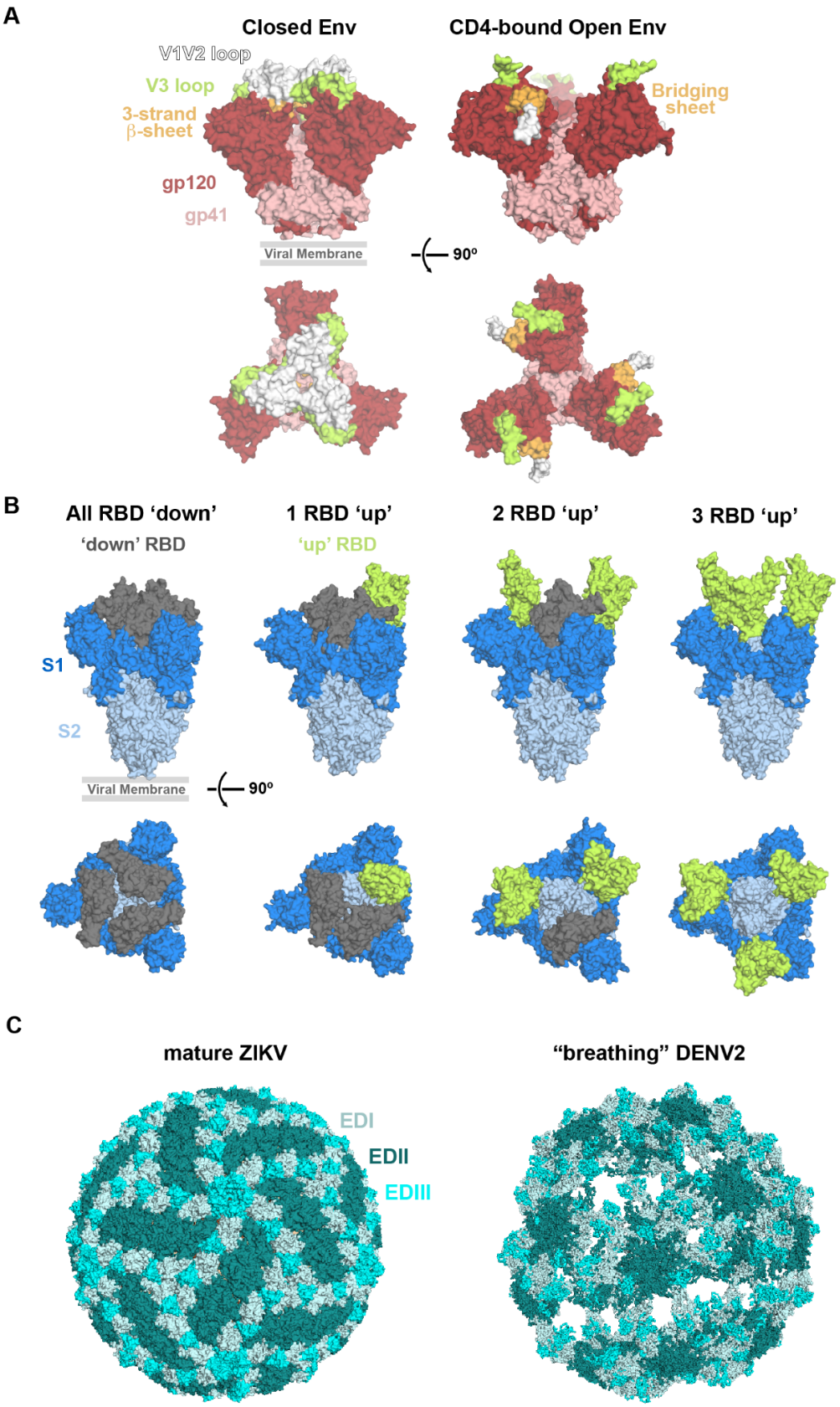
A
Closed Env
CD4-bound Open Env
V1V2 loop
V3 loop
3-strand β-sheet
gp120
gp41
Viral Membrane
Bridging sheet
90°
B
All RBD 'down'
1 RBD 'up'
2 RBD 'up'
3 RBD 'up'
'down' RBD
'up' RBD
S1
S2
Viral Membrane
90°
C
mature ZIKV
"breathing" DENV2
EDI
EDII
EDIII

Figure 3: Conformational changes of HIV-1 Env, SARS-CoV-2 S, and ZIKV E.

(A) Surface depictions of top down and side views of (left) closed, pre-fusion Env (PDB: 6UDJ) and (right) CD4-bound open conformation Env (PDB: 5VN3) highlighting the V1V2 loop (white), V3 loop (green), and 3-strand beta sheet (bright orange). Gp120 = dark red, gp41 = salmon.

(B) Surface depictions of side and top down views of closed, pre-fusion S with three 'down' RBDs (grey, PDB: 7K90), 1 'up' RBD (green, PDB: 7K8V), 2 'up' RBDs (7K8Y), and 3 'up' RBDs (6XCN). The location of the viral membrane is indicated in side views of viral proteins.

(C) Surface depictions comparing the smooth mature ZIKV (PDB: 6CO8) and spiky "breathing" DENV2 (PDB: 3ZKO) structures. In the "breathing" DENV2 structure, EDI and EDIII of the E protein are protruding, giving the virus a "spiky" appearance, and holes are found in the surface.

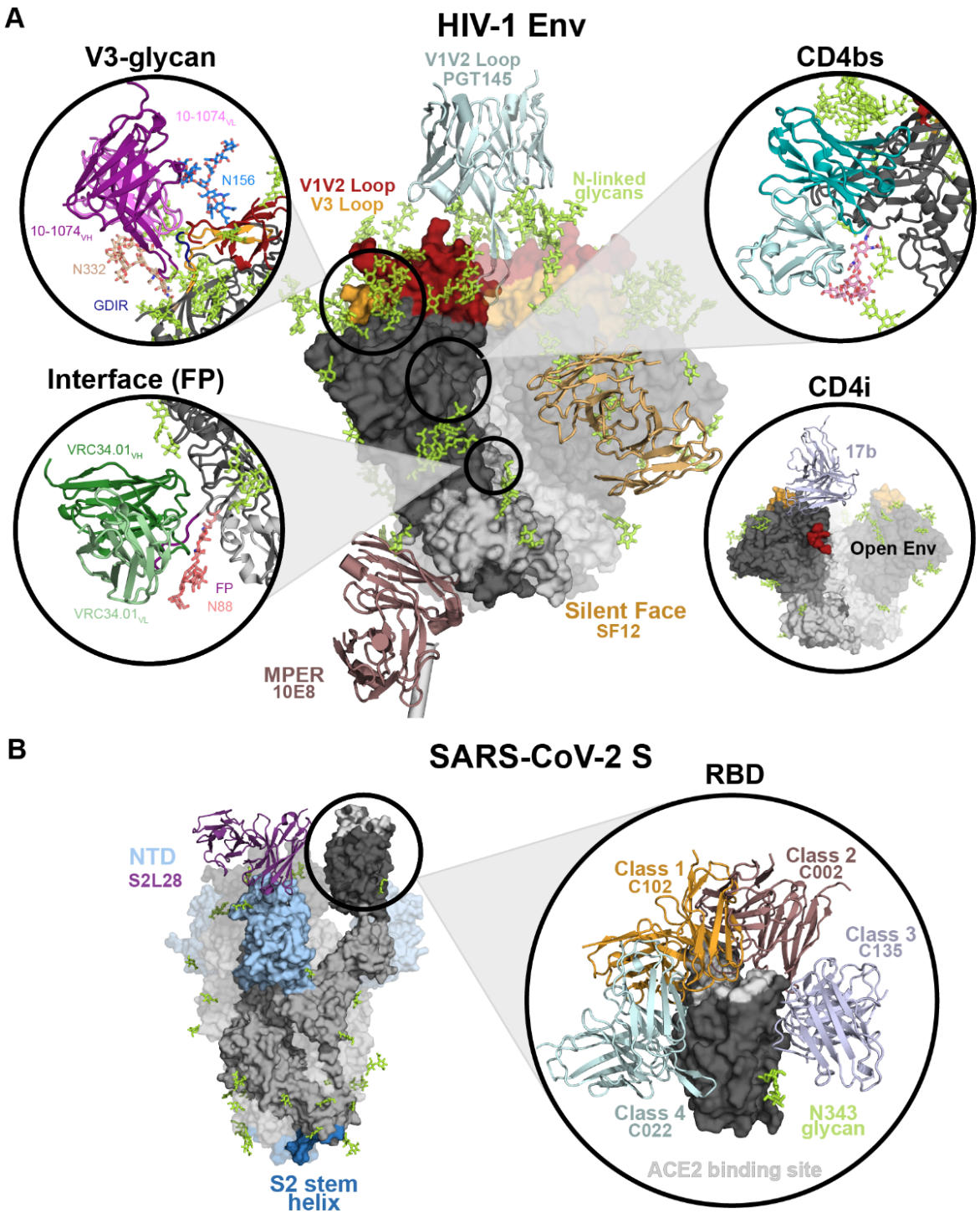
A
HIV-1 Env
V3-glycan
10-1074VL
N156
10-1074VH
N332
GDIR
V1V2 Loop
PGT145
V1V2 Loop
V3 Loop
N-linked
glycans
CD4bs
Interface (FP)
VRC34.01VH
FP
N88
VRC34.01VL
CD4i
17b
Open Env
Silent Face
SF12
MPER
10E8
B
SARS-CoV-2 S
RBD
NTD
S2L28
Class 1
C102
Class 2
C002
Class 3
C135
Class 4
C022
N343
glycan
ACE2 binding site
S2 stem
helix

Figure 4: Neutralizing epitopes on HIV-1 Env and SARS-CoV-2 S.

(A) HIV-1 Env structure (left) highlighting epitopes of representative bNAbs for each bNAb class. Env (PDB: 5T3Z) is shown as a surface with green N-linked glycans shown as sticks. Gp41 is light grey and gp120 is dark grey except for the V1V2 loop (dark red) and V3 loop (light orange). V_HV_L domains of Abs binding the epitopes MPER (mauve, 10E8, PDB: 6VPX), V1V2 loop (pale cyan, PGT145, PDB: 5V8L) or Silent Face (sand, SF12, PDB: 6OKP) are shown as cartoons. Circles show details for Ab binding to the V3-glycan (10-1074, PDB: 5T3Z), interface (VRC34.01, PDB: 5I8H), CD4bs (3BNC117, PDB: 5V8L), and CD4i (17b, PDB: 7LO6).

(B) SARS-CoV-2 S protein structure (left) highlighting the RBD (dark grey), S2 (blue), and NTD (light blue) Ab binding regions. V_HV_L domains of Ab binding to an NTD (S2L28, PDB: 7LXX) epitope is shown as a cartoon representation. The circle (right) shows an enlarged view of the RBD surface with V_HV_L domains for RBD-binding Abs shown as cartoons: Class 1 (light orange, C102, PDB: 7K8M), Class 2 (mauve, C002, PDB: 7K8S), Class 3 (pale purple, C135, PDB: 7K8Z), and Class 4 (pale cyan, C022, PDB: 7RKU). The ACE2 binding site is highlighted on the RBD in white.

Chapter V

COMPARING METHODS FOR IMMOBILIZING HIV-1 SOSIPS IN ELISAS THAT EVALUATE ANTIBODY BINDING

Dam, K.A., Mutia, P.S. & Bjorkman, P.J. Comparing methods for immobilizing HIV-1 SOSIPs in ELISAs that evaluate antibody binding. Sci Rep 12, 11172 (2022). https://doi.org/10.1038/s41598-022-15506-x

Abstract

Enzyme-linked immunosorbent assays (ELISAs) are used to evaluate binding of broadly neutralizing antibodies (bNAbs) and polyclonal sera to native-like HIV-1 Env SOSIPs. Methods for immobilizing SOSIPs on plates differ, which can lead to variable or, in some cases, misleading results. Three methods used to immobilize SOSIPs were compared to determine how antigen immobilization methods affect Env conformation and ELISA results. HIV-1 SOSIPs were directly coated on polystyrene plates, captured by a monoclonal antibody against a C-terminal affinity tag, or randomly biotinylated and coated on a streptavidin plate. Binding of bNAbs with known epitopes were compared for each immobilization method. Binding of bNAbs targeting the V1V2, V3, CD4 binding site, and gp120/gp41 interface was comparable for all antigen immobilization methods. However, directly coated HIV-1 SOSIP ELISAs showed detectable binding of 17b, a CD4-induced antibody that binds a V3 epitope that is concealed on closed prefusion Env trimers in the absence of added CD4, whereas antibody-immobilized and randomly biotinylated Env-coated ELISAs did not show detectable binding of 17b in the absence of CD4. We conclude direct coating of HIV-1 SOSIPs on ELISA plates can result in exposure of CD4-induced antibody epitopes, suggesting disruption of Env structure and exposure of epitopes that are hidden in the closed, prefusion trimer.

Introduction

In 2020, 38 million individuals were living with human immunodeficiency virus-1 (HIV-1), the causative agent of acquired immunodeficiency syndrome (AIDS) (unaids.org). Despite 40 years of effort, a successful vaccine to prevent HIV-1 infection has not been developed. Current work towards vaccine design has focused on understanding how rare cases of natural infection induce broadly neutralizing antibodies (bNAbs) and how such antibody responses could be elicited by vaccination [1,2]. Efforts towards designing bNAb-inducing immunogens are focused on the closed, prefusion state of the HIV-1 Envelope (Env) trimer, the sole viral protein on the virion surface, which interacts with host cell receptors leading to viral entry into host cells [3–6]. The HIV-1 Env is a homotrimer composed of heavily-glycosylated gp120-gp41 heterodimers. To gain entry into cells, the Env gp120 subunit binds host CD4 receptors causing conformational changes that lead to virus and host cell membrane fusion and viral entry. These changes have been structurally characterized and include displacement of the gp120 V1V2 loops to expose occluded V3 loops and the CCR5/CXCR4 co-receptor binding site resulting in CD4-bound "open" trimers (Fig. 1) [7–9].

Broadly neutralizing antibodies (bNAbs) have been isolated from a subset of HIV-1–infected donors and target conserved epitopes of the HIV-1 Env with exceptional breadth and potency [10]. bNAbs have been characterized to contain uncommon features that have been found necessary to accommodate the dense glycan shield concealing conserved Env epitopes and are elicited only in rare cases of natural infection [2,10]. Most bNAbs target epitopes on the closed prefusion HIV-1 Env conformation, although more strain-specific antibodies have been found to bind epitopes that are hidden on closed, prefusion Env trimers that are usually only exposed after CD4 binding (Fig. 1) [7,11,12].

A soluble form of the trimeric Env ectodomain, called Env SOSIP [13], was designed with stabilizing mutations to favor the closed, prefusion Env conformation targeted by bNAbs and to allow Envs to be studied biochemically and structurally and used as immunogens. Structural biology and DEER spectroscopy have characterized the conformational profiles of soluble SOSIP Env proteins, finding that unliganded SOSIP trimers adapt a prefusion,

closed conformation and that interactions of SOSIP trimers with soluble CD4 (sCD4) leads to the above described conformational changes (Fig. 1) [7,8,10,14,15]. Both the closed prefusion and CD4-induced open SOSIP conformations are consistent with cryo-electron tomography and sub-tomogram averaged structures of HIV-1 Envs found on virions [16–20]. Although SOSIP Envs can adopt both open and closed trimer conformations, HIV-1 immunogen design efforts seek to raise bNAbs against closed prefusion Envs, thus methods to evaluate antibody binding to SOSIPs should maintain the closed Env conformation in the absence of added sCD4.

Enzyme-linked immunosorbent assays (ELISAs) are routinely used to characterize bNAb binding and evaluate polyclonal serum responses for vaccine development. In an ELISA, the soluble form of the HIV-1 Env SOSIP is generally immobilized on the surface of the assay plate, and then bNAbs or sera are added and detected through a secondary antibody conjugated to an enzyme capable of a colorimetric readout in the presence of its substrate. Since bNAbs target the closed, pre-fusion conformation of Env, it is essential that Env-coating methods in an ELISA do not alter or disrupt the native-like closed prefusion Env conformation or binding to normally hidden epitopes would be observed. ELISAs that evaluate antibody binding to antigens often involve direct addition of antigen to an ELISA plate, where it associates with the plastic wells in an unknown manner. Although association with plastic likely does not affect the conformation of most antigens, the ability of HIV-1 SOSIP Env trimers to undergo large conformational changes could cause SOSIPs to adopt different conformations when associating with plastic wells. In addition, the dense glycan shield on HIV-1 Envs, which varies between strains, could cause strain-specific differences in how SOSIPs adhere to plastic that could affect binding of some types of antibodies.

To better understand how Env immobilization affects bNAb binding, we compared direct coating of SOSIP Envs on ELISA plates with other attachment methods that avoid direct contact of HIV-1 SOSIP Envs with plastic. In the preferred method, a peptide tag is added to the SOSIP C-terminus, allowing site-specific biotinylation or capture by an antibody for oriented coupling to an ELISA plate [13,21]. Because terminally-tagged proteins can lose their tags due to proteolysis upon storage (unpublished observations) and/or are not always

available for ELISAs involving multiple SOSIPs, we tried a method that would allow already-prepared untagged SOSIPs to be used in an ELISA without direct coating onto plastic: attaching biotins randomly to primary amines on SOSIP Env and coating the randomly biotinylated SOSIPs on a streptavidin assay plate.

Results

Directly coated BG505 SOSIP Env ELISAs show detectable 17b binding in the absence of sCD4

To evaluate how SOSIP Env antigen immobilization affects antibody binding in ELISAs, we compared three different methods for immobilizing HIV-1 Env antigens. SOSIP Envs were either directly coated onto polystyrene plastic wells, captured by a C-terminal D7324 affinity tag using the JR-52 mAb [13], or randomly biotinylated and immobilized on streptavidin-coated wells (Fig. 2a). For randomly biotinylated SOSIP ELISAs, biotins were chemically attached to primary amines (lysine residues and N-termini). Since the biotinylation reaction does not go to completion, not all primary amines have attached biotins, resulting in SOSIPs with different sets of biotinylated lysines. For example, in BG505 SOSIP, we measured only 1-10 biotins per gp120-gp41 protomer, although each protomer contains 33 lysines (Fig. 2b). Since a random set of lysines are biotinylated on each protomer within a population of Env trimers, it is unlikely that particular lysines would be targeted among those that are accessible (Fig. 2b) or that particular antibody epitopes would be occluded within the overall population of Env trimers.

These SOSIP Env immobilization methods were used to compare binding of bNAbs to different epitopes on the clade A BG505 SOSIP trimer (Supplementary Table 1)[13]. We selected the following bNAbs against defined Env epitopes: PG9 against the V1V2 apex, 10-1074 against the V3 loop, 3BNC117 against the CD4 binding site, and 8ANC195 against the gp120-gp41 interface (Fig. 1, Supplementary Table 2). We chose the mAb 17b to assess conformational integrity of immobilized SOSIP Envs because it recognizes an occluded V3 epitope that is exposed only upon CD4 binding (Fig. 1, Supplementary Table 2) [7,8,22–25]. In the original characterization of the native-like BG505 SOSIP Env trimer, 17b

showed binding only in the presence of sCD4, which demonstrated that it was properly folded and stabilized in the closed prefusion conformation [13].

Binding for PG9, 10-1074, 3BNC117, and 8ANC195 was comparable among directly coated, D7324-tag immobilized, and randomly biotinylated BG505 SOSIP ELISAs (Fig. 2c). As expected, all ELISA methods showed binding for 17b in the presence of sCD4 (Fig. 2c). However, directly coated Env ELISAs showed substantial binding of 17b in the absence of sCD4, whereas D7324-immoblized and randomly biotinylated SOSIP ELISAs did not show binding for 17b alone (Fig. 2c). These results demonstrate that all ELISA coating methods allow detection of CD4-induced conformational changes, but that direct coating of the BG505 SOSIP on an ELISA plate inappropriately exposes the 17b epitope that is occluded on the stabilized closed, prefusion Env trimer structure.

Multiple Env SOSIPs and SOSIP-based immunogens showed binding of 17b in the absence of sCD4 when directly coated on plastic

To investigate whether other SOSIP Env trimers exposed the 17b epitope in the absence of added sCD4, we evaluated 17b binding in the absence and presence of sCD4 against SOSIP Envs from diverse HIV-1 strains that were immobilized through direct coating, the D7324 tag, or random biotinylation (Fig. 3a). These included SOSIP Envs from clade B strains B41 and Yu2, clade C strains Du422 and 426c, and ConM and ConC Envs representing consensus sequence of group M and C Env isolates, respectively [26]. We observed 17b binding in all ELISAs in the presence of sCD4, as expected, although 17b binding in the presence of sCD4 was lower for randomly biotinylated SOSIPs compared to directly coated and D7324-tagged Env (Fig. 3a), demonstrating that all SOSIP trimers evaluated were able to undergo CD4-induced conformation changes. However, with the exception of ConM, directly coated SOSIP ELISAs showed 17b binding to SOSIPs in the absence of sCD4, whereas for D7324-tagged and randomly biotinylated Env, 17b binding only occurred in the presence of added sCD4. These results demonstrated exposure of the 17b epitope upon direct coating of most SOSIP Env trimers, thus suggesting that plastic-induced

conformational changes in SOSIP Envs is a commonly-seen phenomenon that could affect interpretation of ELISA results.

An important application of Env antigen ELISAs includes evaluating binding of bNAbs, mAbs, and polyclonal serum from immunized animals against Env-based immunogens that include mutations intended to target or elicit particular bNAb precursors. These ELISAs have been used to characterize how antibodies elicited *in vivo* interact with immunogens. To determine if engineered Env-based immunogens are affected by Env-coating methods, we compared 17b binding in the absence and presence of sCD4 against known SOSIP Env-based immunogens. We chose the RC1, RC1-4fill, and 11MUTB immunogens that were developed to elicit V3 bNAb responses [27,28] and have been tested in immunization regimens in animal studies (Supplementary Table 1) [29]. We also included BG505 SOSIP.v4.1-GT1 (GT1), an immunogen engineered to interact with the V1V2 apex and CD4-binding site bNAb precursors and currently being evaluated in human clinical trials (Supplementary Table 1) [30]. All immunogens included Env residue substitutions and the addition and/or deletion of certain Env N-linked glycan sites. Immunogens were either directly coated and immobilized on ELISA plates or randomly biotinylated and immobilized via streptavidin-coated plates. Consistent with previous observations for the unaltered "wildtype" SOSIP Env trimers, sCD4 bound to diverse Env strains (Fig. 3a) and Env-based immunogens (Fig. 3b) tested (Supplementary Fig. 1). However, once again, detectable 17b binding in the absence of sCD4 was observed for all directly coated Env-based immunogens and not for those that were randomly biotinylated.

Discussion

The HIV-1 Env trimer is a highly evolved fusion machine that undergoes large conformational changes during host receptor engagement. Therefore, methods used to investigate binding properties of soluble Env SOSIPs commonly used as immunogens and to evaluate bNAb binding must ensure the native-like closed, prefusion Env trimer conformation is maintained in the absence of CD4 engagement. ELISAs are widely utilized in HIV-1 research to detect the of binding of bNAbs and polyclonal serum antibodies to

Envs. Several methods have been used to immobilize SOSIP Envs on ELISA plates. In our comparison of three methods commonly used to immobilize HIV-1 SOSIP on ELISA plates and detect bNAb binding, we found that directly coating HIV-1 Env SOSIPs on plates leads to aberrant binding of the CD4-induced 17b antibody in the absence of sCD4. This suggests that the HIV-1 Env is not maintaining a prefusion, closed conformation representative of the closed, prefusion conformation of native Envs on virions [16–20] and instead exposes a concealed V3 epitope found on sCD4-bound open Env trimer structures [7,8]. Exposure of the V3 epitope occurs when CD4 interacts with Env and causes conformational changes in the gp120 subunit leading to displacement of the V1V2 loops by ~40 Å from the trimer apex to the sides of the trimer [7,8]. 17b binding to directly coated SOSIP Env trimers in the absence of sCD4 addition suggests that interactions with plastic can disrupt the native-like closed, prefusion Env structure, leading to V3 exposure and subsequent binding of 17b. Therefore, directly coating SOSIPs on ELISA plates could lead to detection of binding of antibodies against occluded epitopes that would not normally recognize a closed, prefusion Env trimer, confounding interpretation of antibody binding and epitope mapping experiments. This would especially be problematic when using ELISAs for antibody epitope mapping studies in which mutations were introduced in defined Env epitopes, since the original and mutant SOSIPs could differ in their interactions with plastic. This could result in artifactually different antibody binding profiles.

The preferred methodology for SOSIP ELISAs is to use a C-terminal affinity tag capture immobilization so that the SOSIP Env does not interact directly with the plastic wells [13,21]. However, in some cases, an investigator may wish to compare antibody binding to a large number of already-prepared untagged SOSIP Envs. In this instance, random biotinylation and coating onto a streptavidin plate could be used instead of re-expression and purification of tagged SOSIP Env trimers. Since biotinylation methods can be optimized to biotinylate only a fraction of the primary amines (lysine side chains and the N-termini), it is unlikely that any particular antibody epitope would be occluded on all Env trimers within a randomly biotinylated population of SOSIPs, as demonstrated here for bNAb recognition of randomly biotinylated BG505 SOSIP. Importantly, in common with the C-terminal tag-immobilized SOSIPs, but not with directly coated SOSIPs, randomly biotinylated SOSIPs

exhibited binding of the CD4-induced 17b mAb in the presence, but not the absence, of added sCD4. This suggested that proper folding of the closed, prefusion SOSIP Env trimer was maintained during an ELISA experiment involving randomly biotinylated SOSIPs. We note, however, that 17b binding in the presence of sCD4 was reduced in the randomly biotinylated SOSIPs compared with C-terminally tagged or directly coated SOSIPs, suggesting some interference with CD4-induced gp120 and gp41 conformational changes resulting from randomly biotinylation. Therefore, C-terminally tagged SOSIP Env trimers should be used for ELISA experiments involving quantitative assessment of sCD4-induced conformational changes but are not required for ELISAs evaluating antibodies binding to closed, prefusion Env trimers or non-quantitative ELISAs assessing binding to CD4-induced epitopes.

Methods

Protein expression and purification

The Expi293 transient transfection system (Thermo Fisher) was used to express Fabs and sCD4 as previously described [12]. The expression vectors for Fabs contained genes for a light chain (LC) and a C-terminally 6x-His tagged heavy chain (HC), and expression vectors for sCD4 encoded the D1D2 subunits of sCD4 followed by a C-terminal 6x-His tag. Fabs and sCD4 were purified from cell supernatants using a Ni^{2+}-NTA (GE Healthcare) affinity chromatography column, followed by a Superdex 200 10 300 size exclusion chromatography (SEC) column (Cytiva).

HIV-1 SOSIP.664 Env constructs contained the following modifications: disulfide mutations 501C and 650C (SOS), I55P (IP), and the furin cleavage site mutated to six arginine residues (6R) [13]. D7324-tagged Env SOSIPs encoded a GSAPTKAKRRVVQREKR sequence after residue 664 in the gp41 ectodomain [13]. HIV-1 SOSIP.664 Env-based immunogens contained further mutations as described previously (Supplementary Table 1) [27–30]. Genes encoding all HIV-1 SOSIP.664-based constructs were expressed using the Expi293 transient transfection system (Thermo Fisher). All Envs were separated from cell supernatants using a 2G12 or PGT145 immunoaffinity chromatography column followed by SEC using a Superose 6 10/300 column (Cytiva) as described [13,31].

Enzyme-linked immunosorbent assay (ELISA)

HIV-1 SOSIP.664 trimer antigens were coated onto ELISA plates by three different methods. For directly coated antigen ELISAs, Corning Costar high-binding 96-well plates were coated with 5 μg/mL of a SOSIP diluted in 0.1 M $NaHCO_3$ (pH 9.6) and incubated overnight at 4°C. Unbound trimers were removed by washing, and plates were blocked with 3% BSA in TBS-T (20mM Tris, 150 mM NaCl, 0.1% Tween20) for 1 hour at room temperature, and then buffer was removed. For D7324-capture ELISAs involving immobilization of D7324-tagged SOSIPs to the JR52 mAb [13], JR-52 (kind gift from James Robinson, Tulane University) was coated on Corning Costar high-binding 96-well plates

in 0.1 M $NaHCO_3$ (pH 9.6) and incubated overnight at 4°C [13]. Excess JR-52 was removed, plates were blocked for one hour at room temperature in 3% BSA in TBS-T, and blocking buffer was removed. D7324-tagged Envs were added at 5 µg/mL in 3% BSA in TBS-T and incubated at room temperature for one hour before buffer was removed. For randomly biotinylated antigen ELISAs, Env trimers were randomly biotinylated using the EZ-Link NHS-PEG4-Biotin kit (Thermo Fisher Scientific) according to the manufacturer's guidelines. The Pierce Biotin Quantitation kit (Thermo Fisher Scientific) was used to quantify the number of biotin molecules per Env protomer, resulting in an average of 1-10 biotins attached to each Env protomer. Randomly biotinylated Envs were added to streptavidin-coated 96-well plates (Thermo Fisher Scientific) at a concentration of 5 µg/mL diluted in 3% BSA in TBS-T. Plates were incubated for two hours, and then access antigen was removed.

For some experiments, sCD4 was added at 100 µg/mL and incubated at room temperature for two hours. bNAb Fabs or sCD4 were serially diluted in 3% BSA in TBS-T at a top concentration of 20 µg/mL and 100 µg/mL, respectively, and then incubated for two hours at room temperature. Fabs and sCD4 were removed and plates were washed twice with TBS-T. Horseradish peroxidase (HRP) labeled secondary against the human IgG H+L (Southern BioTech) added at 1:10,000 dilution in TBS-T to detect Fab binding or HRP labeled secondary against the 6x-His tag (Genscript) added a 1:5000 dilution in TBS-T to detect His-tagged sCD4 were added and incubated at room temperature for 30 minutes. Plates were then washed three times with TBS-T. Ultra TMB-ELISA Substrate Solution (ThermoFisher Scientific) was added for colorimetric detection and quenched with 1.0 N HCl. Absorption was measure at 450 nm. Two independent biological replicates (n=2) were performed for all assays.

Acknowledgements

We thank J. Vielmetter, P. Hoffman, the Protein Expression Center in the Beckman Institute at Caltech for expression assistance, and J.E. Robinson (Tulane University) for the JR-52 antibody. This work was supported by the National Institute of Allergy and

Infectious Diseases (NIAID) Grant HIVRAD P01 AI100148 (to P.J.B.) and the Bill and Melinda Gates Foundation Collaboration for AIDS Vaccine Discovery (CAVD) grant INV-002143 (P.J.B.).

Author contributions

K.A.D. and P.J.B. designed the research. K.A.D. and P.S.M. performed experiments and K.A.D. and P.J.B. analyzed results. K.A.D. and P.J.B. wrote the manuscript with input from co-authors.

Competing interests

The authors declare that there are no competing interests.

Data Availability

The datasets generated during and analyzed in this study are available from the corresponding author on reasonable request.

References

1. Lee, J. H. & Crotty, S. HIV vaccinology: 2021 update. *Semin. Immunol.* **51**, 101470 (2021).

2. Abernathy, M. E., Dam, K.-M. A., Esswein, S. R., Jette, C. A. & Bjorkman, P. J. How Antibodies Recognize Pathogenic Viruses: Structural Correlates of Antibody Neutralization of HIV-1, SARS-CoV-2, and Zika. *Viruses* **13**, 2106 (2021).

3. Ward, A. B. & Wilson, I. A. The HIV-1 envelope glycoprotein structure: nailing down a moving target. *Immunol. Rev.* **275**, 21–32 (2017).

4. Ward, A. B. & Wilson, I. A. Innovations in structure-based antigen design and immune monitoring for next generation vaccines. *Curr. Opin. Immunol.* **65**, 50–56 (2020).

5. Derking, R. & Sanders, R. W. Structure-guided envelope trimer design in HIV-1 vaccine development: a narrative review. *J. Int. AIDS Soc.* **24**, (2021).

6. Sanders, R. W. & Moore, J. P. Native-like Env trimers as a platform for HIV-1 vaccine design. *Immunol. Rev.* **275**, 161–182 (2017).

7. Ozorowski, G. *et al.* Open and closed structures reveal allostery and pliability in the HIV-1 envelope spike. *Nat. Publ. Group* **547**, 360–363 (2017).

8. Wang, H. *et al.* Cryo-EM structure of a CD4-bound open HIV-1 envelope trimer reveals structural rearrangements of the gp120 V1V2 loop. *Proc. Natl. Acad. Sci. U. S. A.* **113**, E7151–E7158 (2016).

9. Wang, H., Barnes, C. O., Yang, Z., Nussenzweig, M. C. & Bjorkman, P. J. Partially Open HIV-1 Envelope Structures Exhibit Conformational Changes Relevant for Coreceptor Binding and Fusion. *Cell Host Microbe* **24**, 579-592.e4 (2018).

10. West, A. P. *et al.* Structural Insights on the Role of Antibodies in HIV-1 Vaccine and Therapy. *Cell* **156**, 633–648 (2014).

11. Yang, Z., Wang, H., Liu, A. Z., Gristick, H. B. & Bjorkman, P. J. Asymmetric opening of HIV-1 Env bound to CD4 and a coreceptor-mimicking antibody. *Nat. Struct. Mol. Biol.* **26**, 1167–1175 (2019).

12. Yang, Z. *et al.* Neutralizing antibodies induced in immunized macaques recognize the CD4-binding site on an occluded-open HIV-1 envelope trimer. *Nat. Commun.* **13**, 732 (2022).

13. Sanders, R. W. *et al.* A Next-Generation Cleaved, Soluble HIV-1 Env Trimer, BG505 SOSIP.664 gp140, Expresses Multiple Epitopes for Broadly Neutralizing but Not Non-Neutralizing Antibodies. *PLoS Pathog.* **9**, e1003618-20 (2013).

14. Stadtmueller, B. M. *et al.* DEER Spectroscopy Measurements Reveal Multiple Conformations of HIV-1 SOSIP Envelopes that Show Similarities with Envelopes on Native Virions. *Immunity* 1–27 (2018) doi:10.1016/j.immuni.2018.06.017.

15. Lyumkis, D. *et al.* Cryo-EM Structure of a Fully Glycosylated Soluble Cleaved HIV-1 Envelope Trimer. *Science* **342**, 1484–1490 (2013).

16. Bartesaghi, A., Merk, A., Borgnia, M. J., Milne, J. L. S. & Subramaniam, S. Prefusion structure of trimeric HIV-1 envelope glycoprotein determined by cryo-electron microscopy. *Nat. Struct. Mol. Biol.* **20**, 1352–1357 (2013).

17. Merk, A. & Subramaniam, S. HIV-1 envelope glycoprotein structure. *Curr. Opin. Struct. Biol.* **23**, 268–276 (2013).

18. Liu, J., Bartesaghi, A., Borgnia, M. J., Sapiro, G. & Subramaniam, S. Molecular architecture of native HIV-1 gp120 trimers. *Nature* **455**, 109–113 (2008).

19. Li, Z. *et al.* Subnanometer structures of HIV-1 envelope trimers on aldrithiol-2-inactivated virus particles. *Nat. Struct. Mol. Biol.* **27**, 726–734 (2020).

20. Mangala Prasad, V. *et al.* Cryo-ET of Env on intact HIV virions reveals structural variation and positioning on the Gag lattice. *Cell* **185**, 641-653.e17 (2022).

21. Derking, R. *et al.* Comprehensive Antigenic Map of a Cleaved Soluble HIV-1 Envelope Trimer. *PLoS Pathog.* **11**, e1004767-22 (2015).

22. Walker, L. M. *et al.* Broad and Potent Neutralizing Antibodies from an African Donor Reveal a New HIV-1 Vaccine Target. *Science* **326**, 285–289 (2009).

23. Gristick, H. B. *et al.* Natively glycosylated HIV-1 Env structure reveals new mode for antibody recognition of the CD4-binding site. *Nat. Publ. Group* **23**, 906–915 (2016).

24. Scheid, J. F. *et al.* Sequence and Structural Convergence of Broad and Potent HIV Antibodies That Mimic CD4 Binding. *Science* **333**, 1633–1637 (2011).

25. Scharf, L. *et al.* Broadly Neutralizing Antibody 8ANC195 Recognizes Closed and Open States of HIV-1 Env. *Cell* 1–13 (2018) doi:10.1016/j.cell.2015.08.035.

26. Sliepen, K. *et al.* Structure and immunogenicity of a stabilized HIV-1 envelope trimer based on a group-M consensus sequence. *Nat. Commun.* **10**, 2355 (2019).

27. Steichen, J. M. *et al.* HIV Vaccine Design to Target Germline Precursors of Glycan-Dependent Broadly Neutralizing Antibodies. *Immunity* **45**, 483–496 (2016).

28. Escolano, A. *et al.* Immunization expands B cells specific to HIV-1 V3 glycan in mice and macaques. *Nature* **570**, 468–473 (2019).

29. Escolano, A. *et al.* Sequential immunization of macaques elicits heterologous neutralizing antibodies targeting the V3-glycan patch of HIV-1 Env. *Sci. Transl. Med.* **13**, eabk1533 (2021).

30. Medina-Ramírez, M. *et al.* Design and crystal structure of a native-like HIV-1 envelope trimer that engages multiple broadly neutralizing antibody precursors in vivo. *J. Exp. Med.* **214**, 2573–2590 (2017).

31. Cupo, A. *et al.* Optimizing the production and affinity purification of HIV-1 envelope glycoprotein SOSIP trimers from transiently transfected CHO cells. *PLOS ONE* **14**, e0215106 (2019).

32. Pettersen, E. F. *et al.* UCSF ChimeraX : Structure visualization for researchers, educators, and developers. *Protein Sci.* **30**, 70–82 (2021).

33. Goddard, T. D. *et al.* UCSF ChimeraX: Meeting modern challenges in visualization and analysis: UCSF ChimeraX Visualization System. *Protein Sci.* **27**, 14–25 (2018).

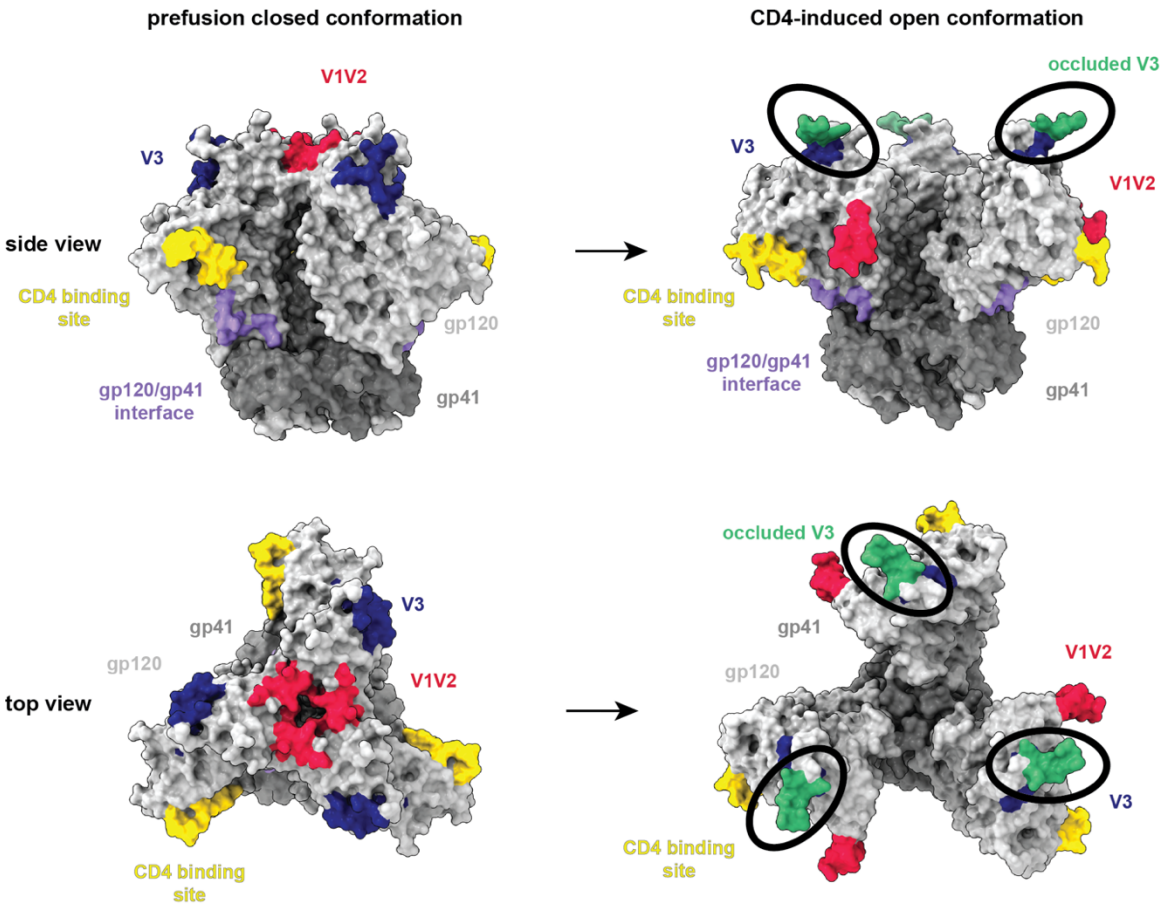

Figure 1: Summary of HIV-1 antibody binding sites on closed and CD4-induced open Env conformations. Surface depictions of HIV-1 Envs in closed and open conformations are shown from the side (top row) and from the top (bottom row). Left: HIV-1 bNAbs target epitopes on the closed, prefusion Env conformation (PDB 5T3Z) including V1V2 (crimson) (e.g., PG9), V3 (blue) (e.g., 10-1074), the CD4 binding site (yellow) (e.g., 3BNC117), and the gp120-gp41 interface (purple) (e.g., 8ANC195). Right: Upon interaction with CD4, Env undergoes conformational changes, including V1V2 displacement and exposure of the V3 base that is occluded in the closed conformation. The CD4-induced, open Env (PDB 5VN3) conformation is depicted with the occluded V3 regions (sea green) indicated in black ovals. 17b is an example of antibody that binds the occluded V3 epitope when Env is in the CD4-induced, open conformation. This figure was generated using UCSF ChimeraXv1.2.5[32,33].

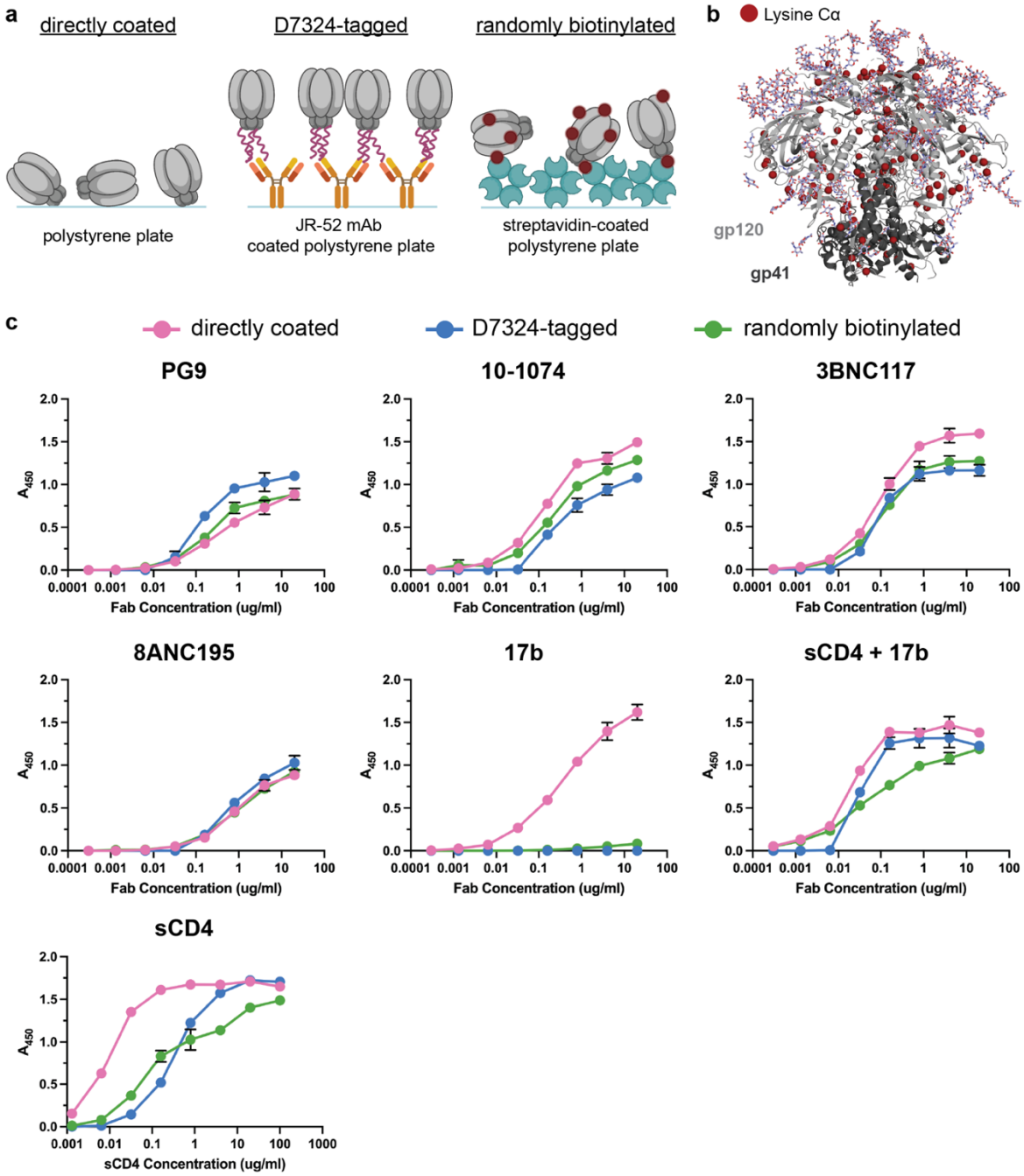
a
directly coated
D7324-tagged
randomly biotinylated
polystyrene plate
JR-52 mAb
coated polystyrene plate
streptavidin-coated
polystyrene plate
b
Lysine Cα
gp120
gp41
c
directly coated
D7324-tagged
randomly biotinylated
PG9
10-1074
3BNC117
8ANC195
17b
sCD4 + 17b
sCD4
A450
Fab Concentration (ug/ml)
sCD4 Concentration (ug/ml)

Figure 2: ELISA methods to immobilize BG505 SOSIP affect binding of the CD4-induced 17b antibody

(**a**) Representation of ELISA methods to immobilize the HIV-1 Env antigen include directly coating the Env on polystyrene plates, capturing Env that contains a D7324 affinity tag with the mAb, JR-52, and randomly biotinylating Env to immobilize on streptavidin-coated plates. Created with BioRender.com. (**b**) Structure of HIV-1 Env (PDB 5T3Z) with the locations of primary amine lysine carbon-alpha atoms (Cα) indicated as red spheres. The abundance of Env lysines allows for minimal disruption to the Env structure when biotinylating only 1-10 lysines per protomer. Created with The PyMolv2.2.3 Molecular Graphics System (Schrödinger, LLC). (**c**) ELISAs comparing binding of bNAbs and sCD4 for directly coated (pink), D7324-tagged (blue), and randomly biotinylated (green) BG505 Env immobilization methods. Values shown are means ± s.d. of two biological replicates (n=2). Error bars are not visible for data points where the bars are smaller than the symbol representing the mean.

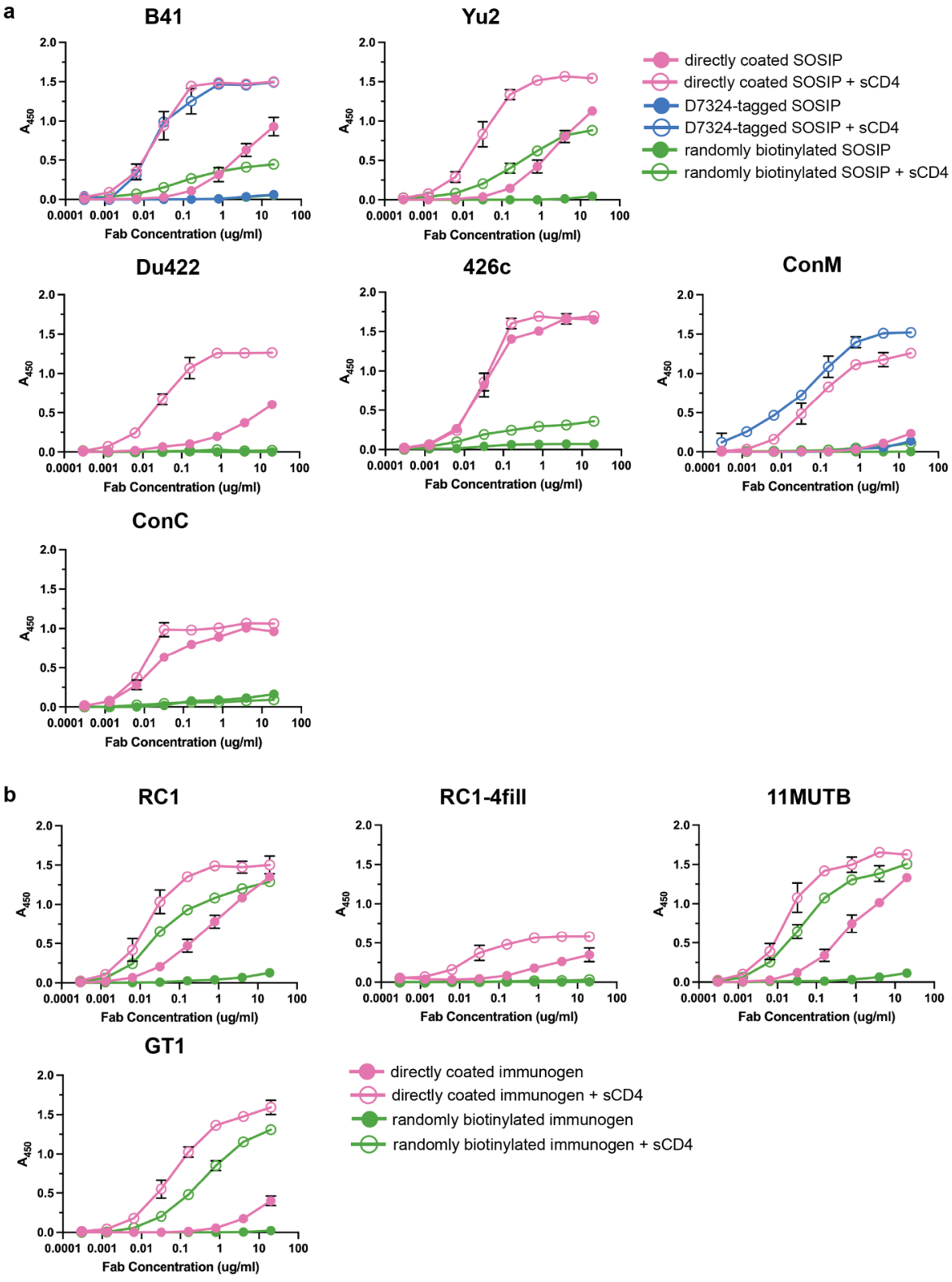
a
B41
Yu2
Du422
426c
ConM
ConC
directly coated SOSIP
directly coated SOSIP + sCD4
D7324-tagged SOSIP
D7324-tagged SOSIP + sCD4
randomly biotinylated SOSIP
randomly biotinylated SOSIP + sCD4
A450
Fab Concentration (ug/ml)
b
RC1
RC1-4fill
11MUTB
GT1
directly coated immunogen
directly coated immunogen + sCD4
randomly biotinylated immunogen
randomly biotinylated immunogen + sCD4

Figure 3: Directed coated ELISAs show 17b binding in the absence of sCD4 for multiple Env strains and Env-based immunogens

(**a**) ELISAs to compare 17b binding in the absence and presence of sCD4 to Clade B (B41, Yu2), Clade C (Du422, 426c) and consensus sequence (ConM and ConC) Envs for directly coated (pink), D7324-tagged (blue), and randomly biotinylated (green) Env immobilization methods. (**b**) ELISAs comparing 17b binding in the absence and presence of CD4 to V3-targeting (RC1, RC1-4fill, 11MUTB) and CD4bs (GT1) Env-based immunogens for directly coated (pink) and randomly biotinylated (green) Env immobilization methods. Values shown are means ± s.d. of two biological replicates (n=2). Error bars are not visible for data points where the bars are smaller than the symbol representing the mean.

Supplemental Information

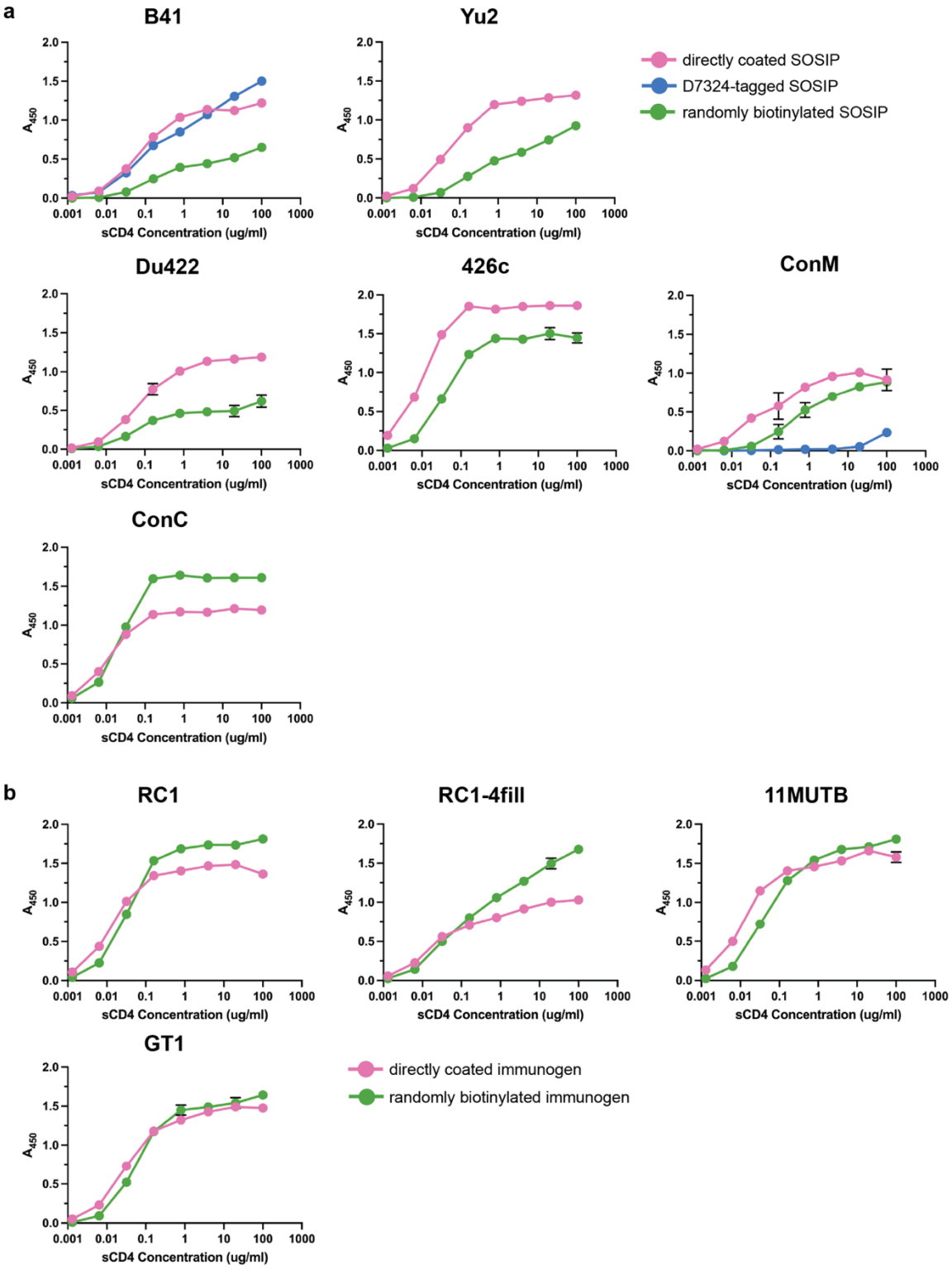

Supplementary Figure 1: All Env coating ELISA methods lead to sCD4 binding

(**a**) ELISAs to compare sCD4 binding to Clade B (B41, Yu2), Clade C (Du422, 426c) and consensus sequence (ConM and ConC) Envs for directly coated (pink), D7324-tagged (blue), and randomly biotinylated (green) Env immobilization methods. (**b**) ELISAs comparing binding of CD4 to V3-targeting (RC1, RC1-4fill, 11MUTB) and CD4bs (GT1) Env-based immunogens for directly coated (pink) and randomly biotinylated (green) Env immobilization methods. Values shown are means ± s.d. of two biological replicates (n=2). Error bars are not visible for data points where the bars are smaller than the symbol representing the mean.

Supplementary Table 1: Summary of HIV-1 Env SOSIPs used in ELISA experiments

Strain	Clade	Tier	Mutations	Reference
BG505	A	2	SOSIP (501C-605C, I559P, R6); added PNGS: 332	Sanders, et al., *PLOS Pathog.,* (2013)
B41	B	2	SOSIP (501C-605C, I559P, R6)	Pugach, et al., *J. Virol*, (2015)
Yu2	B	2	SOSIP (501C-605C, I559P, R6)	Dosenovic, et al., *Cell*, (2015)
Du422	C	2	SOSIP (501C-605C, I559P, R6)	Julien, et al., *PNAS*, (2015)
426c	C	2	SOSIP (501C-605C, I559P, R6)	Borst, et al., Elife, (2018)
ConM	N/A	1A	SOSIP (501C-605C, I559P, R6)	Sliepen, et al., *Nat. Commun.,* (2019)
ConC	N/A	unknown	SOSIP (501C-605C, I559P, R6)	Rutten, et al., *Cell Rep.,* (2018)
RC1	A	N/A	SOSIP (501C-605C, I559P, R6); added PNGS: 332; point mutations: V134Y, N136P, I138L, D140N, N137F, T320F, Q328M, T415V; PNGS deletions: N133, N137, N156	Escolano*, Gristick*, et al., *Nature*, (2019)
RC1-4fill	A	N/A	SOSIP (501C-605C, I559P, R6); added PNGS: 230, 241, 289, 332, 344; PNGS deletions: N133, N137, N157; point mutations: V134Y, N136P, I138L, D140N, N137F, T320F, Q328M, T415V	Escolano*, Gristick*, et al., *Nature*, (2019)
11MUTB	A	N/A	SOSIP (501C-605C, I559P, R6); added PNGS: 332; PNGS deletions: N133, N137; point mutations: V134Y, N136P, I138L, D140N, N137F, T320F, Q328M, T415V	Steichen, et al., *Immunity*, (2016)
GT1	A	N/A	SOSIP (501C-605C, I559P, R6); added PNGS: 332; PNGS deletions: N197, N276, N462; point mutations: K169R, Y173H, S174A, R179K, V181I, Q183P, G188N, N189T, E190S, delR_{185f}SNNSNK_{189}, T278R, G471S	Medina-Ramírez, et al., *JEM*, (2017)

*Indicates authors contributed equally

Supplementary Table 2: Summary of antibodies used in ELISA experiments

mAb	Epitope	PDB accession code	Reference
PG9	V1V2	5VJ6	Wang, et al., *Elife,* (2017)
10-1074	V3	5T3Z	Gristick, et al., *NSMB,* (2016)
3BNC117	CD4 binding site	5V8M	Lee, et al., *Immunity*, (2017)
8ANC195	gp120/gp41 interface	5VJ6	Wang, et al., *Elife,* (2017)
17b	V3 base	5VN3	Ozorowski, et al., *Nature*, (2017)

Chapter VI

HIV-1 CD4-BINDING SITE GERMLINE ANTIBODY–ENV STRUCTURES INFORM VACCINE DESIGN

Dam, K.A., Barnes, C. O., Gristick, H. B., Schoofs, T., Gnanapragasam, P. N. P., Nussenzweig, M. C., & Bjorkman, P. J. (2022). HIV-1 CD4-binding site germline antibody–Env structures inform vaccine design. *Nature Communications*, 13, 6123. https://doi.org/10.1101/2022.03.25.485873

Abstract

BG24, a VRC01-class broadly neutralizing antibody (bNAb) against HIV-1 Env with relatively few somatic hypermutations (SHMs), represents a promising target for vaccine strategies to elicit CD4-binding site (CD4bs) bNAbs. To understand how SHMs correlate with BG24 neutralization of HIV-1, we report 4.1 Å and 3.4 Å single-particle cryo-EM structures of two inferred germline (iGL) BG24 precursors complexed with engineered Env-based immunogens lacking CD4bs N-glycans. Structures reveal critical Env contacts by $BG24_{iGL}$ and identify antibody light chain structural features that impede Env recognition. In addition, biochemical data and cryo-EM structures of $BG24_{iGL}$ variants bound to Envs with CD4bs glycans present provide insights into N-glycan accommodation, including structural modes of light chain adaptations in the presence of the $N276_{gp120}$ glycan. Together, these findings reveal Env regions critical for germline antibody recognition and potential sites to alter in immunogen design.

Introduction

Current strategies to engineer a vaccine towards preventing HIV-1 infection involve designing Env-mimetic immunogens that can elicit broadly neutralizing antibodies (bNAbs)[1–4]. The CD4-binding site (CD4bs) epitope is a target of immunogen design as bNAbs in this class have been shown to be among the most potent and broad[5–9]. Several studies have shown passive immunization using CD4bs bNAbs can confer protection from HIV-1 infection in animal models and human clinical trials, suggesting that immunization strategies to elicit these antibodies at effective concentrations would also be protective[6,10–17]. This includes the VRC01-class of bNAbs that are derived from the VH1-2*02 variable heavy chain gene segment and are characterized by a short 5 amino acid complementary determining region 3 (CDR3) in the antibody (Ab) light chain and a shortened or flexible CDRL1[5,18]. These characteristics are necessary for VRC01-class bNAbs to accommodate the heavily N-glycosylated landscape of the CD4bs of HIV-1 Envs. Thus, VRC01-class bNAbs generally require high levels of somatic hypermutation (SHM), which is challenging to elicit through vaccination.

Germline precursors of bNAbs do not generally show detectable binding to non-engineered, natively-glycosylated HIV-1 Envs[19,20], therefore, the germline targeting approach to HIV-1 vaccine design involves efforts to engineer immunogens that can engage germline B cell receptors (BCRs) and initiate bNAb development[21]. Inferred germline (iGL) versions of mature bNAbs derived from predicted germline gene segment sequences represented in the human B cell repertoire[22,23] are used for the germline targeting approach. Analysis of VRC01-class iGLs has shown that the human VH1-2*02 heavy chain gene segment encodes signature residues that are required for breadth and potency[18]. Furthermore, germline VRC01-class precursors have been isolated from naïve individuals and mature bNAbs have been identified from multiple HIV-1-infected human donors, suggesting that raising this class of bNAbs is not uncommon in natural infection[24,25]. Taken together, VRC01-class bNAbs are attractive targets for immunogen design.

The VRC01-class of bNAbs targets a particularly challenging epitope to elicit bNAbs against due to the presence of the CD4bs N-glycans that sterically obstruct interactions

between Env and Ab CDRs[26]. The glycan at position $N276_{gp120}$ is highly conserved and poses the greatest steric barrier to binding VRC01-class bNAb iGLs, as Ab residues in the iGL CDRL1 that interact with this region are typically 11-12 residues and cannot accommodate the $N276_{gp120}$ glycan. Mature CD4bs Abs develop shortened or flexible CDRL1s to accommodate this glycan[24,27,28]. Thus, understanding the structural basis for how CD4bs iGL Abs mature to effectively accommodate the $N276_{gp120}$ glycan is essential in efforts to develop effective immunogens to prime VRC01-class iGL precursors and shepherd antibody responses towards bNAb development. Furthermore, an overall structural understanding of VRC01-class iGL recognition of HIV-1 Envs and immunogens is limited as the only existing Fab-Env structures involving germline CD4bs Abs are complexed with gp120 or Env trimer immunogens lacking the $N276_{gp120}$ glycan[3,23,29]. In addition, in the case of an iGL Fab complexed with an Env trimer, obtaining a structure required chemical cross-linking between the Env and Ab to form a stable complex[22].

A VRC01-class bNAb isolated from an elite neutralizer, BG24[30], is an attractive target for germline-targeting immunogen design. BG24 shows similar neutralization and breadth to other CD4bs bNAbs, but includes only 22.6% and 19.5% amino acid substitution by SHM in variable heavy and light chain genes, respectively[30], as compared with higher levels of amino acid substitution in VRC01-class bNAbs[7,9,28,31] , with the exception of the PCIN63 lineage that has similar levels of SHM to BG24[32]. Structural characterization of BG24 bound to the clade A BG505 Env revealed a similar binding orientation to more mutated VRC01-class bNAbs, and signature contacts common to VRC01-class bNAbs [30]. Furthermore, neutralization studies using variants of BG24 that reverted variable heavy (V_H) and variable light (V_L) domain residues to germline counterparts showed that even fewer SHMs were necessary to maintain neutralization breadth[30]. Collectively, this suggests broad and potent neutralization targeting the CD4bs could be achieved through immunization without stimulating high levels of SHM.

To better understand how the BG24 bNAb was elicited and inform VRC01-class immunogen design, in this work we structurally characterized the binding of two versions of the BG24 iGL to the CD4bs germline-targeting immunogen BG505-SOSIPv4.1-GT1[3] (hereafter referred to as GT1). We solved two single-particle cryo-electron microscopy

(cryo-EM) structures of GT1 in complex with $BG24_{iGL}$s containing either mature or iGL CDR3s at 4.1 Å and 3.4 Å resolution, respectively, in both cases in the absence of chemical cross-linking. Furthermore, to understand how N-glycans impact germline Ab recognition of Env, we conducted biochemical assays and solved cryo-EM structures of $BG24_{iGL}$ derivatives bound to Envs that included the $N276_{gp120}$ glycan. The structures demonstrated that the CDRL1s of $BG24_{iGL}$s can adopt conformations that accommodate the $N276_{gp120}$ glycan, an important capability for a germline-targeting CD4bs immunogen. Collectively, these structures provide information regarding the physical characteristics of iGLs that recognize HIV-1 Env and provide a structural basis for the design of immunogens engineered to engage and mature germline Abs.

Results

Cryo-EM structures of GT1-$BG24_{iGL}$-10-1074 complexes

To gain insight into how BG24 precursors interact with an HIV-1 Env-based immunogen, we created iGL versions of BG24 and used single-particle cryo-EM to structurally characterize them in complex with GT1, a CD4bs germline-targeting immunogen[3]. GT1 was modified from a soluble clade A BG505 SOSIP.664 native-like Env trimer[33] to permit binding of VRC01-class germline precursors by including $T278R_{gp120}$ and $G471S_{gp120}$ substitutions and mutations to remove potential N-linked glycosylation sites (PNGSs) at positions $N276_{gp120}$, $N462_{gp120}$, $N386_{gp120}$, and $N197_{gp120}$ in the CD4bs[3]. Two iGL versions of BG24 Fab constructs were made starting with the VH1-2*02 and VL2-11*01 heavy and light chain germline gene segment sequences: one containing the CDR3s from mature BG24 ($BG24_{iGL\text{-}CDR3mat}$) and the other containing the iGL CDR3s ($BG24_{iGL\text{-}CDR3iGL}$) (Fig. 1a). Each $BG24_{iGL}$ was structurally characterized in complex with GT1 and the V3 bNAb 10-1074[34].

Cryo-EM structures of $BG24_{iGL\text{-}CDR3iGL}$ and $BG24_{iGL\text{-}CDR3mat}$ Fabs bound to GT1 were solved at 3.4 Å and 4.1 Å, respectively (Fig. 1b,c, Supplementary Fig. 1a-j, Supplementary Table 1). Both 3D cryo-EM reconstructions showed three $BG24_{iGL}$ and three 10-1074 Fabs

bound per Env trimer. However, for the $BG24_{iGL\text{-}CDR3iGL}$-GT1-10-1074 complex, a distinct 3D class contained two $BG24_{iGL\text{-}CDR3iGL}$ Fabs bound to the GT1 Env (Supplementary Fig. 1e-f, Supplementary Table 1). We also solved a 1.4 Å crystal structure of unbound $BG24_{iGL\text{-}CDR3mat}$ Fab (Supplementary Fig. 1k, Supplementary Table 2), which exhibited six disordered residues within CDRL1, but otherwise superimposed with a 1.3 Å root mean square deviation (rmsd; calculated for 225 V_H-V_L C□ atoms) with the Env-bound $BG24_{iGL\text{-}CDR3mat}$ Fab structure, suggesting no major structural differences upon Env binding.

$BG24_{iGL}$ Fabs recognize the modified CD4bs in GT1 Env

The GT1 complexes with $BG24_{iGL}$s included density for CD4bs N-glycans attached to residues $N234_{gp120}$, $N363_{gp120}$, and $N392_{gp120}$ (Fig. 2a-b). These N-glycans were also observed in the crystal structure of BG505 Env complexed with a mature BG24 Fab[30] ($BG24_{mat}$) (PDB 7UCF), which also included densities for N-glycans at $N197_{gp120}$, $N276_{gp120}$, and $N386_{gp120}$ that are not present in GT1 (Fig. 2c). Despite additional glycans in BG505 compared with GT1, the CDR loops in the GT1-bound iGL Fabs showed similar orientations and positions as in the BG505-bound $BG24_{mat}$ Fab, except for CDRL1, which is six residues longer in $BG24_{iGL}$ than in $BG24_{mat}$ (Fig. 1a, 2d-f).

$BG24_{iGL\text{-}CDR3mat}$ and $BG24_{iGL\text{-}CDR3iGL}$ buried comparable surface areas on GT1 gp120 (953 $Å^2$ and 951 $Å^2$, respectively) as compared with an only slightly larger surface area (1086 $Å^2$) buried on BG505 gp120 in the $BG24_{mat}$-BG505 structure (PDB 7UCF) (Fig. 2g). We hypothesize that, although a germline precursor antibody presumably exhibits fewer contacts to an antigen than its counterpart somatically-mutated bNAb, the overall interface BSA values for the gp120 peptide components of the $BG24_{iGL}$-GT1 and $BG24_{mat}$-BG505 structures were similar because the modifications in GT1 (both amino acid substitutions and removals of N-glycans) allowed increased contacts between $BG24_{iGL}$s and the GT1 gp120. However, differences in interactions between the $BG24_{iGL}$-GT1 and $BG24_{mat}$-BG505 structures suggest that SHM substitutions enrich interactions in particular regions within the CD4bs (Fig. 2g-h). For example, in the $BG24_{mat}$-BG505 complex, $BG24_{mat}$ residue $S100A_{HC}$ hydrogen bonds with the gp120 inner domain residue $K97_{gp120}$ (Fig. 2g-

j). $K97_{gp120}$ is ~90% conserved among HIV-1 Envs, making this a crucial interaction of broad and potent CD4bs bNAbs[18]. Residue $S100A_{HC}$ is a germline encoded residue, however, in both $BG24_{iGL}$-GT1 structures, is not within distance to form a hydrogen bond with $K97_{gp120}$ (Fig. 2i-j). Compared to $BG24_{iGL}$-GT1, $BG24_{mat}$-BG505 also showed increased V_H buried surface area (BSA) in the gp120 exit loop (gp120 residues 472-476). Together, this analysis demonstrated differences in the distribution of BSA among $BG24_{mat}$ and $BG24_{iGL}$s in CD4bs regions.

BG24 somatic hypermutation and germline features play a role in CD4bs recognition

We next compared how differences in $BG24_{iGL}$ and $BG24_{mat}$ contribute to their recognition of GT1 and BG505, respectively. $BG24_{iGL}$ contains a germline 11-residue CDRL1 that can recognize the mostly aglycosylated CD4bs in GT1, whereas the $BG24_{mat}$ CDRL1 is six residues shorter and includes a glycine to create a more flexible loop that can accommodate the $N276_{gp120}$ glycan[30]. In the $BG24_{mat}$-BG505 structure, the five-residue BG24 CDRL1 is oriented adjacent to the $N276_{gp120}$ glycan (Fig. 3a). The CDRL1 interface with GT1 in the $BG24_{iGL\text{-}CDR3iGL}$ and $BG24_{iGL\text{-}CDR3mat}$ structures showed the longer CDRL1s in the germline precursor V_L domains in different conformations, demonstrating CDRL1 flexibility (Fig. 3b-c) consistent with cryo-EM data processing. Indeed, the local resolutions for the CDRL1 in these structures were poor and resolved only after iterative rounds of focused classification and local refinements (Supplementary Fig. 2a-b). Overlaying the $BG24_{iGL}$ CDRL1s with the gp120 region surrounding the $N276_{gp120}$ glycan from the $BG24_{mat}$-BG505 structure showed steric clashes, consistent with SHM being necessary for $N276_{gp120}$ glycan accommodation by BG24 (Fig. 3b-c).

The role of SHMs in Env recognition is summarized in Fig. 3d, where $BG24_{iGL\text{-}CDR3iGL}$, $BG24_{iGL\text{-}CDR3mat}$, and $BG24_{mat}$ HC paratope interactions are mapped to individual Ab residues within 4 Å of gp120. Paratope contacts were limited to CDRs H1, H2, and H3, as well as framework region 3 in the heavy chain (FWRH3), with most contacts in CDRH2.

Previous studies showed neutralization by an engineered BG24 minimal construct that contained germline-reverted SHMs in FWRs, CDRH1, and CDRL2, but maintained most SHMs in CDRH2, suggesting the importance of SHMs in this region[30]. The structure of $BG24_{mat}$-BG505 showed a CDRH2 SHM ($N53R_{HC}$) interacted with $Q428_{gp120}$ in gp120 β20/21 (Fig. 1a, 3e). β20/21 interactions with germline-encoded $N53_{HC}$ were absent in $BG24_{iGL\text{-}CDR3iGL}$-GT1 and $BG24_{iGL\text{-}CDR3mat}$-GT1 (Fig. 3f-g). This demonstrates the direct impact of SHM in creating favorable interactions with Env. Other $BG24_{mat}$ somatically hypermutated residues in CDRH2 also interacted with the CD4bs loop (gp120 residues 364-375); e.g., residue $T57V_{HC}$ makes a backbone interaction with $S365_{gp120}$, and $S54G_{HC}$ interacts with $D368_{gp120}$, a highly conserved Env residue (Fig. 3d)[18]. For $BG24_{iGL}$, germline-encoded residues at positions $T57_{HC}$ and $S54_{HC}$, maintain similar interactions with GT1 residues $S365_{gp120}$ and $D368_{gp120}$, respectively (Fig. 3f-g).

To understand the functional role of these CDRH2 SHMs, we tested the neutralization activity of $BG24_{mat}$ constructs in which individual SHMs were reverted to the corresponding germline residue (BG24 $R53N_{HC,}$ BG24 $G54S_{HC}$, and BG24 $V57T_{HC,}$) and a combined construct with all three mutations reverted (BG24 $CDRH2_{iGL\text{-}3mut}$) against a 12-strain global panel of HIV-1 strains[35] plus BG505 T332N[33], comparing potencies and breadth against $BG24_{mat}$ (Fig. 3h). For BG24 constructs with $R53N_{HC}$ and $V57T_{HC}$ single mutations, we observed a greater than 5-fold decrease in potency against 6 of the 13 strains tested compared to $BG24_{mat}$. BG24 $G54S_{HC}$ most closely compared to $BG24_{mat}$, showing a more than 5-fold decrease in potency against only 3 strains. BG24 $CDRH2_{iGL\text{-}3mut}$, was more strongly affected by the SHM reversions, showing more than a 5-fold decrease in potency against almost all strains compared the $BG24_{mat}$. These results demonstrate that SHMs in CDRH2 shown to interact favorably with Env also play a functional role by contributing to neutralization potency and breadth.

Signature residues encoded by the VH1-2*02 germline gene in VRC01-class bNAbs interact with conserved gp120 residues and are correlated with neutralization potency[18]. These interactions have been structurally characterized in the context of VRC01-class iGLs bound to monomeric gp120s[22,23,29], but there are no known structures of VRC01-class iGLs bound to a trimeric Env, except when the iGL was chemically cross-linked to Env[22]. To

evaluate and verify VRC01-class VH1-2*02 germline-encoded interactions with an Env trimer, we compared these interactions in the $BG24_{iGL}$-GT1 and $BG24_{mat}$-BG505 structures (Supplementary Fig. 2c-f). Specifically, as previously described in structures involving gp120 monomers[22,23,29], germline-encoded $R71_{HC}$ in the $BG24_{iGL}$-GT1 and $BG24_{mat}$-BG505 structures formed a salt bridge with the conserved $D368_{gp120}$ side chain, an Ab interaction that mimics the interaction of host receptor residue $R59_{CD4}$ with $D368_{gp120}$ (Supplementary Fig. 2c). In the gp120 D loop, there were interactions between the backbone and side chain of $N280_{gp120}$ with $Y100D_{HC}$ and germline-encoded $W50_{HC}$ side chains (Supplementary Fig. 2d). In the V5 loop, interactions between the conserved $R456_{gp120}$ residue and germline-encoded $N58_{HC}$ are conserved in both structures (Supplementary Fig. 2e). In $BG24_{iGL\text{-}CDR3mat}$-GT1, atoms within these Fab residues were separated by more than 5 Å from atoms within gp120 residues; thus, this is not defined as an interaction. In the light chain, $E96_{LC}$ interacted with the backbone of $G459_{gp120}$ and the sidechain of $N280_{gp120}$ (Supplementary Fig. 2f).

GT1 CD4bs glycan modifications affect BG24 binding

To evaluate how glycan modifications in the GT1 immunogen contributed to $BG24_{iGL}$ binding, we evaluated the binding of BG24 constructs to GT1 with Env PNGSs either restored to or removed from the CD4bs (Fig. 4a). The BG24 constructs included $BG24_{mat}$, BG24 with germline CDRL1 ($BG24_{CDRL1\text{-}iGL}$) (Fig. 1a), $BG24_{iGL\text{-}CDR3mat}$, $BG24_{iGL\text{-}CDR3iGL}$, and BG24 with an iGL light chain ($BG24_{LC\text{-}iGL}$). PNGSs were individually restored at positions $N197_{gp120}$, $N276_{gp120}$, $N386_{gp120}$, and $N462_{gp120}$ and removed at $N234_{gp120}$ to create five GT1 constructs with altered glycan landscapes ($GT1_{N197gp120}$, $GT1_{N276gp120}$, $GT1_{N386gp120}$, $GT1_{N462gp120}$, and $GT1_{del\ N234gp120}$, respectively). BG505 and GT1 binding was evaluated by enzyme-linked immunosorbent assays (ELISAs). Restoring Env PNGSs at positions $N197_{gp120}$, $N386_{gp120}$, and $N462_{gp120}$ and removing the PNGS at $N234_{gp120}$ did not greatly affect binding of BG24 IgG constructs (Fig. 4a). $BG24_{iGL}$ constructs did not bind detectably to GT1 with a PNGS at $N276_{gp120}$; however, $BG24_{mat}$ and mature BG24 constructs with iGL LC features ($BG24_{CDRL1\text{-}iGL}$, $BG24_{LC\text{-}iGL}$) showed comparable binding

to each other on $GT1_{N276gp120}$ (Fig 4a). $BG24_{mat}$ was the only Ab that showed substantial binding to BG505, which unlike the GT1 Env, included all PNGSs. We conclude that BG24 constructs with a long, germline CDRL1 can accommodate the $N276_{gp120}$ glycan on Envs that have been engineered to have a limited glycan landscape in the CD4bs. These results contribute to existing studies of $N276_{gp120}$ glycan accommodation by germline CDRL1 (e.g., [36]).

To gain insight into BG24 CDRL1-iGL interactions in GT1 with an $N276_{gp120}$ glycan, we solved a single-particle cryo-EM structure of $BG24_{LC\text{-}iGL}$ bound to GT1 containing the restored $N276_{gp120}$ PNGS ($GT1_{N276gp120}$) (Fig. 4b, Supplementary Fig. 3a-h, Supplementary Table 1). We identified three unique 3D volumes containing either one, two, or three bound $BG24_{LC\text{-}iGL}$ Fabs, with the highest resolution complex (4.2 Å) being C3 symmetric with three bound $BG24_{LC\text{-}iGL}$ Fabs (Supplementary Fig. 3a-h, Supplementary Table 1). Electron density in the Fab CDRL1 was not optimal after cryo-EM processing; therefore, side chains were not modeled (Supplementary Fig. 3i).

The $BG24_{LC\text{-}iGL}$-$GT1_{N276gp120}$ complex structure showed that the Fab CDRL1 main chain residues adopted a helix-like conformation to accommodate the $N276_{gp120}$ glycan (Fig. 4c). Available crystallographic and cryo-EM Env structures demonstrate that the $N276_{gp120}$ glycan is conformationally heterogeneous[6,27,30,37,38] (Supplementary Fig. 3h). Indeed, the $N276_{gp120}$ glycans in the GT1 and BG505 Envs exhibited different conformations (Fig. 4c). Thus, after superimposing the gp120 residues in the $BG24_{LC\text{-}iGL}$-$GT1_{N276gp120}$ and $BG24_{mat}$-BG505 structures, it was evident that the $N276_{gp120}$ glycan in BG505 showed steric clashes with the CDRL1 iGL in $BG24_{LC\text{-}iGL}$ (Fig. 4c). Flexibility of the $N276_{gp120}$ glycan on BG505 may be more constrained than the counterpart glycan on GT1, as GT1 contains fewer N-glycans in the CD4bs, allowing for increased $N276_{gp120}$ glycan flexibility. This assumption is consistent with the ELISA results showing that $BG24_{LC\text{-}iGL}$ bound to GT1, but not to BG505 Env trimers with an $N276_{gp120}$ glycan (Fig. 4a).

The only other known CD4bs-targeting bNAb with a helical CDRL1 is IOMA, another VH1-2*02 derived bNAb[27]. IOMA contains features that distinguish it from VRC01-class bNAbs, including a normal length (8-residue) CDRL3 and a 13-residue CDRL1, which

adopts a short α-helix to accommodate the glycan at $N276_{gp120}$. However, CLK31, an IOMA-like Ab isolated from naïve human B cells using a VRC01 germline-targeting immunogen, did not include a helical CDRL1[39]. Alignment of the LCs of $BG24_{LC\text{-}iGL}$, IOMA, and CLK31 showed that each CDRL1 adopts a different configuration (Fig. 4d). These observations suggest CDRL1 helical conformations are diverse and have only been observed when bound to gp120s that contain the glycan at $N276_{gp120}$.

$BG24_{CDRL1\text{-}iGL}$ accommodates the $N276_{gp120}$ glycan in a non-engineered Env trimer

A longitudinal study that tracked the development of a VRC01-class lineage (PCIN63) found that bNAb development branched into two types of $N276_{gp120}$ glycan engagement: one that interacted with and depended on the presence of the $N276_{gp120}$ glycan, and one in which CD4bs binding was diminished by the presence of the $N276_{gp120}$ glycan[32]. In the absence of longitudinal data for $BG24_{mat}$ development, an engineered BG24 intermediate, $BG24_{CDRL1\text{-}iGL}$, was tested in previous work for neutralization against a 119-virus cross clade panel to better understand how the germline BG24 CDRL1 interacted with HIV-1 Envs bearing the $N276_{gp120}$ glycan[30]. $BG24_{CDRL1\text{-}iGL}$ exhibited neutralization activity against two viruses that contained PNGSs at $N276_{gp120}$: clade D 6405.v4.c34 (6405) and clade CD 6952.v1.c20 (6952) (Fig. 5a)[30]. The 6405 Env was selected for further investigation by creating a soluble 6405 SOSIP.664 trimer. Sequence alignment of 6405 and BG505 gp120s showed the amino acid identity in the CD4bs and V4 loops differed by more than 50% between BG505 and 6405 Envs (Supplementary Fig. 4). The 6405 gp120 sequence included similar CD4bs PNGSs as BG505, except for the absence of a PNGS at position 363_{gp120} and an added PNGS at position 465_{gp120} (Supplementary Fig. 4). We note that the degree to which each PNGS is utilized, the chemical and structural heterogeneity of N-glycans that are attached, and potential cell line and virus versus soluble Env trimer differences in glycosylation are not known for 6405. Binding of BG24 Fab constructs to 6405 was assessed by ELISA. Consistent with neutralization results (Fig. 5a), ELISAs showed that $BG24_{CDRL1\text{-}iGL}$ and $BG24_{mat}$ each bound the 6405 SOSIP, whereas $BG24_{LC\text{-}iGL}$ bound 6405 to a lesser extent (Fig. 5b). $BG24_{iGL}$s did not bind detectably to 6405 (Fig. 5b).

To understand how the germline CDRL1 of BG24 could be accommodated by a non-engineered Env trimer, we characterized interactions between $BG24_{CDRL1\text{-}iGL}$ and 6405 SOSIP by solving a 3.4 Å cryo-EM structure of a $BG24_{CDRL1\text{-}iGL}$-6405 complex (Fig. 5c, Supplementary Fig. 5a-d, Supplementary Table 1). As expected, $BG24_{CDRL1\text{-}iGL}$ recognized the CD4bs of 6405, which contained N-glycans at positions $N197_{gp120}$, $N234_{gp120}$, $N276_{gp120}$, $N354_{gp120}$, $N386_{gp120}$, $N392_{gp120}$, $N461_{gp120}$, and $N465_{gp120}$ (Fig. 5d). Again, side chains were not modeled for CDRL1 residues (Supplementary Fig. 5e). As also observed in the $BG24_{LC\text{-}iGL}$-$GT1_{N276}$ structure, the CDRL1-iGL in the $BG24_{CDRL1\text{-}iGL}$-6405 complex formed a helical conformation, although the CDRL1 confirmations in the two Fabs in these complexes were not identical (Supplementary Fig. 5f). By aligning gp120s from $GT1_{N276}$ and 6405, we found that the well-ordered portions of the $N276_{gp120}$ glycan occupied similar positions (Fig. 5f), suggesting that the position of $N276_{gp120}$ in these Envs is conducive to CDRL1 accommodation for $BG24_{iGLs.}$

We also evaluated binding of other CD4bs bNAbs to 6405 and a $6405_{delN276gp120}$ Env to determine if the CD4bs glycan landscape in 6405 was conducive to interactions with germline CDRL1s in other VRC01-class bNAbs (Fig. 5g-h, Supplementary Fig. 6). In this experiment, we included mature versions of the BG24, VRC01, N6 and IOMA bNAb Fabs, chimeric bNAb Fabs including an iGL LC, and complete iGL Fabs. PCIN63 and CH103 and intermediates were compared with their unmutated common ancestors (UCAs), as identified from longitudinal studies[32,40], instead of iGLs. The ELISA revealed that the 6405 Env interacted with $VRC01_{LC\text{-}iGL}$ and $N6_{LC\text{-}iGL}$ in addition to $BG24_{LC\text{-}iGL}$. Binding for all species increased for $6405_{del\ N276gp120}$, indicating the $N276_{gp120}$ glycan can sterically impede the CDRL1 of the iGLs tested. We conclude that the 6405 Env tolerates the binding of some germline VRC01-class CDRL1s.

Discussion

VRC01-class bNAbs are promising targets for germline-targeting immunogen design as germline-encoded residues make signature contacts with gp120 that contribute to impressive breadth and potency[5,18,22,23]. However, challenges in eliciting VRC01-class bNAbs through a germline-targeting vaccine regimen include explicitly selecting for the

VH1-2*02 germline gene, overcoming CD4bs glycan barriers, and stimulating high levels of SHM[41,42]. Despite these challenges, progress has been made in developing a VRC01-class bNAb germline-targeting approach[21,42,43], which is initiated by engineering an immunogen that binds to the germline precursors of VRC01 bNAbs. Priming immunogens are engineered to interact with specific germline-encoded residues and lack CD4bs glycans that obstruct germline recognition[3,29,41,44]. VRC01-class priming immunogens include monomeric gp120 cores[25,41,45], SOSIP-based trimers[3], and anti-idiotypic antibodies that recognize target BCRs with VH1-2*02 gene segments[46,47]. Furthermore, selecting a particular strain of Env and a gp120- versus trimeric Env-based platform to engineer priming characteristics that have proven to impact germline BCR selection in vivo[48]. Thus, identifying and developing the optimal priming immunogen for VRC01-like bNAb elicitation will require a robust understanding of the structural and biophysical nature of Env recognition by germline precursors.

In a sequential immunization approach, boosting immunogens are introduced to shape the development of a germline precursor into a bNAb by stimulating favorable SHMs[42]. Example boosting immunogens re-introduce native Env glycans and heterogenous Env strains to develop bNAbs capable of overcoming steric glycan barriers and have heterologous-neutralizing activity[42]. The $N276_{gp120}$ glycan on HIV-1 Env provides a particularly difficult roadblock, as VRC01-like germline CDRL1s must become shorter or more flexible through SHM to avoid steric clashes[23,27,28,32,49]. Several iterations of this approach have been tested in animal models; however, the elicitation of heterologous neutralizing activity has not yet been accomplished[41,50].

$BG24_{mat}$, represents a VRC01-class bNAb that can be targeted for germline-targeting approaches[30]. $BG24_{mat}$ has a fraction of the SHMs found in VRC01 and other VRC01-class bNAbs and maintains notable breadth and potency. Together with previous studies of the VRC01-class PCIN63 lineage and construction of a minimally mutated VRC01, our studies of BG24 suggest that high levels of SHM are not absolutely required for the development of VRC01-class Abs . Our cryo-EM structures of the iGL precursors of BG24 bound to the priming immunogen GT1 contribute to understanding how VRC01-class bNAb precursors interact with immunogens. We found that VH1-2*02 germline-encoded residues make the

predicted signature contacts with gp120 and the long germline CDRL1 is accommodated in the absence of the $N276_{gp120}$ glycan in GT1, rationalizing removal of this glycan in a priming immunogen since modeling suggested the germline CDRL1 conformation would clash with the $N276_{gp120}$ glycan. These observations validate the design of priming immunogens that nurture interactions with germline residues and remove the $N276_{gp120}$ glycan from the CD4bs epitope. We further investigated how the glycan landscape of an immunogen affects germline binding, finding that $BG24_{iGL\text{-}LC}$ can evade clashes with the $N276_{gp120}$ glycan when the BG24 HC includes bNAb features and the CD4bs epitope is only minimally glycosylated. Based on these observations, we propose that boosting immunogens might first aim to target mature HC features, and then introduce the $N276_{gp120}$ glycan in a limited CD4bs glycan landscape before moving to fully glycosylated Env landscape.

We also characterized binding of $BG24_{CDRL1\text{-}iGL}$ to the clade D 6405 Env, which suggested that some non-engineered HIV-1 Envs can accommodate some germline VRC01-class CDRL1s. In the case of $BG24_{CDRL1\text{-}iGL}$, accommodation of the $N276_{gp120}$ glycan occurred through a helix-like conformation in the iGL CDRL1. Furthermore, ELISA data suggested that other VH1-2*02-derived bNAbs with iGL LCs can also bind to the 6405 Env. Taken together, we propose further investigation of the 6405 Env to identify properties of the CD4bs that led to the structural and biochemical observations reported here, which could be applicable for the design of CD4bs-targeting immunogens.

Methods

$BG24_{iGL}$ constructs design

Genes encoding the IGHV1-2*02 and IGLV2-11*02 germline sequences with mature CDR3 loops were used to generate the $BG24_{iGL\text{-}CDR3mat}$ Fab construct. For the $BG24_{iGL\text{-}CDR3iGL}$ construct, amino acids in D- and J- gene regions were reverted based on inferred sequences using IMGT/V-QUEST. Mutations to BG24 IgG and Fab sequences were generated using QuikChange Lightning Site-Directed Mutagenesis Kit (Agilent).

Protein expression and purification

Fabs and IgGs were expressed and purified as previously described[51]. Briefly, Fabs were expressed by transient transfection using the Expi293 expression system (ThermoFisher). Fab expression vectors contained genes of LC and the C-terminally 6x-His tagged HC. The Fab and IgG proteins were purified from cell supernatants by Ni^{2+}-NTA (GE Healthcare) and protein A affinity chromatography (GE Healthcare), respectively, followed by size exclusion chromatography (SEC) using a Superdex 200 10/300 column (GE Healthcare).

SOSIP.664 Env constructs contained the disulfide mutations 501C and 605C (SOS), I559P (IP), and the furin cleavage site mutated to six arginine residues (6R)[33]. Genes encoding BG505 SOSIP.664v4.1-GT1 and 6405 SOSIPs were expressed using by transient transfection of Expi293 cells (ThermoFisher) and purified as described previously[52]. The 6405 SOSIP construct contained gp120 residues 46-477 from the 6405 sequence, with remaining gp120 residues derived from BG505 and the extracellular portion of the BG505 gp41[53]. Trimeric Env was separated from cell supernatants by PGT145 immunoaffinity chromatography, and SEC using a Superose 6 10/300 column (GE Healthcare) as described[54].

X-ray crystallography

Purified $BG24_{iGL\text{-}CDR3mat}$ Fab was concentrated to 8-15 mg/mL. Matrix crystallization screens were performed at room temperature using the sitting drop vapor diffusion method by mixing equal volumes of protein sample and reservoir using a TTP LabTech Mosquito

robot and commercially-available screens (Hampton Research and Qiagen). Initial hits were optimized and crystals were obtained in 20% PEG 3350 at 20 ˚C. Crystals were cryo-protected in glycerol stepwise until 20% before being cryopreserved in liquid nitrogen.

X-ray diffraction data were collected to 1.4 Å for $BG24_{iGL\text{-}CDR3mat}$ Fab at the Stanford Synchroton Radiation Lightsource (SSRL) beamline 12-2 on a Pilatus 6M pixel detector (Dectris). Data from a single crystal were indexed and integrated in XDS[55] and merged with AIMLESS in the CCP4 software suite[56]. Structures were determined by molecular replacement in PHASER[57] using coordinates of the $BG24_{mat}$ Fab (PDB 7UCE), after removal of CDR loops and independent searches of the V_HV_L and C_HC_L domains. Models were refined using rigid body and B-factor refinement in Phenix[58], followed by several cycles of iterative manual building in Coot[59] and real-space refinement with TLS groups in Phenix[58,60] (Supplementary Table 2).

Assembly of protein complexes and cryo-EM sample preparation

Protein complexes for cryo-EM were generated by incubating a purified $BG24_{iGL}$ Fab and the 10-1074 Fab with an Env trimer in a 3:1 Fab:trimer molar ratio and incubating at 4°C overnight. The complex was then SEC purified over a Superdex 200 1/150 column (GE Healthcare). The peak corresponding to complex was pooled and concentrated to 1.0 mg/ml. Quantifoil R2/2 400 mesh cryo-EM grids (Ted Pella) were prepared by glow-discharging for 1 min at 20 mA using a PELCO easiGLOW (Ted Pella). Fab-Env complexes (3 μL) were then applied to grids and blotted with Whatman No. 1 filter paper for 3-4 s at 100% humidity at room temperature. The grids were vitrified by and plunge-freezing in liquid ethane using a Mark IV Vitrobot (ThermoFisher).

Cryo-EM data collection and processing

Data for single-particle cryo-EM were collected on either a Talos Arctica ($BG24_{iGL\text{-}CDR3mat}$-GT1-10-1074, $BG24_{iGL\text{-}CDR3iGL}$ -$GT1_{N276gp120}$ -10-1074, $BG24_{CDRL1\text{-}iGL}$ -6405-10-1074) or a Titan Krios ($BG24_{iGL\text{-}CDR3iGL}$-GT1-10-1074) transmission electron microscope, operating at 200 kV and 300 kV, respectively. Movies were collected with beam-image shift over a single exposure per hole in a 3-by-3 pattern of 2 μm holes. For datasets collect on the Talos

Arctica, movies were recorded in super-resolution mode on a Falcon III camera (Thermo Fisher) at 1.436 Å•pixel^{-1} or a K3 camera (Gatan) at 0.4345 Å•pixel^{-1}. Movies obtained from samples on the Titan Krios were collected in super-resolution mode on a K3 camera (Gatan) equipped with an BioQuantum energy filter (Gatan) with a 20 eV slit width at 0.4327 Å•pixel^{-1}. The defocus range was set from 1.0-3.0 μm for each dataset.

The data processing workflow described below was performed similarly for all datasets using RELION[61,62]. Movies were motion-corrected using MotionCor2[63] after binning. GCTF[64] was used to estimate CTF, and micrograph power spectra that showed poor CTF fits or bad ice were removed. A subset of particles was manually picked and used for reference-free 2D classification. Classes representing the defined complex were used as references for RELION AutoPicking[61,62] to generate 2D classes. Subsequent 2D classes were inspected, and 2D classes representing a defined complex were selected for 3D classification. An ab initio model was generated using cryoSPARC[65] using a subset of particles for each dataset and used as a reference in 3D classification which assumed C1 symmetry. 3D classes representing a defined complex were selected for 3D auto-refinement and post processing in Relion. Particles used in 3D refinement were then re-extracted and un-binned. Particles were then subjected to 3D classification with the map generated with un-binned particles used as a reference. Distinct classes representing a particular defined complex (C1 or C3 symmetric) were selected for 3D auto-refinement after masking out Fab C_HC_L domains. Iterative rounds of particle CTF refinement, particle polishing, 3D auto-refinement, and post processing were used for each class to generate final maps. To improve resolution of Fab_{LC} CDRL1s, a soft mask surrounding the Fab VH-VL-gp120 interface was created in chimera and used for local refinements in cryoSPARC to improve density in this region and allow for CDRL1 fitting and refinement. Resolutions were calculated in RELION using the gold-standard FSC 0.143 criterion[66]. FSCs were generated by the 3DFSC program[67].

Cryo-EM model building and refinement

Model coordinates were generated by fitting reference gp120 (PDB 5T3Z), gp41(PDB 5T3Z), 10-1074 (PDB 5T3Z), and BG24-derivative Fabs (this study) chains into cryo-EM density with UCSF Chimera[68]. Initial models were refined using the Phenix command *phenix.real_space_refine*[58,60]. Sequence updates to the model and further manual refinement was conducted with Coot[59]. Iterative rounds of Phenix auto-refinement and manual refinements were done to generate the final models (Supplementary Table 1).

Structural analyses

Structure figures were made using PyMol (Schrödinger LLC), UCSF Chimera[68], and UCSF ChimeraX[69,70]. PyMol was used to calculate r.m.s.d. values after pairwise alignment of Cα atoms. PDBePISA[71] was used to calculate buried surface areas using a 1.4 Å probe. Calculations for gp120 BSA were for peptide components of gp120 and did not include glycan interactions. Defined interactions were assigned tentatively due to the low resolution of complexes using the following criteria: hydrogen bonds were assigned pairwise interactions that were less than 4.0 Å and with an A-D-H angle >90°, and van der Waals interactions were assigned as distances between atoms that were less than 4.0 Å.

TZM.bl Neutralization Assay

The neutralizing activities of BG24 CDRH2 mutant IgGs were measured using a luciferase-based TZM.bl assay according to standard protocols[72]. Each assay was performed in duplicate. Data were analyzed using Antibody Database (v2.0)[73]. 5-parameter curve fitting was used to determine 50% inhibitory concentrations (IC_{50}s), and non-specific activity was detected by testing against murine leukemia virus (MuLV).

Enzyme-linked immunosorbent assay

SOSIP trimers were randomly biotinylated following manufacturer's guidelines using the EZ-Link NHS-PEG4-Biotin kit (Thermo Fisher Scientific). The Pierce Biotin kit (Thermo Fisher Scientific) was used to quantify biotin molecules per SOSIP protomer: biotin estimations ranged from 1-10 biotin molecules per SOSIP protomers. Streptavidin-coated

96-well plates (Thermo Fisher Scientific) were coated with 5 µg/mL of randomly biotinylated SOSIPs diluted in 3% BSA in TBS-T (20mM Tris, 150 mM NaCl, 0.1% Tween20) and incubated at room temperature (RT) for 2 hours. Plates were washed to remove unbound SOSIPs. Serial dilutions of IgGs were made in 3% BSA in TBS-T and applied to the plates. After a 2-hour incubation at RT, plates were washed twice in TBS-T. Goat anti-human IgG Fc conjugated to horse-radish peroxidase (Southern BioTech) was added at 1:8000 dilution for 30 minutes, followed by 3 washes with TBS-T. 1-Step™ Ultra TMB-ELISA Substrate Solution (ThermoFisher Scientific) was added for colorimetric detection and color development was quenched with 1N HCl. Absorbance was measured at 450nm. Two independent, biological replicates (n =2) were performed.

Data availability

The atomic model generated for the X-ray crystallography structure of the $BG24_{iGL\text{-}CDR3mat}$ Fab in this study has been deposited in the Protein Data Bank (PDB) under accession code 7UGM [http://doi.org/10.2210/pdb7ugm/pdb]. The cryo-EM maps and atomic structures have been deposited in the PDB and/or Electron Microscopy Data Bank (EMDB) under accession codes 7UGN [http://doi.org/10.2210/pdb7ugn/pdb] and EMD-26490 [https://www.ebi.ac.uk/pdbe/entry/emdb/EMD-26490] for $BG24_{iGL\text{-}CDR3iGL}$-GT1-10-1074 Class I, EMD-26491 [https://www.ebi.ac.uk/pdbe/entry/emdb/EMD-26491] for $BG24_{iGL\text{-}CDR3iGL}$-GT1-10-1074 Class II, 7UGO [http://doi.org/10.2210/pdb7ugo/pdb] and EMD-26492 [https://www.ebi.ac.uk/pdbe/entry/emdb/EMD-26492] for $BG24_{iGL\text{-}CDR3mat}$-GT1-10-1074, 7UGP [http://doi.org/10.2210/pdb7ugp/pdb] and EMD-26493 [https://www.ebi.ac.uk/pdbe/entry/emdb/EMD-26493] for $BG24_{iGL\text{-}LC}$-$GT1_{N276gp120}$-10-1074 Class I, EMD-26494 [https://www.ebi.ac.uk/pdbe/entry/emdb/EMD-26494] for $BG24_{iGL\text{-}LC}$-$GT1_{N276gp120}$-10-1074 Class II, EMD-26495 [https://www.ebi.ac.uk/pdbe/entry/emdb/EMD-26495] for $BG24_{iGL\text{-}LC}$-$GT1_{N276gp120}$-10-1074 Class III, and 7UGQ [http://doi.org/10.2210/pdb7ugq/pdb] and EMD-26496 [https://www.ebi.ac.uk/pdbe/entry/emdb/EMD-26496] for $BG24_{CDRL\text{-}iGL}$-6405-10-1074. Local refinement maps used to model CDRL1s of BG24-derivatives have been deposited

with PDB and EMDB accession codes for each respective structure. The ELISA data generated in this study are provided in the Supplementary Information and Source Data file.

Acknowledgements

We thank J. Vielmetter, P. Hoffman, and the Protein Expression Center in the Beckman Institute at Caltech for expression assistance. Electron microscopy was performed in the Caltech Cryo-EM Center with assistance from S. Chen and A. Malyutin. We thank the Gordon and Betty Moore and Beckman Foundations for gifts to Caltech to support the Molecular Observatory (Dr. Jens Kaiser, Director) and the beamline staff at SSRL for data collection assistance. Use of the Stanford Synchrotron Radiation Lightsource, SLAC National Accelerator Laboratory, is supported by the U.S. Department of Energy, Office of Science, Office of Basic Energy Sciences under Contract No. DE-AC02-c76SF00515. The SSRL Structural Molecular Biology Program is supported by the DOE Office of Biological and Environmental Research, and by the National Institutes of Health, National Institute of General Medical Sciences (P41GM103393). The contents of this publication are solely the responsibility of the authors and do not necessarily represent the official views of NIGMS or NIH. C.O.B. was supported by a Burroughs Wellcome PDEP fellowship and HHMI Hanna Gray Fellowship. This work was supported by the National Institute of Allergy and Infectious Diseases (NIAID) Grant HIVRAD P01 AI100148 (to P.J.B. and M.C.N.), the Bill and Melinda Gates Foundation Collaboration for AIDS Vaccine Discovery (CAVD) grant INV-002143 (P.J.B., M.C.N.), and NIH P50 AI150464 (P.J.B.).

Author contributions statement

K.A.D., C.O.B., H.B.G., T.S., M.C.N., and P.J.B. designed the research. K.A.D. performed protein purification, structural studies, and ELISA experiments. P.N.P.G. performed in

vitro neutralization assays. K.A.D., C.O.B., and H.B.G. analyzed results. K.A.D. and P.J.B. wrote the manuscript with input from co-authors.

Competing interests statement

The authors declare that there are no competing interests.

References

1. Escolano, A. *et al.* Immunization expands B cells specific to HIV-1 V3 glycan in mice and macaques. *Nature* **570**, 468–473 (2019).

2. Lee, J. H. & Crotty, S. HIV vaccinology: 2021 update. *Semin. Immunol.* **51**, 101470 (2021).

3. Medina-Ramírez, M. *et al.* Design and crystal structure of a native-like HIV-1 envelope trimer that engages multiple broadly neutralizing antibody precursors in vivo. *J. Exp. Med.* **214**, 2573–2590 (2017).

4. Sanders, R. W. & Moore, J. P. Native-like Env trimers as a platform for HIV-1 vaccine design. *Immunol. Rev.* **275**, 161–182 (2017).

5. Zhou, T. Structural Basis for Broad and Potent Neutralization of HIV-1 by Antibody VRC01. *Science*. 1–8 (2010).

6. Schommers, P. *et al.* Restriction of HIV-1 Escape by a Highly Broad and Potent Neutralizing Antibody. *Cell* **180**, 471-489.e22 (2020).

7. Huang, J. *et al.* Identification of a CD4-Binding-Site Antibody to HIV that Evolved Near-Pan Neutralization Breadth. *Immunity* **45**, 1108–1121 (2016).

8. Scheid, J. F. *et al.* Sequence and Structural Convergence of Broad and Potent HIV Antibodies That Mimic CD4 Binding. *Science* **333**, 1633–1637 (2011).

9. Wu, X. *et al.* Rational Design of Envelope Identifies Broadly Neutralizing Human Monoclonal Antibodies to HIV-1. *Science* **329**, 856–861 (2010).

10. Bar, K. J. *et al.* Effect of HIV Antibody VRC01 on Viral Rebound after Treatment Interruption. *N. Engl. J. Med.* **375**, 2037–2050 (2016).

11. Bar-On, Y. *et al.* Safety and antiviral activity of combination HIV-1 broadly neutralizing antibodies in viremic individuals. *Nat. Med.* **24**, 1701–1707 (2018).

12. Miner, M. D., Corey, L. & Montefiori, D. Broadly neutralizing monoclonal antibodies for HIV prevention. *J. Int. AIDS Soc.* **24**, (2021).

13. Mendoza, P. *et al.* Combination therapy with anti-HIV-1 antibodies maintains viral suppression. *Nature* 1–21 (2018) doi:10.1038/s41586-018-0531-2.

14. VRC 602 Study Team *et al.* Safety, pharmacokinetics and neutralization of the broadly neutralizing HIV-1 human monoclonal antibody VRC01 in healthy adults. *Clin. Exp. Immunol.* **182**, 289–301 (2015).

15. Lynch, R. M. *et al.* Virologic effects of broadly neutralizing antibody VRC01 administration during chronic HIV-1 infection. *Sci. Transl. Med.* **7**, (2015).

16. Mayer, K. H. *et al.* Safety, pharmacokinetics, and immunological activities of multiple intravenous or subcutaneous doses of an anti-HIV monoclonal antibody, VRC01, administered to HIV-uninfected adults: Results of a phase 1 randomized trial. *PLOS Med.* **14**, e1002435 (2017).

17. Escolano, A., Dosenovic, P. & Nussenzweig, M. C. Progress toward active or passive HIV-1 vaccination. *J. Exp. Med.* **214**, 3–16 (2017).

18. West Jr, A. P. Structural basis for germ-line gene usage of a potent class of antibodies targeting the CD4-binding site of HIV-1 gp120. *PNAS* 1–8 (2012) doi:10.1073/pnas.1208984109/-/DCSupplemental.

19. Xiao, X. *et al.* Germline-like predecessors of broadly neutralizing antibodies lack measurable binding to HIV-1 envelope glycoproteins: Implications for evasion of immune responses and design of vaccine immunogens. *Biochem. Biophys. Res. Commun.* **390**, 404–409 (2009).

20. Bonsignori, M. *et al.* Analysis of a Clonal Lineage of HIV-1 Envelope V2/V3 Conformational Epitope-Specific Broadly Neutralizing Antibodies and Their Inferred Unmutated Common Ancestors. *J. Virol.* **85**, 9998–10009 (2011).

21. Burton, D. R. Advancing an HIV vaccine; advancing vaccinology. *Nat. Rev. Immunol.* **19**, 77–78 (2019).

22. Borst, A. Germline VRC01 antibody recognition of a modified clade C HIV-1 envelope trimer and a glycosylated HIV-1 gp120 core. *eLife*. 1–32 (2018).

23. Scharf, L. *et al.* Structural basis for HIV-1 gp120 recognition by a germ-line version of a broadly neutralizing antibody. *Proc. Natl. Acad. Sci.* **110**, 6049–6054 (2013).

24. Zhou, T. *et al.* Structural Repertoire of HIV-1-Neutralizing Antibodies Targeting the CD4 Supersite in 14 Donors. *Cell* **161**, 1280–1292 (2015).

25. Jardine, J. G. *et al.* HIV-1 broadly neutralizing antibody precursor B cells revealed by germline-targeting immunogen. *Science* **351**, 1458–1463 (2016).

26. Zhou, T. *et al.* Quantification of the Impact of the HIV-1-Glycan Shield on Antibody Elicitation. *Cell Rep.* **19**, 719–732 (2017).

27. Gristick, H. B. *et al.* Natively glycosylated HIV-1 Env structure reveals new mode for antibody recognition of the CD4-binding site. *Nat. Publ. Group* **23**, 906–915 (2016).

28. Zhou, T. *et al.* Multidonor Analysis Reveals Structural Elements, Genetic Determinants, and Maturation Pathway for HIV-1 Neutralization by VRC01-Class Antibodies. *Immunity* **39**, 245–258 (2013).

29. Jardine, J. G. *et al.* Priming a broadly neutralizing antibody response to HIV-1 using a germline-targeting immunogen. *Science* **349**, 156–161 (2015).

30. Barnes, C. O. *et al.* A naturally arising broad and potent CD4-binding site antibody with low somatic mutation. *Sci. Adv.* 8, eabp8155 (2022).

31. Huang, D. *et al.* B cells expressing authentic naive human VRC01-class BCRs can be recruited to germinal centers and affinity mature in multiple independent mouse models. *Proc. Natl. Acad. Sci.* **117**, 22920–22931 (2020).

32. Umotoy, J. *et al.* Rapid and Focused Maturation of a VRC01-Class HIV Broadly Neutralizing Antibody Lineage Involves Both Binding and Accommodation of the N276-Glycan. *Immunity* **51**, 141-154.e6 (2019).

33. Sanders, R. W. *et al.* A Next-Generation Cleaved, Soluble HIV-1 Env Trimer, BG505 SOSIP.664 gp140, Expresses Multiple Epitopes for Broadly Neutralizing but Not Non-Neutralizing Antibodies. *PLoS Pathog.* **9**, e1003618-20 (2013).

34. Mouquet, H. *et al.* Complex-type N-glycan recognition by potent broadly neutralizing HIV antibodies. *Proc. Natl. Acad. Sci.* **109**, E3268–E3277 (2012).

35. deCamp, A. *et al.* Global Panel of HIV-1 Env Reference Strains for Standardized Assessments of Vaccine-Elicited Neutralizing Antibodies. *J. Virol.* **88**, 2489–2507 (2014).

36. Bonsignori, M. *et al.* Inference of the HIV-1 VRC01 Antibody Lineage Unmutated Common Ancestor Reveals Alternative Pathways to Overcome a Key Glycan Barrier. *Immunity* **49**, 1162-1174.e8 (2018).

37. Scharf, L. *et al.* Broadly Neutralizing Antibody 8ANC195 Recognizes Closed and Open States of HIV-1 Env. *Cell* 1–13 (2018).

38. Lee, J. H. *et al.* A Broadly Neutralizing Antibody Targets the Dynamic HIV Envelope Trimer Apex via a Long, Rigidified, and Anionic β-Hairpin Structure. *Immunity* **46**, 690–702 (2017).

22. Borst, A. Germline VRC01 antibody recognition of a modified clade C HIV-1 envelope trimer and a glycosylated HIV-1 gp120 core. *Sci. Transl. Med*, **10,** 1–32 (2018).

40. Liao, H.-X. *et al.* Co-evolution of a broadly neutralizing HIV-1 antibody and founder virus. *Nature* **496**, 469–476 (2013).

41. Parks, K. R. *et al.* Overcoming Steric Restrictions of VRC01 HIV-1 Neutralizing Antibodies through Immunization. *CellReports* **29**, 3060-3072.e7 (2019).

42. Stamatatos, L., Pancera, M. & McGuire, A. T. Germline-targeting immunogens. *Immunol. Rev.* **275**, 203–216 (2017).

43. Dimitrov, D. S. Therapeutic antibodies, vaccines and antibodyomes. *mAbs* **2**, 347–356 (2010).

44. McGuire, A. T. *et al.* Specifically modified Env immunogens activate B-cell precursors of broadly neutralizing HIV-1 antibodies in transgenic mice. *Nat. Commun.* **7**, 10618 (2016).

45. Jardine, J. *et al.* Rational HIV Immunogen Design to Target Specific Germline B Cell Receptors. *Science* **340**, 711–716 (2013).

46. Seydoux, E. *et al.* Development of a VRC01-class germline targeting immunogen derived from anti-idiotypic antibodies. *Cell Rep.* **35**, 109084 (2021).

47. Dosenovic, P. *et al.* Anti-idiotypic antibodies elicit anti-HIV-1–specific B cell responses. *J. Exp. Med.* **216**, 2316–2330 (2019).

48. Lin, Y.-R. *et al.* HIV-1 VRC01 Germline-Targeting Immunogens Select Distinct Epitope-Specific B Cell Receptors. *Immunity* **53**, 840-851.e6 (2020).

49. Jardine, J. G. *et al.* Minimally Mutated HIV-1 Broadly Neutralizing Antibodies to Guide Reductionist Vaccine Design. *PLoS Pathog.* **12**, e1005815-33 (2016).

50. Briney, B. *et al.* Tailored Immunogens Direct Affinity Maturation toward HIV Neutralizing Antibodies. *Cell* **166**, 1459-1470.e11 (2016).

51. Yang, Z., Wang, H., Liu, A. Z., Gristick, H. B. & Bjorkman, P. J. Asymmetric opening of HIV-1 Env bound to CD4 and a coreceptor-mimicking antibody. *Nat. Struct. Mol. Biol.* **26**, 1167–1175 (2019).

52. Escolano, A. *et al.* Sequential immunization of macaques elicits heterologous neutralizing antibodies targeting the V3-glycan patch of HIV-1 Env. *Sci. Transl. Med.* **13**, eabk1533 (2021).

53. Joyce, M. G. *et al.* Soluble Prefusion Closed DS-SOSIP.664-Env Trimers of Diverse HIV-1 Strains. *CellReports* **21**, 2992–3002 (2017).

54. Cupo, A. *et al.* Optimizing the production and affinity purification of HIV-1 envelope glycoprotein SOSIP trimers from transiently transfected CHO cells. *PLOS ONE* **14**, e0215106 (2019).

55. Kabsch, W. Integration, scaling, space-group assignment and post-refinement. *Acta Crystallogr. D Biol. Crystallogr.* **66**, 133–144 (2010).

56. Winn, M. D. *et al.* Overview of the *CCP* 4 suite and current developments. *Acta Crystallogr. D Biol. Crystallogr.* **67**, 235–242 (2011).

57. McCoy, A. J. *et al. Phaser* crystallographic software. *J. Appl. Crystallogr.* **40**, 658–674 (2007).

58. Adams, P. D. *et al. PHENIX*: a comprehensive Python-based system for macromolecular structure solution. *Acta Crystallogr. D Biol. Crystallogr.* **66**, 213–221 (2010).

59. Emsley, P., Lohkamp, B., Scott, W. G. & Cowtan, K. Features and development of *Coot*. *Acta Crystallogr. D Biol. Crystallogr.* **66**, 486–501 (2010).

60. Afonine, P. V. *et al.* Real-space refinement in *PHENIX* for cryo-EM and crystallography. *Acta Crystallogr. Sect. Struct. Biol.* **74**, 531–544 (2018).

61. Zivanov, J. *et al.* New tools for automated high-resolution cryo-EM structure determination in RELION-3. *eLife* **7**, e42166 (2018).

62. Scheres, S. H. W. RELION: Implementation of a Bayesian approach to cryo-EM structure determination. *J. Struct. Biol.* **180**, 519–530 (2012).

63. Zheng, S. Q. *et al.* MotionCor2: anisotropic correction of beam-induced motion for improved cryo-electron microscopy. *Nat. Methods* **14**, 331–332 (2017).

64. Zhang, K. Gctf: Real-time CTF determination and correction. *J. Struct. Biol.* **193**, 1–12 (2016).

65. Punjani, A., Rubinstein, J. L., Fleet, D. J. & Brubaker, M. A. cryoSPARC: algorithms for rapid unsupervised cryo-EM structure determination. *Nat. Methods* **14**, 290–296 (2017).

66. Scheres, S. H. W. & Chen, S. Prevention of overfitting in cryo-EM structure determination. *Nat. Methods* **9**, 853–854 (2012).

67. Tan, Y. Z. *et al.* Addressing preferred specimen orientation in single-particle cryo-EM through tilting. *Nat. Methods* **14**, 793–796 (2017).

68. Pettersen, E. F. *et al.* UCSF Chimera?A visualization system for exploratory research and analysis. *J. Comput. Chem.* **25**, 1605–1612 (2004).

69. Goddard, T. D. *et al.* UCSF ChimeraX: Meeting modern challenges in visualization and analysis: UCSF ChimeraX Visualization System. *Protein Sci.* **27**, 14–25 (2018).

70. Pettersen, E. F. *et al.* UCSF ChimeraX : Structure visualization for researchers, educators, and developers. *Protein Sci.* **30**, 70–82 (2021).

71. Krissinel, E. & Henrick, K. Inference of Macromolecular Assemblies from Crystalline State. *J. Mol. Biol.* **372**, 774–797 (2007).

72. Sarzotti-Kelsoe, M. *et al.* Optimization and validation of the TZM-bl assay for standardized assessments of neutralizing antibodies against HIV-1. *J. Immunol. Methods* **409**, 131–146 (2014).

73. West, A. P. *et al.* Computational analysis of anti–HIV-1 antibody neutralization panel data to identify potential functional epitope residues. *Comput. Biol.* 6.

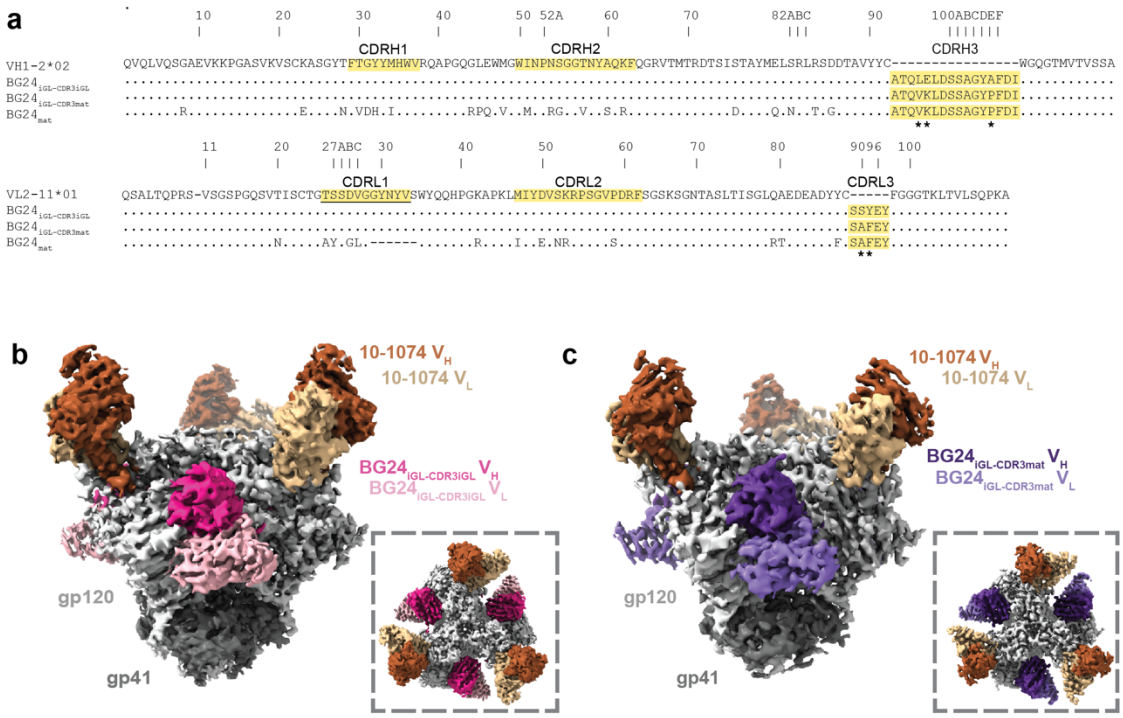

Fig. 1 | BG24$_{iGL}$s bind the CD4bs of the GT1 immunogen

a, Sequence alignment of V_H and V_L iGL precursors of BG24 (VH1-2*02 and VL2-11*01), BG24$_{iGL\text{-}CDR3iGL}$, BG24$_{iGL\text{-}CDR3mat}$, and BG24$_{mat}$. CDRs are highlighted in yellow. Asterisks (*) indicate residue differences between mature and iGL CDR3s. Underlined CDRL1 indicates sequence used for the CDRL1 in the BG24$_{CDRL1\text{-}iGL}$ construct. **b**,**c,** Side and top-down (inset) views of cryo-EM density of BG24$_{iGL\text{-}CDR3iGL}$-GT1-10-1074 (**b**) and BG24$_{iGL\text{-}CDR3mat}$-GT1-10-1074 (**c**). Highlighted in colors include: gp120 subunits (light gray), gp41 (dark gray), BG24$_{iGL\text{-}CDR3iGL}$ VH (bright pink) and VL (light pink) domains, BG24$_{iGL\text{-}CDR3mat}$ VH (dark purple) and VL (light purple) domains, and 10-1074 VH (dark brown) and VL (light brown) domains.

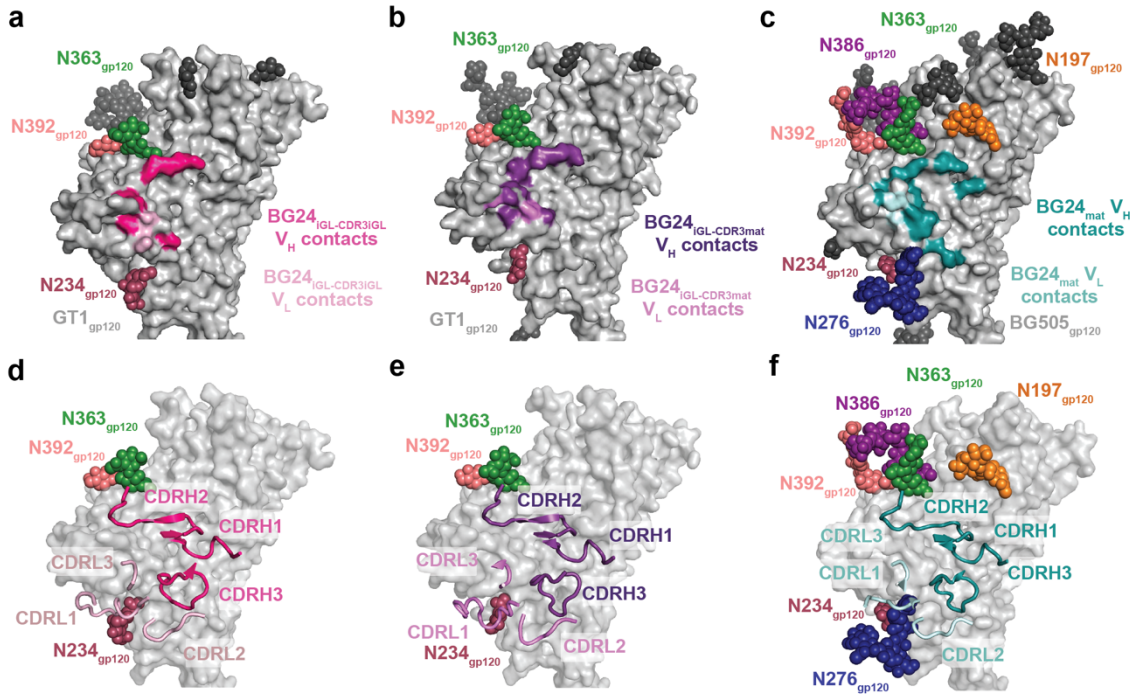

g

		gp120 Buried Surface Area (Å^2)									
Fab	Variable region	Inner	D Loop	CD4 Binding Loop	β20/21	β23	V5 Loop	β24	Exit Loop	V_H/V_LTotal	Total
$BG24_{iGL-CDR3iGL}$	V_H	0	203	176	87	86	120	36	14	722	951
	V_L	0	161	0	0	10	58	0	0	229	
$BG24_{iGL-CDR3mat}$	V_H	0	203	188	26	87	97	40	12	653	953
	V_L	0	198	0	0	7	95	0	0	300	
$BG24_{mat}$	V_H	16	243	181	74	136	118	36	42	846	1086
	V_L	0	107	0	0	20	113	0	0	240	

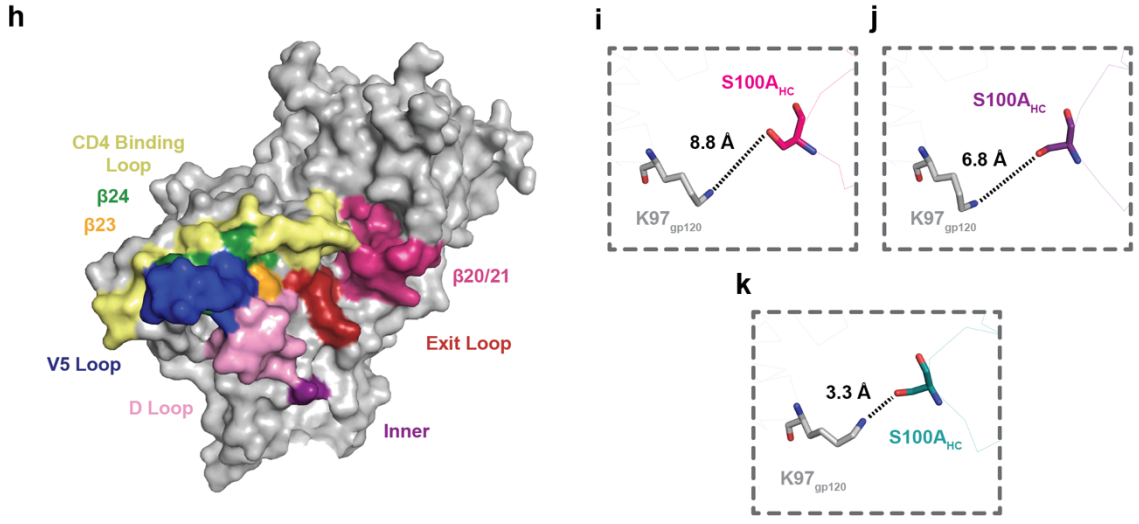

Fig. 2 | Comparison of $BG24_{iGL}$ and $BG24_{mat}$ CD4bs epitopes

Surface contacts made by $BG24_{iGL\text{-}CDR3iGL}$ V_H (bright pink) and V_L (light pink) on GT1 gp120 (light gray) (**a**), $BG24_{iGL\text{-}CDR3mat}$ V_H (dark purple) and V_L (light purple) on GT1 gp120 (light gray) (**b**), $BG24_{mat}$ V_H (deep teal) and V_L (light teal) surface contacts on BG505 gp120 (light gray) by $BG24_{mat}$ (PDB 7UCF) (**c**). Surface representation of gp120 (light gray) with cartoon representations of $BG24_{iGL\text{-}CDR3iGL}$ (**d**), $BG24_{iGL\text{-}CDR3mat}$ (**e**), and $BG24_{mat}$ (**f**) CDR loops. VH and VL CDR loops are colored the same as in (**a-c**) **g**, Summary table of gp120 buried surface area (BSA) ($Å^2$) calculations for $BG24_{iGL\text{-}CDR3iGL}$, $BG24_{iGL\text{-}CDR3mat}$, and $BG24_{mat}$ at the inner domain (inner), D loop, CD4bs loop, β20/21, β23, V5 loop, β24, and exit loop of the CD4bs. BSA calculations were conducted for gp120 peptide components and did not include glycan interactions. **h**, Surface representation of gp120 (PDB 5T3Z) with CD4bs motifs colored and labeled (inner domain - purple, D loop – light pink, CD4bs loop – yellow, β20/21 – bright pink, β23 – orange, V5 loop – blue, β24 – green, and exit loop – red). Distance measurements between $K97_{gp120}$ and $S100A_{HC}$ for **i,** $BG24_{iGL\text{-}CDR3iGL}$-$GT1_{gp120,}$ j, $BG24_{iGL\text{-}CDR3mat}$-$GT1_{gp120}$, and **k**, $BG24_{mat}$-$BG505_{gp120}$ structures. The distances between atoms are represented by black dotted lines.

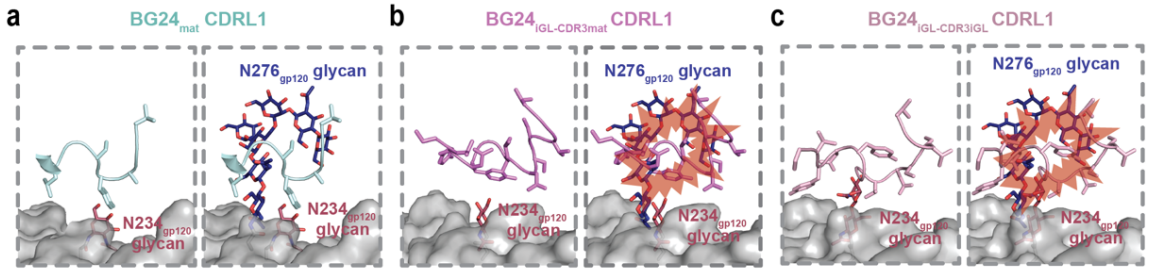

d

Region	CDRH1					CDRH2																FWRH3												CDRH3				
HC Residue	31	32	33	34	35	50	51	52	52A	53	54	55	56	57	58	59	60	61	62	63	64	65	66	67	68	69	70	71	72	73	74	75	100A	100B	100C	100D	100E
VH1-2*02	G	Y	Y	M	H	W	I	N	P	N	S	G	G	T	N	Y	A	Q	K	F	Q	G	R	V	T	M	T	R	D	T	S	I	S	A	G	Y	A
BG24 SHM	D	H	.	I	.	.	M	.	.	R	G	.	.	V	.	.	S	.	R	.	.	.	.	.	.	.	.	.	.	.	.	.	.	.	.	.	.	P
BG24iGL-CDR3iGL						*					*	*		*	*	*		*										*					*			*	
BG24iGL-CDR3mat			*			*					*	*		*	*			*			*							*								*	
BG24mat			*							*	*	*		*	*	*		*			*							*					*	*		*	

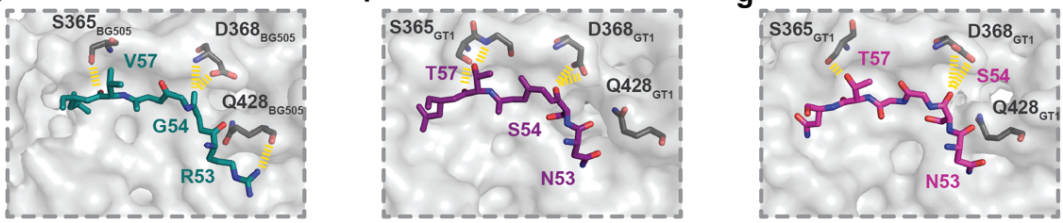

h

			IC50 (μg/mL)				
Virus Strain	Clade	Tier	BG24mat	BG24 R53NHC	BG24 G54SHC	BG24 V57THC	BG24 CDRH2iGL-3mut
246F3	AC	2	0.39	0.57	0.28	0.56	3.7
25710	C	1B	0.20	2.9	0.69	1.2	>200
398F1	A	2	0.05	0.87	0.41	0.82	47
BJOX002000	BC	2	0.25	2.0	0.17	2.4	>200
CE1176	C	2	1.8	16	9.7	9.7	>200
TRO11	B	2	0.71	1.9	1.0	1.6	>200
CNE8	AE	2	0.21	1.1	1.9	5.5	30
CE0217	C	2	0.29	0.75	0.35	3.1	>200
CNE55	AE	2	0.49	1.4	0.72	1.1	>200
X1632	G	2	>200	>200	>200	>200	>200
CH119	BC	2	0.65	3.0	0.99	1.1	49
X2278	B	2	0.064	0.67	0.18	0.24	2.6
BG505 T332N	A	2	0.29	0.56	0.32	0.39	1.2

Potency decrease compared to BG24mat

< 2 fold | 2-5 fold | > 5 fold

Fig. 3 | Somatic hypermutation and germline features play a role in BG24 recognition of the CD4bs interface

gp120 (light gray) surface in the vicinity of the CD4bs with cartoon representation main chain/stick side chains for the CDRL1s of **a**, $BG24_{mat}$ (light teal), **b**, $BG24_{iGL\text{-}CDR3mat}$ (light purple) **c**, $BG24_{iGL\text{-}CDR3iGL}$ (light pink) overlaid with the $N276_{gp120}$ N-glycan (dark blue) from the $BG24_{mat}$-BG505 complex (PDB 7UCF). Steric clashes are represented with red bursts. **d,** Table summarizing HC paratope residues in $BG24_{iGL\text{-}CDR3iGL}$-GT1, $BG24_{iGL\text{-}CDR3mat}$-GT1 and $BG24_{mat}$-BG505 structures. The paratope was defined by Ab residues that make contacts with gp120 within 4 Å for each structure. Stick representations of the CDRH2 residues from **e**, $BG24_{mat}$ (deep teal), **f**, $BG24_{iGL\text{-}CDR3mat}$ (dark purple), **g**, $BG24_{iGL\text{-}CDR3iGL}$ (bright pink) interacting with BG505 or GT1 gp120 residues. Yellow dashed lines indicate Ab-gp120 interactions within 4 Å. **h**, Neutralization data of BG24 CDRH2 mutants against a global 12 virus panel[35] and BG505 T332N[33]. IC_{50} values represent the average mean from duplicate neutralization measurements. A heatmap describes >2-fold (white), 2-5 fold (light red), and >5-fold (dark red) potency decreases compared to $BG24_{mat}$.

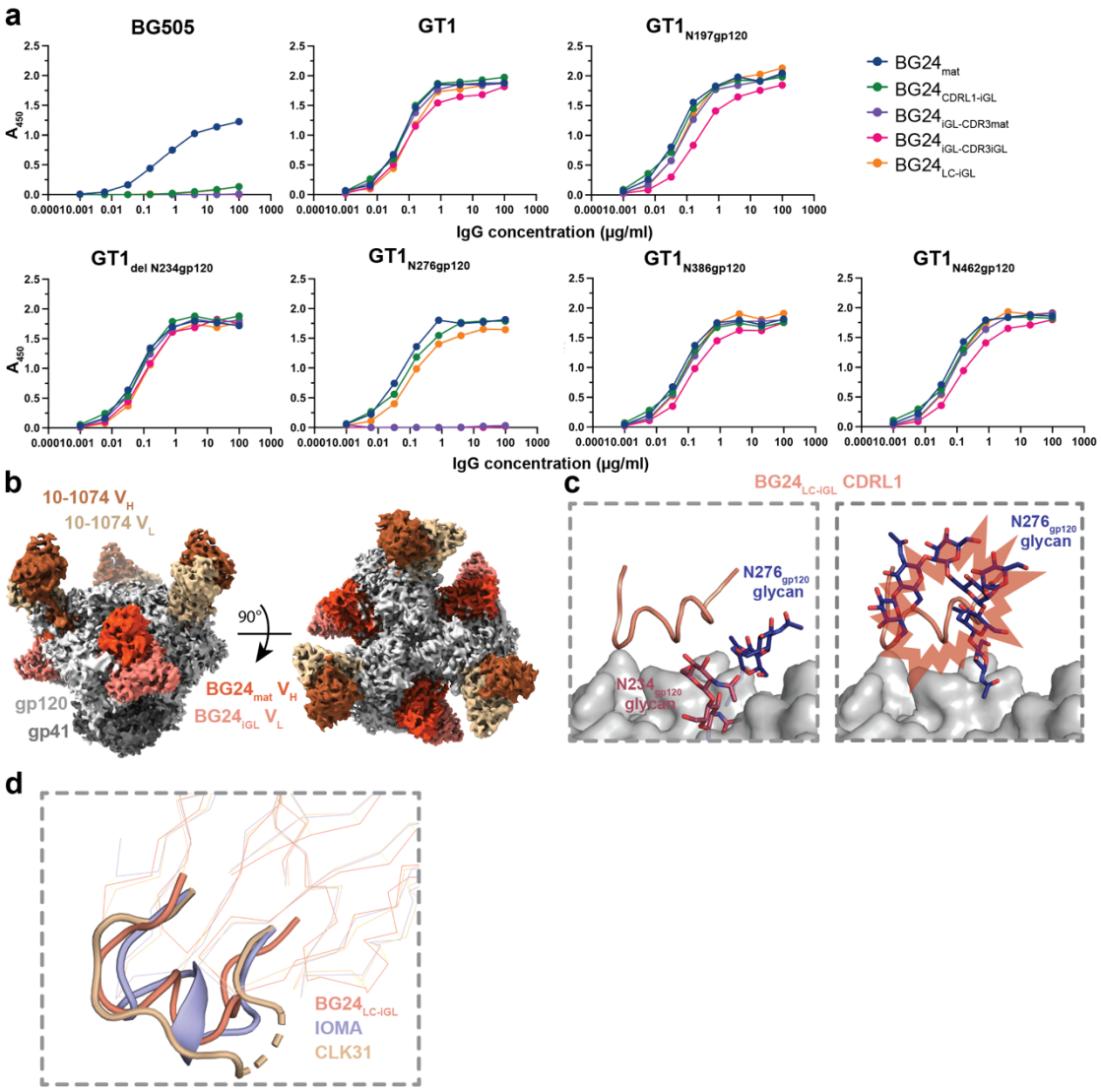
a
BG505
GT1
GT1N197gp120
BG24mat
BG24CDRL1-iGL
BG24iGL-CDR3mat
BG24iGL-CDR3iGL
BG24LC-iGL
A450
IgG concentration (μg/ml)
GT1del N234gp120
GT1N276gp120
GT1N386gp120
GT1N462gp120
b
10-1074 VH
10-1074 VL
90°
BG24mat VH
BG24iGL VL
gp120
gp41
c
BG24LC-iGL CDRL1
N276gp120 glycan
N234gp120 glycan
d
BG24LC-iGL
IOMA
CLK31

Fig. 4 | $BG24_{iGL}$ binding is mediated by CD4bs glycans

a, ELISA to access binding of the indicated BG24 Abs to BG505, GT1, and GT1 SOSIP Envs with altered N-glycans in the CD4bs. Streptavidin plates were coated with randomly biotinylated SOSIPs and incubated with IgGs at increasing concentrations. Values are shown as mean of two individual biological replicates (n=2). Source data are provided as a Source Data file. **b**, Side and top-down views of cryo-EM density of $BG24_{LC\text{-}iGL}$-GT1-10-1074. Highlighted in colors include: gp120 subunits (light gray), gp41 (dark gray), $BG24_{mat}$ VH (deep coral) and VL (light coral) domains, and 10-1074 VH (dark brown) and VL (light brown) domains. **c**, Cartoon representation of the CDLR1 of $BG24_{LC\text{-}iGL}$ (left) (light coral) and overlaid with the $N276_{gp120}$ N-glycan (dark blue) from a $BG24_{mat}$-BG505 (PDB 7UCF) (right). Predicted steric clashes are indicated by red bursts. **d,** Alignment of $BG24_{LC\text{-}iGL}$ (from the $BG24_{LC\text{-}iGL}$-$GT1_{N276gp120}$-10-1074 structure) (light coral), IOMA (PDB 5T3Z) (lilac), and CLK31 (PDB 6D2P) (wheat) LC with CDRL1s represented in cartoon.

a

Virus ID	Tier	Clade	$BG24_{CDRL1\text{-}iGL}$ IgG (μg/ml)	
			IC_{50}	IC_{80}
6405	unknown	D	6.8	>25
6952	2	CD	22.5	>25

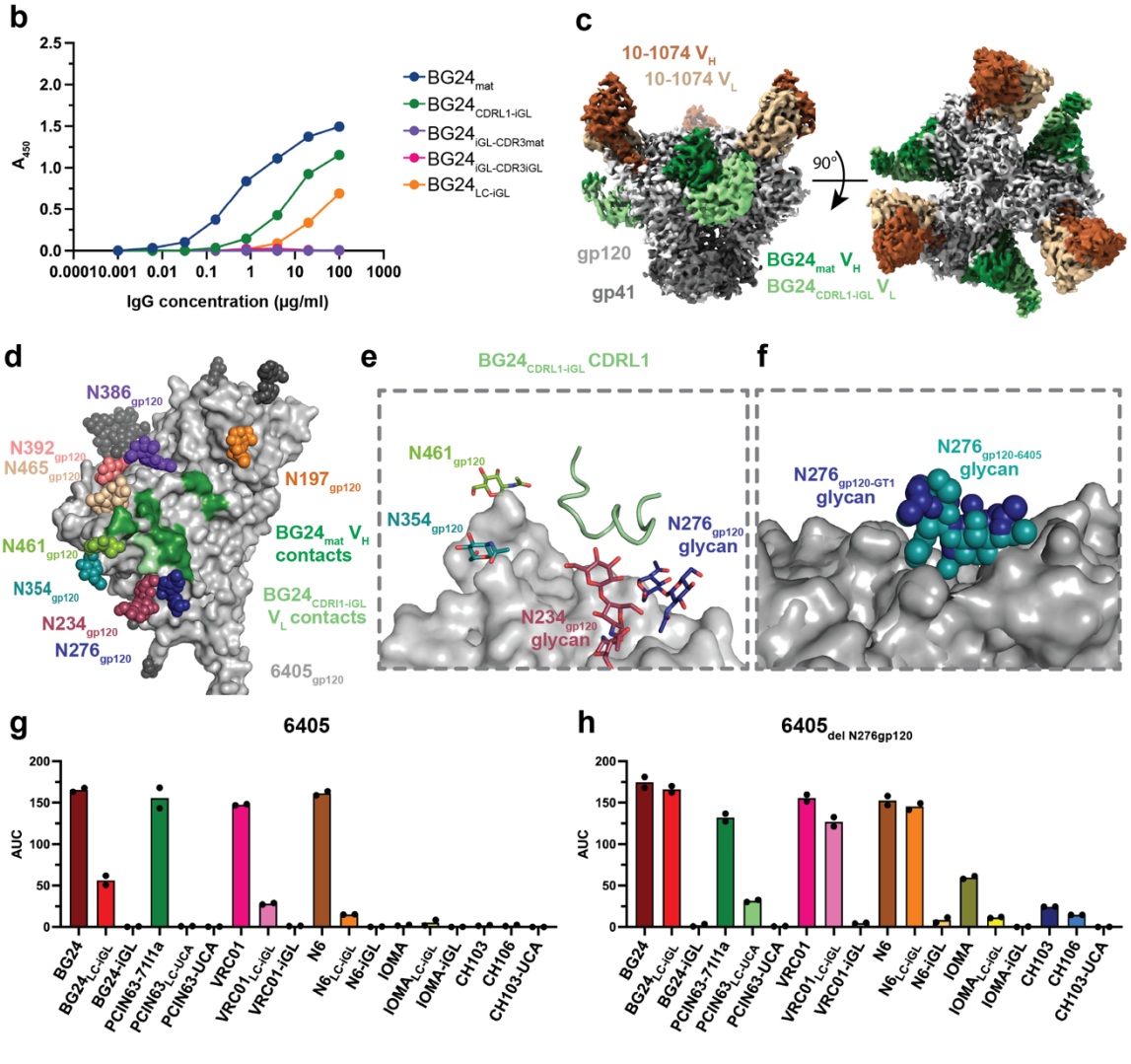

Fig. 5 | Non-engineered 6405 SOSIP recognizes BG24$_{CDRL1\text{-}iGL}$

a, Summary of neutralization of 6405 and 6952 pseudoviruses by BG24$_{CDRL1\text{-}iGL}$ IgGs. **b**, ELISA to access binding of BG24-derived Abs to 6405 SOSIP. Streptavidin plates were coated with randomly biotinylated SOSIPs and incubated with BG24-derived IgGs, at increasing concentrations. Values are shown as mean of two individual biological replicates (n=2) with associated. **c,** Side and top-down views of cryo-EM density of BG24$_{CDRL1\text{-}iGL}$-6405-10-1074. Highlighted in colors include: gp120 subunits (light gray), gp41 (dark gray), BG24$_{CDRL1\text{-}iGL}$ VH (dark green) and VL (light green) domains, and 10-1074 VH (dark brown) and VL (light brown) domains. **d**, Surface contacts made by BG24$_{CDRL1\text{-}iGL}$ V_H (dark green) and V_L (light green) on 6405 gp120 (light gray). **e**, Cartoon representation for the CDLR1 of BG24$_{CDRL1\text{-}iGL}$ (light green). **f**, Alignment of GT1$_{N276gp120}$ (light gray) and 6405 gp120s (light gray) in surface representation and N276 glycans (dark blue and deep teal) in sphere representation. **g,h,** Summary for area under the curve (AUC) values derived from ELISAs that accessed binding of CD4bs IgGs to **g**, 6405 and **h,** 6405$_{delN276gp120}$ SOSIPs. Streptavidin plates were coated with randomly biotinylated SOSIPs and incubated with CD4bs IgGs at increasing concentrations. Values are shown as mean of two individual biological replicates (n=2). Source data are provided as a Source Data file.

Supplementary Information

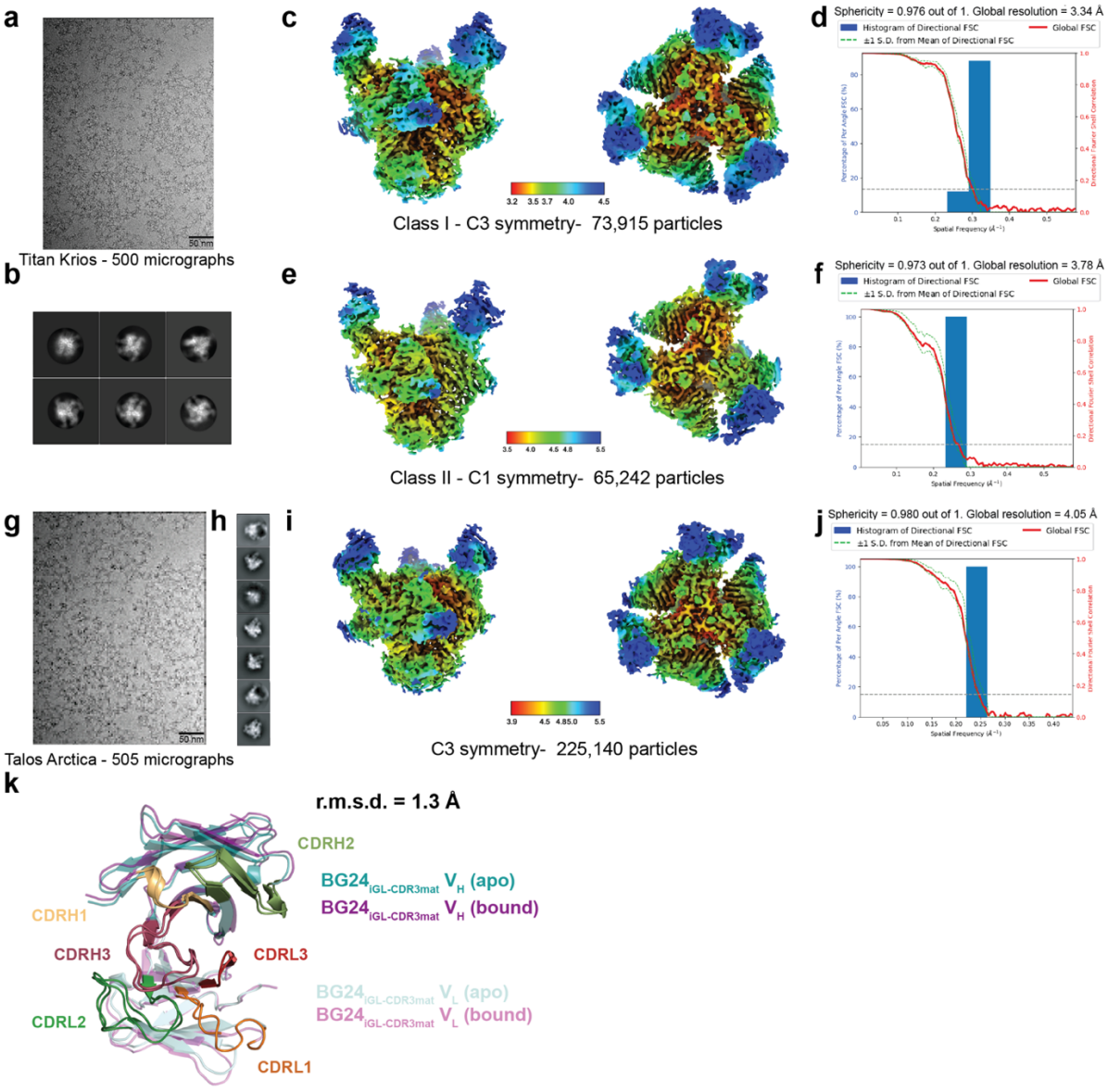

Supplementary Fig. 1 | Cryo-EM data processing and validation for $BG24_{iGL}$- GT1-10-1074 complexes and $BG24_{iGL\text{-}CDR3mat}$ Fab alignment

a, Representative micrograph and **b**, cryo-EM 2D class averages for the $BG24_{iGL}$-$_{CDR3iGL}$-GT1-10-1074 cryo-EM structures. For this dataset, two classes were resolved: Class I with three $BG24_{iGL\text{-}CDR3iGL}$ Fabs bound to GT1, and Class II with two $BG24_{iGL\text{-}CDR3iGL}$ Fabs bound to GT1. Differences in the cryo-EM density map for Class I and Class II of the $BG24_{iGL}$-$_{CDR3iGL}$-GT1-10-1074 complex were not observed. The **c**, local resolution map and **d**, gold-standard Fourier shell correlation (FSC) plots for $BG24_{iGL}$-$_{CDR3iGL}$- GT1-10-1074 Class I. The **e**, local resolution map and **f**, gold-standard Fourier shell correlation (FSC) plots for $BG24_{iGL}$-$_{CDR3iGL}$- GT1-10-1074 Class II. **g**, Representative micrograph, **h**, cryo-EM 2D class averages, **i**, local resolution estimations, and **j**, gold-standard Fourier shell correlation (FSC) plots for $BG24_{iGL\text{-}CDR3mat}$-GT1-10-1074. **k**, Alignment and r.m.s.d. (Å) of the crystal structure of apo $BG24_{iGL\text{-}CDR3mat}$ Fab and the $BG24_{iGL\text{-}CDR3mat}$ Fab bound to GT1 in the cryo-EM structure.

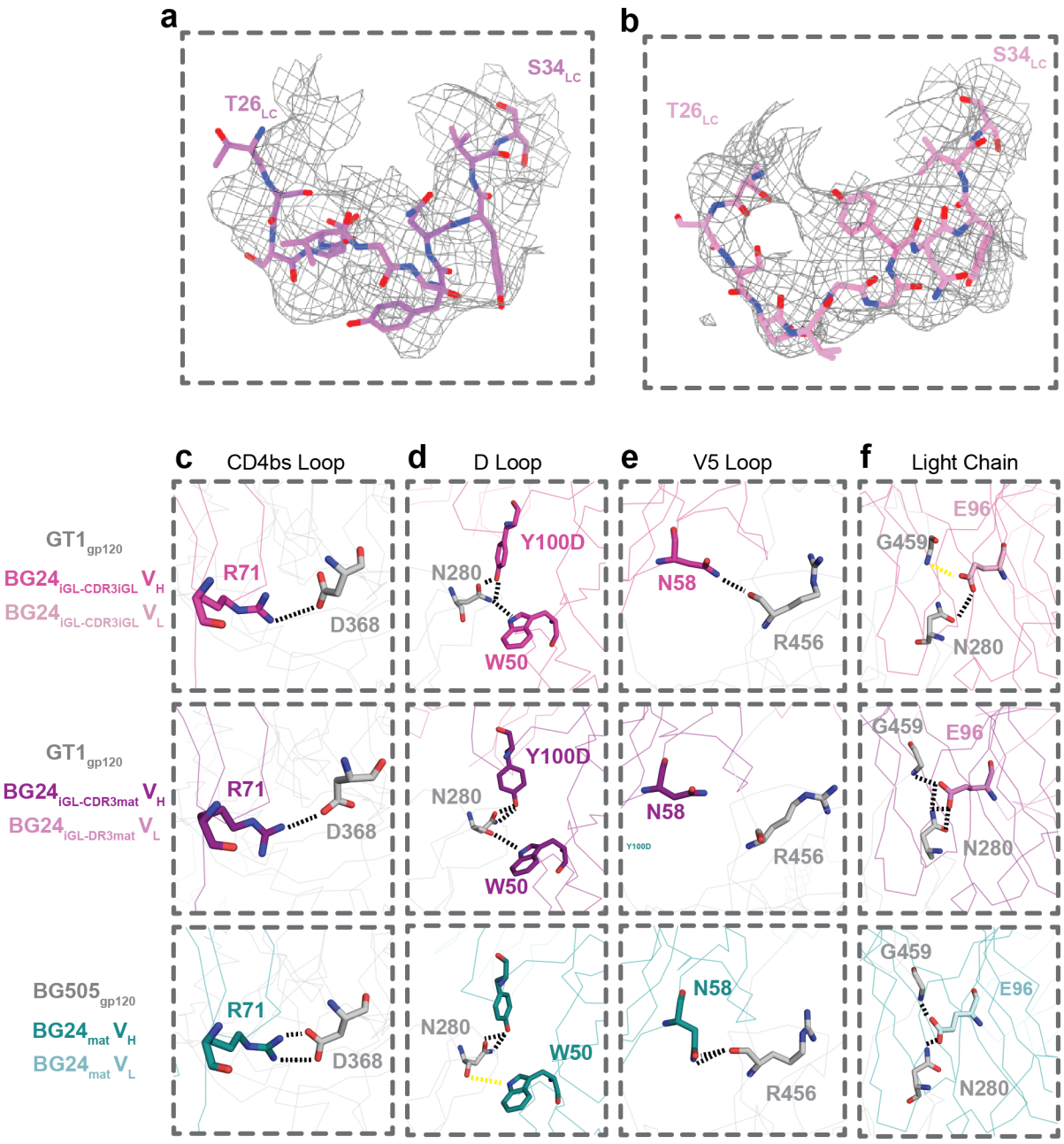
a
T26LC
S34LC
b
T26LC
S34LC
c CD4bs Loop
d D Loop
e V5 Loop
f Light Chain
GT1gp120
BG24iGL-CDR3iGL VH
BG24iGL-CDR3iGL VL
R71
D368
Y100D
N280
W50
N58
R456
E96
G459
GT1gp120
BG24iGL-CDR3mat VH
BG24iGL-DR3mat VL
BG505gp120
BG24mat VH
BG24mat VL

Supplementary Fig. 2 | $BG24_{iGL}$ CDRL1 local density and VH1-2*02 signature contacts comparison among $BG24_{iGL}$ and $BG24_{mat}$ structures

Local density for CDRL1 with modeled LC residues T26-$S34_{LC}$ (stick representation) for **a**, $BG24_{iGL\text{-}CDR3mat}$ and **b**, $BG24_{iGL\text{-}CDR3iGL}$ contoured to 3.8 and 3.6 σ, respectively. Interactions in **c**, CD4bs, **d**, D Loop, **e**, V5 loop, and **f**, LC for $BG24_{iGL\text{-}CDR3iGL}$-$GT1_{gp120,}$ $BG24_{iGL\text{-}CDR3mat}$-$GT1_{gp120}$, and $BG24_{mat}$-$BG505_{gp120}$ structures. Contacts between atoms within 4 Å are represented by black dotted lines; contacts between 4-5 Å are represented by yellow dotted lines.

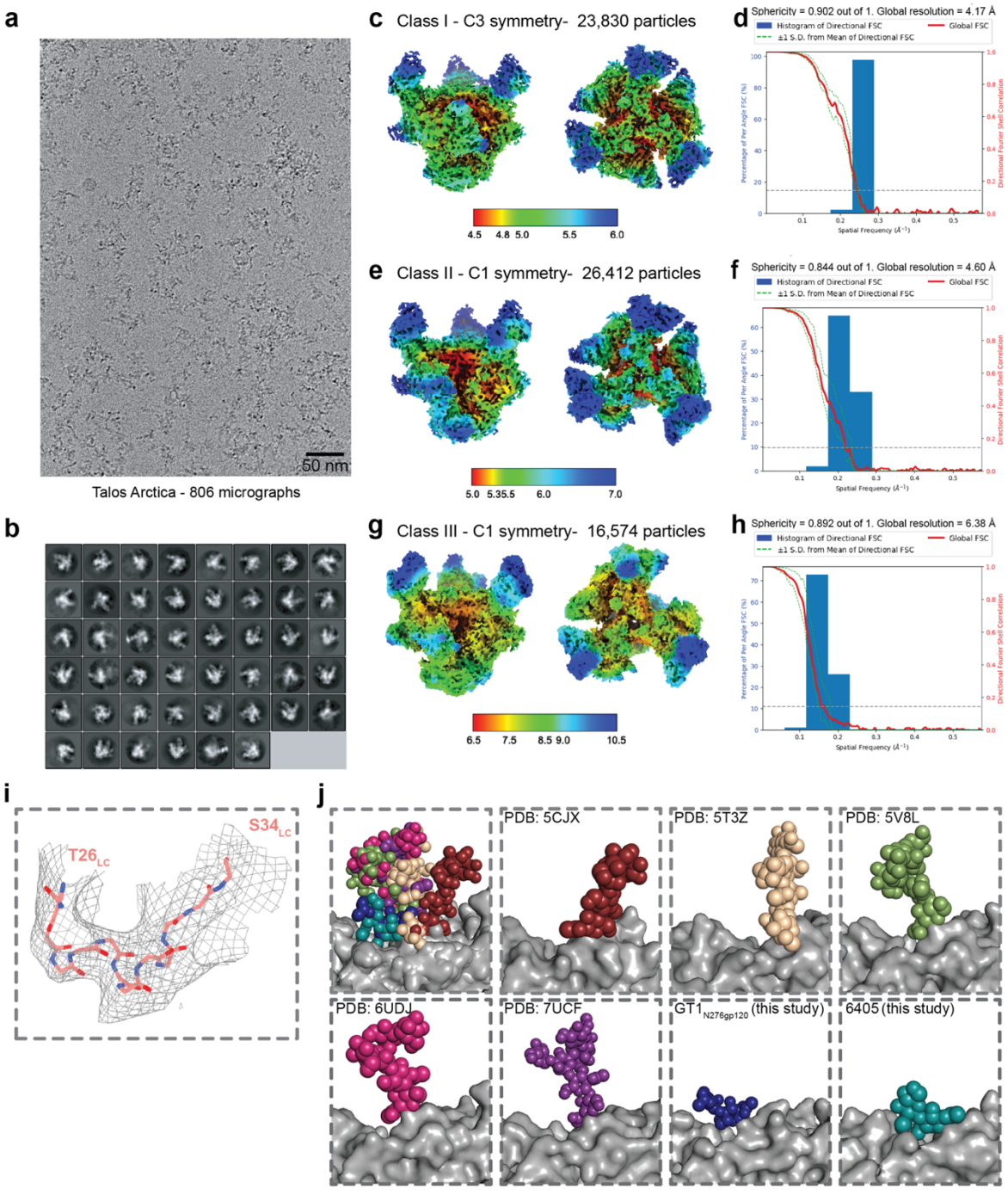
a
50 nm
Talos Arctica - 806 micrographs
b
c Class I - C3 symmetry- 23,830 particles
4.5 4.8 5.0 5.5 6.0
d Sphericity = 0.902 out of 1. Global resolution = 4.17 Å
Histogram of Directional FSC
Global FSC
±1 S.D. from Mean of Directional FSC
Percentage of Per Angle FSC (%)
Directional Fourier Shell Correlation
Spatial Frequency (Å⁻¹)
e Class II - C1 symmetry- 26,412 particles
5.0 5.35.5 6.0 7.0
f Sphericity = 0.844 out of 1. Global resolution = 4.60 Å
Histogram of Directional FSC
Global FSC
±1 S.D. from Mean of Directional FSC
Percentage of Per Angle FSC (%)
Directional Fourier Shell Correlation
Spatial Frequency (Å⁻¹)
g Class III - C1 symmetry- 16,574 particles
6.5 7.5 8.5 9.0 10.5
h Sphericity = 0.892 out of 1. Global resolution = 6.38 Å
Histogram of Directional FSC
Global FSC
±1 S.D. from Mean of Directional FSC
Percentage of Per Angle FSC (%)
Directional Fourier Shell Correlation
Spatial Frequency (Å⁻¹)
i
S34LC
T26LC
j
PDB: 5CJX
PDB: 5T3Z
PDB: 5V8L
PDB: 6UDJ
PDB: 7UCF
GT1N276gp120 (this study)
6405 (this study)

Supplementary Fig. 3 | Cryo-EM data processing and validation for $BG24_{LC\text{-}iGL}$-$GT1_{N276gp120}$-10-1074 complex, $BG24_{LC\text{-}iGL}$ CDRL1 local density, and analysis of $N276_{gp120}$ glycan flexibility

a, Representative micrograph, **b**, cryo-EM 2D class averages for the $BG24_{LC\text{-}iGL}$-$GT1_{N276gp120}$-10-1074 cryo-EM structures. For this dataset, three classes were resolved: Class I with three $BG24_{LC\text{-}iGL}$ Fabs bound to $GT1_{N276gp120}$, Class II with two $BG24_{LC\text{-}iGL}$ Fabs bound to $GT1_{N276gp120}$, and Class III with one $BG24_{LC\text{-}iGL}$ Fab bound to $GT1_{N276gp120}$. The **c**, local resolution map and **d**, gold-standard Fourier shell correlation (FSC) plots for $BG24_{LC\text{-}iGL}$- $GT1_{N276gp120}$-10-1074 Class I. The **e**, local resolution map and **f**, gold-standard Fourier shell correlation (FSC) plots for $BG24_{LC\text{-}iGL}$- $GT1_{N276gp120}$-10-1074 Class II. The **g**, local resolution map and **h**, gold-standard Fourier shell correlation (FSC) plots for $BG24_{LC\text{-}iGL}$- $GT1_{N276gp120}$-10-1074 Class III. **i**, Local density for CDRL1 with modeled backbone for LC residues T26-$S34_{LC}$ (stick representation) for $BG24_{LC\text{-}iGL}$ contoured to 5.4 σ. **j**, Comparison and overlay of the $N276_{gp120}$ glycan from existing Env structures and $GT1_{N276gp120}$ and 6405 from this study.

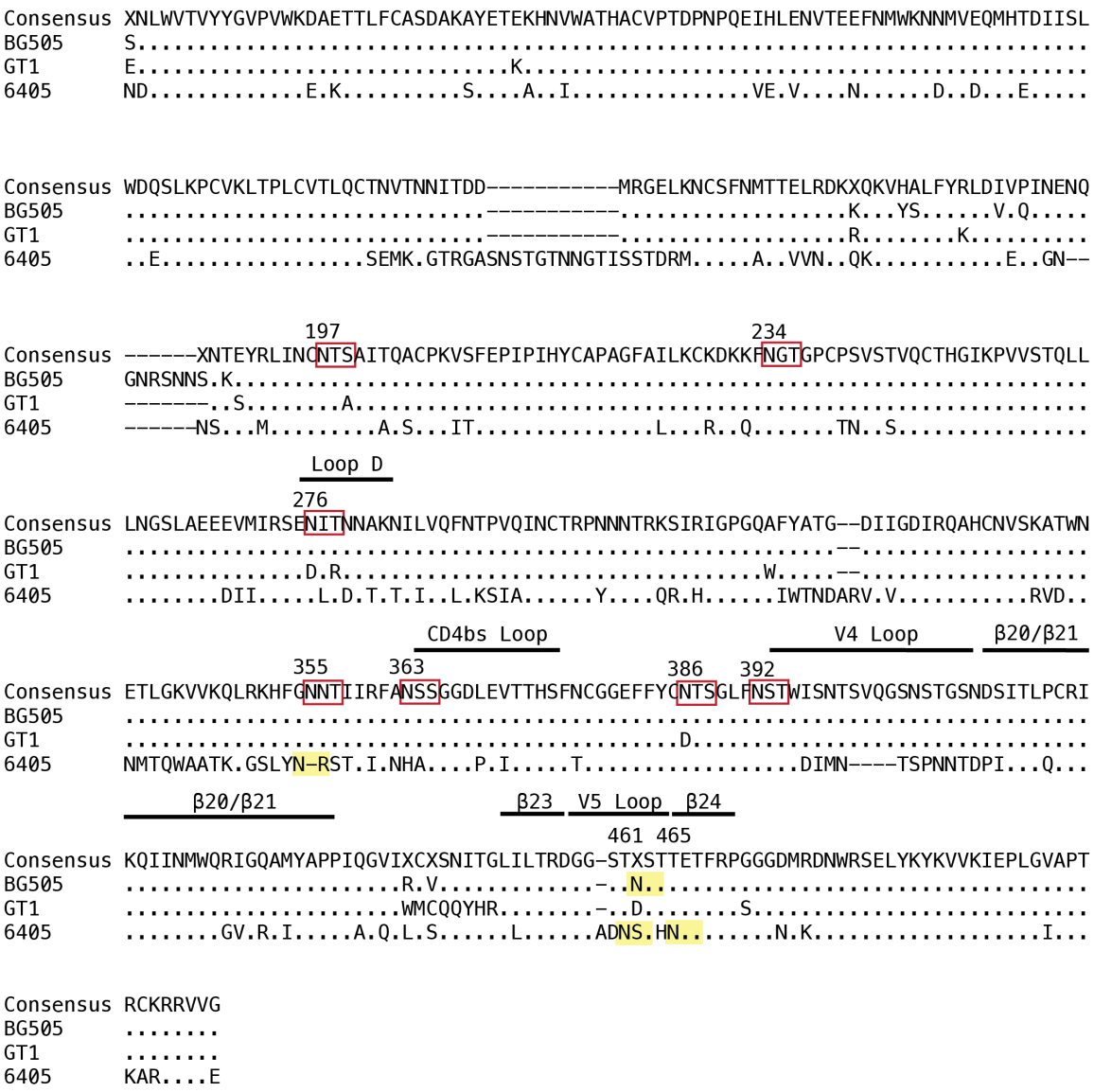

Supplementary Fig. 4 | Sequence Alignment of BG505, GT1, and 6405 gp120

The sequence alignment for BG505, GT1, and 6405 gp120 residues and assigned consensus sequence. PNGS sequons in the consensus sequence are boxed in red, with residues numbers corresponding to Asn in the PNGS indicated above the sequence. PNGSs that are not conserved are highlighted in yellow, again with residues numbers corresponding to the Asn in the PNGS indicated above the sequence.

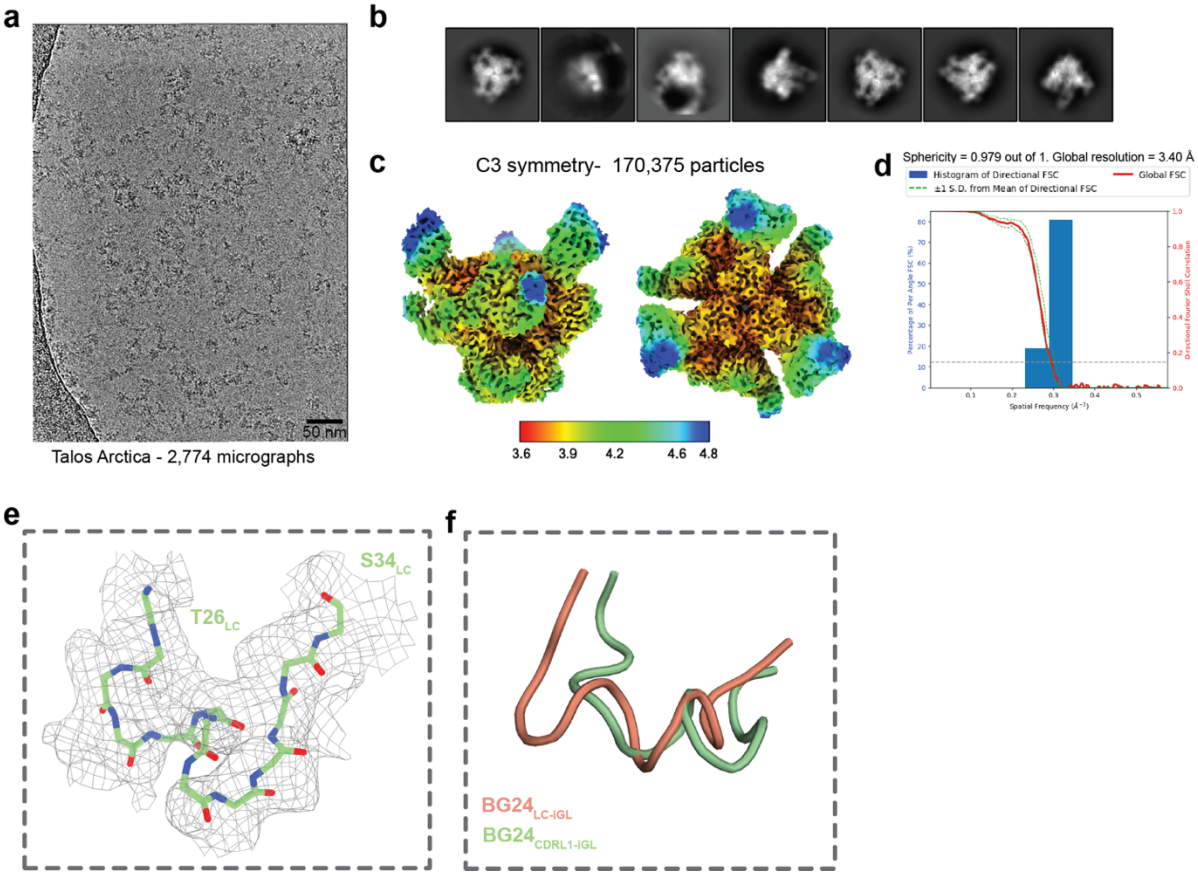

Supplementary Fig. 5 | Cryo-EM data processing and validation for BG24$_{CDRL1\text{-}iGL}$-6405-10-1074 complex and BG24$_{CDRL1\text{-}iGL}$ CDRL1 local density

a, Representative micrograph, **b**, cryo-EM 2D class averages, **c**, local resolution estimations, and **d**, gold-standard Fourier shell correlation (FSC) plots for BG24$_{CDRL1\text{-}iGL}$-6405-10-1074. **e**, Local density for CDRL1 with modeled backbone for residues T26-S34$_{LC}$ (stick representation) for BG24$_{CDRL1\text{-}iGL}$ contoured to 4.4 σ. **f**, Alignment of BG24$_{iGL}$ CDLR1s from the BG24$_{LC\text{-}iGL}$-GT1$_{N276gp120}$-10-1074 structure and from the BG24$_{CDRL1\text{-}iGL}$-6405-BG24$_{LC\text{-}iGL}$-10-1074 structure. CDRL1s are represented in cartoon.

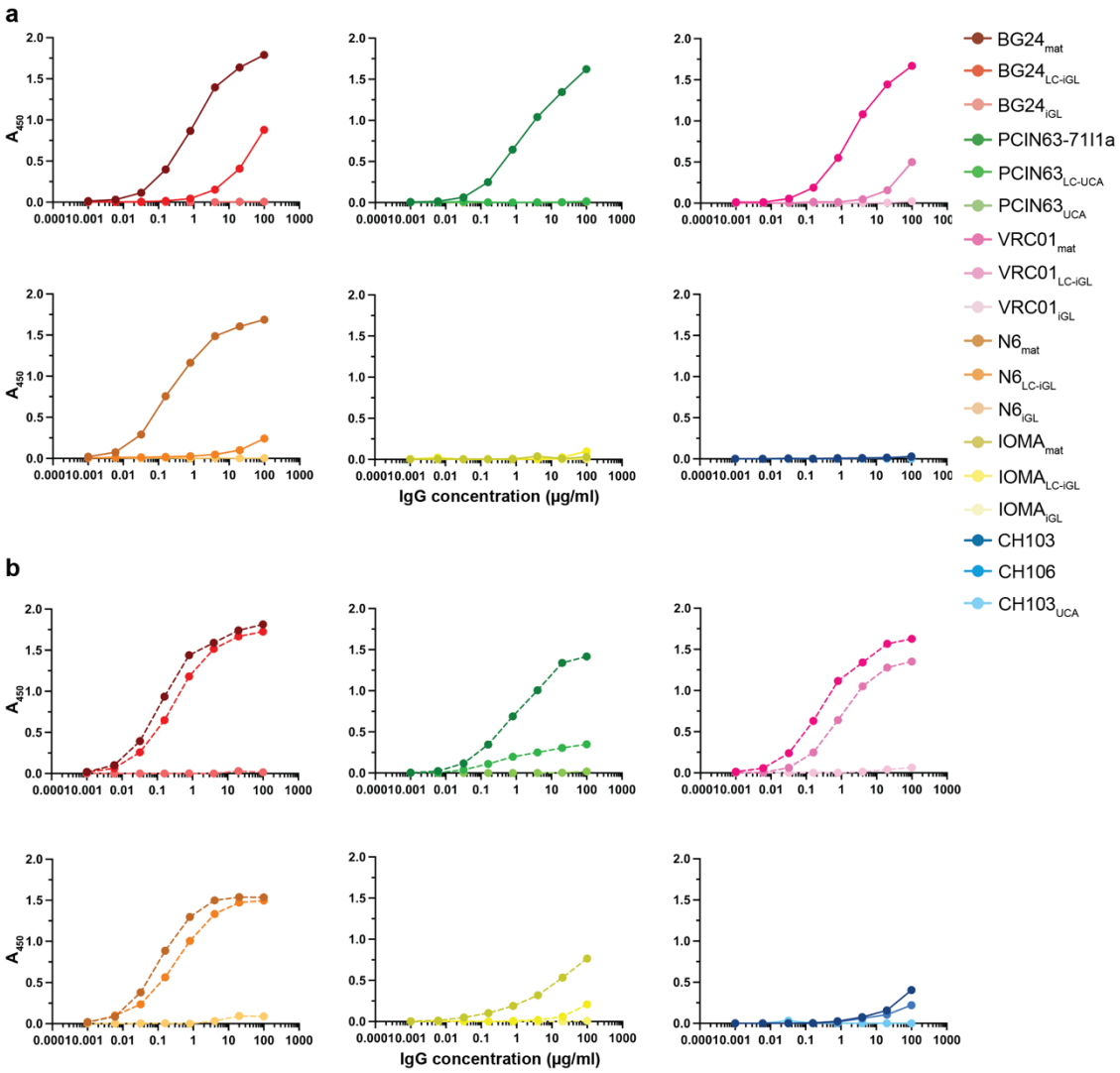

Supplementary Fig. 6 | ELISA curves of CD4bs IgGs bound to 6405 and 6405$_{delN276gp120}$ ELISA curves corresponding to CD4bs IgGs bound to **a**, 6405 and **b,** 6405$_{delN276gp120}$ SOSIPs. Values are shown as mean ± s.d. of two individual biological replicates (n=2).

Supplementary table 1. Cryo-EM data collection, refinement, and validation statistics

	$BG24_{iGL\text{-}CDR3iGL}$- GT1-10-1074	$BG24_{iGL\text{-}CDR3mat}$- GT1-10-1074	$BG24_{LC\text{-}iGL}$- $GT1_{N276gp120}$-10-1074	$BG24_{CDRL1\text{-}iGL}$-6405-10-1074
EMDB:	EMD-26490	EMD-26492	EMD-26493	EMD-26496
PDB:	7UGN	7UGO	7UGP	7UGQ
Data collection and processing				
Magnification*	105,000x	73,000x	45,000x	45,000x
Voltage (kV)	300	200	200	200
Electron exposure (e–/Å^2)	60	60	60	60
Defocus range (μm)	1.2-3.0	1.2-3.0	1.2-3.0	1.2-3.0
Pixel size (Å)	0.8654	1.436	0.869	0.869
Recording mode	Counting	Counting	Counting	Counting
Symmetry imposed	C3	C3	C3	C3
Initial particle images (no.)	139,157	422,161	178,814	770,375
Final particle images (no.)	73,915	225,140	23,830	170,897
Overall map resolution (Å) (masked/unmasked)**	3.4 (3.7)	4.1 (5.0)	4.2 (4.8)	3.4 (3.7)
Refinement				
Initial model used (PDB code)	5T3Z	5T3Z	5T3Z	5T3Z
Map and model CC	0.84	0.82	0.73	0.79
Map sharpening *B* factor (Å^2)	-77	-150	-138	-119
Model composition				
Protein residues	3150	3138	3111	3162
Glycan residues	67	87	66	135
Validation				
MolProbity score	1.64	1.72	1.97	2.08
Clashscore	5.95	5.97	11.63	13.18
Poor rotamers (%)	0.04	0	0.11	0.26
Ramachandran plot				
Favored (%)	95.5	94.2	94.3	92.9
Allowed (%)	4.5	5.8	5.7	7.1
Disallowed (%)	0	0	0	0
RMS deviations				
Length (Å)	0.002	0.002	0.002	0.004
Angles (°)	0.508	0.491	0.539	0.606

* Nominal magnification; ** FSC threshold 0.143

Supplementary table 2. X-ray data collection and refinement statistics (molecular replacement)

	iGL BG24 Fab *(12-2, SSRL)*
PDB ID	**7UGM**
Data collection[a]	
Space group	$P2_12_12_1$
Unit cell (Å)	53.2, 70.8, 134.9
α, β, γ (˚)	90, 90, 90
Wavelength (Å)	1.0
Resolution (Å)	38-1.4 (1.42-1.4)
Unique Reflections	101,139 (49,320)
Completeness (%)	100 (99.9)
Redundancy	19.7 (19.2)
$CC_{1/2}$ (%)	99.3 (67.2)
<I/σI>	11.0 (1.2)
Mosaicity (˚)	0.17
R_{merge} (%)	16 (103)
R_{pim} (%)	3.7 (237)
Wilson *B*-factor	14.2
Refinement and Validation	
Resolution (Å)	38-1.4
Number of atoms	
Protein	3,189
Water	447
R_{work}/R_{free} (%)	19.3/20.8
R.m.s. deviations	
Bond lengths (Å)	0.006
Bond angles (˚)	0.93
MolProbity score	1.42
Clashscore (all atom)	4.6
Poor rotamers (%)	0.3
Ramachandran plot	
Favored (%)	96.9
Allowed (%)	3.1
Disallowed (%)	0.2
Average *B*-factor (Å)	
Protein	24.3
Water	32.7

Chapter VII

ENGINEERING IOMA FOR OPTIMAL CD4 BINDING SITE FEATURES INFORMS VACCINE DESIGN

Kim-Marie A. Dam[1], Harry B. Gristick[1], Priyanthi N.P. Gnanapragasam[1], Evelyn Y. Li[1], Pamela J. Bjorkman[1]

[1]Division of Biology and Biological Engineering, California Institute of Technology, Pasadena, CA, USA

Abstract

HIV-1 broadly neutralizing antibodies (bNAbs) that target the CD4 binding site (CD4bs) epitope include rare features that pose challenges in efforts to elicit these bNAbs through vaccination. The IOMA-class of CD4bs bNAbs require fewer rare mutations to achieve broad neutralization, thus presenting a more accessible pathway for vaccine-induced bNAb development. Here, we investigated the role that somatic hypermutations (SHMs) play in conferring IOMA's neutralization potency and breadth by creating a library of IOMA mutants in which each SHM was individually reverted to its inferred germline (iGL) counterpart. Impacts on neutralization for each mutant were evaluated and this information was used to design $IOMA_{min}$ mutants that incorporated a minimal amount of SHM needed to maintain neutralization. These results demonstrate IOMA-class bNAbs require even fewer mutations for neutralization and further elucidates how IOMA's structural features correlate with its neutralization mechanism, informing the design of IOMA-targeting immunogens.

Introduction

The discovery and extensive characterization of broadly neutralizing antibodies (bNAbs) against HIV-1 that are capable of potently neutralizing a large fraction of circulating isolates have provided avenues to combat the ongoing HIV-1/AIDS pandemic including the development of bNAbs for passive transfer and vaccine design[1–6]. bNAbs target several epitopes on the sole viral glycoprotein on the surface of HIV-1, called envelope (Env), and high-resolution structures of HIV-1 Env:bNAb complexes have informed our understanding of bNAb features that confer neutralization and enabled structure-based immunogen design[6–12]. Although substantial progress has been made on this front[1,13–15], an HIV-1 vaccine capable of eliciting bNAbs and providing robust, diverse protection has yet to be developed.

The binding site for the HIV-1 host receptor, CD4 (CD4bs), is composed of a recessed pocket in gp120 that is obstructed by the presence of bulky, highly conserved N-linked glycans (Figure 1)[14,21,23]. It is an attractive target for HIV-1 immunogen design because bNAbs that bind this epitope are among the most potent and broad[6,12,16–20]. Many of the bNAbs that target the CD4bs share distinct V_H gene segments that encode particular features compatible with the CD4bs epitope and lead to impressive potency[12,17,21]. One class of CD4bs bNAbs are V_H1-2 gene-restricted and include two sub-classes: the well-studied VRC01-class[16,17,21] and the more recently described IOMA-class[8,22]. Although these two bNAb sub-classes share a V_H ontogeny, they have distinct sequence characteristics and binding mechanisms. The VRC01-class is defined by its rare, five-residue light chain complementary determining region (CDRL3) that is present in less than 1% of human light chain genes[16,21]. Other features include a CDRL1 with deletions or multiple glycine mutations that are necessary to accommodate the Env $N276_{gp120}$ glycan and generally high levels of somatic hypermutation (SHM)[16,21]. In contrast, the IOMA-class of CD4bs bNAbs are characterized by an eight-residue CDRL3, which is more commonly represented in the human B cell repertoire compared to VRC01-class five-residue CDRL3s[8,22]. IOMA-class CDRL1 mutations that confer $N276_{gp120}$ glycan accommodation include deletions or single glycine mutations[8,22]. IOMA-class bNAbs also have lower levels of SHM compared to the VRC01-class[8,22]. High levels of SHM associated with HIV-1 CD4bs bNAbs is considered as a hurdle in vaccine

development[10,23] because these mutations often require several years to accumulate in cases of natural infection and have been found vital to confer neutralization breadth[23].

Current efforts to elicit CD4bs bNAbs have adopted a germline targeting approach that seeks to create immunogens that specifically bind and activate germline precursors known to develop into a particular class of bNAb[14]. This method has been explored for the V_H1-2 gene-restricted class of CD4bs bNAbs, both VRC01 and IOMA subclasses, since they have defined and well-characterized features[24–29]. Although the VRC01-class is more broad and potent, the IOMA-class is thought to have features that are more feasible to elicit (i.e., more common-length CDRL3, lower levels of SHM)[8,22,27]. Recent studies involving design and evaluation of IOMA-targeting sequential immunization strategies demonstrated heterologous serum neutralization in knock-in and wildtype mice[27]. To further inform IOMA-targeting immunogen design, we evaluated IOMA's structural features and identified characteristics that contribute to IOMA's neutralization potency and breadth. We engineered IOMA mutants with minimal amounts of SHMs and identified SHMs that play or do not play a role in IOMA's neutralization function. This information illuminates IOMA's mechanism of neutralization and informs the design of IOMA-targeting immunogens and the evaluation of potential IOMA-class bNAbs from natural infection or elicited by IOMA-targeting vaccine regimens.

Results

Identifying SHMs that contribute to IOMA neutralization potency and breadth

Although CD4bs bNAbs typically contain high levels of SHM, the design of minimally mutated CD4bs bNAbs and discovery of VRC01-class bNAbs with lower levels of SHM have demonstrated that many SHMs are accessories of prolonged maturation during chronic infection and do not contribute to bNAb neutralization activity[11,23,30,31]. Here, we sought to characterize the role of SHM in IOMA to understand how SHM influences neutralization and inform immunogen design that seeks to elicit IOMA-class bNAbs. To identify SHMs in

IOMA that contribute to neutralization potency and breadth, we designed a panel of IOMA mutants in which individual SHMs were reverted to their iGL counterparts and evaluated effects on neutralization against a screening panel of HIV-1 pseudoviruses.

We designated two cohorts of IOMA SHMs by analyzing a crystal structure (PDB 5T3Z) of IOMA Fab in complex with a clade A native-like soluble Env trimer (BG505 SOSIP.664)[32]: SHMs that participate in the Ab:Env interface and interact with Env gp120 residues, termed internal face SHMs (inFACE), and SHMs that do not participate in Ab:Env interactions, termed external face SHMs (exFACE). SHM residues in the IOMA variable heavy (V_H) and variable light (V_L) domains that formed interactions with BG505 within 4.0 Å were considered inFACE residues, and the remaining SHMs were designated exFACE residues. This analysis assigned 9 V_H/9 V_L exFACE residues and 13 V_H/7 V_L inFACE residues (Figure 2A,B).

We first evaluated IOMA SHMs in the exFACE. Although these mutations were not involved in antibody (Ab):Env interactions, we hypothesized that some exFACE mutations could play a role in maintaining IOMAs structural integrity, and thus, could have indirect contributions to neutralization potency and breadth. We created individual V_H/V_L $IOMA_{exFACE}$ IgGs and tested neutralization against a small screening panel composed of HIV-1 strains IOMA neutralizes to varying degrees (Figure 2C). Our panel included CNE20 (IOMA IC_{50}: <0.1μg/ml), 426c (IOMA IC_{50}: 0.1-0.99 μg/ml), BG505 (IOMA IC_{50}: 1-9.9 μg/ml), and CNE8 (IOMA IC_{50}: 10-50 μg/ml).

In the V_H domain, 4 of 9 exFACE mutants ($Q10E_{HC}$, $T19K_{HC}$, $I77T_{HC}$, $F78A_{HC}$) resulted in >3-fold decreases in IC_{50} compared to IOMA against 3 strains (Figure 2C). In the context of all exFACE mutations, these 4 mutations are in closest proximity (within 5-10 Å) to the $N197_{gp120}$ glycan, suggesting these mutations evolved to stabilize interactions with N-glycans. In the V_L domain, most exFACE mutants resulted in comparable neutralization compared to IOMA in the screening panel suggesting LC exFACE mutants play a lesser role in neutralization activity compared to V_H exFACE mutants. Only 3 exFACE V_L mutants ($N51S_{LC}$, $I58V_{LC}$, $A64G_{LC}$, $Y89C_{LC}$) had a >2-fold increase in IC_{50} compared to IOMA

against at least 2 strains. Based on these results, we sought to design a $IOMA_{exFACEmin}$ mutant that incorporates SHMs in the exFACE that had negligible effects on IOMA's neutralization activity.

We applied the following criteria to select individual exFACE mutations: IC_{50} values for each mutant must be within 2-fold of IOMA against at least two strains and must not be >3-fold worse against IOMA against more than one strain. These mutations were combined to create $IOMA_{exFACEmin}$ (Figure 2D). To validate our design of $IOMA_{exFACEmin}$, we compared IOMA neutralization to $IOMA_{exFACEmin}$ and $IOMA_{exFACE}$, a mutant with all exFACE SHMs reverted to iGL residues, against the screening panel. We found that $IOMA_{exFACEmin}$ had IC_{50}s that were within 2-fold of IOMA's IC_{50} values against all strains, whereas $IOMA_{exFACE}$ had IC_{50}s that were 3-fold greater than that of IOMA against four strains (Figure 2C). These results supported our hypothesis that exFACE residues contribute to IOMA's neutralization activity without directly interacting with Env residues, although V_H exFACE residues potentially play a role in $N197_{gp120}$ glycan accommodation.

We applied the same methodology to examine IOMA inFACE residues (Figure 2E). Given that these residues interact with Env gp120, we expected inFACE mutants would impact neutralization adversely. Indeed, 8 of 12 V_H inFACE mutants resulted in >3-fold increases in IC_{50} values compared to IOMA against at least two strains. Four of these 8 mutants ($F53N_{HC}$, $R54S_{HC}$, $V57T_{HC}$, $K58N_{HC}$) demonstrated this increase against all strains. Furthermore, 6 of 9 V_H inFACE mutants in the variable domain complementary determining region 2 (CDRH2) regions showed such impaired neutralization against at least 2 strains indicating the importance of SHM in this region. In the V_L domain, 4 of 7 inFACE mutants ($R27S_{LC}$, $G29S_{LC}$, $D94G_{LC}$, $G95S_{LC}$) resulted in >3-fold increases in IC_{50} compared to IOMA against at least 2 strains. In one of these mutants, $G29_{LC}$ was reverted to the iGL Ser residue. The Gly in this position was hypothesized to facilitate CDRL1 flexibility necessary to accommodate the $N276_{gp120}$ glycan[8]. Our results support the pertinent role of this mutation in IOMA's neutralization function.

IOMAmin constructs show comparable neutralization potency and breadth to IOMA

Based on the data from the exFACE and inFACE single mutant neutralization screen, we designed $IOMA_{min}$ constructs with the minimal numbers of mutations required to maintain IOMA's neutralization potency and breadth across the entire V_H and V_L. To do so, we built upon the exFACEmin mutant by incorporating inFACE mutations. We designed three mutants based on the following criteria: $IOMA_{min3}$ included inFACE mutations that had IC_{50} values within 2-fold of IOMA against all four strains, $IOMA_{min4}$ included inFACE mutations that had IC_{50} values within 2-fold of IOMA against at least three strains, and $IOMA_{min4v2}$ included inFACE mutations from $IOMA_{min4}$ in the V_H and no inFACE mutations in the V_L as found in $IOMA_{min3}$ (Figure 2E).

We evaluated $IOMA_{exFACEmin}$, $IOMA_{min3}$, $IOMA_{min4}$, and $IOMA_{min4v2}$ against the 12-strain neutralization panel and six additional screening strains (Figure 3A). Overall, $IOMA_{exFACEmin}$ had the most comparable neutralization profile compared to IOMA, exhibiting IC_{50} values within 2-fold of IOMA against all strains except one. $IOMA_{min3}$ showed IC_{50}s within 2-fold of IOMA against all strains except for two, and $IOMA_{min3}$ showed IC_{50} values within 2-fold of IOMA against all strains except for three. $IOMA_{min4}$ demonstrated the worst neutralization profile compared to IOMA, with IC_{50}s within 2-fold of IOMA against only half of the strains tested. Together this data suggests that IOMA inFACE SHMs evolved to improve neutralization and potency unlike the neutral SHMs identified in the exFACE.

Discussion

The development of an effective HIV-1 vaccine has proved to be an immense challenge (cite reviews). The identification and characterization of bNAbs against conserved Env epitopes has provided a framework that have led to immunogens that are engineered to elicit bNAbs against particular epitopes and/or bNAbs of a particular class[26–28,33–35]. Immunogen design to elicit bNAbs that bind the CD4bs are of especial interest, considering CD4bs bNAbs have

been well-characterized and are of the most broad and potent[14,21]. However, the CD4bs epitope is composed of a recessed pocket that is framed by bulky N-linked glycans, which present steric challenges that require CD4bs bNAbs to adopt rare features that further challenge vaccine design efforts[14,21,23,36,37].

The IOMA-class of CD4bs bNAbs is thought to alleviate some of these barriers because its neutralization activity does not require many of the rare features that other CD4bs bNAb classes do, making it a potentially more realistic vaccine target. IOMA-class bNAbs contain lower levels of SHM compared to most CD4bs bNAbs, an 8-amino acid CDRL3, and fewer mutations in CDRL1 to accommodate the $N276_{gp120}$ glycan[8,22,27]. We further characterized IOMA's neutralization mechanism by evaluating the role of SHMs. We identified 5 V_H and 2 V_L exFACE SHMs that contribute to neutralization by IOMA but are not predicted to interact with Env gp120 residues. In the V_H domain, the proximity of these mutations to the $N197_{gp120}$ glycan suggested they evolved to stabilize or accommodate glycan interactions. Furthermore, we found that almost half of all V_L SHMs mutations are in the exFACE and appear to play no role in neutralization by IOMA. This suggested that the V_L domain accumulated some unrequired mutations, likely resulting from IOMA's prolonged maturation process. For inFACE SHMs that were predicted to contact gp120 residues, we found that most mutations in the V_H and V_L domains contribute to IOMA's neutralization activity. In particular, inFACE SHMs in CDRL1, adjacent to the $N276_{gp120}$ glycan, proved to be necessary for IOMA's potency and breadth. Again, this suggests IOMA accrued these mutations to accommodate CD4bs glycans.

Together, the identification of mutations in IOMA that confer bNAb neutralization activity reveal some of the viral pressures that influenced IOMA's development towards neutralization breadth. Furthermore, we anticipate that this information can be used to engineer IOMA-targeting immunogens and evaluate potential IOMA-class bNAb sequences isolated from experimental vaccine regimens.

Methods

IOMA mutant construct design

IOMAmin exFACE and inFACE mutations were determined by analyzing the interactions using PyMol (Schrödinger LLC) between BG505 and IOMA in a BG505-IOMA-10-1074 structure (PDB 5T3Z). IOMA residues that formed bonds with BG505 that were ≤4.0 Å were determined as inFACE residues, and the remaining SHMs were defined as exFACE residues. IOMA exFACE and inFACE single mutants were generated using site-directed mutagenesis (Agilent QuikChange) in the p3BNC expression vector. $IOMA_{exFACEmin}$ and $IOMA_{min}$ mutants were generated using Gibson cloning(NEB Gibson Assembly).

Protein expression and purification

DNA encoding IgGs and Fabs were transfected using the transient Expi293 expression system (ThermoFisher) according to the manufacture protocol[7,38]. Expression vectors included genes of IgG HC or Fab HC and LC. Fab HC expression vectors included a C-terminal 6x-His tag. Cell supernatants from IgG and Fab transfections were first purified using protein A (GE Healthcare) and Ni^{2+}-NTA (GE Healthcare) affinity chromatography, respectively. Subsequently, IgG and Fabs were purified over size exclusion chromatography (SEC) using a Superdex 200 10/300 column (GE Healthcare).

BG505 SOSIP.664 Env constructs encoded SOSIP mutations including disulfide mutations 501C and 605C (SOS), I559P (IP), and the furin cleavage site mutated to six arginine residues (6R)[32]. BG505 SOSIP.664 Env expression vectors were transfected using the transient Expi293 expression system (ThermoFisher) according to the manufacture protocol. Env was separated from cell supernatants using PGT145 immunoaffinity chromatography and SEC using a Superose 6 10/300 column (GE Healthcare)[32,39].

In Vitro HIV-1 TZM.bl Neutralization Assays

Neutralization activities of IOMA-based IgGs were determined using a luciferase-based TZM.bl pseudovirus assay operating with standard protocols[40,41]. IC_{50} values were

determined from independent replicates (n=2) analyzed using Antibody Database (v2.0)[42] with 5-parameter curve fitting. Non-specific activity was determined by testing against murine leukemia virus (MuLV).

Structural analyses

PyMol (Schrödinger LLC) and UCSF ChimeraX[43] were used to prepare structure figures. Defined interactions were assigned tentatively due to the low resolution of complex structures using the following criteria: hydrogen bonds were assigned pairwise interactions that were less than 4.0 Å and with an A-D-H angle >90°, and van der Waals interactions were assigned as distances between atoms that were less than 4.0 Å.

Acknowledgements

We thank J. Vielmetter, A. Rorick, K. Storm, and the Protein Expression Center in the Beckman Institute at Caltech for expression assistance. This work was supported by the National Institute of Allergy and Infectious Diseases (NIAID) Grant HIVRAD P01 AI100148 (to P.J.B.), the Bill and Melinda Gates Foundation Collaboration for AIDS Vaccine Discovery (CAVD) grant INV-002143 (P.J.B.), and NIH P50 AI150464 (P.J.B.). The contents of this publication are solely the responsibility of the authors and do not necessarily represent the official views of NIAID or NIH.

Author contributions

K.A.D., H.B.G., and P.J.B. designed the research. K.A.D. and E.Y.L. cloned IOMA constructs and performed protein purification. K.A.D. completed structural studies. P.N.P.G. performed in vitro neutralization assays. K.A.D., H.B.G., and P.J.B. analyzed results. K.A.D. and P.J.B. wrote the manuscript with input from co-authors.

Competing interests

The authors declare that there are no competing interests

References

1. Lee, J.H., and Crotty, S. (2021). HIV vaccinology: 2021 update. Semin. Immunol. *51*, 101470. 10.1016/j.smim.2021.101470.

2. Escolano, A., Dosenovic, P., and Nussenzweig, M.C. (2017). Progress toward active or passive HIV-1 vaccination. J. Exp. Med. *214*, 3–16. 10.1084/jem.20161765.

3. Bar, K.J., Sneller, M.C., Harrison, L.J., Justement, J.S., Overton, E.T., Petrone, M.E., Salantes, D.B., Seamon, C.A., Scheinfeld, B., Kwan, R.W., et al. (2016). Effect of HIV Antibody VRC01 on Viral Rebound after Treatment Interruption. N. Engl. J. Med. *375*, 2037–2050. 10.1056/NEJMoa1608243.

4. Bar-On, Y., Gruell, H., Schoofs, T., Pai, J.A., Nogueira, L., Butler, A.L., Millard, K., Lehmann, C., Suárez, I., Oliveira, T.Y., et al. (2018). Safety and antiviral activity of combination HIV-1 broadly neutralizing antibodies in viremic individuals. Nat. Med. *24*, 1701–1707. 10.1038/s41591-018-0186-4.

5. VRC 602 Study Team, Ledgerwood, J.E., Coates, E.E., Yamshchikov, G., Saunders, J.G., Holman, L., Enama, M.E., DeZure, A., Lynch, R.M., Gordon, I., et al. (2015). Safety, pharmacokinetics and neutralization of the broadly neutralizing HIV-1 human monoclonal antibody VRC01 in healthy adults. Clin. Exp. Immunol. *182*, 289–301. 10.1111/cei.12692.

6. Schommers, P., Gruell, H., Abernathy, M.E., Tran, M.-K., Dingens, A.S., Gristick, H.B., Barnes, C.O., Schoofs, T., Schlotz, M., Vanshylla, K., et al. (2020). Restriction of HIV-1 Escape by a Highly Broad and Potent Neutralizing Antibody. Cell *180*, 471-489.e22. 10.1016/j.cell.2020.01.010.

7. Yang, Z., Dam, K.-M.A., Bridges, M.D., Hoffmann, M.A.G., DeLaitsch, A.T., Gristick, H.B., Escolano, A., Gautam, R., Martin, M.A., Nussenzweig, M.C., et al. (2022). Neutralizing antibodies induced in immunized macaques recognize the CD4-binding site on an occluded-open HIV-1 envelope trimer. Nat. Commun. *13*, 732. 10.1038/s41467-022-28424-3.

8. Gristick, H.B., von Boehmer, L., West Jr, A.P., Schamber, M., Gazumyan, A., Golijanin, J., Seaman, M.S., Fätkenheuer, G., Klein, F., Nussenzweig, M.C., et al. (2016). Natively glycosylated HIV-1 Env structure reveals new mode for antibody recognition of the CD4-binding site. Nat. Publ. Group *23*, 906–915. 10.1038/nsmb.3291.

9. Barnes, C.O., Gristick, H.B., Freund, N.T., Escolano, A., Lyubimov, A.Y., Hartweger, H., West, A.P., Cohen, A.E., Nussenzweig, M.C., and Bjorkman, P.J. (2018). Structural characterization of a highly-potent V3- glycan broadly neutralizing antibody bound to natively-glycosylated HIV-1 envelope. Nat. Commun., 1–12. 10.1038/s41467-018-03632-y.

10. Abernathy, M.E., Dam, K.-M.A., Esswein, S.R., Jette, C.A., and Bjorkman, P.J. (2021). How Antibodies Recognize Pathogenic Viruses: Structural Correlates of Antibody Neutralization of HIV-1, SARS-CoV-2, and Zika. Viruses *13*, 2106. 10.3390/v13102106.

11. Barnes, C.O., Schoofs, T., Gnanapragasam, P.N.P., Golijanin, J., Huey-Tubman, K.E., Gruell, H., Schommers, P., Suh-Toma, N., Lee, Y.E., Cetrulo Lorenzi, J.C., et al. (2022). A naturally arising broad and potent CD4-binding site antibody with low somatic mutation. Sci. Adv. *8*, eabp8155. 10.1126/sciadv.abp8155.

12. West Jr, A.P., Scharf, L., Scheid, J.F., Klein, F., Bjorkman, P.J., and Nussenzweig, M.C. (2014). Structural Insights on the Role of Antibodies in HIV-1 Vaccine and Therapy. Cell *156*, 633–648. 10.1016/j.cell.2014.01.052.

13. Sanders, R.W., and Moore, J.P. (2017). Native-like Env trimers as a platform for HIV-1 vaccine design. Immunol. Rev. *275*, 161–182.

14. Stamatatos, L., Pancera, M., and McGuire, A.T. (2017). Germline-targeting immunogens. Immunol. Rev. *275*, 203–216. 10.1111/imr.12483.

15. Burton, D.R. (2019). Advancing an HIV vaccine; advancing vaccinology. Nat. Rev. Immunol. *19*, 77–78. 10.1038/s41577-018-0103-6.

16. Zhou, T., Georgiev, I., Wu, X., Yang, Z.-Y., Dai, K., Finzi, A., Do Kwon, Y., Scheid, J.F., Shi, W., Xu, L., et al. (2010). Structural Basis for Broad and Potent Neutralization of HIV-1 by Antibody VRC01. Science *329*, 811–817. 10.1126/science.1192819.

17. Zhou, T., Zhu, J., Wu, X., Moquin, S., Zhang, B., Acharya, P., Georgiev, I.S., Altae-Tran, H.R., Chuang, G.-Y., Joyce, M.G., et al. (2013). Multidonor Analysis Reveals Structural Elements, Genetic Determinants, and Maturation Pathway for HIV-1 Neutralization by VRC01-Class Antibodies. Immunity *39*, 245–258. 10.1016/j.immuni.2013.04.012.

18. Huang, J., Kang, B.H., Ishida, E., Zhou, T., Griesman, T., Sheng, Z., Wu, F., Doria-Rose, N.A., Zhang, B., McKee, K., et al. (2016). Identification of a CD4-Binding-Site Antibody to HIV that Evolved Near-Pan Neutralization Breadth. Immunity *45*, 1108–1121. 10.1016/j.immuni.2016.10.027.

19. Scheid, J.F., Mouquet, H., Ueberheide, B., Diskin, R., Klein, F., Oliveira, T.Y.K., Pietzsch, J., Fenyo, D., Abadir, A., Velinzon, K., et al. (2011). Sequence and Structural Convergence of Broad and Potent HIV Antibodies That Mimic CD4 Binding. Science *333*, 1633–1637. 10.1126/science.1207227.

20. Wu, X., Yang, Z.-Y., Li, Y., Hogerkorp, C.-M., Schief, W.R., Seaman, M.S., Zhou, T., Schmidt, S.D., Wu, L., Xu, L., et al. (2010). Rational Design of Envelope Identifies Broadly Neutralizing Human Monoclonal Antibodies to HIV-1. Science *329*, 856–861. 10.1126/science.1187659.

21. West Jr, A.P. (2012). Structural basis for germ-line gene usage of a potent class of antibodies targeting the CD4-binding site of HIV-1 gp120. PNAS, 1–8. 10.1073/pnas.1208984109/-/DCSupplemental.

22. van Schooten, J., Farokhi, E., Schorcht, A., van den Kerkhof, T.L.G.M., Gao, H., van der Woude, P., Burger, J.A., Meesters, T.G.R., Bijl, T., Ghalaiyini, R., et al. (2022).

Identification of IOMA-class neutralizing antibodies targeting the CD4-binding site on the HIV-1 envelope glycoprotein. Nat. Commun. *13*, 4515. 10.1038/s41467-022-32208-0.

23. Landais, E., and Moore, P.L. (2018). Development of broadly neutralizing antibodies in HIV-1 infected elite neutralizers. Retrovirology *15*, 61. 10.1186/s12977-018-0443-0.

24. Jardine, J.G., Ota, T., Sok, D., Pauthner, M., Kulp, D.W., Kalyuzhniy, O., Skog, P.D., Thinnes, T.C., Bhullar, D., Briney, B., et al. (2015). Priming a broadly neutralizing antibody response to HIV-1 using a germline-targeting immunogen. Science *349*, 156–161. 10.1126/science.aac5894.

25. Jardine, J.G., Kulp, D.W., Havenar-Daughton, C., Sarkar, A., Briney, B., Sok, D., Sesterhenn, F., Ereno-Orbea, J., Kalyuzhniy, O., Deresa, I., et al. (2016). HIV-1 broadly neutralizing antibody precursor B cells revealed by germline-targeting immunogen. Science *351*, 1458–1463. 10.1126/science.aad9195.

26. Jardine, J., Julien, J.-P., Menis, S., Ota, T., Kalyuzhniy, O., McGuire, A., Sok, D., Huang, P.-S., MacPherson, S., Jones, M., et al. (2013). Rational HIV Immunogen Design to Target Specific Germline B Cell Receptors. Science *340*, 711–716. 10.1126/science.1234150.

27. Gristick, H.B., Hartweger, H., Maximillian, L., van Schooten, J., Ramos, V., Oliveira, T., Nishimura, Y., Koranda, N., Wall, A., Kai-Hui, Y., et al. (2022). CD4-binding site immunogens elicit heterologous anti-HIV-1 neutralizing antibodies in transgenic and wildtype animals. Submitted.

28. Parks, K.R., MacCamy, A.J., Trichka, J., Gray, M., Weidle, C., Borst, A.J., Khechaduri, A., Takushi, B., Agrawal, P., Guenaga, J., et al. (2019). Overcoming Steric Restrictions of VRC01 HIV-1 Neutralizing Antibodies through Immunization. CellReports *29*, 3060-3072.e7. 10.1016/j.celrep.2019.10.071.

29. Lin, Y.-R., Parks, K.R., Weidle, C., Naidu, A.S., Khechaduri, A., Riker, A.O., Takushi, B., Chun, J.-H., Borst, A.J., Veesler, D., et al. (2020). HIV-1 VRC01 Germline-Targeting

Immunogens Select Distinct Epitope-Specific B Cell Receptors. Immunity *53*, 840-851.e6. 10.1016/j.immuni.2020.09.007.

30. Jardine, J.G., Sok, D., Julien, J.-P., Briney, B., Sarkar, A., Liang, C.-H., Scherer, E.A., Henry Dunand, C.J., Adachi, Y., Diwanji, D., et al. (2016). Minimally Mutated HIV-1 Broadly Neutralizing Antibodies to Guide Reductionist Vaccine Design. PLoS Pathog. *12*, e1005815-33.

31. Umotoy, J., Bagaya, B.S., Joyce, C., Schiffner, T., Menis, S., Saye-Francisco, K.L., Biddle, T., Mohan, S., Vollbrecht, T., Kalyuzhniy, O., et al. (2019). Rapid and Focused Maturation of a VRC01-Class HIV Broadly Neutralizing Antibody Lineage Involves Both Binding and Accommodation of the N276-Glycan. Immunity *51*, 141-154.e6. 10.1016/j.immuni.2019.06.004.

32. Sanders, R.W., Derking, R., Cupo, A., Julien, J.-P., Yasmeen, A., de Val, N., Kim, H.J., Blattner, C., de la Peña, A.T., Korzun, J., et al. (2013). A Next-Generation Cleaved, Soluble HIV-1 Env Trimer, BG505 SOSIP.664 gp140, Expresses Multiple Epitopes for Broadly Neutralizing but Not Non-Neutralizing Antibodies. PLoS Pathog. *9*, e1003618-20. 10.1371/journal.ppat.1003618.

33. Escolano, A., Steichen, J.M., Dosenovic, P., Kulp, D.W., Golijanin, J., Sok, D., Freund, N.T., Gitlin, A.D., Oliveira, T., Araki, T., et al. (2016). Sequential Immunization Elicits Broadly Neutralizing Anti-HIV-1 Antibodies in Ig Knockin Mice. Cell *166*, 1445-1458.e12.

34. Medina-Ramírez, M., Garces, F., Escolano, A., Skog, P., de Taeye, S.W., Del Moral-Sanchez, I., McGuire, A.T., Yasmeen, A., Behrens, A.-J., Ozorowski, G., et al. (2017). Design and crystal structure of a native-like HIV-1 envelope trimer that engages multiple broadly neutralizing antibody precursors in vivo. J. Exp. Med. *214*, 2573–2590.

35. Steichen, J.M., Kulp, D.W., Tokatlian, T., Escolano, A., Dosenovic, P., Stanfield, R.L., McCoy, L.E., Ozorowski, G., Hu, X., Kalyuzhniy, O., et al. (2016). HIV Vaccine Design to

Target Germline Precursors of Glycan-Dependent Broadly Neutralizing Antibodies. Immunity *45*, 483–496.

36. Kwong, P.D., Wyatt, R., Robinson, J., Sweet, R.W., Sodroski, J., and Hendrickson, W.A. (1998). Structure of an HIV gp120 envelope glycoprotein in complex with the CD4 receptor and a neutralizing human antibody. Nature *393*, 648–659. 10.1038/31405.

37. McCoy, L.E. (2018). The expanding array of HIV broadly neutralizing antibodies. Retrovirology *15*, 70. 10.1186/s12977-018-0453-y.

38. Dam, K.-M.A., Mutia, P.S., and Bjorkman, P.J. (2022). Comparing methods for immobilizing HIV-1 SOSIPs in ELISAs that evaluate antibody binding. Sci. Rep. *12*, 11172. 10.1038/s41598-022-15506-x.

39. Cupo, A., Cruz Portillo, V.M., Gelfand, P., Yasmeen, A., Klasse, P.J., and Moore, J.P. (2019). Optimizing the production and affinity purification of HIV-1 envelope glycoprotein SOSIP trimers from transiently transfected CHO cells. PLOS ONE *14*, e0215106. 10.1371/journal.pone.0215106.

40. Sarzotti-Kelsoe, M., Bailer, R.T., Turk, E., Lin, C., Bilska, M., Greene, K.M., Gao, H., Todd, C.A., Ozaki, D.A., Seaman, M.S., et al. (2014). Optimization and validation of the TZM-bl assay for standardized assessments of neutralizing antibodies against HIV-1. J. Immunol. Methods *409*, 131–146. 10.1016/j.jim.2013.11.022.

41. deCamp, A., Hraber, P., Bailer, R.T., Seaman, M.S., Ochsenbauer, C., Kappes, J., Gottardo, R., Edlefsen, P., Self, S., Tang, H., et al. (2014). Global Panel of HIV-1 Env Reference Strains for Standardized Assessments of Vaccine-Elicited Neutralizing Antibodies. J. Virol. *88*, 2489–2507. 10.1128/JVI.02853-13.

42. West, A.P., Scharf, L., Horwitz, J., Klein, F., Nussenzweig, M.C., and Bjorkman, P.J. Computational analysis of anti–HIV-1 antibody neutralization panel data to identify potential functional epitope residues. Comput. Biol., 6.

43. Goddard, T.D., Huang, C.C., Meng, E.C., Pettersen, E.F., Couch, G.S., Morris, J.H., and Ferrin, T.E. (2018). UCSF ChimeraX: Meeting modern challenges in visualization and analysis: UCSF ChimeraX Visualization System. Protein Sci. *27*, 14–25. 10.1002/pro.3235.

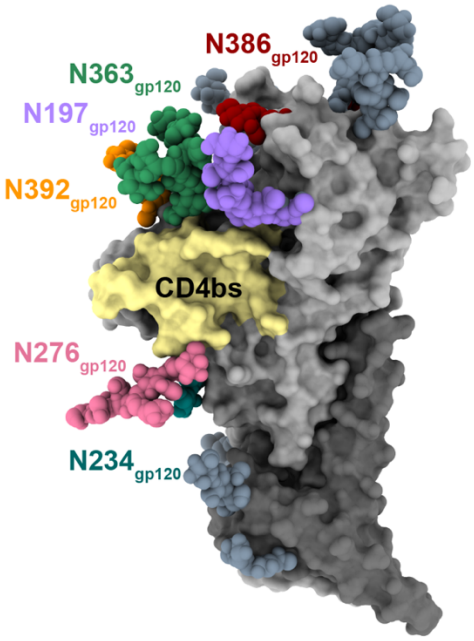

gp120 PNGS	Percent Conserved (%)
N197	89
N234	81
N276	94
N362/N363	33/9
N386	79
N462	30

Figure 1: Env CD4bs glycans are highly conserved

(Left) Surface representation of HIV-1 Env gp120/gp41 protomer with glycans represented as spheres (PDB 5T3Z). CD4bs glycans and the CD4bs gp120 epitope are depicted in various colors.

(Right) Table summarizing CD4bs PNGS conservation. The PNGS percent conserved was calculated using HIV Antibody Database[42].

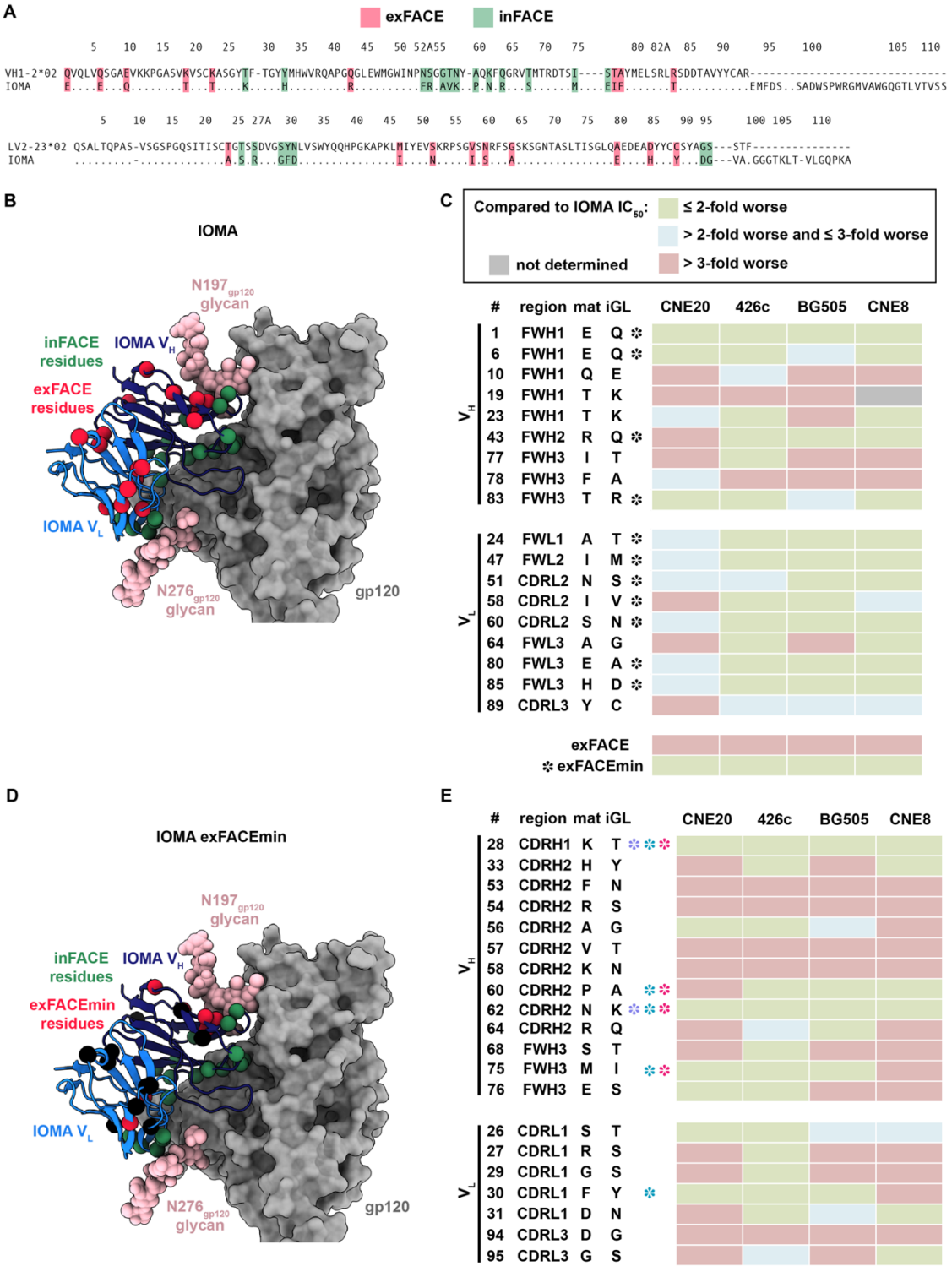
A
exFACE
inFACE
VH1-2*02 QVQLVQSGAEVKKPGASVKVSCKASGYTF-TGYYMHWVRQAPGQGLEWMGWINPNSGGTNY-AQKFQGRVTMTRDTSI----STAYMELSRLRSDDTAVYYCAR----------
IOMA E....E...Q.....T...T....K.....H.....R.....FR.AVK..P.N.R...S.....M....EIF.....T.....EMFDS..SADWSPWRGMVAWGQGTLVTVSS
LV2-23*02 QSALTQPAS-VSGSPGQSITISCTGTSSDVGSYNLVSWYQQHPGKAPKLMIYEVSKRPSGVSNRFSGSKSGNTASLTISGLQAEDEADYYCCSYAGS---STF----------
IOMA .....-.....A.S.R...GFD.....I....N.....I.S...A.....E....H...Y...DG---VA.GGGTKLT-VLGQPKA
B
IOMA
N197gp120 glycan
inFACE residues
IOMA VH
exFACE residues
IOMA VL
N276gp120 glycan
gp120
C
Compared to IOMA IC50:
≤ 2-fold worse
> 2-fold worse and ≤ 3-fold worse
not determined
> 3-fold worse
region mat iGL CNE20 426c BG505 CNE8
VH
1 FWH1 E Q
6 FWH1 E Q
10 FWH1 Q E
19 FWH1 T K
23 FWH1 T K
43 FWH2 R Q
77 FWH3 I T
78 FWH3 F A
83 FWH3 T R
VL
24 FWL1 A T
47 FWL2 I M
51 CDRL2 N S
58 CDRL2 I V
60 CDRL2 S N
64 FWL3 A G
80 FWL3 E A
85 FWL3 H D
89 CDRL3 Y C
exFACE
exFACEmin
D
IOMA exFACEmin
N197gp120 glycan
inFACE residues
IOMA VH
exFACEmin residues
IOMA VL
N276gp120 glycan
gp120
E
region mat iGL CNE20 426c BG505 CNE8
VH
28 CDRH1 K T
33 CDRH2 H Y
53 CDRH2 F N
54 CDRH2 R S
56 CDRH2 A G
57 CDRH2 V T
58 CDRH2 K N
60 CDRH2 P A
62 CDRH2 N K
64 CDRH2 R Q
68 FWH3 S T
75 FWH3 M I
76 FWH3 E S
VL
26 CDRL1 S T
27 CDRL1 R S
29 CDRL1 G S
30 CDRL1 F Y
31 CDRL1 D N
94 CDRL3 D G
95 CDRL3 G S

Figure 2: Neutralization profile of IOMA exFACE and inFACE mutants informs $IOMA_{min}$ designs

(A) Sequence alignment of germline and mature IOMA V_H and V_L exFACE SHMs are highlighted in crimson and inFACE SHMs are highlighted in green.

(B) Structure of the IOMA-BG505 complex (PDB 5T3Z). BG505 gp120 is shown as a surface rendering with spheres representing $N197_{gp120}$ and $N276_{gp120}$ glycans. IOMA is represented in cartoon, with crimson spheres identifying exFACE SHMs and green spheres identifying inFACE SHMs.

(C) Table summarizing IOMA V_H and V_L exFACE mutant neutralization compared to IOMA against CNE20, 426c, BG505, and CNE8. Mutant IC_{50}s ≤2-fold worse than IOMA are represented with green boxes, IC_{50}s >2-fold worse and ≤3-fold worse than IOMA are represented with blue boxes, and IC_{50}s >3-fold worse than IOMA are represented with red boxes. Grey boxes indicate IC_{50}s that were not determined. ✻ indicates exFACE mutations that were incorporated in $IOMA_{exFACEmin}$.

(D) Structure of the IOMA-BG505 complex (PDB 5T3Z). BG505 gp120 is shown as a surface rendering with spheres representing $N197_{gp120}$ and $N276_{gp120}$ glycans. IOMA is represented in cartoon, with crimson spheres identifying exFACEmin SHMs and green spheres identifying inFACE SHMs. Black spheres represent the remaining SHMs.

(E) Table summarizing IOMA V_H and V_L inFACE mutant neutralization compared to IOMA, against CNE20, 426c, BG505, and CNE8. Mutant IC_{50}s ≤2-fold worse than IOMA are represented with green boxes, IC_{50}s > 2-fold worse and ≤3-fold worse than IOMA are represented with blue boxes, and IC_{50}s >3-fold worse than IOMA are represented with red boxes. Grey boxes indicate IC50s that were not determined. Lilac ✻ indicates inFACE mutations that were incorporated in IOMAmin3, teal ✻ indicates inFACE mutations that were incorporated in IOMAmin4, and pink ✻ indicates inFACE mutations that were incorporated in IOMAmin4v2.

A

Compared to IOMA IC_{50}: ≤ 2-fold worse; > 2-fold worse and ≤ 3-fold worse; > 3-fold worse; not determined

	strain	clade	tier	IOMA	exFACE min*	min3*	min4*	min4v2*
12-strain	246F3	AC	2	>200	>200	>200	>200	>200
	BJOX002000	BC	2	>200	>200	>200	>200	>200
	CH119	BC	2	>200	>200	>200	>200	>200
	CNE55	AE	2	12	4.5	8.2	28	3.4
	CNE8	AE	2	31	43			
	CE1176	C	2	2.6	0.73	1.7	0.94	0.88
	25710	C	1B	1.90	2.6	3.8	11.6	7.1
	X1632	G	2	1.8	0.63	1.2	0.83	0.67
	X2278	B	2	1.4	0.33	0.83	0.52	0.7
	TRO11	B	2	1.0	0.5	1.3	1.9	1.6
	CE0217	C	2	0.35	0.09	0.17	0.13	0.12
	398F1	A	2	0.25	3.4	3.7	2.7	0.93
screening	BG505 T332N	A	2	18	10	12	8.7	7.2
	ZM214M.PL15	G	2	1.9	1.2	1.7	2.3	1.9
	PVO.4	B	3	1.7	1.4	2	2.2	2.10
	426c	C	2	0.84	0.71	0.98	2.1	1.3
	Yu2	B	2	0.61	0.36	0.86	1.8	1.6
	CNE20	BC	2	0.27		0.92	0.57	

Figure 3: Summary of neutralization profile of IOMAmin constructs

(A) Table summarizing IOMA, $IOMA_{exFACEmin}$, $IOMA_{min3}$, $IOMA_{min4}$, and $IOMA_{min4v2}$ mutant neutralization against the 12-strain neutralization panel and 6 additional screen mutations. Mutant IC_{50}s ≤2-fold worse than IOMA are represented with green boxes, IC_{50}s >2-fold worse and ≤3-fold worse than IOMA are represented with blue boxes, and IC_{50}s >3-fold worse than IOMA are represented with red boxes. Grey boxes indicate IC_{50}s that were not determined.